CLIMATOLOGY AND FORCING MECHANISMS OF FUNNEL CLOUDS IN ALASKA

By

Stanley G. Edwin, B.S.

A Thesis Submitted in Partial Fulfillment of the Requirements

for the Degree of

Master of Science

in

Atmospheric Sciences

University of Alaska Fairbanks

August 2016

APPROVED:

Dr. Dr. Nicole Mölders, Committee Chair
Dr. Uma S. Bhatt, Committee Member
Dr. Richard L. Collins, Committee Member
Dr. Uma S. Bhatt, Chair
    Department of Atmospheric Sciences
Dr. Paul W. Layer, Dean
    College of Natural Science and Mathematics
Dr. Michael Castellini
    Interim Dean of the Graduate School

Abstract

There are no forecasting systems for funnel clouds for Alaska. The inability of forecasting is problematic because funnel clouds pose a threat to aviation, which serves as Alaska's main form of transportation. Motivated by the lack of research on the formation of funnel clouds in Alaska, this research investigated characteristics of funnel clouds and atmospheric conditions under which funnel clouds form using operational Doppler weather radars and radiosonde soundings as well as synoptic weather maps. In Alaska, funnel clouds usually occur during the summer months May to September with a maximum of occurrence in July and around 1500 Alaska Daylight Time as shown in the funnel cloud observational data. The observed funnel clouds are usually not associated with severe thunderstorms and do not occur with strong synoptic scale forcing. As such, it was hypothesized that local effects from sea breeze fronts and orographic circulations might be the main forcing. Operational soundings indicate that some, but not all funnel cloud events occurred under large Convective Available Potential Energy (greater than 500 J) and strong low-level wind shear. Funnel clouds were difficult to identify in routine operational Doppler weather radars because the funnel clouds display small cross-sectional area compared to the radar resolution. An algorithm to retrieve similar vertical profiles from the entire radiosonde data than those observed during documented funnel cloud events was developed. By using similarity between radiosonde profiles of days of the observed funnel clouds and the similar radiosonde profiles scanned over the years, an idea of funnel cloud or severe storm occurrence can be ascertained. The mechanisms for funnel cloud formation differ by region. In Interior Alaska, the Alaska Range's katabatic slope winds and the Tanana Valley wind create the needed vorticity. Along the west coast of Alaska, air-sea interaction plays a role. In Cook Inlet, topography and land-sea play a role. All funnel cloud events have weak synoptic scale forcing.

Table of Contents

List of Figures

List of Tables

Acknowledgements

Chapter 1 Introduction

Alaska is known for its rugged beauty and unforgiving wilds to the public. It is also known for its harsh environment, with temperature ranges from -50 degree Fahrenheit to 100 degree above (-45.6°C to 100°C) (Shulski and Wendler 2007).

What is the least common weather phenomenon that one would expect in Alaska? It is not so well known that Alaska does, on occasion, have funnel clouds (Fig. 1.1a), and may even have tornados as in the Great Plains (Fig. 1.1b). Funnel clouds and tornados are distinguished in that a tornado touches the ground and a funnel cloud does not (Wakimoto and Wilson 1989; Modahl and Gray 1971). Furthermore, it is not known whether funnel clouds have been observed with greater frequency over the years in Alaska (Fig. 1.2, Table 1.1).

a)   b)

Fig. 1.1. a) Funnel cloud on 22 July 2010, 9:47am local time directly over Fairbanks Alaska (with permission Dr. Uma Bhatt). b) Supercell 13 June 2011 Colorado plains out of Denver (S. Edwin).
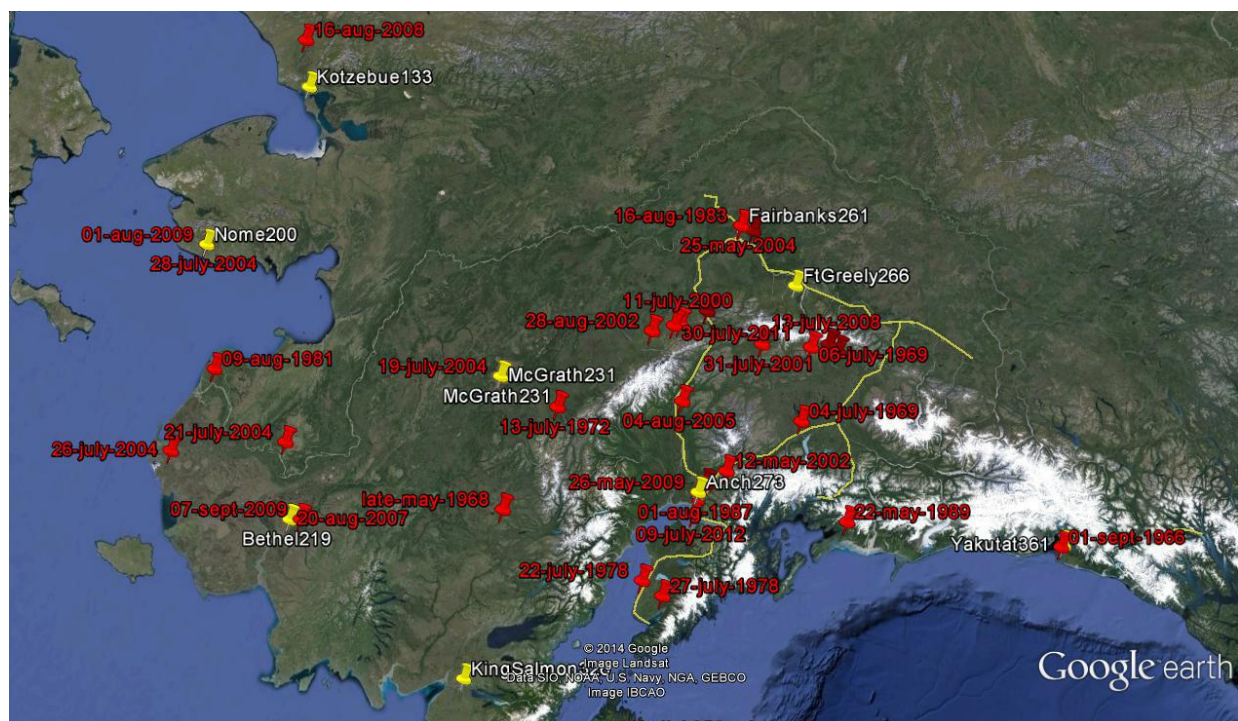
Fig. 1.2. Funnel cloud sightings in Alaska from 1955 to 2014. Red pins denote sightings and dates. Yellow pins denote radiosonde launch locations. Alaska map from Google earth.

Table.1.1. Funnel cloud sighting dates and times with location and UTC date and time with the closest radiosonde launch station. The white rows are sightings without any time given, these row are estimated at 12 noon UTC and midnight, or 00 for next day UTC, for the date given, this is due to the 8 hour and 9 hour difference between local AKST and UTC. The other color is with a time given during the sighting.

Year	Month	Day	Local Time	Location	Direction & Coordinate	UTC	Radiosonde date, bfr	Radiosonde date,aft	Radiosonde Station
1955	7	3		Den Nat Park	5mi W of Den Nat Park HQ		1955070312	1955070400	denali
1966	9	1	4pm AST	Yakutat	W-SW from Airport, aloft	0100 nd	1966090200		yakutat
1968	5	late		Sparrevohn AFB	61*06'N 155*33'W				
1969	7	4		Snowshoe Lake	62*02'N 146*40'W		1969070412	1969070500	anch-2
1969	7	6		Tangle Lakes	25mi from Paxson, aloft		1969070612	1969070700	anch-3
1972	7	13	1:28pm ADT	Farwell	62*31'N 153*53'W near Ak Range Mountains	2128		1972071400	mcg
1978	7	22	10:00am ADT	Ninilchick	25mi N-NW from Ninilchick	1800	1978072212	1978072300	anch-2
1978	7	27	5:30pm ADT	Snowshoe Lake	N of Snowshoe Lake	0130 nd	1978072800		anch-2
1980	7	27	6:30pm ADT	Paxson	20mi N-NW of Paxson	0230 nd	1980072800		anch-3
1981	8	9	4:45pm ADT	Emmonak	Near Village	0045 nd	1981080700		west coast
1981	8	11			NW Interior Western Brooks Range				
1982	7	10	3:35pm ADT	North Pole	10mi NE of North Pole	2335		1982071100	fbks
1983	7	31	2:30pm ADT	Fairbanks	two just S of fairbanks	2230		1983080100	fbks
1983	8	16 ·	1:40pm ADT	Fairbanks	just NW of Fairbanks	2140		1983081700	fbks
1987	6	14	10:45am ADT	Anchorage	over Anchorage	1845	1987061412	1987061500	anch-1
1987	8	1	9:23pm ADT	Anchorage	over Anchorage	0523 nd	1987080200		anch-1
1989	5	22	4:30pm ADT	Cordova	reported by FAA observer	0030 nd	1989052300		anch-2
1994	8	24	4:10pm ADT	Yakutat	15mi E of Airport	0010 nd	1994082500		yakutat
2000	7	11	3:43pm ADT	Den Nat Park	from Parks, W of Savage River crossing, MP 14.7	2343		2000071200	denali
2001	7	31	5:30pm ADT	Denali Highway	Seen from Susitna River Bridge, 56mi from Cantwell, 79mi from Paxsion	130 nd	2001080100		anch-3
2002	5	12	2pm ADT	Palmer	Over Pioneer Peak	2200		2002051300	anch-1
2002	6	25	12:55pm ADT	Blue Mountain	6mi NW from Blue Mountain, 110mi S of King Salmon, NW of Pilot Point	2055		2002062600	anch-1
2002	6	25	1pm AST NOAA	Pilot Point		2200		2002062300	anch-1
2002	8	28	3pm ADT	Den Nat Park	From Wonder Lake, several mi N	2300		2002082900	denali
2002	8	28	8am AST NOAA	Den Nat Park		1700	2002082812		denali
2002	8	28	3pm AST NOAA	Den Nat Park		0000 nd	2002082900		denali
2004	6	21	3:55pm AST NOAA	Marshall		0055 nd	2004072200		beth
2004	5	25	6pm ADT NOAA	Fairbanks	few mi S of Fairbanks from Ft Wainwright	0200 nd	2004052600		fbks
2004	7	19	8:30pm ADT	McGrath		0430 nd	2004072000	2004072012	mcg
2004	7	28	1:25pm AST	Nome		2225		2004072900	west coast
2004	7	26	3pm AST NOAA	Chevak		0000 nd	2004072700		west cost
2005	8	4	3pm AST NOAA	Chulitna River Lodge		0000 nd	2005080500		anch-2
2007	7	31	5am AST NOAA	Metlakatla		1400	2007073112		Annette Is
2007	8	20		Bethel	Near Bethel		2007080712	2007080800	beth
2007	8	20	early evening,late afternoon	Bethel		00 nd - 12 nd	2007082100		beth
2008	7	13	9:15am AST NOAA	Paxson		1815	2008071312	2008071400	anch-3
2008	8	16		Noatak	Lower Noatak River Valley		2008081612	2008081700	west coast
2009	5	26	6pm ADT NOAA	Anchorage	11 mi E-SE of Anch, 61.1406 lat, -149.6091 lon, Wolverine Peak, Muni Bird Crk	0200 nd	2009052700		anch-1
2009	9	7	6:45pm AST	Kwethluk		345 nd	200909800		beth
2009	8	1		Nome	Norton Sound near Nome		2009080112	2009080200	west coast
2010	5	25		Paxson	20mi SE of Paxson		2010052512	2010052600	anch-3
2010	7	22	9:47am ADT	Fairbanks	Over Fairbanks	1747	2010072212		fbks
2011	7	30		Den Nat Park	Western Den Nat Park, between Eielson VC and Wonder Lake		2011073012	2011073100	denali
2012	7	9		Anchorage	Upper Cook Inlet S of Anchorage		2012070912	2012071000	anch-1
2014	7	20	6:30am AST NOAA	Anchorage	Anch Muni Bird Crk	1530	2014072012		anch-1

The idea that Alaska is immune to extreme weather turbulence is shattered by those few who have witnessed such occurrences. Forecasting and now-casting of funnel clouds is nonexistent in the broad and complex terrain of Alaska. Most funnel clouds are not associated with severe thunderstorms as in the Great Plains, but can pose a great risk to aviation. Another question related to Alaska's funnel clouds is the following: where in the dynamical scheme of dust devils, funnel clouds, water spots, and tornados from F0 to F5, do Alaska's funnels clouds fit in relation to their dynamic forcing mechanism (Table 1.2)?

Note that tornado intensity is classified on the Fuijta scale or F-scale Developed in 1971 by T. Theodore Fujita of the University of Chicago according to the damage caused on buildings and vegetation with F0 representing the least and F5 the strongest damage. The scale was developed based on surveys carried out by engineers and meteorologists. They looked at cyclonic marks, radar tracking, testimonies, and remote sensing techniques like aerial damage imagery, videogrammetry and photogrammetry (https://weather.com/storms/tornado/news/enhanced-fujita-scale-20130206).

Given the destructive forces of tornados, wind speeds can only be estimated. Tornados of scale F0, F1, F2, F3, F4, and F5 are estimated to have wind speeds of about 64-116 km/h (40.3-73.1 mph), 117-180 km/h (73.7-113.4 mph), 181-253 km/h (114-159.4 mph), 254-332 km/h (160-209.2 mph), 333-418 km/h (209.8-263.3 mph), and 419-512 km/h (264-322.6 mph), respectively. The wind speed of an F5 is close to half the speed of sound in a dry isothermal atmosphere at a temperature of 300 K, which is ~347 m/s or ~776 mph (e.g. Lin 2007). The width of a tornado's path is about 10-50 m, 30-150 m, 110-250 m, 200-500 m, 400-900 m, and 1.1 km, respectively. The damage caused is rated as light, moderate, significant, severe, devastating to incredible, respectively.

Table.1.2. Comparison of non-supercell tornados. From (Smith 1996)

Tornado type	Visual appearance	F-scale rating	Location in storm	Circulation depth	Range of radar detection	Threat to life and property
Gustnado	Whirl of dust or debris at or near ground; no condensation funnel	F0-F1 (possibly higher)	Along gust front or outflow; often with squall line or bow echo	Generally less than 1 to 2 km	Generally less than 25 nm (nautical miles)	YES
Landspout	Narrow, rope-like condensation funnel, often resembling a tube	F0-F2	Form with rapidly developing updrafts near convergence boundaries	Generally from 1 to 4 km; may grow upward with time	Generally less than 25 nm	YES

Due to the low population density in Alaska, the road network is sparse (Fig. 1.3). Many villages are off the road network and can only reached by water or air. The major highways connect the two major cities and run into Canada to the Lower 48 states. Thus, small aircrafts are flying below 3 km (10,000 ft.) throughout Alaska, and between the Brooks Range and Alaska Range (Fig. 1.3). While some Department of Transportation (DOT) airports exist, there are many landing stripes for hunting and fishing lodges, camps, and mining sites. Water aircrafts use large enough lakes or straight river-stretches for takeoff and landing.

The majority of the flights between villages are concentrated along the major valleys paralleling the major rivers, Yukon River, Tanana River, Kuskoquim River, etc. (Fig. 1.3). Furthermore, other major flying areas are the Cook Inlet basin around Anchorage and along all the coastlines of Alaska. The river valleys are situated from the Southwest and run to the Northeast. These valleys are a major corridor for small aircrafts crossing the state. Those aircrafts crossing any one of the three mountain ranges going from North to South or vice versa fly through mountain passes or over the mountain ranges (Fig. 1.3).

Flying in Alaska from the villages to the cities for shopping and gathering supplies is as common as public transportation may be for city residents using subways, trams, taxis and buses. Flying exposes Alaska's residents to a large list of hazards such as treacherous mountain passes and valleys, chaotic weather patterns and temperature extremes. Understanding the forcing

mechanisms of extreme weather phenomena and characteristics is vital for the safety of Alaska's residents and particularly those that fly.

Current observational networks of radiosondes (Fig. 1.2), weather radars, and surface stations are unable to identify and/or monitor funnel clouds due to their spatial and temporal resolution of small cross-sectional footprint and slow rotational wind speeds and duration of less than an hour. As such, funnel clouds pose a real aviation hazard in Alaska. Observations of funnel clouds by the public, pilots, and station meteorologist have increased with the increased use of camera phones and interest in climate change. The majority of the reports are mostly issued in densely populated areas or at weather stations, and observations occur mostly within transportation corridors (Fig. 1.3). Transportation corridors being mostly through mountain passes and along the river valleys of the interior, the coast being more flat is not so restrictive. It can be assumed that the number of funnel clouds is most likely much higher than it seems from the reported sightings listed in Table 1.1.
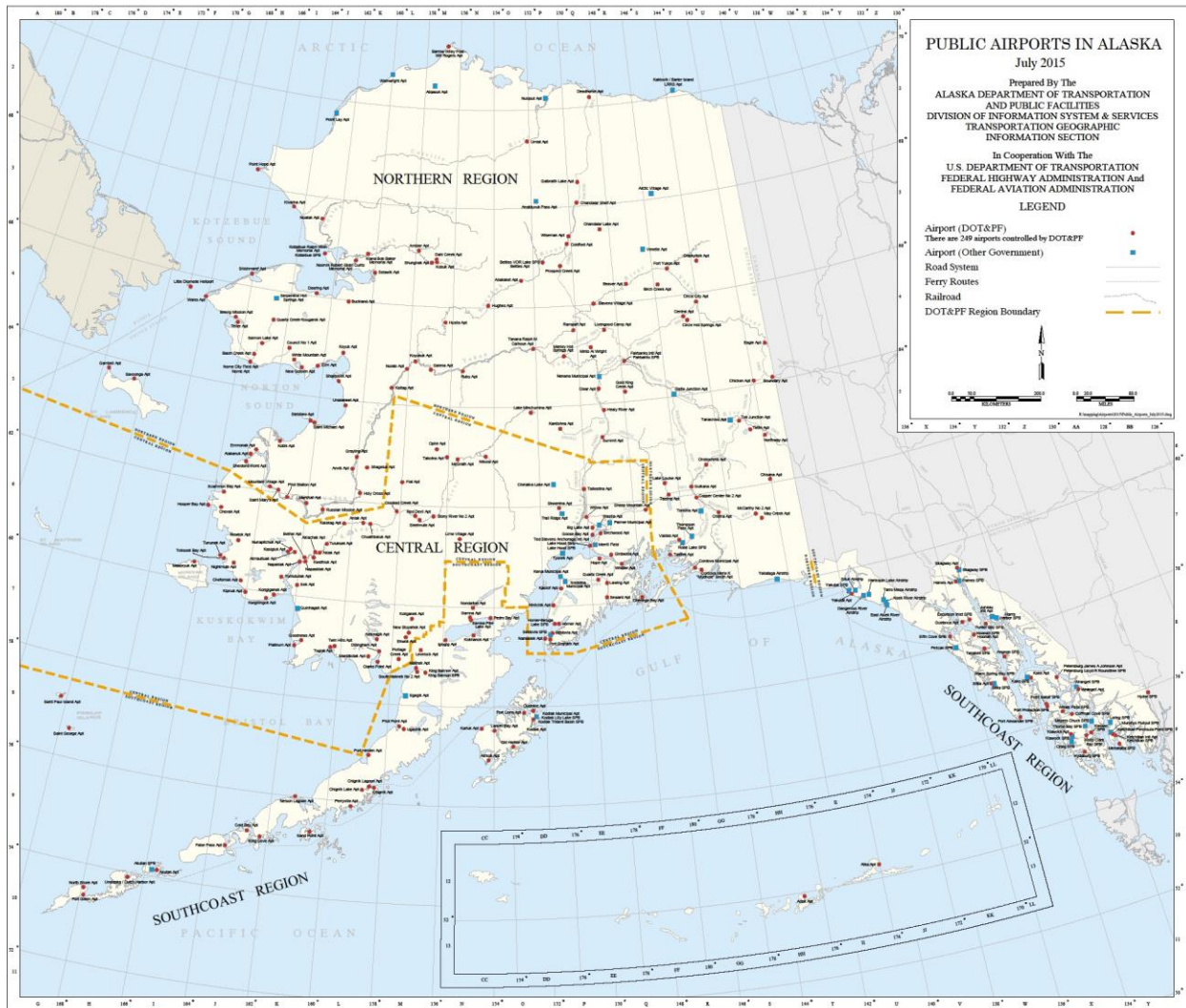
Fig. 1.3. Map of Alaska illustrating the location of villages and Department of Transportation (DOT) airports (red dots). Landing stripes for hunting and fishing lodges, camps, and mining sites are not shown. Retrieved 2016.
dot.alaska.gov/stwdping/mapping/dataproducts/public_airports.pdf

1.1 Motivation

The main motivation for my study is rooted in climate change. Since climate change may be the precursor for the increase in sightings of tornados in the South East of Alaska and funnel clouds in the Interior, an important question is whether increases in global temperatures would transform the number of funnel clouds recorded in Alaska into more destructive weather phenomena, namely

tornados. Tornados are a destructive force of property and lead to loss of life currently occur in the prairies of the United States – the so-called Tornado Alley (e.g. Lin 2007).

However, before it is possible to address this question, it is necessary to first understand the mechanism for funnel cloud formation in Alaska. Within this framework, it is important to understand the climatology of funnel cloud occurrence and whether there has been a change in their occurrence in the past. One could argue that the increase in sightings is due to the increase in population and ability to document the funnel clouds. According to personal communication with Alaska Elders, funnel clouds have not been witnessed in the past in the Interior nor do they occur in traditional story telling that I am aware of being Gwich'in, further in USA Today, 2005 edition reports similar outcome.

The main goal of this thesis is to establish such climatology and to shed light on the mechanism and characteristics of funnel clouds in Alaska.

1.2 What are Funnel Clouds?

Funnel clouds are closely related to tornados (Wakimto and Wilson 1989; Modahl et al. 1971), for which a distinction between one and the other is seldom used. Modern dynamic understanding of tornados and funnel clouds distinguishes these atmospheric phenomena (Cooley, 1978). However, tornados have been researched extensively due to property damage and subsequent cost to the population. Further, Modahl showed that within the mainland of the United States, tornados and funnel clouds are distinct through the summer season, but interlinked. These authors have shown that a funnel cloud can be a precursor to tornado development and exhibit similar measured physical properties, (i.e., vertical shear profile, temperature and dew point profiles, etc.).

Funnel clouds are generally associated with supercell thunderstorms in the mid-latitudes, but they can also form within non-supercell storms along frontal boundaries or colliding boundaries (Lin 2007). In those cases, pre-existing horizontal vorticity is tiled and stretched to form areas of intense vorticity that can also referred to as land- and waterspouts (Golden 1974; Fujita and Wakimoto 1981; Bluestein 1985; Wakimoto and Wilson 1989; Wilczak et al. 1992; Doswell and Burgess 1988). Non-supercell tornados occur along a slow moving front, or a stationary front, and often in a horizontal wind shift line, also known as a type-2 tornado. In this classification, type-1 is a supercell tornado. When a type-2 tornado occurs over water it is known as a waterspout, and over land as a land spout (Table 1.2).

The initialization of a non-supercell funnel cloud begins with several small vortices generated by shear instability resulting in a horizontal shear across boundaries, such shear vorticity even a small land sea (or vice versa) breeze or a down slope wind (Lin 2007).

1.3 Tornado Formation in the Great Plains

In the Great Plains, many tornados form within supercells. A supercell is a convective severe thunderstorm system with a mesocyclone. It has one major rotating updraft and one rotating downdraft. Due to this rotation, the public often calls supercells rotating thunderstorms. Supercells encompass an area of about 32 km.

Three types of supercells exist that differ by their precipitation amount. Meteorologists speak of classic, low precipitation and high precipitation supercells (Lin 2007). Low precipitation supercells occur mainly in arid climate regions like the high plains, while the other extreme mainly occurs in humid climate regions. Theoretically, supercells can form anywhere on Earth under the right synoptic conditions (Lin 2007).

In contrast to thunderstorms, supercells have a lifetime of several hours. Not every supercell forms a tornado. Tornados often start out as a funnel cloud. For a vortex to be called a tornado, it has to touch the ground (e.g. Lin 2007).

The vortex can be invisible. As the pressure decreases in the mesocyclone, the spinning increases. The fast rotation for cyclostrophic balance typically leads to condensation due to adiabatic cooling and the vortex becomes visible (e.g. Lin 2007).
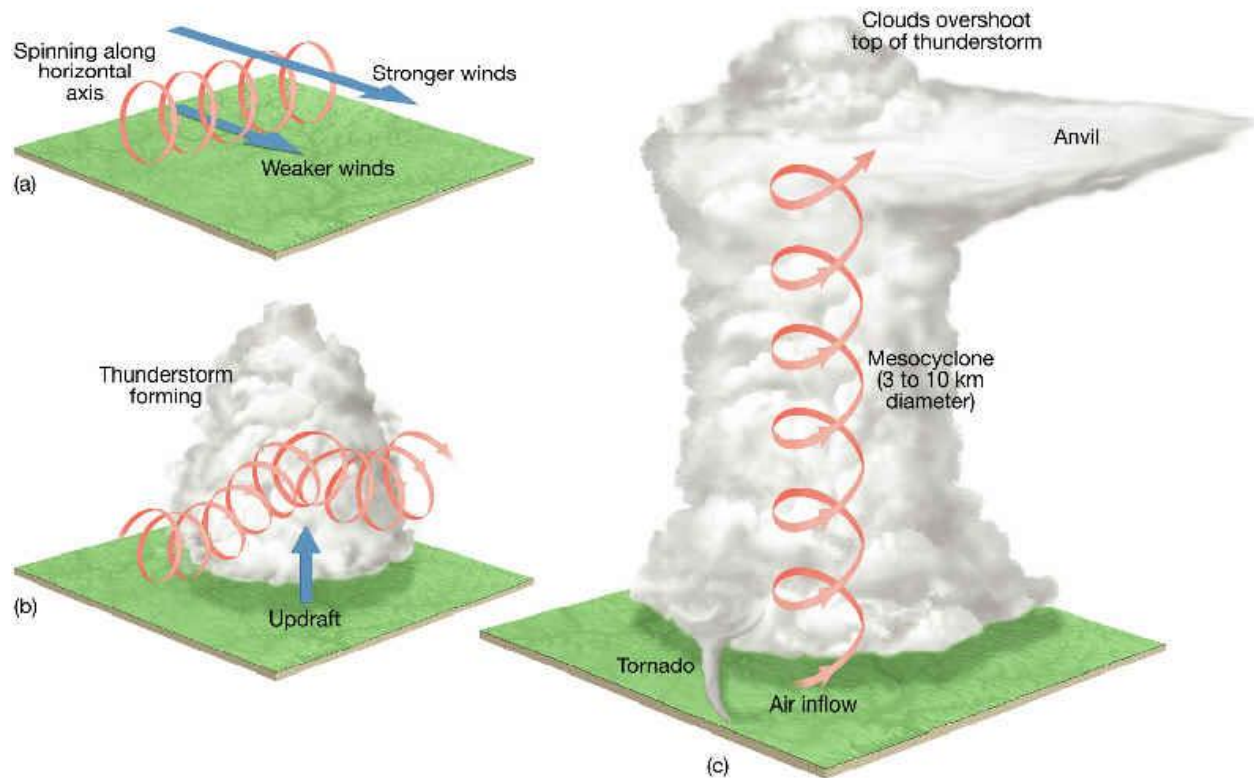
Fig. 1.4. Schematic view of a) vorticity formation by wind shear, b) initiation of rotating updrafts due to convection, and c) a supercell prior to downdraft formation. See text for details and explanation. Retrieved 2016 from:
http://www.geography.hunter.cuny.edu/~tbw/wc.notes/10.thunderstorms.tornados/tornado_dev_a.b.c_jpg.htm.

The rotation is initiated by wind shear (Fig. 1.4) for instance when subtropical warm, moist air is moving from the Gulf of Mexico northward while at the same time cold, dry polar air moves southward (Lin 2007). The wind shear along the front yields to a horizontal rotation along the frontal surface like, leading air to spin. This horizontal vortex is invisible as there is no condensate. From the South, moist air moves northward at low levels, thus vorticity is initiated in the mid troposphere. At the 300 hPa level, the jet is often orientated from the west to the east and brings relatively warm dry air from the Rocky Mountain plateau (Fig. 1.5).
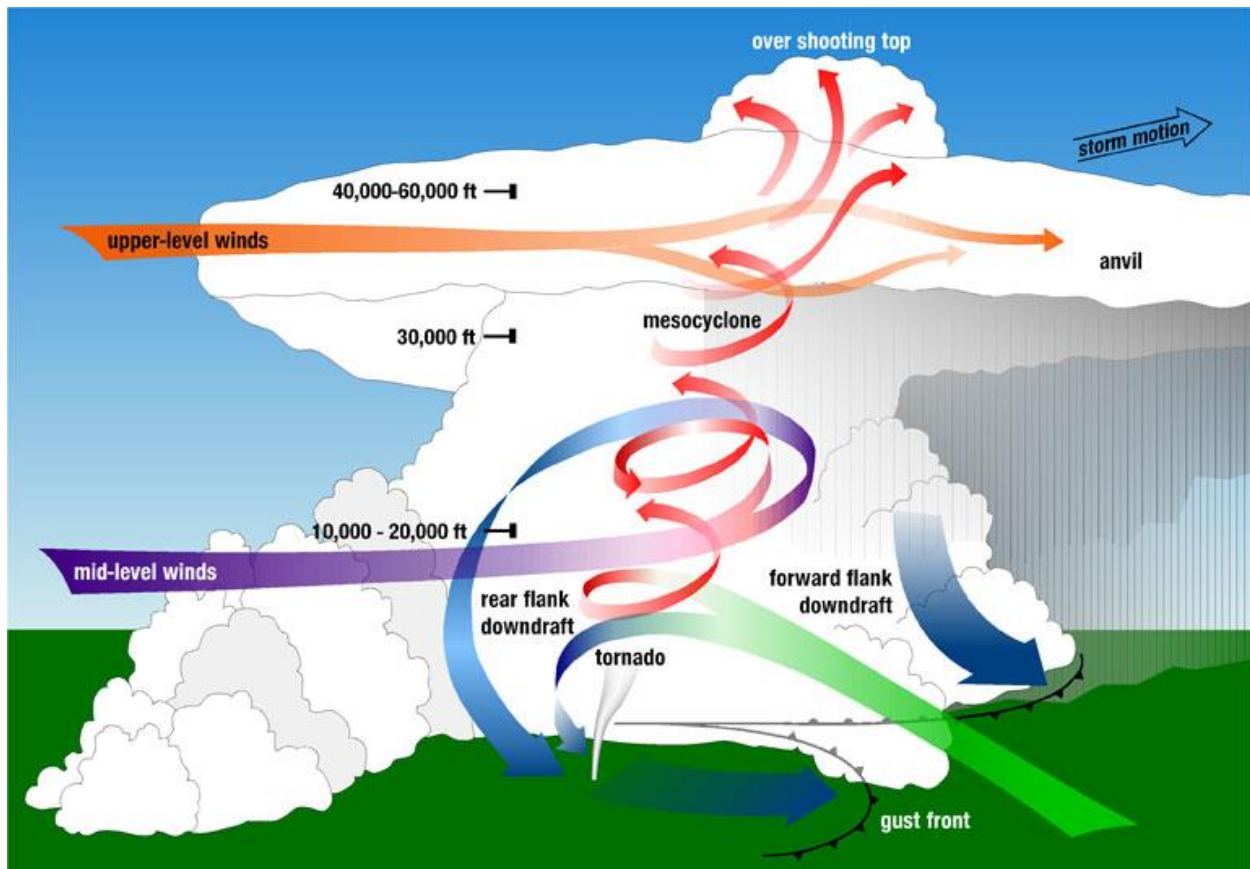
Fig. 1.5. Schematic view of mesoscale dynamics within a supercell storm with tornado. From: NOAA 2016 http://www.nssl.noaa.gov/

When in the Great Plains, the surface warms up after sunrise, and the convective inhibition (CIN) of the nighttime inversion is overcome and the inversion lid breaks, the horizontal vorticity is tilted in the updraft and turns it into vertical vorticity (Fig. 1.4). As the updraft reaches the tropopause, the air spreads along the tropopause building the large anvil (Fig. 1.5). Overshooting of the cloud can occur into the stratosphere (Lin 2007).

Since temperature decreases with height, temperatures can be cool enough that some of the condensate is ice. Since ice is the best nuclei for droplet formation, (Houze 1993) excess water vapor deposits onto these ice crystals. Furthermore, due to the lower vapor pressure over ice than water ice crystals grow at the cost of cloud drops (Findeisen-Bergeron process). The ice crystals grow in size and become large enough to overcome the updraft and start sedimentation (Houze 1993). Due to the increase of wind speed with height, the water- and ice-crystal loaded air is positioned at a different location than the updraft and builds the downdraft (Fig. 1.5). Since the vertical vorticity is now turned around, the rotation in the downdraft is opposite to that in the

11

updraft when looking at a horizontal cross-section (Lin 2007). The mammatus clouds visualize the turbulence where relatively warmer air moves over relatively colder air.

In supercells, tornado genesis begins when increasing rainfall drags ambient air with it in the rotating downdraft (Fig. 1.5), the rear flank downdraft (RFD). The downward motion in the downdraft increases and pulls the rotating mesocyclone downward as well. In the mature stage, the RFD with the cool winds wraps around the updraft and cuts the updraft off its warm, moist air inflow that feeds the tornado (Lin 2007). Thus, the tornado weakens and dissipates. When a new mesocyclone develops in the supercell, the tornado lifecycle can start again (Lin 2007).

1.4 Hypothesis

Since synoptic forcing in Alaska is thought to be much weaker than in the Lower 48 states, I hypothesize *that the wind shear necessary for the maintenance of severe thunderstorms does not come from a synoptic scale cold front and a dryline like in the Great Plains, but from local mesoscale circulations initiated by the terrain*. This means that the terrain might play a key role in the formation of funnel clouds in Alaska, and the large scale (synoptic) forcing is weak.

Alaska is a state with three mountain ranges, running west to east: The Brooks Range, the White Mountains and the Alaska Range. They are surrounded on three sides by seas: The Beaufort Sea, Chukchi Sea, Bering Sea, and the Gulf of Alaska (Fig. 1.6). Furthermore, this arrangement exhibits spatial temperature gradients of extreme cold in the North and comparatively warm humid in the South (Shulski and Wendler 2007). Between these mountain ranges are valleys: north of the Brooks is the North Slope Plateau, or tundra. South of the Brooks Range and north of the White Mountains are the Yukon Flats. South of the White Mountains and north of the Alaska Range is the Tanana Valley and Fairbanks. South of the Alaska Range is Anchorage, and the Alaska Range extends further south along the Panhandle towards Juneau, the State Capital. The West of Alaska is made up by the coastal plains with water and tundra bogs, and small stunted trees that are quite different from the boreal forest of the Interior or the large densely forests of the Tongass Forest of South East Alaska (Fig. 1.6).
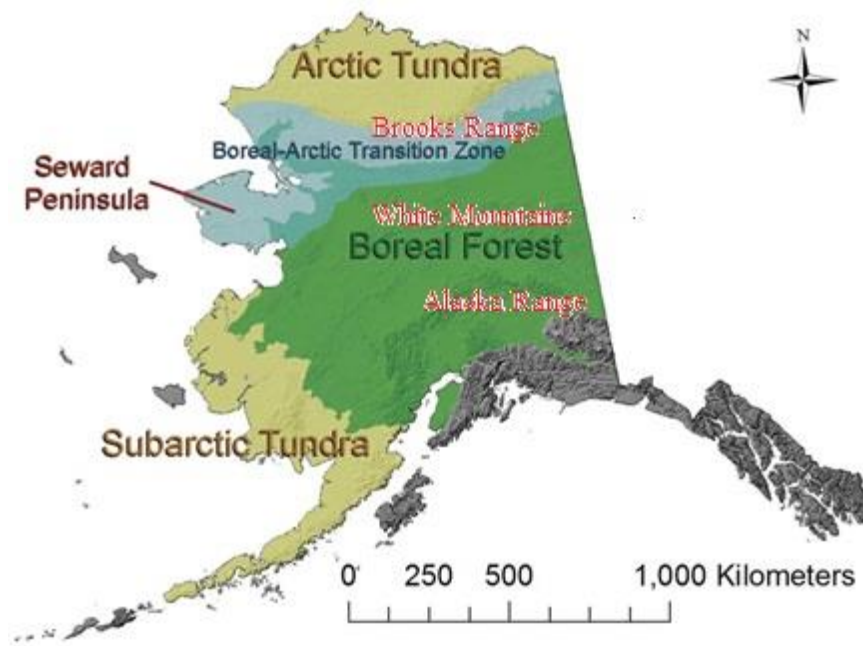
Fig.1.6. Alaska's fauna varies similarly in regions of common atmospheric characteristics. Source: USGS. Retrieved 2015 from:
http://alaska.usgs.gov/science/interdisciplinary_science/cae/boreal_arctic.php

Given the complex landscape of Alaska, I formulated the following sub-hypotheses: In the coastal terrain, in which the Yukon River and the Kuskoquim drain into the Bering Sea, *land sea atmosphere interaction may play a role in the funnel cloud formations along the western coast of Alaska. Within the Interior, terrain may play a more prominent role especially along the valleys between the mountain ranges, in which large drainage rivers flow. Along the southern coast, a combination of both land-sea-atmosphere interaction, may be in conjunction with terrain forcing, may prove to be the dominating forcing mechanism.*

1.5 Research Questions

In this study, funnel cloud characteristics and the synoptic scale weather situation associated with funnel cloud occurrence are investigated. I will focus on the following research questions:

- Are funnel clouds influenced by synoptic scale forcing?
- Are funnel clouds of low magnitude velocities and/or cross-sectional area detectable and predictable by operational observations?
- What are the driving dynamical and thermodynamical processes that produce funnel clouds in non-supercell storms in Alaska?
- Is there a change in funnel cloud frequency and characteristics over time?

13

1.6 Why Do You Care

Sighting and software detection protocols for funnel clouds and tornados by the National Weather Service (NWS) are derived and fashioned, based on extreme weather of the central United States. This means there are no forecasting systems for funnel clouds in Alaska (Thoman 2014, pers. Comm.). This fact is problematic because funnel clouds pose a threat to aviation, which serves as Alaska's main form of transportation.

Motivated by the scientific lack of understanding of the formation of funnel clouds in Alaska, the goal of the research of this thesis was to investigate the characteristics of funnel clouds in Alaska, and the atmospheric conditions under which they form using operational Doppler weather radars and radiosonde soundings as well as synoptic weather maps.

Chapter 2 Data Description, Processing and Development of a Data Analysis Algorithm

First, I briefly outline the steps of my data analysis and my reasoning to provide the reader with my line of thought. First, I collected dates of and information on documented sightings of funnel cloud (FC) formation and occurrence in Alaska. This search revealed 43 confirmed and documented FC sightings (cf. Table 1.1).
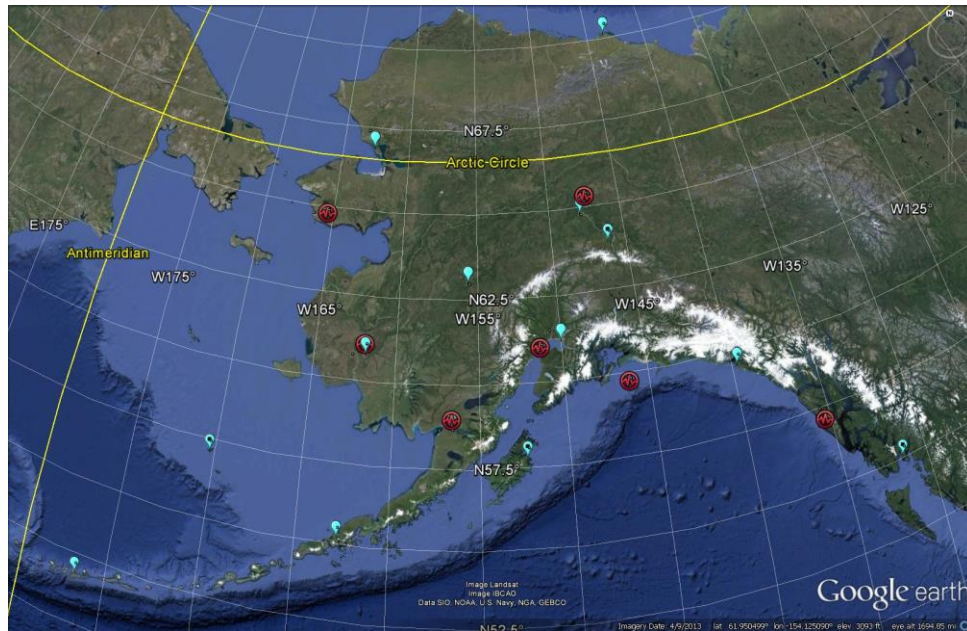
Fig. 2.1. The light blue upside-down teardrops, and red balloons are the locations of radiosonde launch and radar sites, respectively.

The second step was to group these sightings with the nearest (spatial distance) radiosonde station, or stations. There are 12 radiosonde stations in Alaska (Fig. 2.1). The grouping of FC sightings to the nearest radiosonde station reduced the number of relevant regions to six: Fairbanks, Anchorage-1, Anchorage-2, Anchorage-3, McGrath, Denali (label for the area between Fairbanks-McGrath), Bethel, and Nome-Bethel labeled Alaska West Coast (Fig. 2.2). The Anchorage groups are combined for the analysis since they have only one radiosonde station, despite the various potential mechanisms (mountainous terrain vs. land-sea, both) that would necessitate that they should be separated. For the Anchorage 2 and 3 groups, the controlling parameters fall within the limits of the first group and cannot be distinguished from one another by using spatial means. Thus, there are six groups to be investigated Fairbanks, Anchorage, McGrath, Denali, Bethel, and the Alaska West Coast.
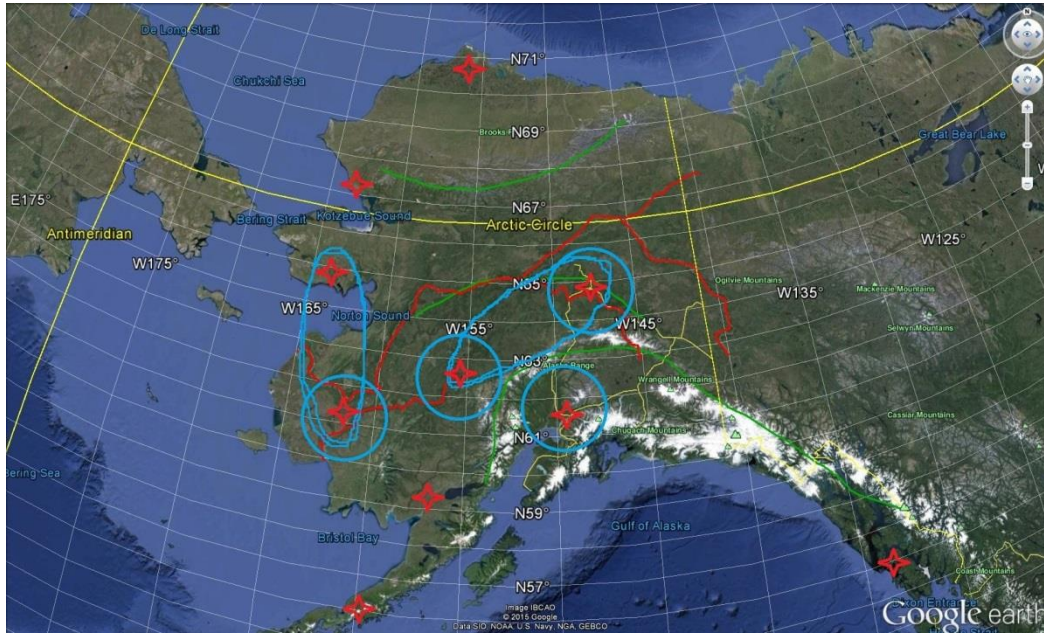
Fig. 2.2. Grouping of funnel cloud sightings based on similar atmospheric and regional characteristics, and their proximity to a radiosonde launch station. Singular radiosonde stations are Fairbanks, Bethel, McGrath, and Anchorage. Areas with multiple radiosonde stations are the Alaska West Coast (Nome, Bethel), and Denali (McGrath, Fairbanks) groups. There were no sightings near other radiosonde sites.

Multiple stations within a group must have similar regional atmospheric characteristics, for instance, temperature, dew point temperature, etc. (Bieniek et al. 2012; Bieniek et al. 2015; Cassano et al. 2011). There are insufficient numbers of sightings for the Kotzebue area, along the Aleutian chain, and the Panhandle area, i.e. Kenia, Yakutat, and Juneau.

In a third step, a search algorithm to find profiles similar to those on days with funnel cloud observations in the radiosonde data was developed. It was constructed from the parameters (i.e., temperature, dew point temperature, wind) of the radiosonde profiles of confirmed funnel cloud sightings. The resulting mean profiles and standard deviations obtained for a specific group from the radiosonde profiles of FC observation served as baselines for the algorithm. The algorithm used these observational data profiles to search the National Oceanic and Atmospheric Administration (NOAA) database (ftp://ftp.ncdc.noaa.gov/pub/data/igra/data-por/) for similar profiles. This NOAA database encompasses radiosonde data in Alaska from 1948 to present.

There are two possibilities regarding what could be found through the algorithm's data search. One finding could be that the frequency of similar profiles may increase as the data files are searched forward in time. Note that Alaskan Elders of the Interior report no sightings in older times

(USA TODAY 2005). The other possibility could be that funnel clouds have always existed in Alaska, but due to the size of Alaska and the low population density have never been documented in the past. No matter what the finding will be, the major benefit of this research to weather forecasters and the scientific community would be not only a better understanding of funnel clouds, but also knowledge on the formation and parameters. The analysis will benefit public safety as well as the scientific community.

In a fourth step, I used synoptic reanalysis maps from multiple pressure levels. I examined the large-scale forcing impact and influence on regional weather for the days of the confirmed FC sightings. This investigation served to determine if Alaska's unique topography has an influence on the formation of funnel clouds and could be one of the drivers for funnel cloud formation in Alaska.

2.1 Observed Funnel Cloud Sighting Data

A majority of the FC reports stem from public observations either from the ground or from aircrafts. FC reports collected by the NWS in Alaska are based on historic reports, from observer and media reports. Reports of waterspouts are excluded in this collection because they occur only along the coast of Alaska. Additionally, tornado events are not included except for persuasive purposes on radar detection capabilities.

Table 2.1 Date and general location of funnel-cloud sightings in Alaska between 1955, and 2014. Time is give either as Alaska Standard Time (AKST) or Alaska daylight time (AKDT).

year	mnth	day	Time	Town	Added information
1955	7	3		Denali Nat Park	5mi W of DNP HQ
1966	9	1	1600 AkST	Yakutat	west-southwest of airport
1969	7	4		Snowshoe Lake	
1969	7	6		Tangle Lakes	25 mi from Paxson
1972	7	13	1328 AkDT	Farewell	week, short duration
1978	7	22	1000 AkDT	Ninilchick	25 mi N-NE
1978	7	27	1730 AkDT	Snowshoe Lake	N
1980	6	27	1830 AkDT	Paxson	25 mi N-NW
1981	8	6	1645 ADT	Emmonak	near village
1981	8	11		Northern Interior	Western Brooks Range
1982	7	10	1535 AkDT	North Pole	10 mi NE
1983	8	16	1340 AkDT	Fairbanks	just NW
1983	7	31	1430 AkDT	Fairbanks	just South
1987	6	14	1045 AkDT	Anchorage	over
1987	8	1	2123 AkDT	Anchorage	over
1989	5	22	1630 AkDT	Cordova	
1994	8	24	1610 AkDT	Yakutat	15mi E of airport
2000	7	11	1543 AkDT	Denali Nat Park	W of Savage River milepost 14.7
2001	7	31	1730 AkDT	Denali Highway	Susitna river bridge milepost 56 from cantwell, mile 79 from Paxson
2002	8	28	0800 AkST	Denali Nat Park	
2002	6	25	1255 AkDT	Blue Mountan	6mi NW
2002	6	25	1300 AkST	Pilot Point	
2002	5	12	1400 AkDT	Palmer	near Palmer, over Pioneer Peak only reading, cause mountains
2002	8	28	1500 AkDT	Denali Nat Park	from Wonder Lake, N 2mi
2004	7	28	1325 AkST	Nome	
2004	7	26	1500 AkST	Chevak	
2004	6	21	1555 AkST	Marshall	
2004	5	25	1700 AkST	Fairbanks	On Richardson HW
2004	7	19	2030 AkST	McGrath	
2005	8	4	1700 AkST	Chulitna Riv Lodge	
2007	7	31	500 AkST	Metlakatla	
2007	8	20		Bethel	near Bethel
2007	8	20		Bethel	early evening, late afternoon 0->600 GMT
2008	7	13	915 AkST	Paxson	
2008	8	16		Noatak	Lower Noatak Riv Valley, above Noatak
2009	5	26	1700 AkST	Anchorage	
2009	7	9	1845 AkST	Kwethluk	
2009	8	1		Nome	Norton Sound near Nome
2010	7	22	0947 AkDT	Fairbanks	directly over Steese highway
2010	5	25		Paxson	20mi SE
2011	7	30		Denali Nat Park	W of DNP between Eielson VC and Wonder Lake
2012	7	9		Anchorage	upper cook inlet, S of Anch
2014	7	20	630 AkST	Anchorage	14 km, south

As mentioned earlier, there were 43 reports between 1955 and 2014 (Table 2.1). While all sightings were reported to NOAA, only the 13 most recent cases (2002-2014) are listed on the NOAA extreme weather website, the algorithm search was between 1971 and 2014. http://www.ncdc.noaa.gov/stormevents/listevents.jsp?eventType=%28C%29+Funnel+Cloud&beginDate_mm=05&beginDate_dd=01&beginDate_yyyy=1971&endDate_mm=08&endDate_dd=30&endDate_yyyy=2014&county=ALL&hailfilter=0.00&tornfilter=0&windfilter=000&sort=DT&submitbutton=Search&statefips=2%2CALASKA

Some of the reports indicate latitude, longitude, and time of occurrence, while most reports come with general description of landmarks, cities, or villages (Table 2.1). Some sighting data comes with photos (e.g., Fig. 1.1a).
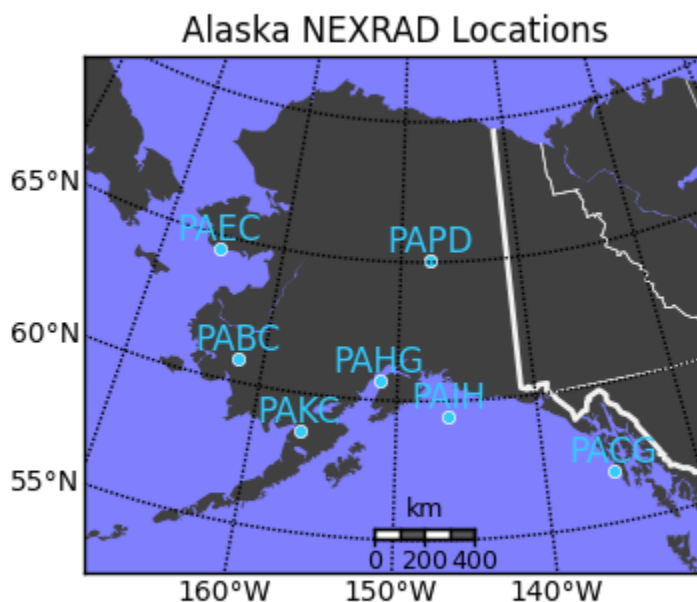
Fig. 2.3. Alaska NEXRAD locations Bethel (PABC), Bjorka Island (PACG), Nome (PAEC), Kenai (PAHG), Middleton Island (PAIH), King Salmon (PAKC), and Pedro Dome (PAPD). Source: Retrieved from: http://www.atmos.uwyo.edu/~bguy/nexradloc.shtml

As can be seen in Table 2.1, all FC have been reported near populated areas and along air-traffic corridors (common flight paths), along the coast and within major valleys (Fig. 2.1). Only 15 reports fall within the 230 km range of the seven Next Generation Radar Doppler (NEXRAD)

radars (Fig. 2.3), which started their operations in 1997. Radars are located at Fairbanks (operating since 21 March 1997), Nome (21 March 1997), Bethel (3 October 1997), King Salmon (16 December 1997), Anchorage (18 December 1997), Middleton Island (8 September 1997), and Sitka (27 August 1997).

Only nine of the 15 sightings that were within the radars' range were usable for analysis within the framework of the research of this thesis. The other sighting reports either were not close enough to one of the seven radar sites in Alaska or contained notable uncertainty in their location, and/or the date of observation occurred before the radar site went into operation (cf. Table 2.1). Of the nine usable reports, four are in the radar range of Anchorage, two are in the radar range of Fairbanks, two are in the radar range of Bethel, and two are in the radar range of Nome. Of these nine sightings, only four have usable latitude and longitude information (cf. Table 2.1) for locating and analysis in radar data.

Of the 43 funnel-cloud sighting reports, only 32 reports are near operational radiosonde sounding sites and occurred within ±6 hours of the launch (Fig. 2.4; Table 2.1). Of these 32 sighting, 19 occurred within ±2 hours of a radiosonde launch, and inside a 40 km (20 mi) radius of the sounding launch site.
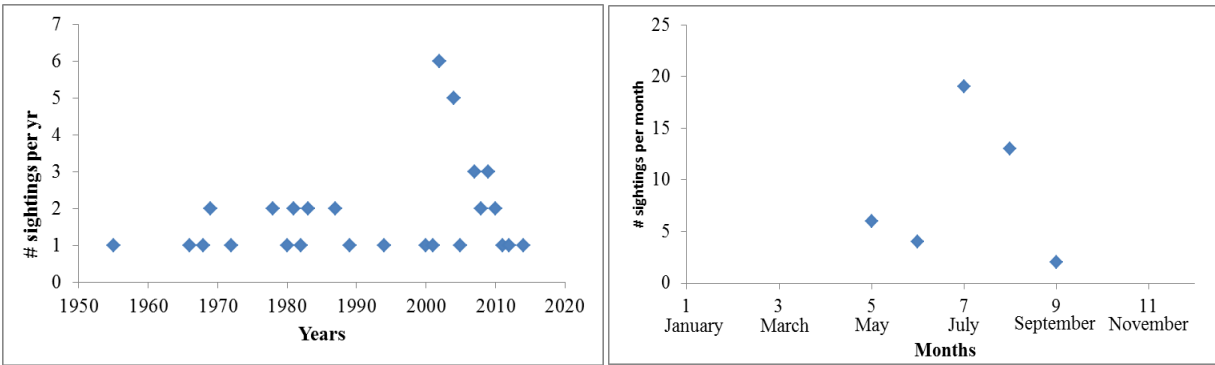
a)

b)
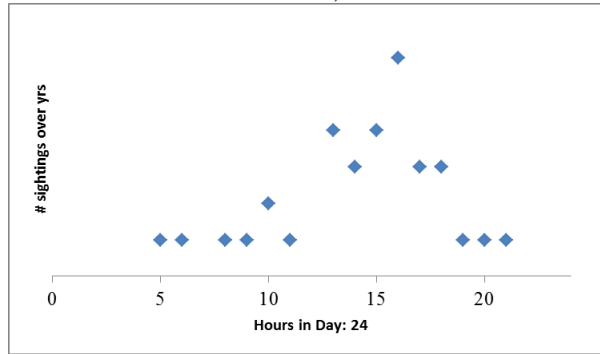
c)

Fig. 2.4. Number of observed funnel cloud sightings a) per year since 1950, b) per month over the time frame from 1950 to today, and c) per hour during the day with respect to Alaska Daylight Time (AKDT).

The number of FC sighting reports has increased over the last decade (Fig. 2.4) as has been the usage of cell phones. While the number of funnel cloud events is small, four events occurred in 1950s and 1960s, the number of reports increased to 12 in the 1980s and 1990s and to 26 for 2000 to 2014 (Fig. 2.4a). Most of the funnel cloud sightings occurred in summer between May and September with a peak in July (Fig. 2.4b). Funnel cloud events occurred mainly in the afternoon between 11 am and 6 pm AKDT (Fig. 2.4c).

2.2 Radiosonde Data

The NOAA database site for access to the Fairbanks radiosonde data is ftp://ftp.ncdc.noaa.gov/pub/data/igra/data-por/70261. Herein the number 70261 is the code for Fairbanks. The codes for the other radiosondes in Alaska are for Adak 70454, Anchorage 70273,

Barrow 70026, Barter Island 70086, Bethel 70219, Cold Bay 70316, Kotzebue 70133, McGrath 70231, Nome 70200, Shemya 70414, and Yakutat 70361. The locations of the Alaska radiosonde sites are indicated in Figure 2.1.

The following variables were provided by the radiosonde soundings: Pressure (p), height (Z), temperature (T), dew point temperature (T_d), wind direction (dir), and wind speed (v). There are 19 possible data levels: 1000, 925, 850, 700, 500, 400, 300, 200, 250, 150, 100, 70, 50, 30, 20, 10, 7, and 5 hPa (or mb). The relevant range of pressure levels is from 1000 hPa to 200 hPa for this thesis. Unfortunately, the usable data for my research are limited to May 1971 to September 2014 due to missing dew point-temperature values in the earlier radiosonde profile data.

As aforementioned, the radiosonde data recording started in 1948. Data have been recorded daily at 00 UTC and 12 UTC. The abbreviation UTC stands for Universal Time Coordinated. Alaska Standard Time (AKST) is 8 hours behind UTC, i.e. AKST=UTC-9h. In years where daylight saving time is observed during summer, the relationship is AKDT=UTC-8h, AKDT is Alaska Daylight Time. Thus, the radiosonde data have been available for 2 pm on the previous day, and 2 am AKDT on the same day.

2.2.1 Radiosonde Data Accuracy and Consistency

Prior to discussing the quality assurance and quality control (QA/QC) applied to the radiosonde data, I want to cite Durre et al. (2006) and the Federal Handbook for radiosonde data (1997) as these sources provide the history and describe the technological development and the related improvement of data quality and data quantity over time.

Integrated Global Radiosonde Archive (IGRA) is a collection of over 1500 distributed stations over the globe. Radiosonde observations records vary over periods extending from the 1960s to present. IGRA procedures is to insure proper station identification, removing duplicated levels of data, and select one sounding for every station, date and time. The most complete spatial and temporal coverage is over the United States, Western Europe, Russia, and Australia. IGRA is the largest and most extensive dataset of quality-assured, freely available radiosonde observation data. Over the observation period, vertical resolution and height coverage has increased, most soundings have data up to 100 hPa since 2003, (Durre et al. 2006).

Atmospheric observations started in the United States with kites carrying simple instruments in 1749. Tethered balloons were utilized in the 18th century so observations could be made during all weather conditions, not just on windy days. A more established governmental program was started in the 1920 with Dailey airplane measurements over 20 locations. Over the years, other methods

and means were used but in the 1930 radio telemetry was incorporated into balloon atmospheric sensing observations, the forerunner of today's radiosonde system.

Before digital computerizations radiosonde balloon observations and data collection required two people and a number of hours computing measurements; a third person overseen quality control and oversight of procedure. In the 1960's computerization of radiosonde data was being experimented with, and radiosonde observations was almost totally automated. This automation experimentation was being researched by the Department of Defense (DOD) and the National Ocean and Atmospheric Administration (NOAA). NOAA is today's current caretaker of radiosonde IGRA dataset. Radiosonde observation has become an operation with improved data quality, (OFCM: Federal Meteorological Handbook 1997).

It is obvious that the progress in measurement technique, the change in tools used, and the increase in vertical resolution of the data have impact on the accuracy of the data. This means the dataset to be searched by my algorithm is inhomogeneous with respect to quality, accuracy, and data quantity. The increased data quantity means an increase in vertical resolution as well as an increase in temporal resolution over the duration of ascend.

Consequently, the baseline profiles of funnel-cloud characteristics to be derived from the radiosonde profiles of the documented sightings may be sensitive to the technical limitations existing at the time of their launches. These aspects and the homogenization of the data will be discussed among other things, in a later section.

2.2.1.1 QA/QC Performed by NOAA on the Radiosonde Data

Before I describe the QA/QC that I applied to my data for building the search algorithm, I will briefly describe the QA/QC that NOAA applied to their radiosonde data. A detailed description can be found in Durre et al. (2006).

NOAA's QA/QC is fully automated, and applied to temperatures in the Integrated Global Radiosonde Archive (IGRA). The algorithm searches for various errors as they can lead to pretending events that actually were none. First, 14 tests for persistence, climatological outliers, and vertical and temporal inconsistencies are performed sequentially so the algorithm detects of data variety and potential errors. Then random samples of flagged data are manually reviewed to identify suitable "thresholds" for each individual sample to minimize the number of valid values erroneously identified as errors. Lastly, the entire data is inspected manually using random samples of the quality-assured data. This temperature QA removes the grossest errors with a false-positive rate of about 10% (Durre et al. 2006).

2.3 Development of a Search Algorithm for Identification of Funnel Cloud Characteristics

This section describes the data homogenization and the search algorithm that I developed and used for data analysis. This search algorithm serves to identify profiles similar to those observed on days with FC events. The complete computational-technical details are described in section 2.3.1. In the following discussion, I limited technical details to the minimum as needed for understanding of how I processed the data to develop the algorithm and to gain baseline profiles for potential funnel cloud events from the profiles of days with reported funnel-cloud sightings.

There are three aspects of what needs to be addressed regarding the radiosonde data, and the synoptic map characteristics based on the observational data of FC in Alaska for this research. First, there is the grouping of FC sightings to radiosonde areas and locations based on similar environmental characteristics, topography, and proximity to radiosonde recording station (Fig. 2.2) (Durre et.al. 2006). See discussion above.

The difference of data collection methods used over the past sixty years has to be addressed as well. The number of measuring altitudes resulted in differences in the length of the radiosonde data files per ascent of the measuring instruments. It also meant an increase in vertical and temporal resolution. Even though the radiosonde started at 00 and 12 UTC, the actual ascent takes about an hour depending at what altitude the balloon bursts. Furthermore, as the radiosonde ascends, it is displaced in space at different speed and in different directions. Consequently, the radiosonde may drift farther away from the place of the sighting and might not be representing the conditions that led to the occurrence. Furthermore, the events and the times of the radiosonde (2 am, 2 pm) data do not match up (see Fig. 2.4c).

Third, the creation of the baseline profiles for the search algorithm aims to obtain a reasonable range of conditions for FC within a group. However, deriving limits based on the small number of FC observations provides statistical uncertainty in the profiles generated for acquiring similar profiles. Ideally, one would need at least 30 events (von Storch and Zwiers 2000) of FC per group to have a representative sample and to obtain a representative FC profile.

In the radiosonde data, I will ignore the spatial and temporal differences due the limited number of observations per radiosonde location and the limited number of radiosonde sites for such large area (Fig. 2.1). In the following, I describe how I addressed these points.

The grouping of the FC observations into areas of similar environmental conditions by using Bieniek et al. (2012) as guidance for considering the topography and proximity of radiosonde stations (Fig. 2.2). For observational dates and times of FC in close proximity to only one radiosonde station within an environmental region of similar atmospheric and topographic

conditions, those observations will be considered as one group. Doing so, places the radiosonde sites of Fairbanks, Bethel, and McGrath, and the sightings in their vicinity into one group each (Fig 2.2).

If there are multiple sightings, at varying distances from a single radiosonde station, within a region of common environmental and topographic area, the distance between the sighting and the radiosonde will be used to group the sighting profiles. This scenario is the case for the Anchorage radiosonde site and the FC sightings in the Anchorage area. Doing so, would lead to the groups Anchorage 1, Anchorage 2, and Anchorage 3. The reasoning is based on the spatial and temporal differences of the radiosonde measurements of these events. However, spatial and temporal characteristics are not considered for the observational data used for determining the similarity limit settings in the case of Anchorage. My grouping takes into account the spatial distances and similar environmental regional characteristics. Based on the criteria, the sightings in the Anchorage area would fall into three different groups. Unfortunately, there is only one radiosonde site (Fig. 2.2). Therefore, I have to use the same site for all three.

For those funnel-cloud sighting location, dates, and times common to multiple radiosonde stations, regional environmental similarity is considered as it was suggested for climate divisions by Bieniek et al. (2012, 2015). The sightings in Denali Park fall in between the radiosonde sites of Fairbanks and McGrath (Fig. 2.1). These sightings occurred in terrain with similar environmental characteristics, and were located between the same mountain ranges, the White Mountain and Alaska Range (Figs. 1.6, 2.2). The Alaska West Coast (Bethel-Nome) also has the same environmental characteristics (cf. BienIek et al. 2012; BienIek et al. 2015) and all the sightings are located in close proximity on the western coastline (Table 1.1).

The differences in the length of rows in each radiosonde data file, either determined by pressure and/or height of the radiosonde-ascend data presented a unique computational problem. It goes along with a difference in the vertical resolution as well. The variability in the number of data rows of measurements as the balloon ascends is primarily due to changes in digital technology supplementing and replacing older techniques of using analog systems and calculations by hand. These changes of data record length represent a greater number of pressure levels with associated height, temperature, dew point temperature depression, wind direction, and wind velocity for the present measurements, and less pressure levels with more errors for the past systems, i.e., the early years of atmospheric vertical profiles. From a data quality point of view, the earlier data have a lower vertical resolution than the more recent data.

To avoid artifacts and incorrect conclusion, I introduced mandatory pressure levels required for measurements in the radiosonde data. Determining the baseline profiles at prescribed pressure levels ensures that the obtained baseline profiles for the various groups become independent of the

vertical resolution used at the time of the documented sighting. Thus, the inhomogeneous dataset will be forced into a homogeneous one. Of course, some information is lost. However, the homogenization serves to not conclude falsely that more FC occurred in the younger pasts when actually the better technique permitted detecting them. A test with and without the homogenization of the data with the advanced technique permits assessment of uncertainty regarding the data collected with the old-fashioned techniques.

For a single radiosonde profile of a given date and launch time and of variable length: the number of measurements made at a given pressure (p) level with associated height (Z), temperature (T), dew point temperature (T_d), wind direction (dir), and wind speed (v) at that level; this means that the older radiosonde profiles may have either missing data at the required pressure levels or data of the variables at that level. On the contrary, the more recent radiosonde profiles may have many measurements at about the required pressure levels. Of course, the introduction of mandatory pressure levels for the data bears the disadvantage of reducing the vertical resolution available in the more recent data when determining the baseline profiles for the various groups. However, it has the advantage to have data at similar levels over the timeframe of available data.

By categorizing and implementing a pressure range around the required pressure levels, I allow for the variability of vertical resolution of the radiosonde profile data over the years. Herein, also the different start date to the records at the various radiosonde sites was key.

The above-described method allows for calculating the mean, standard deviation, and standard deviation error for the variables in the radiosonde profiles that were observed during the documented funnel-cloud sightings. The variability in observed profiles is used for setting the limits of allowed deviations of measured variables for given pressure levels when determining the baseline profiles. Later when the algorithm searches the entire database of a group for similar profiles to the baseline profile for a given location, this procedure also permits consideration of variability among potential funnel-cloud conditions.

The mandatory pressure levels I chose are 1000, 925, 850, 700, 500, 400, 300, and 200 hPa. I chose the following ranges to best represent the levels:

- 1015 to 962.5 hPa for the 1000 hPa level,
- 962.5 to 887.5 hPa for the 925 hPa level,
- 887.5 to 812.5 hPa for the 850 hPa level,
- 737.5 to 650 hPa for the 700 hPa level,
- 550 to 450 hPa for the 500 hPa level,
- 450 to 350 hPa for the 400 hPa level,
- 350 to 250 hPa for the 300 hPa level, and
- 250 to 150 hPa for the 200 hPa level.

This procedure of allowing a pressure range centered on the required pressure levels places the variability of the radiosonde data length per sounding in the older balloon ascends in a common footing with the new digital methods. Furthermore, it allows for testing of the entire radiosonde data for similar profiles than those determined based on the radiosonde data of documented sightings of FC.

The third data quality issue was addressed as follows: I derived a procedure for singling out radiosonde profiles similar in dew point temperature and air temperature to the baseline profiles within the range of the above-described limits. However, the observational radiosonde data at a given time and day presents unique challenges. At any given day and time, each radiosonde profile is different. Even if the data was recorded at the same time and distance from an atmospheric event, no two profiles are the same due to the nature and dynamics of the atmosphere. To add to this challenge, all the FC sightings occurred at different times and dates spanning five months, namely May through September over the past 45 years (Fig. 2.4). Furthermore, some locations have three usable sightings and others up to eight for any one location (Fig. 2.4). Each sighting has a different temporal and spatial characteristic in relation to the radiosonde launch location. As pointed out before, ideally a sample should hold at least 30 values (von Storch and Zwiers 2000).

Considering the size of Alaska, and only 12 radiosonde locations (Fig. 2.1), finding radiosonde profiles similar to those observed is a daunting task. The best course of action is to find those radiosonde profiles that are very similar, and within a set range of variability. Doing so allows these profiles to be the most probable for FC based on their similarity to the profiles that were determined as baselines based on the radiosonde data gathered on days close in time and space to the documented sightings.

For any pressure level that falls within the limits of one of the pressure ranges, the associated variables of height, temperature, dew point temperature depression were stored to an array. When data was found for a mandatory pressure level, the data were screened to the maximum and minimum range limits of each of the variables for the pressure range. These minimum and maximum values served later in the search algorithm to decide whether a radiosonde profile of another day and time falls within the limits of similarity to the documented FC profiles.

As aforementioned, for all documented sightings in a group, I took all the data profiles in which data were recorded within the ranges of the mandatory pressure levels. For each pressure level, I used their associated height, and observed dew point temperature, and air temperature values to determine the minimum and maximum values for those variables over their respective pressure level range. For example, for all pressure levels between 1015 hPa and 962.5 hPa, I assigned for each of the meteorological variables a range limit. This range limit is then associated to the mandatory 1000 hPa level that encompasses the pressure range between 1015 and 962.5 hPa. Doing so provided for each mandatory pressure level unique values of height, dew point temperature, and air temperature valid within the particular pressure range. Thus, a limit of maximum and minimum values for each variable can be determined.

Using Matlab, the means, standard deviations, and standard deviation of error were calculated as exemplarily shown for the temperature of the range around 1000 hPa. Technically, this temperature data are stored in an array 'A'. Then the mean is given as

$$\text{mean}_{t1} = \text{mean}(A) = \frac{\text{sum}(A)}{\text{length}(A)} = \overline{X} = \frac{1}{n}\sum_{i=1}^{n} X_I \tag{2.1}$$

$$\text{std}_{t1} = \text{std}(A) = \left(\frac{1}{n-1}\sum_{i=1}^{n}(X_i - \overline{X})^2\right)^{\frac{1}{2}} \tag{2.2}$$

Here n is the length of elements in A.

$$\text{error}_{t1} = \frac{\text{std}(A)}{\sqrt{\text{length}(A)}} \tag{2.3}$$

For the temperature values of all days with documented FC sightings that fall within the pressure range of 1015 hPa to 962.5 hPa, the minimum and maximum of acceptable similarity range limits are then given by:

$$\text{minimum}_{t1} = \text{mean}_{t1} - \text{std}_{t1} - \text{error}_{t1} \tag{2.4}$$

$$\text{maximum}_{t1} = \text{mean}_{t1} + \text{std}_{t1} + \text{error\_t1}. \tag{2.5}$$

This procedure is applied also for the height and dew point temperatures that fall within the pressure range. Then the procedure is repeated for all the other ranges around the mandatory pressure levels to determine the ranges for dew point temperature, temperature, and height.

Of course, one could choose the maximum and minimum values for each variable within the respective pressure ranges from the radiosonde data of days with FC sightings as the limits of the maximum and minimum. However, doing so would not permit the consideration of temporal and spatial differences between the recorded radiosonde data and the time and location of FC sightings (Fig. 2.2, 2.4; Table. 2.1). Using just the minimum and maximum values would also neglect the observed seasonal spread over five months over 45 years of funnel clouds (Fig. 2.4) and the spatial extension of Alaska (Fig. 2.2). A statistical mean of similarity would be more desirable to work with from a theoretical point of view (von Storch and Zwiers 2000). However, it is more appropriate to envelop the range as described above considering the limited numbers of documented observations of FC within a certain group.

For the similarity test of a given radiosonde profile collected between May and September in the last 45 years since 1971, the search algorithm used only the pressure range, as well as the dew point temperature and temperature limits. Of the seven pressure ranges, only the lowest six were used for the similarity test. The algorithm also applied a fourth test looking at the Convective Available Potential Energy (CAPE). I will provide more details on CAPE, its meaning and calculation in Section 2.3.1.

The CAPE value was calculated based on the data identified by the search algorithm as being similar to the profiles observed on days with documented FC sightings. The CAPE is utilized as a final test for examining atmospheric stability, and the capacity for storm formation, and a possible FC event, or worse.

As aforementioned, any pressure value and associated temperature and dew point temperature value within a given pressure range must fall within the maximum and minimum limits assigned for these quantities to this pressure range. If the given pressure, temperature, and dew point temperature all fall within one of the lower six pressure ranges, the search algorithm assigns this case a switch value of 1. Once the switch is activated, it does not matter how many more temperature and dew point temperature values fall within the pressure range of a given profile. However, when at any pressure level, no data fall within the given limits for all quantities, the respective radiosonde profile is discarded as not being a potential funnel cloud event.

Furthermore, a profile will be discarded if the lower six pressure ranges that were assigned a switch value of 1 do not fall within the combination check of the switch values of: $\binom{6}{4} + \binom{6}{5} + \binom{6}{6} =$ 22 combinations over the pressure ranges. Each of the lower six pressure ranges, with the exception of the ranges around 800 hPa and 600 hPa, is given an activation switch value for a combination check for four, five and six pressure ranges that do fall within the similarity range to the altitude of 250 hPa. When there are already four, or more of the six switches assigned to each pressure range active, the out of range profile is retained and the test continues.

The logic for the combination of switches is made in consideration of the old radiosonde data, which often miss required pressure levels. Unfortunately, in the old data, the missing of a pressure range occurs especially at the low altitude ranges, which are of interest in my analysis.

It has to be understood that there is uncertainty due to the variability in vertical resolution, missing data and the limited number of observations, as well as due to the spatial and temporal differences between the radiosonde and FC observations and the number of events in a group's area. Thus, one has to be aware that the similarity between radiosonde data derived for FC events and the actual profiles at the time and location of the FC are just similar in the sense of mesoscale arguments.

Due to the fact that for a given time and location the available radiosonde data have a 12 h resolution, a similar profile encompasses ±6 h. In other words, the radiosonde profiles on days with documented radiosonde profiles may represent the situation prior to, around the event or past the events. It is well known for tornados in the Great Plains that the conditions prior, during and after an event differ (e.g. Houze 1993; Lin 2007). Therefore, one has to assume that similar may be true/found for funnel cloud events in Alaska.

For FC sightings located between multiple radiosonde stations, the same test as for those with one radiosonde site is utilized with one exception. The same observational dates and times are used to generate the limit ranges for all station locations. The limits for the dew point temperature and temperature ranges are drawn from those profiles generated for each radiosonde station location. Consequently, each limit range is unique to the station, but for the same FC event, i.e. the same dates and times. For the areas within the range of multiple radiosonde sites, the search algorithm uses the respective site's limits. Then it checks the profiles that were identified as similar to those of FC events. Only the profiles on dates identified as possible FC events by the entire suit of radiosonde profiles are kept for the CAPE calculations (see Section 2.3.1 for details). The schematic diagram in Figure 2.5 illustrates how the search algorithm relates the distance of the FC with the CAPE value and the ratio between multiple station values as the determining factor for the limit ranges of the search algorithm.

MAXm McG ● MINf

$\dfrac{MAXm}{MINf}$ →X

$\dfrac{MINf}{MAXm}$

$\dfrac{1}{4}\left(\dfrac{MAXm}{MINf}\right)$ $\dfrac{3}{4}\left(\dfrac{MINm}{MAXf}\right)$ $\dfrac{3}{4}\left(\dfrac{MAXm}{MINf}\right)$ $\dfrac{1}{4}\left(\dfrac{MINm}{MAXf}\right)$

$\dfrac{1}{2}\left(\dfrac{MAXm}{MINf}+\dfrac{MINm}{MAXf}\right)$

$\dfrac{1}{2}\left(\dfrac{MAXf}{MINm}+\dfrac{MINf}{MAXm}\right)$

$\dfrac{3}{4}\left(\dfrac{MAXf}{MINm}\right)$ $\dfrac{1}{4}\left(\dfrac{MINf}{MAXm}\right)$ $\dfrac{1}{4}\left(\dfrac{MAXf}{MINm}\right)$ $\dfrac{3}{4}\left(\dfrac{MINf}{MAXm}\right)$

$\dfrac{MINm}{MAXf}$ MINm Fbks

$\dfrac{MAXf}{MINm}$ MAXf

$$\dfrac{MAXm}{MINf} \neq \dfrac{MINf}{MAXm}$$

$$\dfrac{MINm}{MAXf} \neq \dfrac{MAXf}{MINm}$$

McG ● —X—— McG largest CAPE to smallest —X——X—— —X—— ● Fbks

Fbks largest CAPE to smallest

Range of Common largest, related CAPE of both stations, w/ same date & time

Fig 2.5. Schematic diagram of procedure of relating the distance between a sighting and the radiosonde location, with the CAPE value and the ratio between multiple station-values as the determining factor for limit ranges. Here McG and Fbks stand for McGrath and Fairbanks, Maxm and Minm stand for the ratio variable starting at that location towards the other, CAPE value relative to McGrath maximum and minimum, as well as Maxf and Minf are CAPE values relative to Fairbanks maximum and minimum. NOTE: that the same is applied for the West Coast group. See text for details.

From the data of these common dates and times, a ratio of the stations' CAPE, one station to the other is used as a limiting range for further investigation. The ratios that fall between the two sets of value limits are compared to a second limit range based on the second to the third station's ratio. Those dates and times within both limiting ranges of each station are considered as potential FC events that may have occurred somewhere between the two stations.

This logic is based on the spatial assumption that a large CAPE value occurs at a site when a FC is close to a station, and a small CAPE value is observed when the FC occurs at a large distance

31

from the station. The algorithm finally considers only those dates and times as potential FC events that have CAPE values greater than 500 J. Note that this multiple sounding testing is only applied for the Denali and Alaska West Coast groups (Fig. 2.2).

For the group with only one station and multiple distances, for each of the three regions around the radiosonde site, unique CAPE limits are determined for each of the Anchorage groups, Anchorage group 1, Anchorage group 2, and Anchorage group 3.

The fourth aspect to be considered is the data processing software used in my research. It is described in section 2.3.2.

2.3.1 CAPE

Convective Available Potential Energy is a measure of a storm's potential energy of convection, a measuring index of reference used in synoptic meteorology (Lin 2007). Convective available potential energy is derived from the first law of thermodynamics and the idea of buoyancy (B) and the theory of air parcels (e.g. Houze 1993; Lin 2007; Mölders and Kramm 2014).

In hydrostatic equilibrium, the following equation applies for the ambient air

$$\frac{dp}{dz} = -\rho g \qquad . \tag{2.6}$$

Here p is pressure, z is height, ρ is density and g is the acceleration of gravity. When an air parcel is displaced vertically, it either goes up or down or stays where it was moved to, depending on its buoyancy. It has some vertical acceleration

$$\ddot{z} = \frac{d^2z}{dt^2} \qquad , \tag{2.7}$$

when assuming that gravity and the vertical pressure gradient force are the only forces acting on the air parcel. Then

$$\rho' \frac{d^2z}{dt^2} = -\rho' g - \frac{dp'}{dz} \qquad , \tag{2.8}$$

where ρ' is the density of the parcel, and p' is the pressure of the air parcel. We can assume

$$\frac{dp'}{dz} = \frac{dp}{dz} \qquad , \tag{2.9}$$

where the parcel's pressure is equivalent to the environmental pressure. Then

$$\ddot{z} = \frac{d^2z}{dt^2} = -g - a'\left(-\frac{g}{a}\right) \tag{2.10}$$

where $a' = \frac{1}{\rho'}$, and

$$g\left(\frac{a'-a}{a}\right) = g\left(\frac{\rho-\rho'}{\rho'}\right) = B \qquad (2.11)$$

Buoyancy is defined as the force due to the difference in density between the air parcel and the environment for a unit mass.

By using the ideal gas law for both the environment and the parcel of air, $p = \rho RT$ and $p' = \rho' RT'$ where R and R' are the individual gas constants and inserting these relationships in the hydrostatic equilibrium equation (2.6), we get:

$$\ddot{z} = g\left(\frac{\rho-\rho'}{\rho'}\right) = g\left(\frac{T'-T}{T}\right). \qquad (2.12)$$

Let us now assume an air parcel that does not exchange heat with its environment as it ascends or descends. Under these assumptions, it moves dry adiabatically, in which the thermodynamic condition exist, $\delta Q = T \, ds = 0$. Here δQ and ds are the change in heat and entropy, respectively. Also, assume that there is no mixing as the air parcel expands or compresses, i.e. the air parcel is a closed system. When the air parcel experiences an upward motion under the assumed circumstances, it experiences a decrease in pressure as its volume V expands $(dV > 0)$, and performs work

$$w_{top \to bottom} = \int_{bottom}^{top} p(V)dV \qquad . \qquad (2.13)$$

According to the first law of thermodynamics, the sum of the internal energy and work equal the heat added $dU + pdV = \delta Q$, i.e. under adiabatic conditions $dU = -pdV$. Using the relation $mc_v dT = dU = -pdV = -\frac{mRT}{V}dV$ then yields $\frac{dT}{T} = -\frac{R}{c_v}\frac{dV}{V}$ where m is unit mass (m=1 kg). By using the identity of specific heat at constant volume (c_v) and constant pressure (c_p): $c_v = c_p - R$, we get $(c_p - R)\frac{dT}{T} = -R\frac{dV}{V}$. Furthermore, by using the ideal gas law $pV = mRT$ and taking the natural logarithm, we get $\ln(p) + \ln(V) = \ln(mR) + \ln(T)$. When we take the differential, we find $\frac{dp}{p} + \frac{dV}{V} = \frac{dT}{T}$ in which the term $\ln(mR)$ disappears because the differential is a constant. By substituting the original adiabatic equation to remove the volume dependence, we get $c_p\frac{dT}{T} = R\frac{dp}{p}$. By dividing through c_p and defining $k = \frac{R}{c_p}$ and integrating from (T_o, p_o) to (T, p), and then taking the antilog, we have $T = T_o(\frac{p}{p_o})^k$, the Poisson's equation. With $(\theta = T_o$ at $p = 1000hPa)$ we have

$$\theta = T \left(\frac{p_0}{p}\right)^k \qquad\qquad (2.14)$$

which is known as the potential temperature. This potential temperature gives the temperature that a parcel of air would have, if brought dry adiabatically to a pressure of 1000 hPa. Where ever the parcel is located within the environment, its potential temperature is defined, and if it is moved dry adiabatically the potential temperature does not change. This fact makes the potential temperature a conservative property of dry adiabatic air.

So using the potential temperature equation (2.12), and solving it for temperature and inserting it into the equation of motion for a hydrostatic equilibrium (Eq. 2.10), we get

$$\ddot{z} = B = g\left(\frac{T'-T}{T}\right) = g\left(\frac{\theta'-\theta}{\theta}\right) \qquad\qquad (2.15)$$

a relationship between buoyancy and potential temperature for the dry adiabatic motion of a parcel of air.

$$CAPE = \int_{bottom}^{top} B \, dz \qquad\qquad (2.16)$$

As shown above CAPE represents the amount of buoyant energy available to accelerate a parcel of air vertically. It is used as an index in measuring the severity of a convective storm for a given temperature and moisture profile (Lin 2007). By using the potential temperature of an adiabatically moving air parcel and the potential temperature of the environment, the CAPE can be calculated quite readily with buoyancy and the relation between potential temperature and temperature.

The fact that an accelerating parcel of air rising adiabatically has a constant potential temperature and that potential temperature is also determined by the environmental temperature that is known through the radiosonde data permits assessment of the convective available potential energy.

CAPE is a measure of the amount of energy available for convection, and certain values are indicators of vertical stability or instability. CAPE, as shown above, is directly related to the maximum potential vertical speed available within an updraft. The CAPE value does not indicate a funnel cloud or tornado will occur, but does give an indication of vertical air stability.

The value of a given CAPE at zero joules (J) has a convective potential of stable air, but a CAPE value between zero and thousand joules has a convective potential of marginally unstable, from 1000 J to 2500 J it is moderately unstable, 2500 J to 3500 J vary unstable and beyond 3500 J extremely unstable air.

2.3.2 Computational Technical Details and Data Flow of the Data Analysis Method

2.3.2.1 Software Used

I used two different program languages, Matlab and NCL, as each has its own characteristics and advantages in processing the data. The former has many mathematical statistical packages that were advantageous for the data analysis from this point of view, but not available in the NCL package. Matlab is used for to its ease in writing, manipulating and searching the data for the measured variables. NCL is used for its abundance of already available programs written for finding relevant atmospheric indices used in analyzing atmospheric characteristics. Further reasons will become more evident later in this chapter, when I explain the algorithm that I developed within the framework of this research. Here, I just give a brief description of the general data processing with these software packages.

When scanning and converting the 70xxx.dat files with Matlab and NCL and converting them into a usable format for the respective programs within a given language, certain differences need addressing. Matlab's statistical programs require valid data only. This means missing data have to be removed prior to its application. Thus, for all the dates scanned between May and September 1948 to 2014, any row found with missing data of any variable of pressure, dew point temperature, air temperature, height, wind speed and wind direction is removed from that profile of the specific date and time. This procedure allows the usage of only viable data with all variables intact over any pressure level, making any limits generated from these data points sound.

On the other hand, NCL has built-in features that handle missing data. Thus, by generating a NetCDF file from the 70xxx.dat files I was able to use the pressure levels with missing values in NCL. This procedure allows for a smooth transition between levels of some of the variables in plots. The NCL Skew-T function for generating a profile fills in the gaps with the most probable values for missing data.

Although this procedure is acceptable, it leads to the questionability of the soundness of the logic behind the statistical limits generated with the limited number of observations. To remove any question of viability set by the similarity scans, the NCL software is used only in generating the final and most probable profiles for the Skew-T diagram and the calculation of the CAPE values.

2.3.2.2 Data Flow and Data Processing

Radiosonde data for Alaska is characterized with an identity of a five number 'dat' file such as: 70xxx.dat. The last three numbers are unique for one of the 12 radiosonde launch sites in Alaska (Fig. 2.1). Here, the letters xxx stand for 219 for Bethel, 261 for Fairbanks, 231 for McGrath, 133 for Nome and 273 for Anchorage. As mentioned before, these stations are the sites used in the radiosonde analysis of my research.

The search algorithm needs the full suite of data to check for similarity of profiles with those of documented FC events. Each of the 70xxx.dat files is converted over to whole unit numbers and not the tenth values of the data files. Each of these files is also scanned for missing values for each given location analysis. For example, for Fairbanks the 70261 file is scanned and converted by the Matlab algorithm for usable dates and variable measurements without the -9999 and -8888 values that indicate missing values or data discarded by the QA/QC performed by the NWS/NOAA. The -9999 and -8888 tags mean that not the complete set of pressure, height, air temperature, dew point temperature, wind speed, and wind direction data exists. Thus, any row of a given altitude with a -9999 and/or -8888 value is removed and not used by the Matlab program. This procedure reduces the radiosonde data files to only the usable data for my research, i.e. only real viable values.

On the contrary, NCL can identify the -9999 and -8888 numbers as missing values and has built-in features that skip data operations when missing values exist. This difference of NCL to Matlab allows reading in the complete dataset in the NCL program. In this research, the Matlab algorithms are the controlling procedures. Consequently, I produced a radiosonde dataset that only included the valid values. Figure 2.6 gives a schematic illustration of the data processing.

Based on the removal of the missing data, there are gaps of missing data within the results. This data gap is due to the stringent methods used in using actual, real measured data and not interpolated or model values. The radiosonde data file is scanned and converted three times into the required and needed formats, twice in Matlab and once in NCL.

The algorithm for this analysis falls into three parts. Each part will be described in the following with respect to procedure, purpose, and required input data. The first procedural step is to locate the radiosonde vertical profiles for all dates and times on which funnel clouds were observed. These profiles will be the basics for setting the range limits of the dew point temperature and air temperature ranges over a given pressure range (see previous section for details). These limits will be used by the search algorithm to determine which other radiosonde profiles in the dataset of radiosonde profiles are similar to those radiosonde profiles that were collected at the times and days on which funnel clouds were observed for a given group. See the description in section 2.3 for how similar profiles were characterized.
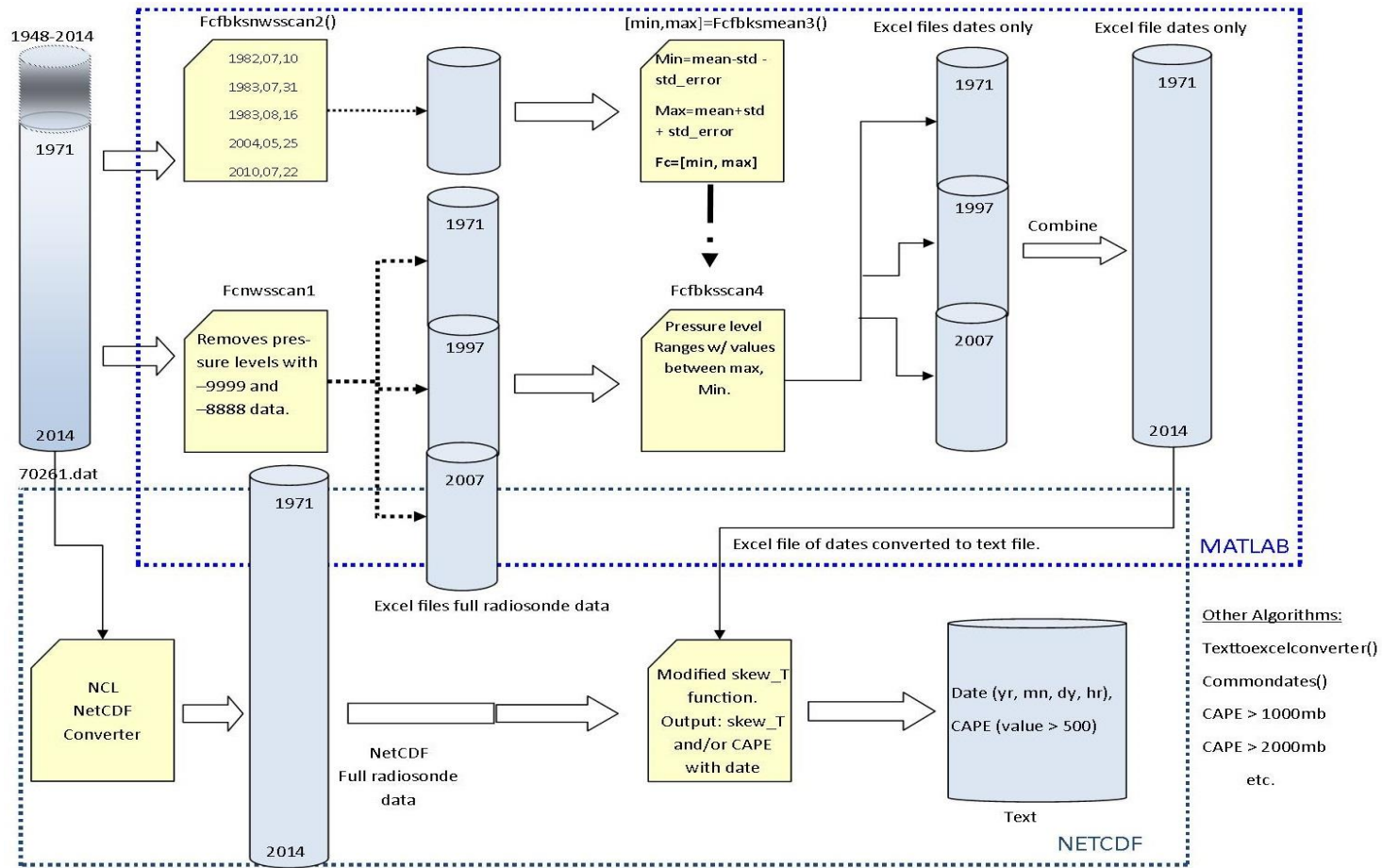
Fig. 2.6. Schematic representation of the search algorithm used, identifying similar profiles of days with documented funnel cloud sightings, using atmospheric radiosonde data.

The second procedural run is the scanning of the 70xxx.dat file between May and September for all years for missing values at all height levels. If a -9999 and -8888 marker for missing data of geopotential height, dew point temperature, air temperature, wind speed, wind direction, and relative humidity occurs for any of these quantities, the row of values at that level is removed, i.e. not used. The remaining valid data is then converted to SI units (m, kg) and stored.

The removal of missing data creates an uneven length of the daily data for any given radiosonde profile between the older and the more recent radiosonde profiles. This means the older radiosonde data has a smaller number of pressure levels in comparison to the more recent radiosonde profiles, which were collected by digital instrumentation.

After the removal of missing data, the new data file is scanned again, this time, however, with the search algorithm (Fig. 2.6). As discussed above, the search algorithm uses the limiting values identified in the first scan to search the radiosonde profile dataset obtained in the second scan for profiles that are similar to those of the funnel clouds observed in the respective groups. The output of this new scan is the dates with profiles similar to the observed FC profiles. These dates are saved as a text file for use in calculating the CAPE values in the NCL Skew-T program that I modified for this purpose.

The third procedural step is performed in the NCL software. The original 70xxx.dat file is converted into a NetCDF format for use in the NCL function of the modified Skew-T program (Fig. 2.6). The Skew-T program was modified by me to run in a while loop and to calculate the CAPE values for each date identified in the text file created from the Matlab program of similar radiosonde profiles to profiles on the funnel cloud observational dates, i.e. the output of the search algorithm in the previous step. For any CAPE value above 500 J, the date and CAPE values are saved as probable dates of radiosonde profiles similar to the funnel cloud radiosonde profiles that were observed for a given group.

On this data, further analysis can be performed for that group using the date and values of CAPE above a given limit larger than 500 J. Synoptic reanalysis maps can be analyzed for any CAPE value of the given dates, and also the Skew-T profiles and winds, etc.

2.4 NEXRAD Weather Radar: WSR88D radar

Radar reflectivity (Z) and Doppler velocity (VR) were provided by the WSR-88D radars in Alaska. Radars are located at Bethel (PABC), Bjorka Island (PACG), Nome (PAEC), Kenai (PAHG), Middleton Island (PAIH), King Salmon (PAKC), and Pedro Dome (PAPD). These locations are indicated in Figure 2.3. Radar coverage is limited to 230 km around the radar (e.g. Houze 1993) and therefore only covers parts of the coastal area to the South and West of Alaska and Anchorage (Fig. 2.3). Some radar can operate at differing angles, but typical operation uses $0.5°$ (Fig. 2.7). Low-elevation scans are blocked by local topography (Figs. 2.7, 2.8) including the Alaska Range, White Mountains, and Brooks Range and other ranges smaller than the aforementioned ranges as can be derived from comparison of Figures 2.3 and 2.9.
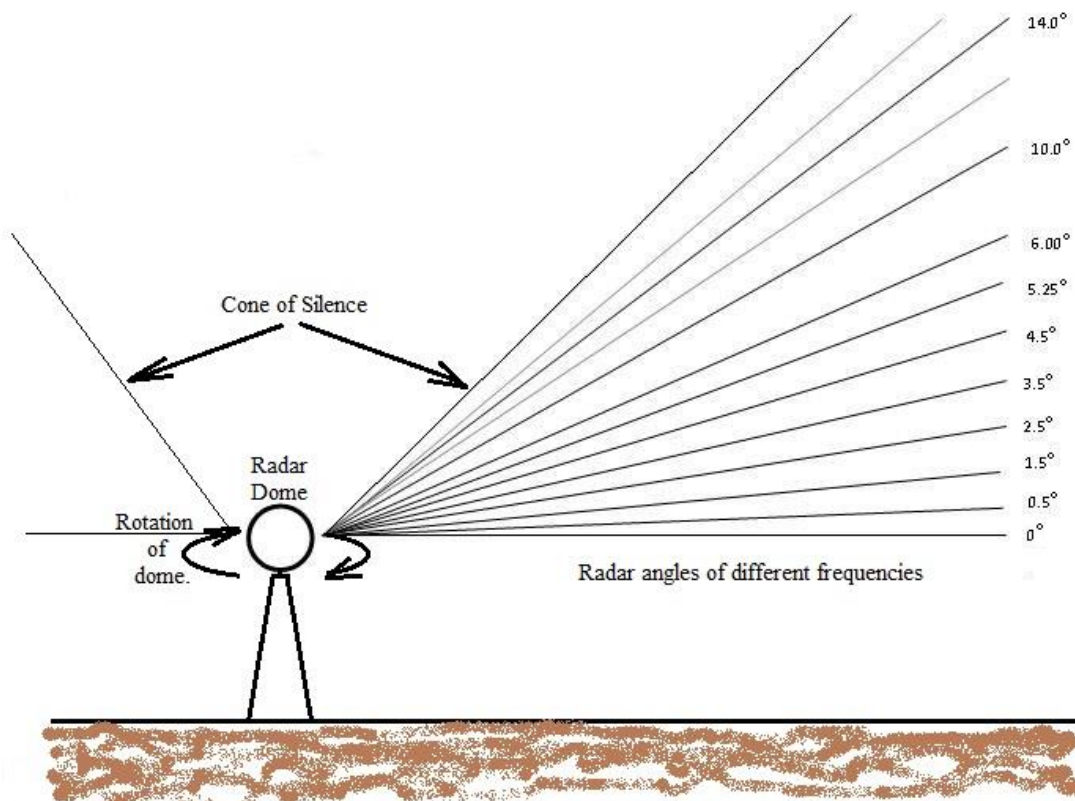

Fig 2.7. NEXRAD weather Doppler radar basic operating characteristics. Source: NOAA. Retrieved 2016.
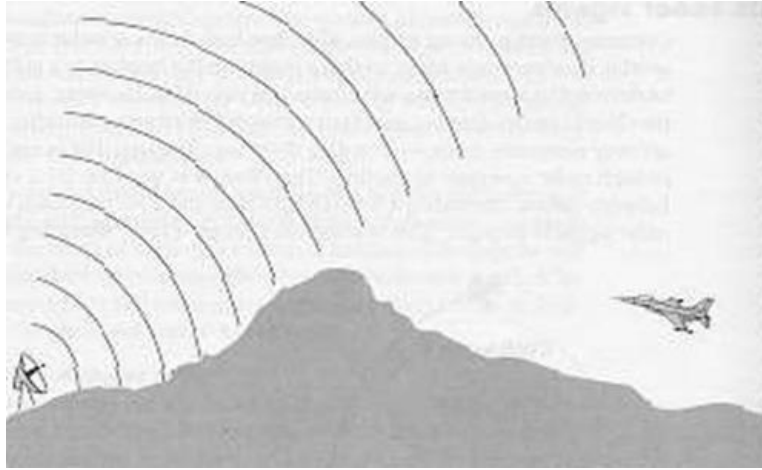
Fig. 2.8 Schematic view of radar masking by mountains. A funnel cloud occurring behind the mountains would be invisible to the radar like the plane in this figure. Retrieved from: http://voodoo-world/falcon/AFT.html (2016)

The radar scanned with the deep convection configuration 146 (denoted as Volume Coverage Pattern #12 or VCP12) with 14 elevation angles that 147 ranged from 0.5° to 19.5° with finer elevation angle separation of ~0.5° close to the 148 surface and coarser resolution of up to ~3°-4° at higher elevation angles (Fig. 2.7). More details about the scan strategy can be found in the Federal Meteorological Handbook No. 11, 150 Chapter 5 (OFCM 1997). As can be seen in Figure 2.9, a full 360 degree sweep is blocked by mountains for the majority of the radars. Furthermore, the resolution drops the further away a target is located from the site. The volume coverage area decreases four fold with distance. Thus, it limits the size of what is observable in relation to back reflectivity of the radar beam.

The power decrease is synchronous to the inverse square power decrease, except radar uses volume. The power reflected back is proportional to the cross-sectional area (σ) divided by the distance r to the fourth power:

$$P \sim \frac{\sigma}{r^4}. \tag{2.15}$$

Resolution and blockage is the greatest drawback for locating funnel clouds with a small cross-sectional footprint and low velocity rotation.
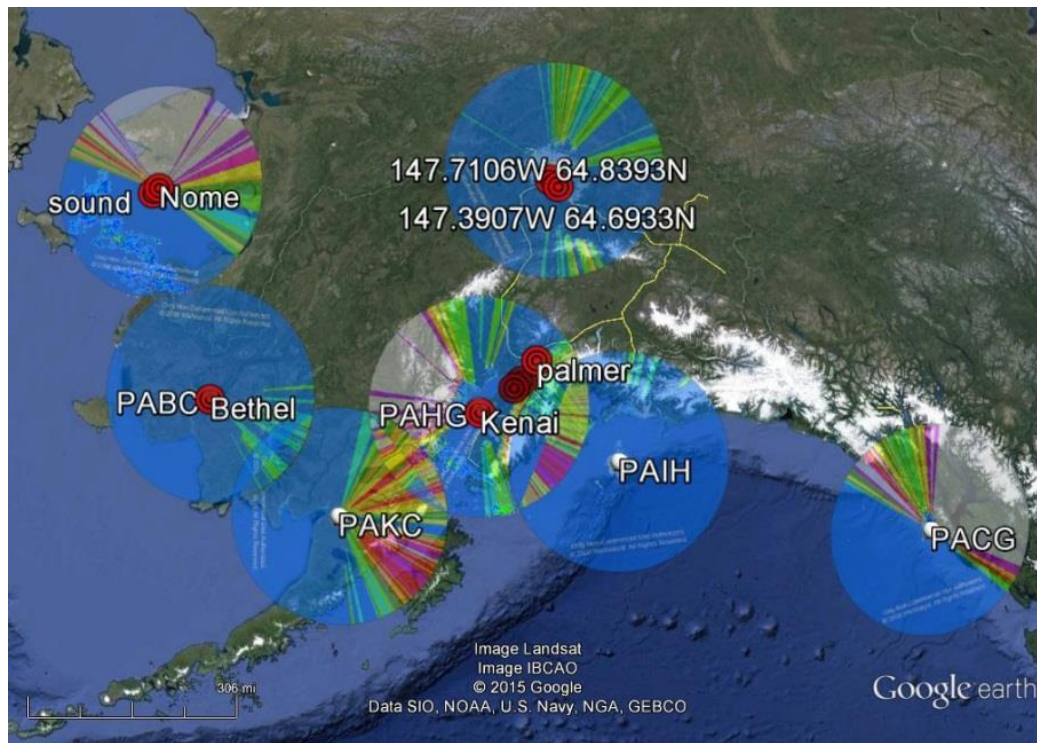
Fig 2.9. Illustration of the scanning radius of the seven NEXRAD radar sites in Alaska. The red targets show where some of the nine usable sighting reports fell within radar range.

My analysis includes level 3 data because level 2 data is not available before 2010. Only 15 of the reported funnel-cloud sightings were within in the 230 km range of the seven NEXRAD radars that started operations in 1997 (see section 2.1 for onset of operations at the various sites).

The difference of levels in Doppler radar data is the level of post processing: level 1 data is the raw data from the radar. Level 2 data has a small amount of processing of the Base Reflectivity (0.5 dBz increments), Radial Velocity (1 kt increments) and Spectral Width. Radial resolution of the velocity product is 250 m, with vertical resolution angles of 9-14 vertical tilts available. Level 3 radar data is known as NIDS data and has the most processing with a lower resolution than level 2 and less number of vertical resolution tilt available, only 4.

Level 3 data processing resolution and data available are Base Reflectivity (5 dBz increments), Radial Velocity (5 kt increments), Storm-Relative Radial Velocity (5 kt increments), Echo Tops, Vertically Integrated Liquid (VIL), 1hr/3hr/storm total precipitation estimates and Vertical Azimuth Display (VAD) wind profile.

41

I analyzed the radar data to see if there is signature that could help in the identification of potential FC events. Due to the small cross-sectional area footprint (<< 1 km) and poor radar resolution at the distance relative the radar site and mountain and hill blockage the NEXRAD radar systems are not a viable funnel cloud detection system to detect the small rotational velocities for they fail.

Figure 2.10 shows the location of the funnel clouds that were within radar range of Anchorage. However, during the time of the funnel cloud occurrence, all the funnel clouds were blocked by mountains and hills. Further, at the distance relative to the radar site; the spatial resolution makes it impossible or very difficult to distinguish the small cross-sectional footprint and low rotational velocity of the size of a funnel vortex.
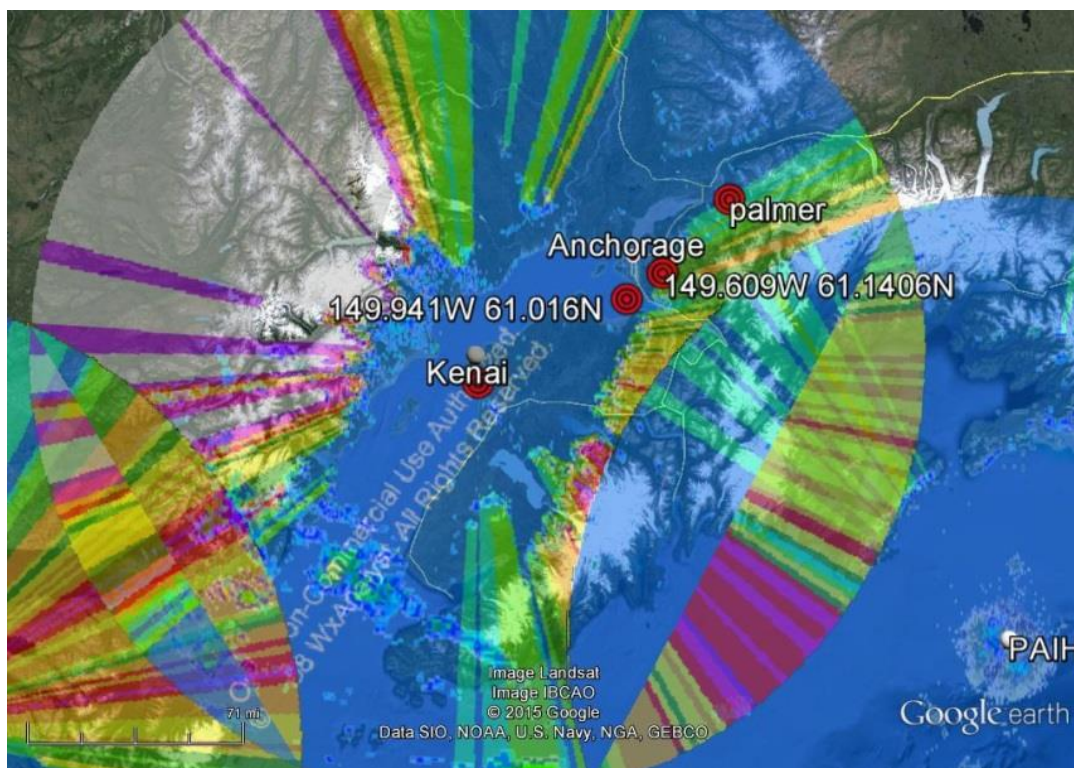

Fig 2.10. Location of the four funnel cloud sightings with usable latitude and longitude within Anchorage's NEXRAD radar range. The different colors represent different levels of blockage over the varying angles of the radar sweep.
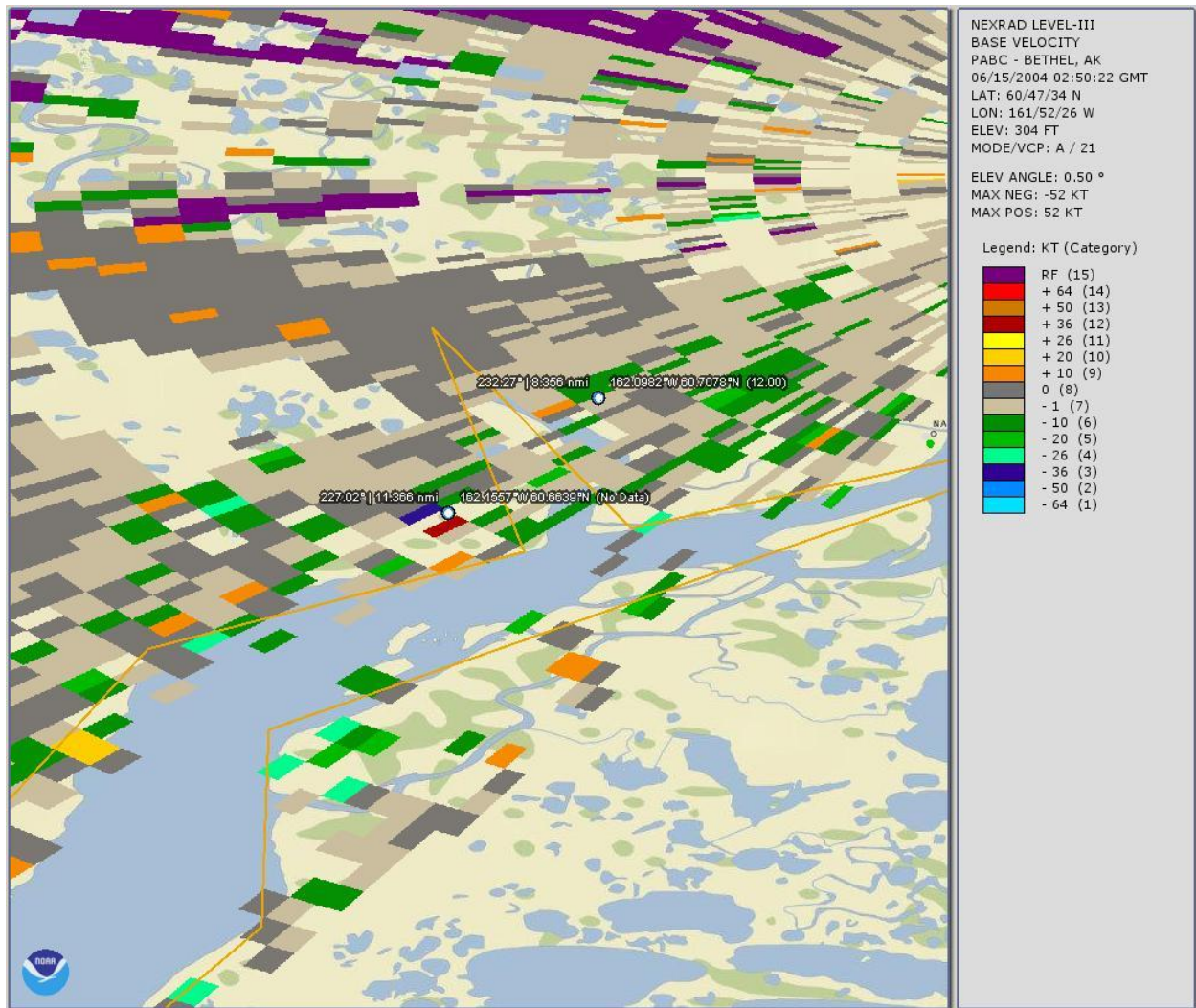
Fig. 2.11. The two white circles with distance and coordinates are two occurrences of a tornado observed in Bethel Alaska on June 15th, 2004 at 02:22 am GMT, local time was June 14th, 2004 5:22 pm in the afternoon. The cloud rotation was counter clockwise as was the tornado were red is moving towards the radar site and blue away, the legend give the relative rotational speed at +64 kt (knots) (~28.8 m/s) for red and -36 kt (~ 16.2 m/s) for blue, so the storm is traveling towards the radar at +14 kt (~ 6.3 m/s). The first dot is 11.366 nmi (nautical miles) (~ 21 km) and the second is 8.356 nmi (~ 15.48 km). These are the only two indications of the tornado over the whole level 3 radar data of 24 hrs during this day.

Figure 2.11 shows an example of a tornado detected by Doppler radar from the West Coast group in June 2004, however, the detection, or characteristics signature of a rotational system, a tornado barely shows. Resolution and the time required for a 360° rotational sweep makes detection an act

43

of luck, an act of chance especially if you are not looking for it. The low speed of the precipitation cloud's rotation does not show a hook echo due to resolution, and large radar sweep areas.

These investigations led to the conclusion that in Alaska, radar has limited value in funnel cloud detection. This finding is due to the relative low likelihood that the vortex is at the right distance that the radar resolution would be able to capture the vortex ($\ll 1.1$ km). Since the analysis of the radar data did not provide any further funnel cloud cases, and did not capture the documented cases (e.g. Figs. 2.10, 2.11), the radar data is not further-discussed for brevity.

2.5 Synoptic Reanalysis Maps

In this research, the National Center for Environmental Protection/National Center for Atmospheric Research (NCEP/NCAR) global reanalysis dataset is used as a substitute for spatial data. Since many regions of Alaska have no data within 100 km, the use of reanalysis is necessary (Cassano et al. 2011). I used the synoptic reanalysis data to compare the forcing between different pressure levels for the days on which funnel cloud sightings were reported.

This following analysis was carried out on the 300 hPa, 500 hPa and surface pressure maps to understand funnel cloud formation in Alaska. Such understanding could be helpful for forecasting funnel cloud events. The analysis was carried out as follows:

- In the 300 hPa map (about 9200 m, 29,900 ft in altitude), the wind is analyzed for its forcing effect on the 500 hPa level.
- In the 500 hPa map (about 5600 m, 18,200 ft), I analyzed for the reanalysis data for forcing from the surface and if the 500 hPa level is influenced by processes occurring at the 300 hPa level.
- The 1000 hPa map served to examine the forcing of winds and wind direction by the pressure field or the surface characteristics.

The synoptic maps are also used to identify the forcing mechanism.

Chapter 3 Results

Cassano et al. (2011) demonstrated a relationship between large-scale synoptic circulation patterns and the local surface weather and temperatures extremes at several locations across Alaska, i.e. an influence of synoptic scale features on local weather. Surface synoptic pressure patterns with such impacts that occurred most frequently were: moderate to strong Aleutian lows centered in Gulf of Alaska, patterns with Beaufort/Chukchi Sea low, and patterns with low pressure over the Canadian Archipelago with broad low pressure over Alaska and high pressure to the west of Alaska. Though Cassano et al. (2011) also gave specific synoptic surface configurations for extreme temperatures during the summer, none seems to apply to the funnel cloud events as will be discussed in the following.

3.1 Observed Funnel Clouds

The dates and times of funnel-cloud sightings in Alaska as well as coordinates, if available, were listed already in Table 2.1 in Chapter 2. The visualization of these events, as a function over time (1948 to today), months, and hour of the day were shown in Figure 2.4 in Chapter 2. According to Figure 2.4, there were more sightings since the turn of the millennium. July had the highest number of observed FC events, while during the day most events occurred around local noon. Note that due to the large size of Alaska local noon differs often more than 2 hours from Alaska Daylight Time (AKDT).

From a theoretical point of view (cf. Lin 2007; Pielke 2005), a large variation in time of the day and spread over months suggests that topography may play a role. On the contrary, similar CAPE values during FC events hint at thermodynamics as an important factor (e.g. Houze 1993; Lin 2007).

3.2 Fairbanks

Table 3.1 shows the dates of funnel clouds events near Fairbanks. In total, there were five events, three of them in the 80s, and two of them in the new millennium. In the 2004 case, there were three funnels visible at the same time, but under different clouds south over the Tanana Flats visible from the University Alaska Fairbanks campus (Mölders 2014, pers. Comm.).

Table 3.1. Dates, and times of observed funnel clouds in the Fairbanks area.

Year	Month	Day	Local Time	Radiosonde,bfr	Radiosonde,aft
1982	7	10	3:35pm ADT		1982071100
1983	7	31	2:30pm ADT		1983080100
1983	8	16	1:40pm ADT		1983081700
2004	5	25	6pm ADT NOAA	2004052600	
2010	7	22	9:47am ADT	2010072212	

Figure 3.1 shows the occurrence of observed funnel clouds as a function of year and month for the Fairbanks area. In the Fairbanks area, most sightings occurred after 1982, and in May, July, and August during the day between 9 am and 6 pm AKDT time.
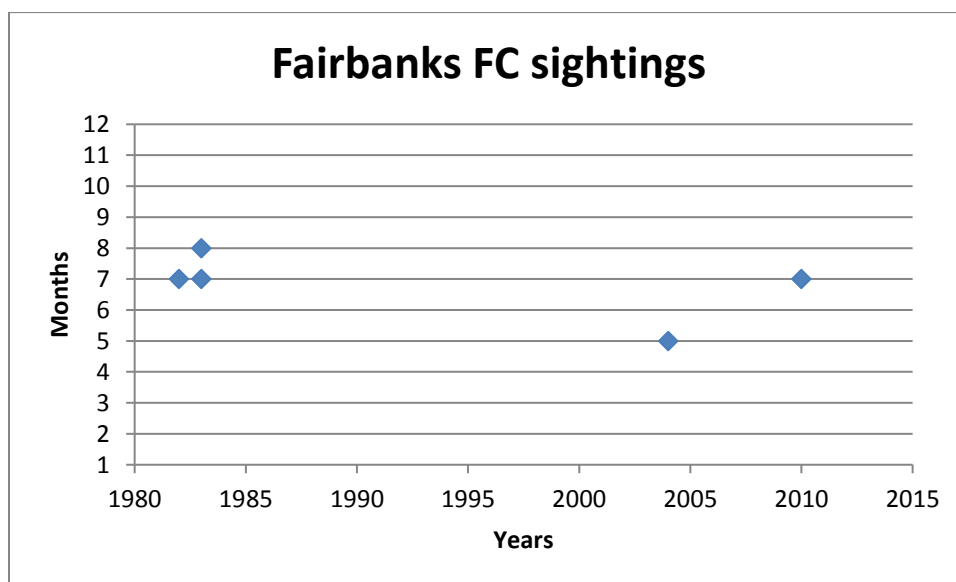

Fig. 3.1. Funnel cloud sightings by year and months for the Fairbanks group.

Figure 3.2 shows the Skew-T diagrams for dates of three observed funnel cloud events. These plots demonstrate that in the Fairbanks area, environmental conditions during funnel cloud events vary over a broad range. Table 3.2 lists the air temperature, dew point temperature, wind speed and direction ranges obtained by scanning for the various pressure levels.
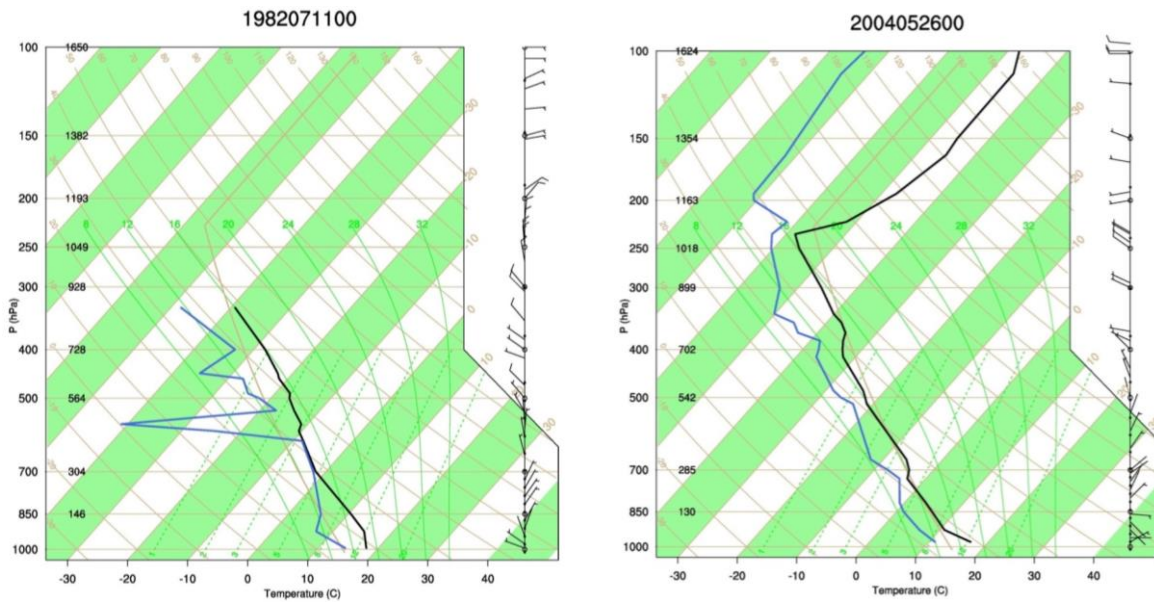
a)   b)
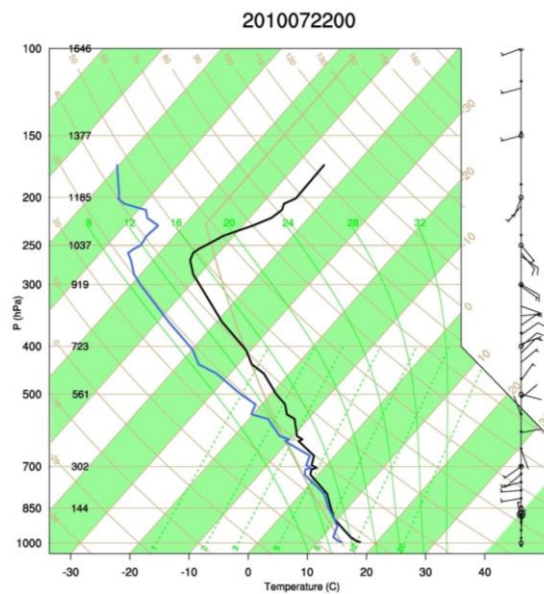
c)

Fig. 3.2. Skew-T diagrams of three of the reported funnel cloud events in the Fairbanks group with temperature (black line) and dew point temperature (blue line), wind speed and direction (barbs). Radiosonde Skew-T date and time of atmospheric profiles, displayed for Fairbanks: Figure 3.2a) July 11, 1982, 00 GMT, Figure 3.2b) May 5, 2004, 00 GMT, and Figure 3.2c) July 22, 2010, 00 GMT.

47

Table 3.2. Ranges of air temperature (T), dew point temperature (T_d), and wind speed (v) as obtained for the various pressures ranges (p) for Fairbanks based on the profiles of observed funnel clouds. See Chapter 2 for reasoning of the choice of the pressure ranges.

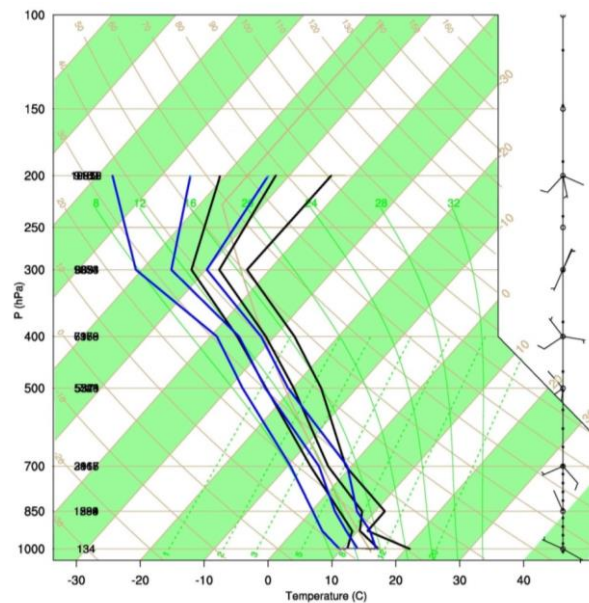| P (hPa)	Range (hPa)	T (C°)	T_d(C°)	v (m/s)
1000	1015-962.5	10.8 - 21	9.6 - 15	1.6 - 4
925	962.6-887.5	9.1 - 12	4.4 - 12	0.0 - 1.7
850	887.5-812.5	4.4 - 11	0.2 - 7	2.4 - 4
700	737.5 - 650	-6.4 - -1	-9.5 - -1	0.0 - 8
500	550 - 450	-24.1 - -16	-27.8 - -21	0.0 - 8
400	450 - 350	-35.9 - -27	-39 - -32	0.0 - 8
300	350 - 250	-52.2 - -44	-61 - -50	5.2 - 6
200	250 - 150	-60.8 - -43	-77.6 - -53	0.8 - 12

Fig. 3.3. Resultant ranges for potential funnel cloud profiles with CAPE greater than 500 J as obtained based on documented funnel cloud sightings for the Fairbanks group. Note that here the Skew-T limits of minimum (left), mean (middle), and maximum (right) temperature (black lines), dew point temperature (blue lines), wind speed and wind directions (barbs) are shown.

In Figure 3.3, the minimum, mean, and maximum wind direction over the pressure ranges listed in Table 3.2 are shown. However, these values of minimum, mean, and maximum are a concern.

Examination of the wind directions (Figs. 3.2a-c) indicates that no common direction seems to be present in the atmospheric boundary layer (ABL) and mid-troposphere. This finding may be a hint

that the mountains are not the primary forcing or only forcing. However, it cannot exclude that they have an important impact as all funnel cloud cases have a wind shear in the ABL and in the lower mid-troposphere in common (Fig. 3.2).
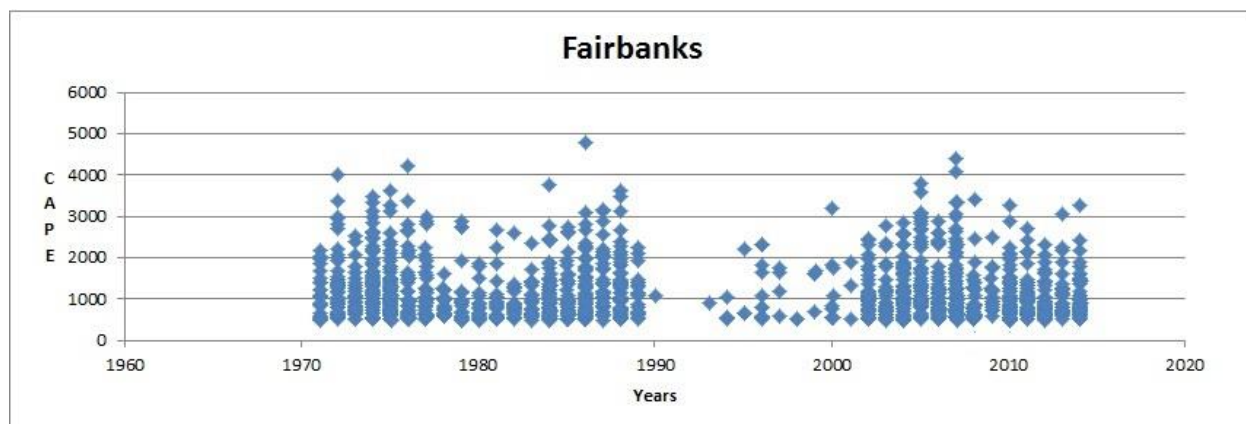

Fig. 3.4. Frequency (number of diamonds), and CAPE (in J), of events with radiosonde profiles similar to those during the observed funnel cloud events in the Fairbanks group as identified by the search algorithm and testing for CAPE. Note that between 1992 and 1994, there were problems with the dew point measurements data values excluded: as a result of stringent 1st requirement as depicted in (Fig. 2.6).

The gap between 1992 and 1994 is due to missing data and the stringent requirement of the first step of the search algorithm that all data must be present at a given pressure level. See Chapter 2 for details on the search algorithm. Thus, the gap in the results shown in Figure 3.4 is an artifact due to incomplete data and not a climatological feature. Analysis of Figure 3.4 clearly shows a wavelike structure overlain with higher CAPE in the early 70s, lower CAPE after 1976 to the mid-80s, followed by higher CAPE in the late 80s. In the mid-1990s, CAPE again is lower than after 2002.
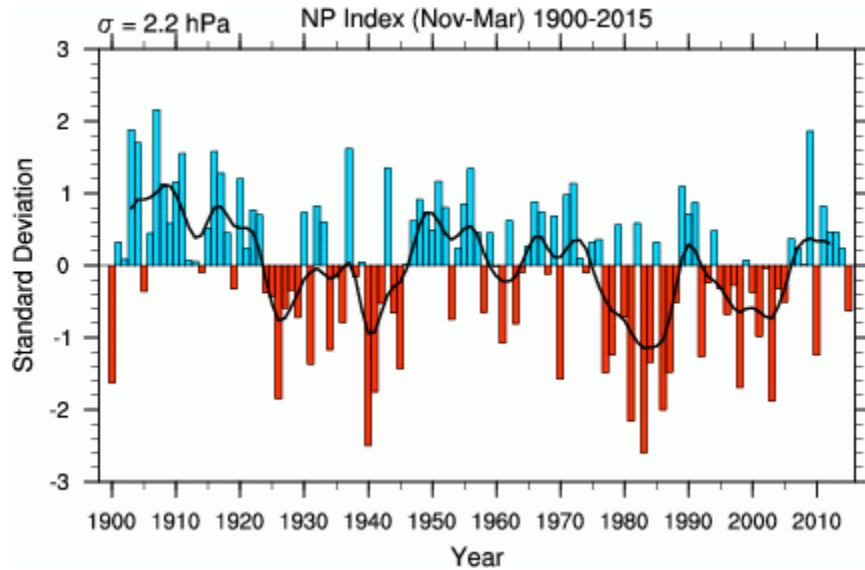
Fig. 3.5. NDJFM Northern Pacific index standardized anomalies as a function of time. The black line is a weighted (1-3-5-6-5-3-1) running mean. From: Hurrell et al. (2012).

The frequency found for potential funnel events (Fig. 3.4) shows a similar structure than the North Pacific index (NP) shown in Figure 3.5. The NP index is the area-weighted sea-level pressure over the region 30N–65N, 160E–140W. It is a measure for inter-annual to decadal variations in the atmospheric circulation. In this area the North Pacific, atmospheric changes are about one to two months ahead of changes in sea-surface temperatures (SST).

Figure 3.6 shows the atmospheric synoptic conditions at the pressure levels of 300 hPa, 500 hPa, and 1000 hPa for the dates of observed FC sightings. Obviously, there exist two slightly different synoptic scale situations, under which funnel clouds occur.

At 300 hPa, a common feature is a strong gradient in geopotential height south of the Alaska Range over the northern Gulf of Alaska and a much weaker gradient over the Interior of Alaska than over the Gulf of Alaska. This feature means that the polar jet is located far south of the area of interest. However, this situation can be accomplished by a high pressure over the Beaufort Sea and North Slope and low pressure over the Gulf of Alaska or by a low-pressure system off the Pacific Northwest coast and marginal pressure differences north of the Alaska Range (Fig. 3.6).

At 500 hPa, the geopotential height weakly varies over the Interior. This means that winds are calm in the mid-troposphere. There seems to be no distinct forcing from the 300 hPa on the 500 hPa surface over the Interior in both cases. In contrast, south of the Alaska Range over the Gulf of Alaska, the polar front is visible by dense geopotential height lines in both the 300 and 500 hPa map (Fig. 3.6). In all cases, the jet is more or less west to east orientated and parallel to the coast.

In all cases, the polar front slopes from south to north with increasing height. This means that in the range of the polar front, warmer air is located over colder air when looking at the vertical profile. Such temperature profile means an inversion. Inversions are visible at different heights in the mid-troposphere in the Skew-T diagrams of the documented funnel cloud events (cf. Fig. 3.3).

In the surface map, the Interior is under calm wind conditions like at the 500 hPa level. This feature means that any air parcel in an updraft would be only slightly offset from its location at the cloud base during its vertical transport in the ABL and mid troposphere while at 300 hPa, in other words close to the tropopause, it would be displaced eastwards. Such a feature means that a forming cloud has good chances for development, as the updraft is constrained (cf. Lin 2007).

However, the dew point temperature profiles suggest cloud tops are located in the upper ABL to mid-troposphere (e.g. Fig. 3.2).
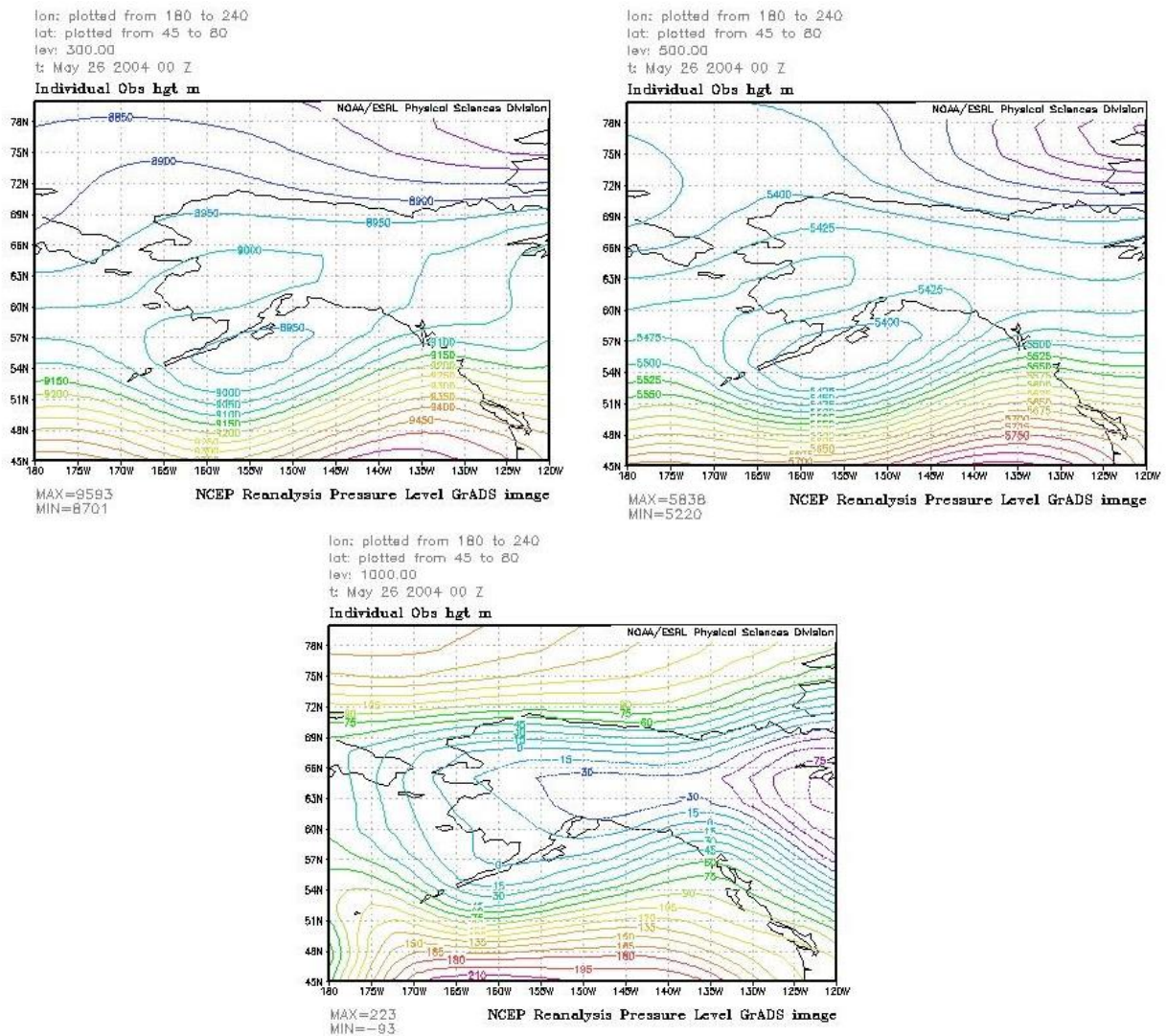
Fig. 3.6a. Geopotential heights at the 300 hPa (top left), 500 hPa (top right), and 1000 hPa (bottom) from reanalysis data on date of observed funnel cloud (May on the 26, 2004 at 00z) in GMT for the Fairbanks group.
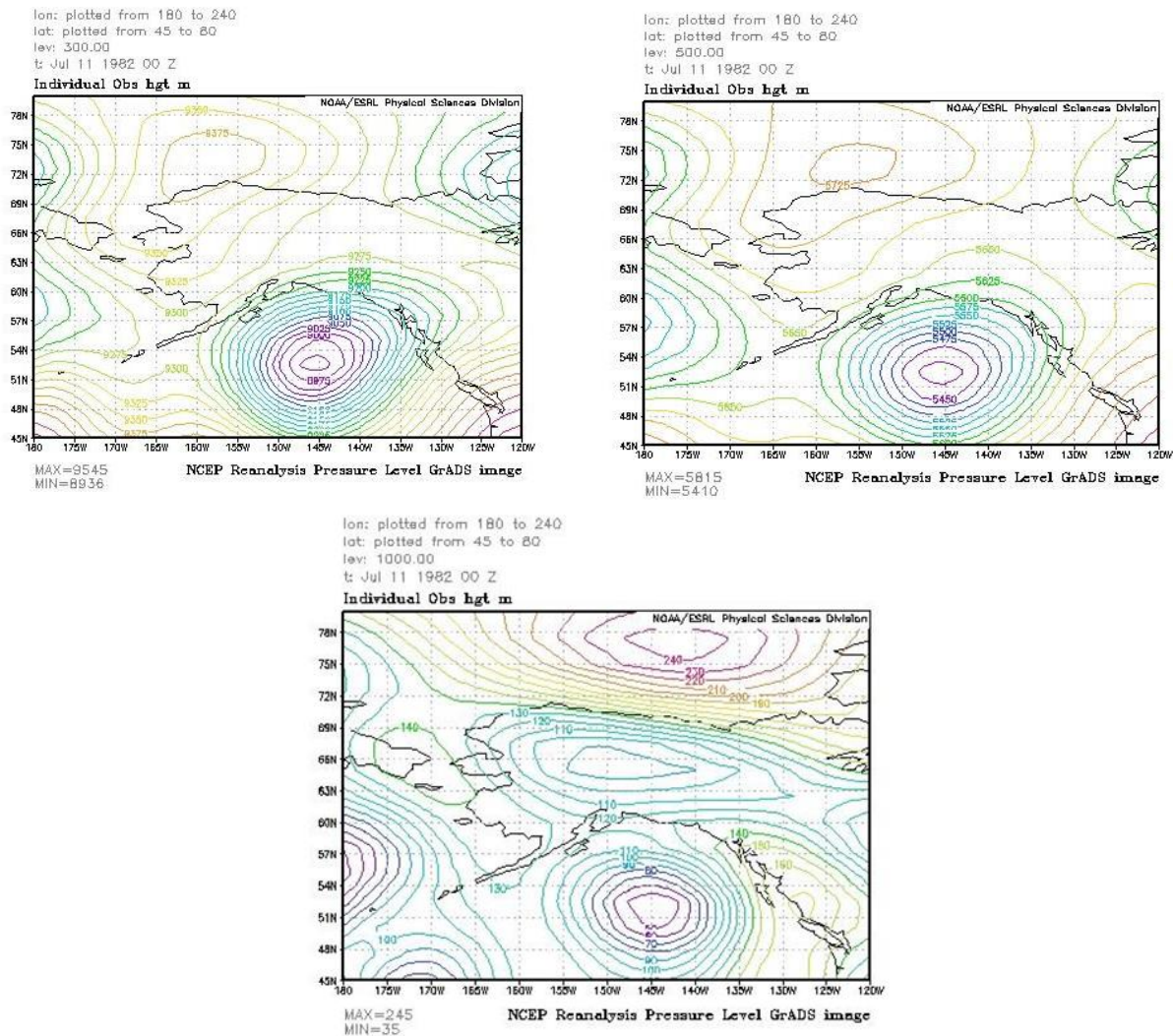
Fig. 3.6b. Geopotential heights at the 300 hPa (top left), 500 hPa (top right), and 1000 hPa (bottom) from reanalysis data on date of observed funnel cloud (July on the 11, 1982 at 00z) in GMT for the Fairbanks group.
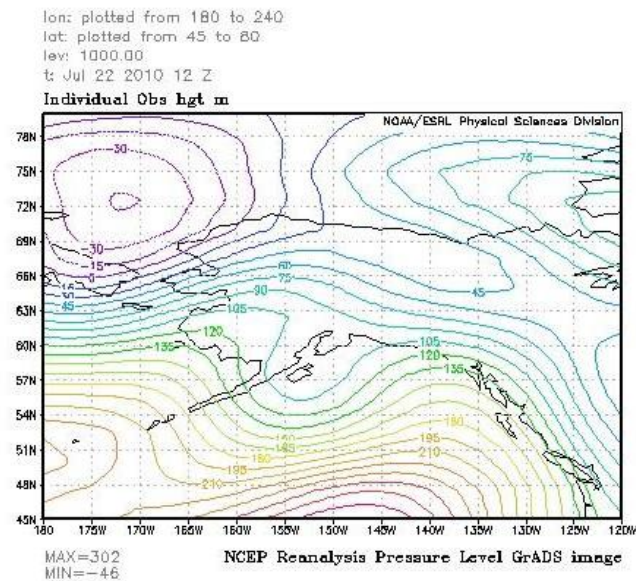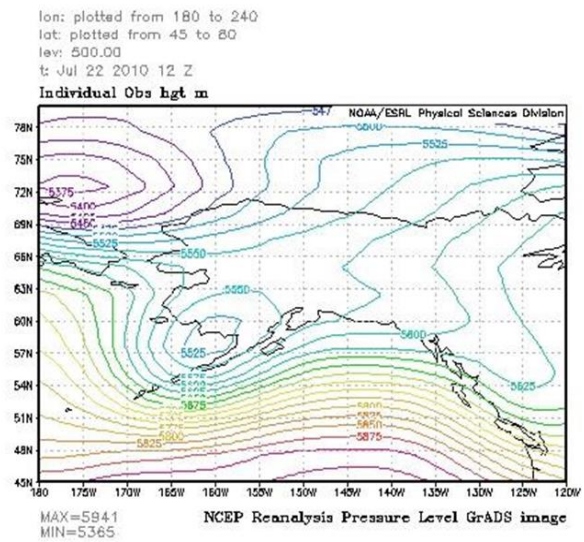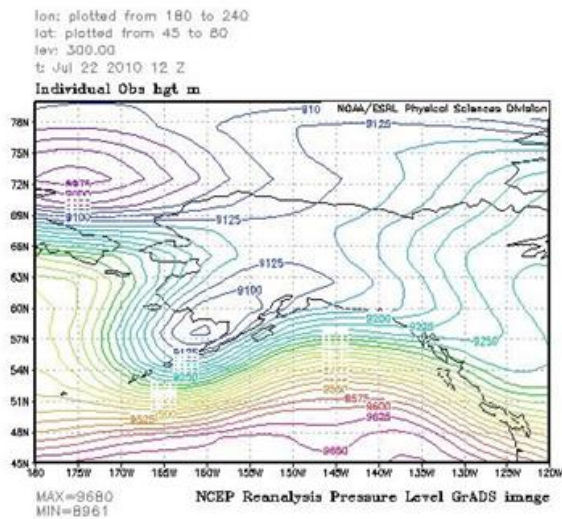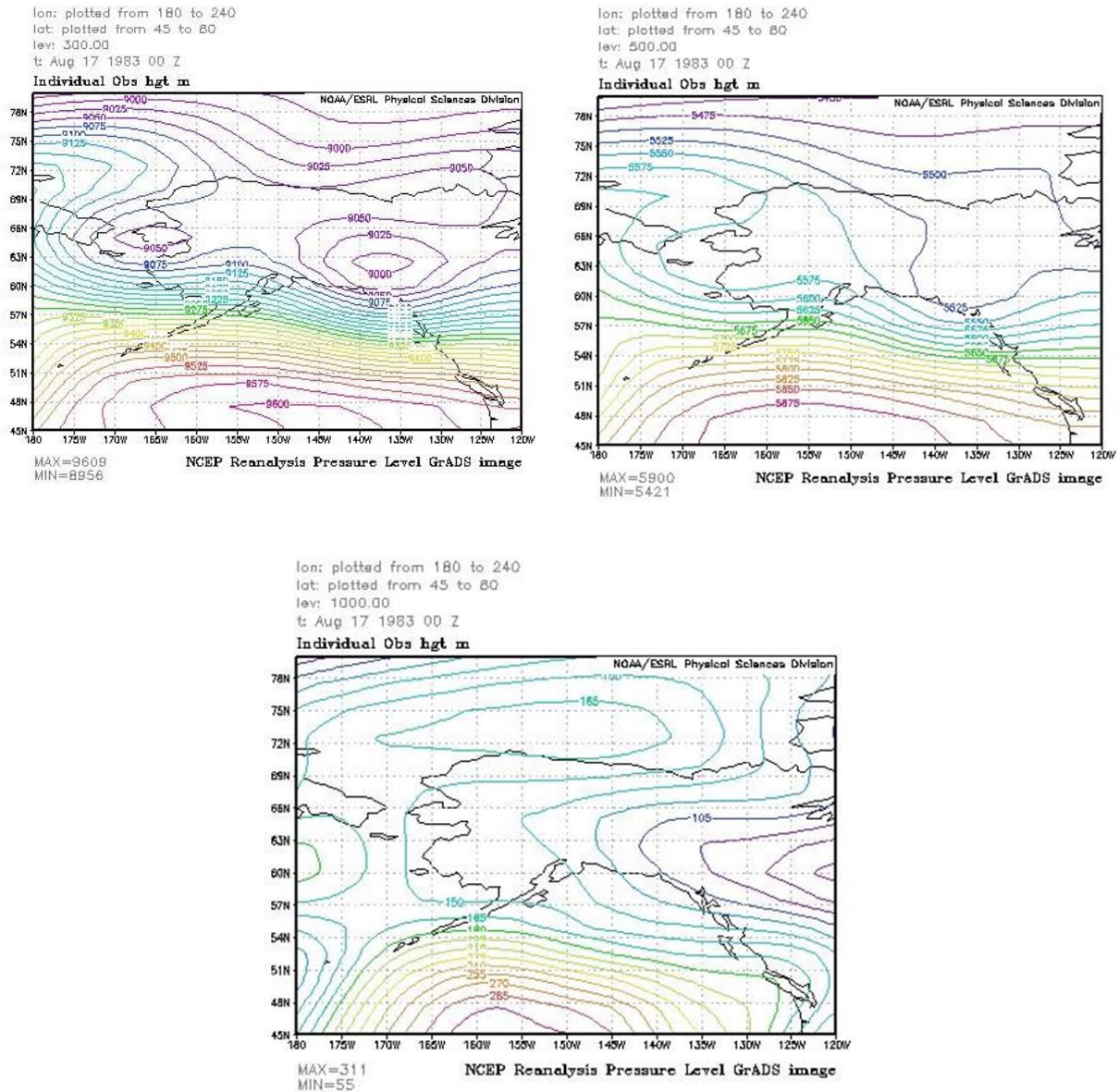
Fig. 3.6c. Geopotential heights at the 300 hPa (top left), 500 hPa (top right), and 1000 hPa (bottom) from reanalysis data on date of observed funnel cloud (July on the 22, 2010 at 00z) in GMT for the Fairbanks group.

Fig. 3.6d. Geopotential heights at the 300 hPa (top left), 500 hPa (top right), and 1000 hPa (bottom) from reanalysis data on date of observed funnel cloud (August on the 17, 1983 at 00z) in GMT for the Fairbanks group.

First, I will analyze Fairbanks reanalysis synoptic pressure maps of 300 hPa, 500 hPa and surface weather level (Fig. 3.6). Though some of the surface maps are similar to Cassano et al.'s (2011) most frequent patterns, yet others do stray away from the general patterns though are similar. The general characteristic of the 300 hPa (jet stream) pressure level is similar to the 500 hPa synoptic

map. Both indicate weak synoptic forcing over the area. Thus, we can conclude that the jet stream has no significant forcing to the surface. This is true for all the 300 hPa synoptic maps of all groups. The surface maps all have a broad low pressure system over central Alaska, centered between two high pressure systems at local time, May 25, 2004, and July 22, 2010 or between a high pressure system and a high pressure ridge at local time July 10, 1982.

In the Fairbanks group, the surface maps all have the gradient surface winds blowing across Fairbanks from West to East, adjacent to the floor of the Tanana valley in which the Tanana River, one of Alaska's major tributaries flows. At 500 hPa, the gradient winds blow from the Alaska Panhandle and Gulf of Alaska across the Alaska Range into the Tanana Valley.

The analysis shows that the 500 hPa level winds blow across the Alaska Range, the lee waves created by the mountains encounter the warm humid valley convectional air, thus forcing the cold mountain air down the northern slopes of the Alaska Range in which encountering the warm humid air flowing along the valley. The valley near-surface winds and the cold air moving downslope mean a wind shear that forces the air to rotate in a horizontal tube along the valley. When this rotating tube is turned vertically by buoyancy a rotating updraft forms. For Fairbanks, weak synoptic forcing does occur, but the only aspect is forcing winds across the Alaska Range in which the topography is the major influencing dynamical forcing structure.

Comparison of the findings gained from the reanalysis data with the profiles of documented FC sightings (Fig. 3.2) confirms that weak synoptic scale forcing must be present over the Interior in the ABL and mid-troposphere as the winds show various directions (Fig. 3.3). Obviously, there must also be a vertical wind shear within the ABL to the lower mid-troposphere. The radiosonde data also suggest that there must be a layer of saturated air at the top of the ABL (Fig. 3.4).

The west-east orientation of the polar frontal surface means that conditions are zonal and hence quasi-stationary with respect to the temperature conditions above the ABL. This means that the surface conditions can modify the conditions in the ABL.

From a mesoscale point of view, the following situation occurs (Fig. 3.7). The mountains to the South of Fairbanks are glacier-covered for which near-surface air is relatively cold, while the Tanana Flats are low and comparatively warm. In the White Mountains north of Fairbanks, the near-surface air is relatively cooler than the air at same pressure level over the Tanana Flats. This feature permits for slope wind formation where the cold air drains down the slope and lifts the air over the valley (Fig. 3.7).
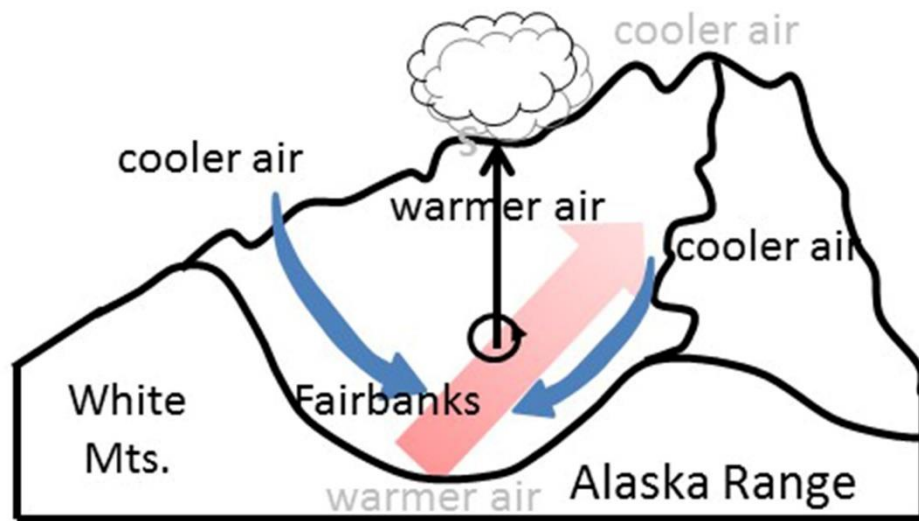
Fig. 3.7. Schematic view of slope winds and mountain valley circulation, further that circulation may also occur when the flow is up the valley. The blue arrows represent colder air draining down into the valley as some sort of katabatic wind. The light to red arrow stands for the warm air that moves down the valley in the ABL. The shading in color represents the temperature gradient due to the slope of the valley. The black with rotational circle-arrow symbolizes the updraft of a convective cloud. Figure 3.7 is modified after a sketch from Mölders and Kramm (2014).

In the valley, terrain has a west-east gradient with higher elevation to the east than west. Thus, a mountain valley wind may form as well and a flow down the valley may establish (Fig. 3.7). Unfortunately, there are no surface meteorological data to examine whether these dynamical features occur. However, they may provide the horizontal wind shear and hence vorticity to create rotation. Note: that the analysis of the synoptic maps and radiosonde profiles of the Fairbanks group suggest that the flow could also be up the valley.

To examine whether the search algorithm identified profiles that have similar synoptic scale forcing over the Interior as the observed funnel clouds, I pulled the reanalysis data for the dates identified by the search algorithm as potential funnel cloud events. I plotted the average geopotential heights on the surface, 500 hPa, and 300 hPa maps as a composite. The comparison of these maps with the maps of the funnel cloud sightings indicates that the search algorithm captures profiles that occur on dates with similar synoptic situations than on the days with observed funnel cloud events (Fig. 3.8).
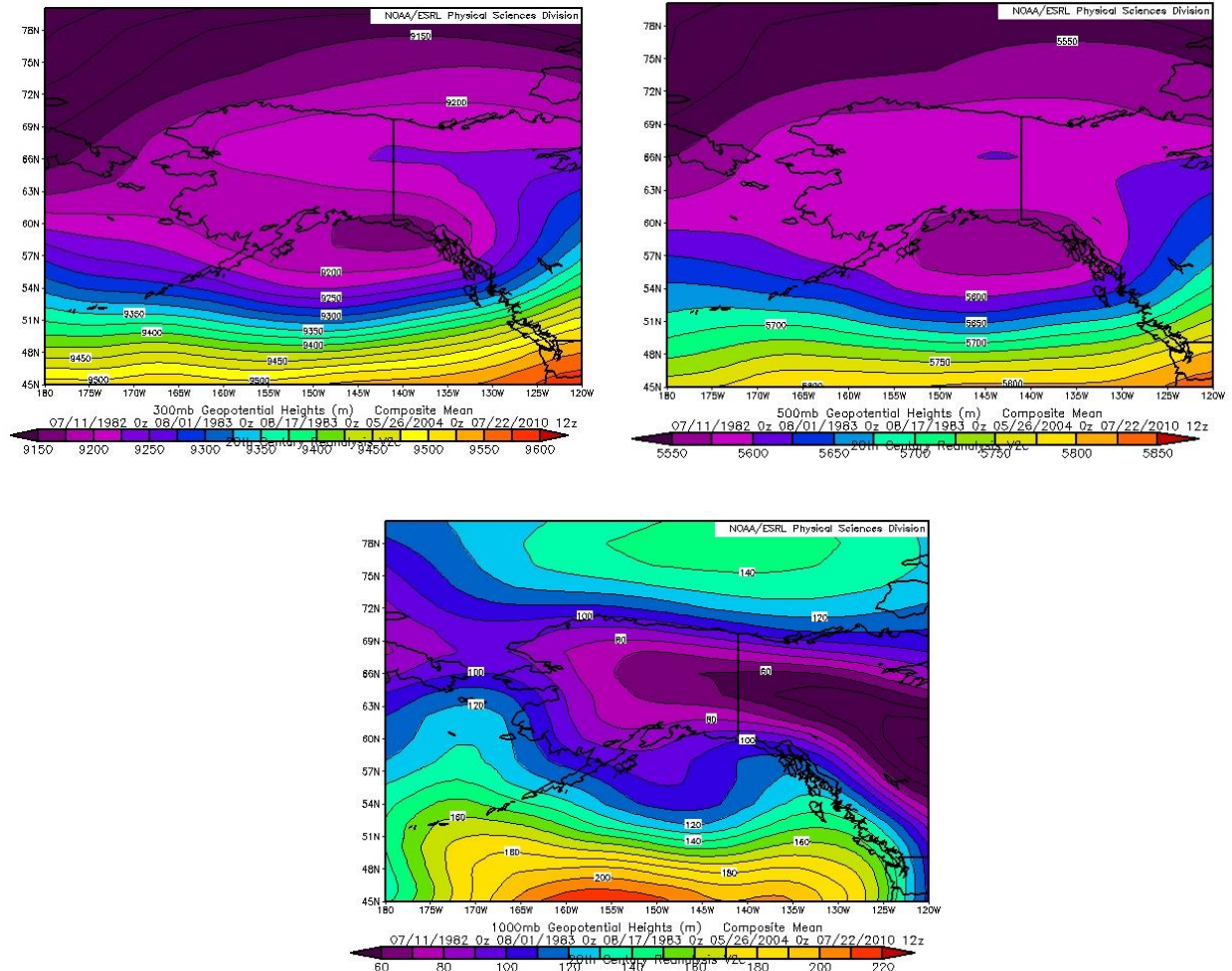
Fig. 3.8a. Composites of mean geopotential heights at the 300 hPa (top left), 500 hPa (top right), and surface map at 1000 hPa (bottom) of days with funnel cloud sightings.
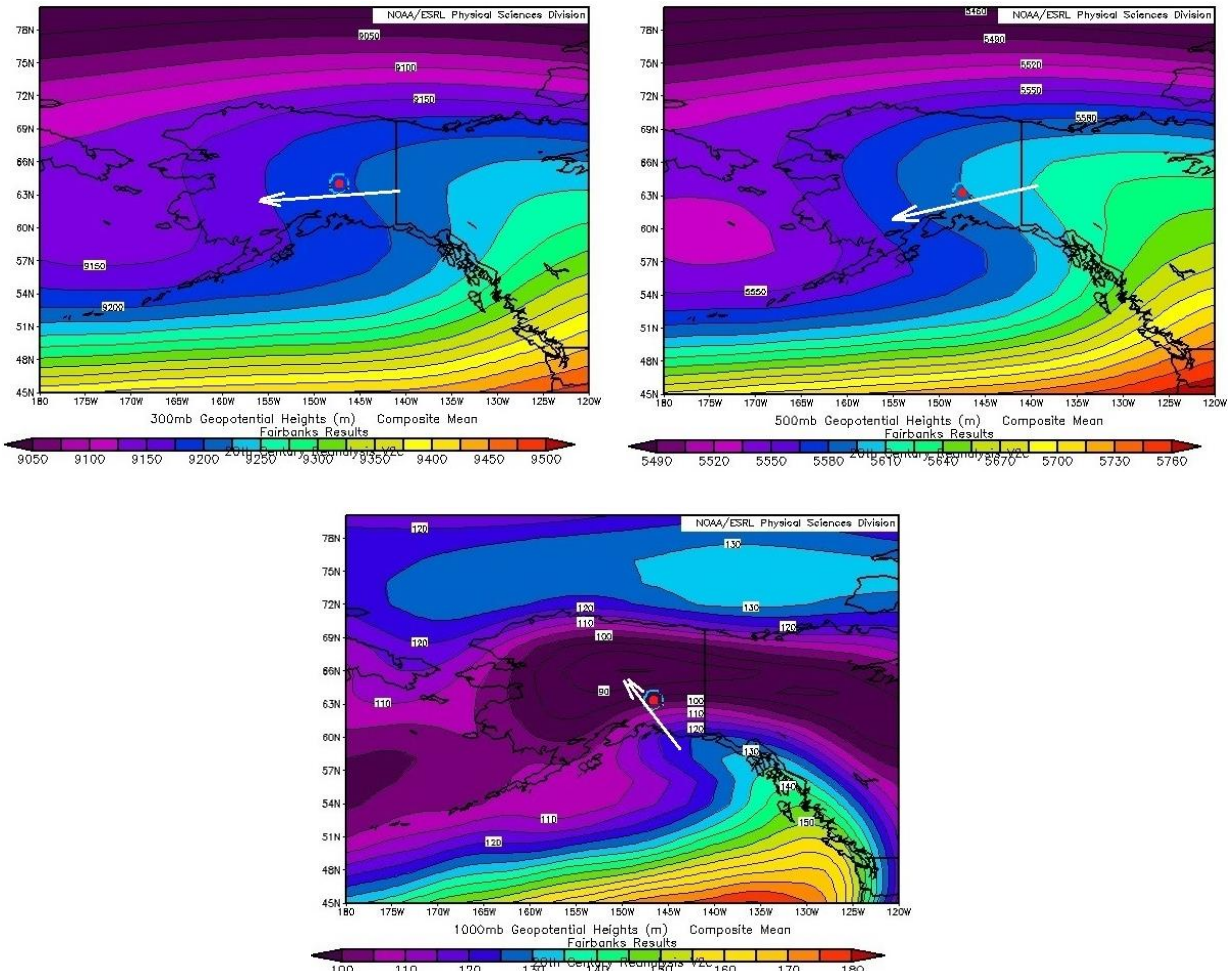
Fig. 3.8b. Composites of mean geopotential heights at the 300 hPa (top left), 500 hPa (top right), and surface map at 1000 hPa (bottom) of days identified by the search algorithm as having similar profiles like those of funnel cloud events for the observed Fairbanks group.

The surface synoptic maps of Figure 3.8a and 3.8b are similar, while the means of the upper 300 hPa and 500 hPa maps differ for the Fairbanks group. However, the mid and upper air distribution obtained by averaging over all days of funnel cloud sightings and those obtained by averaging over all potential funnel cloud profiles identified by the search algorithm have in common that they represent weak synoptic scale forcing over the Fairbanks area and the jet stream and polar front positioned to the south. Since the mid and upper air maps of the funnel-cloud sightings also suggested that that there might be at least two situations with respect to the upper air, this finding is not unexpected. The upper and mid tropospheric maps all showed weak forcing over the Fairbanks area. Together all these findings suggest topography influence on vorticity production.

3.3 McGrath

Table 3.3 shows the dates of funnel cloud events near McGrath. Both sightings were in the direction of Denali Park, i.e. southeastward of McGrath. McGrath is located at the north side of the valley while the sightings were on the southern side of the valley. The sightings occurred in 1972 at 1:28 pm and 2004 at 11 am AKDT both in July (Table 3.3).

Figure 3.10 shows the Skew-T diagrams for the two observed funnel cloud events. The two cases have in common a saturated layer in the lower mid-troposphere, while the upper atmosphere is relatively dry. Furthermore, there is wind shear in the lower ABL. At pressure levels above 400 hPa, winds come from south-southeast. The 700 hPa level commonly stirs the movement of thunderstorms (e.g. Mölders and Kramm 2014). Here, winds are from the west to east in both cases. A wind shear is visible around 500 hPa for both events.

The radiosonde profile of the 2004 event indicates that prior to the event there was a capping inversion. Unfortunately, the radiosonde ascend of 1972 took place after the funnel cloud event. In contrast to the 2004 event, it shows no capping inversion (Fig. 3.9). This finding is consistent with the thermodynamic theory of thunderstorm formation. There is often a capping inversion with CIN. Once the air below warmed up enough to break thru the inversion, convection sets on (cf. Lin 2007).

Table 3.3. Dates and times of observed funnel cloud dates in the McGrath area.

Year	Month	Day	Local Time	Radiosonde date, bfr	Radiosonde date,aft
1972	7	13	1:28pm ADT		1972071400
2004	7	19	8:30pm ADT	2004072000	

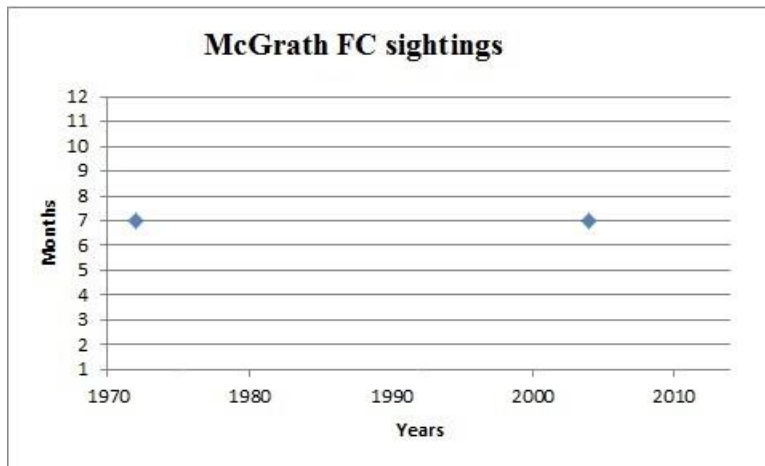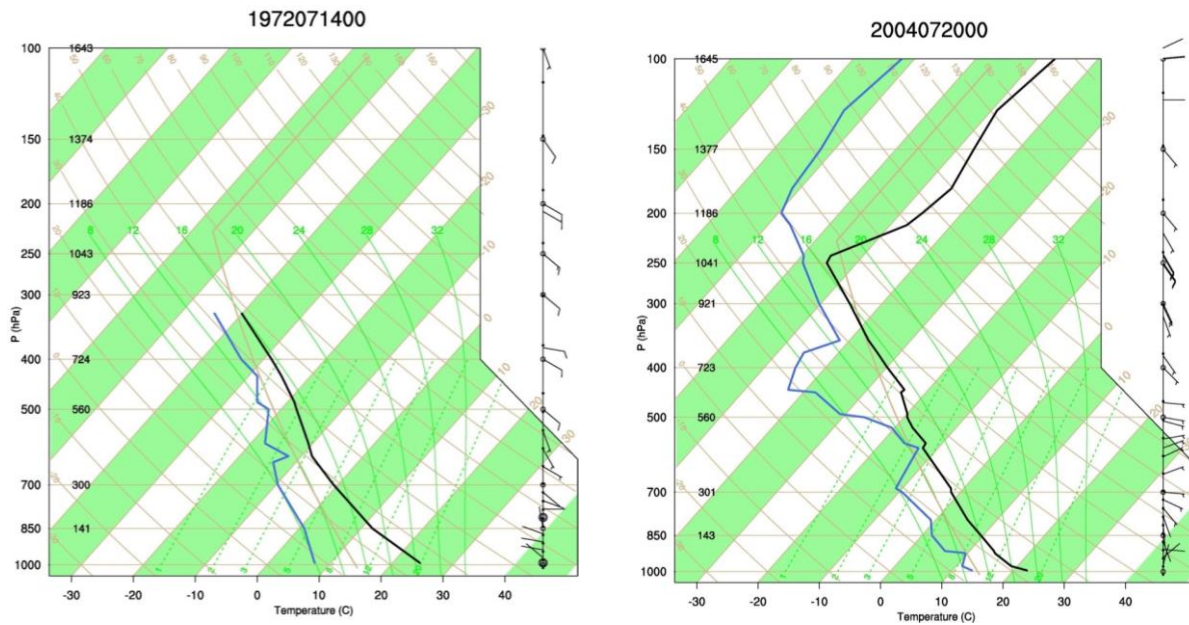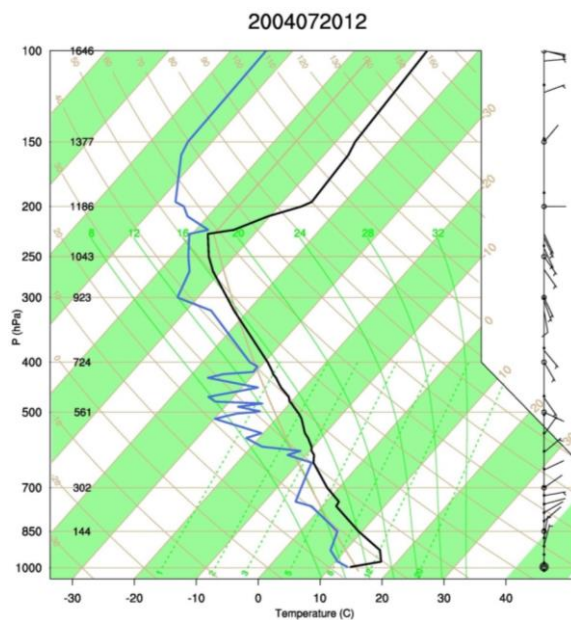Fig. 3.9. Funnel cloud sightings by year and months for the McGrath group.

a)   b)

c)

Fig. 3.10. Skew-T diagrams of three (a)-(c) of the reported funnel cloud events in the McGrath group, two are on the same date, but at different times with temperature (black line) and dew point temperature (blue line), wind speed and direction (barbs). The solid tan line is the US standard atmosphere. Figure 3.10a) July 14, 1972 at 00 z, Figure 3.10b) July 20, 2004 at 00z, and Figure 3.10c) July 20, 2004 at 12z.

Of course, no reliable statistic can be made, based on two events. To be able to search the radiosonde dataset for similar profiles I used these two cases as a guidance to determine a possible range of funnel cloud events. Table 3.4 lists for the various pressure levels the air temperature, dew point temperature, wind speed and direction ranges that the search algorithm used to find similar environmental conditions in the McGrath radiosonde dataset. Figure 3.11 shows the ranges of potential funnel clouds that were used by the search algorithm to find radiosonde profiles that fall within a similar range as the documented funnel cloud events. The actual values are listed in Table 3.4.

Table 3.4. Ranges of air temperature (T), dew point temperature (T_d), and wind speed (v) as obtained for the various pressures ranges (p) for McGrath based on the profiles of observed funnel clouds. See Chapter 2 for reasoning of the choice of the pressure ranges.

P (hPa)	Range (hPa)	T (C^o)	T_d(C^o)	v (m/s)
1000	1015-962.5	21.3-14	6.8 – 29	0 – 3
925	962.6-887.5	6-11	14.2 – 16	0 -8
850	887.5-812.5	-1.6-7	8.2 – 12	.4 – 2
700	737.5-650	-11.6 - -5	-2.3 – 0	.9 – 5
500	550-450	-27.9 - -21	-20 - -16	0 – 12
400	450-350	-47.8 - -26	-30.3 - -20	1 – 11
300	350-250	-55.4 - -48	-45.3 - -45	5.6 – 6
200	250-150	-71.2 - -54	-57.5 - -43	.9 – 11
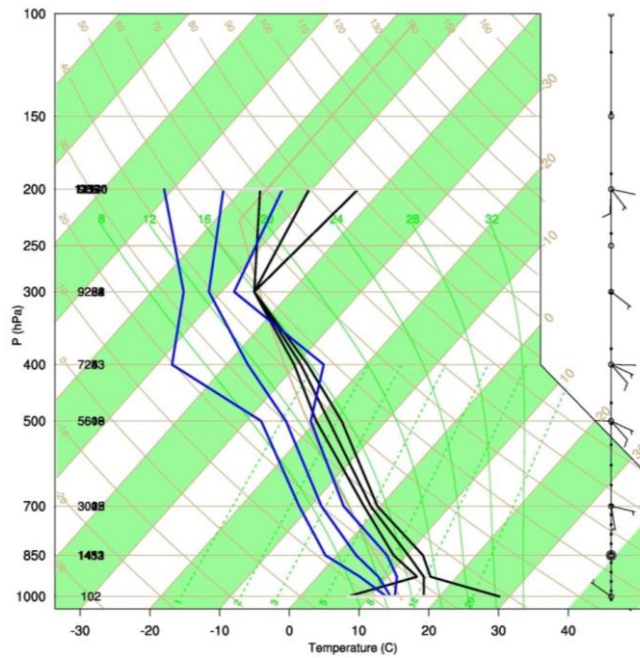
Fig. 3.11. Resultant ranges for potential funnel cloud profiles with CAPE greater than 500 J as obtained based on the two funnel cloud sightings for the McGrath group. Note that here the Skew-T limits of minimum (left), mean (middle), and maximum (right) temperature (black), dew point temperature (blue), wind speed and direction (barbs) over the pressure ranges listed in Table 3.4 are shown.
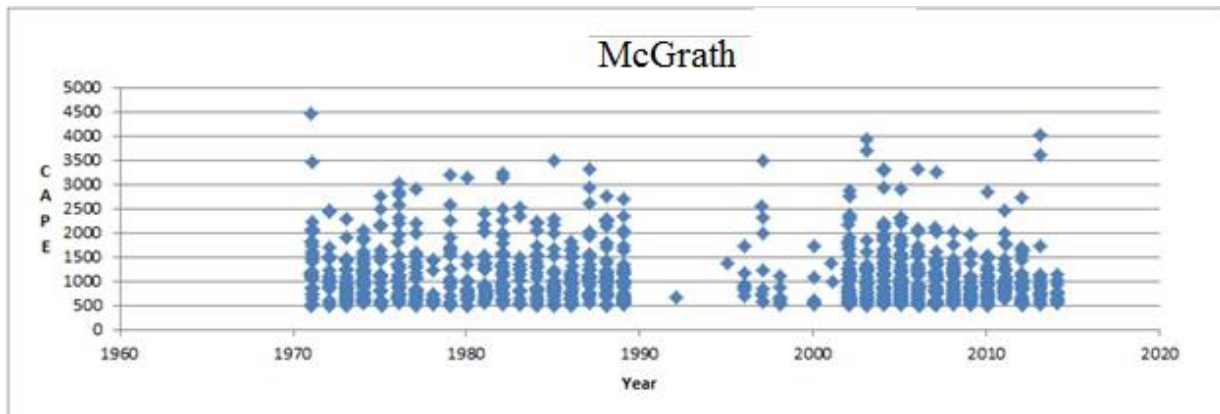

Fig. 3.12. Frequency (number of diamonds) and CAPE (in J) of events with radiosonde profiles similar to those during the observed funnel cloud events in the McGrath group as identified by the search algorithm and testing for CAPE. Note that between 1990 and 1996 and in 1999 there were problems with the dew point temperature measurements for which they are excluded as result of the stringent 1st requirement as depicted in Figure 2.6.

The pattern of high and low CAPE obtained for potential funnel cloud events (Fig. 3.12) is quite different from that for Fairbanks (Fig. 3.4). This fact may support that topography plays a larger role here than for the Fairbanks group. Note that at McGrath the valley is comparatively narrower than in the Fairbanks area.
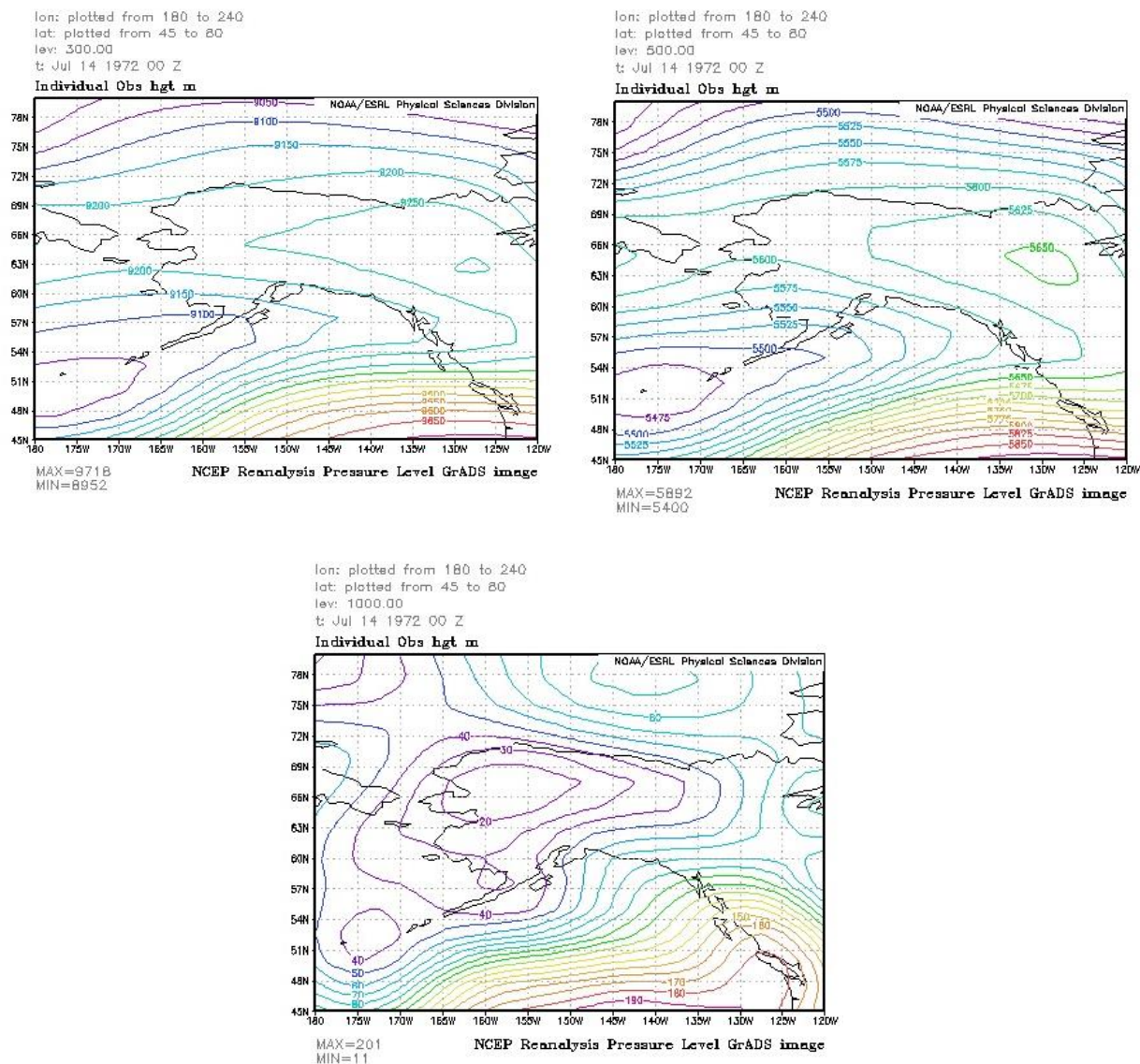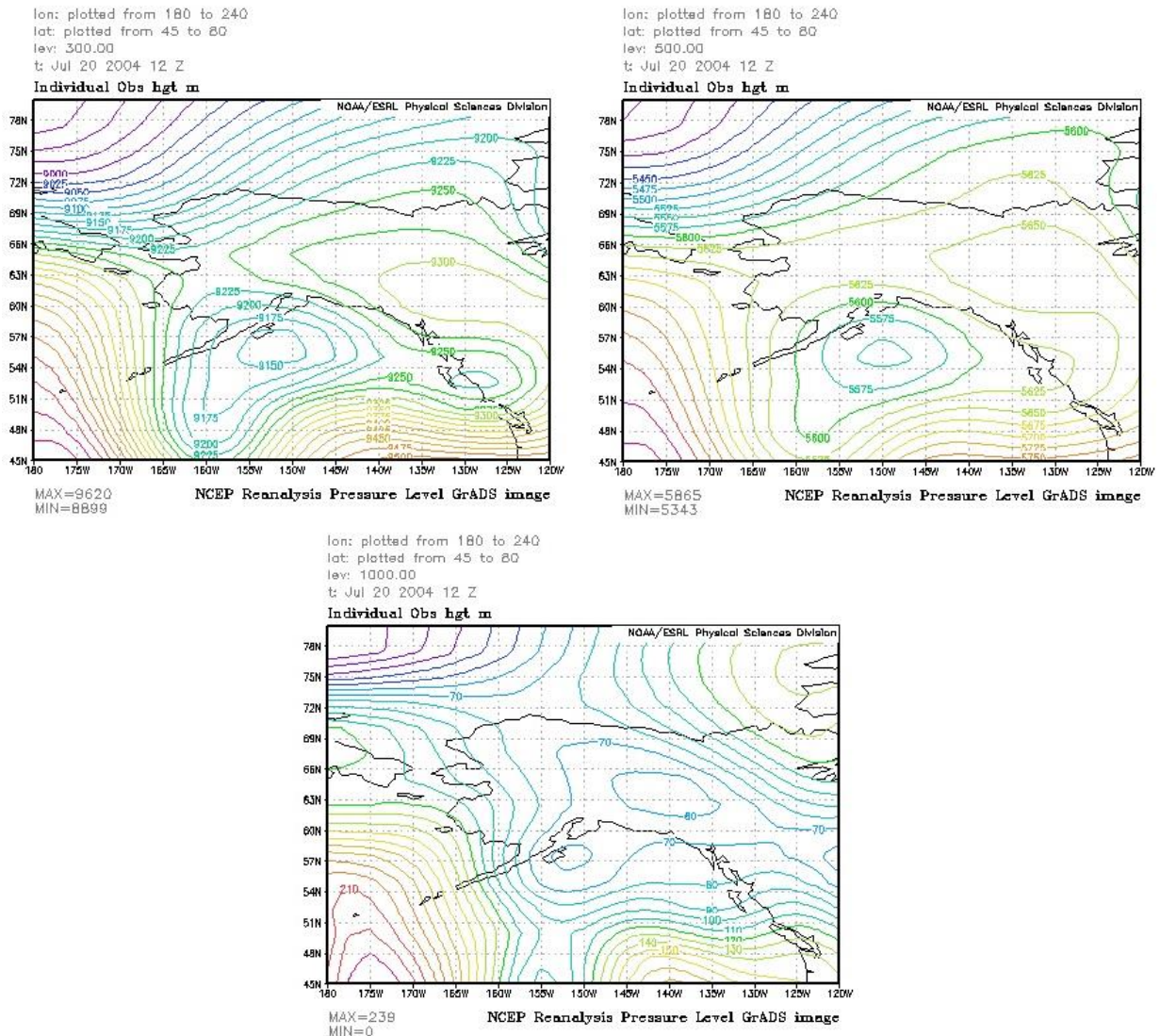

Fig. 3.13a. Geopotential heights at the 300 hPa (top left), 500 hPa (top right), and 1000 hPa (bottom) from reanalysis data on date of observed funnel cloud (July on the 14, 1972 at 00z) in GMT for the McGrath group.
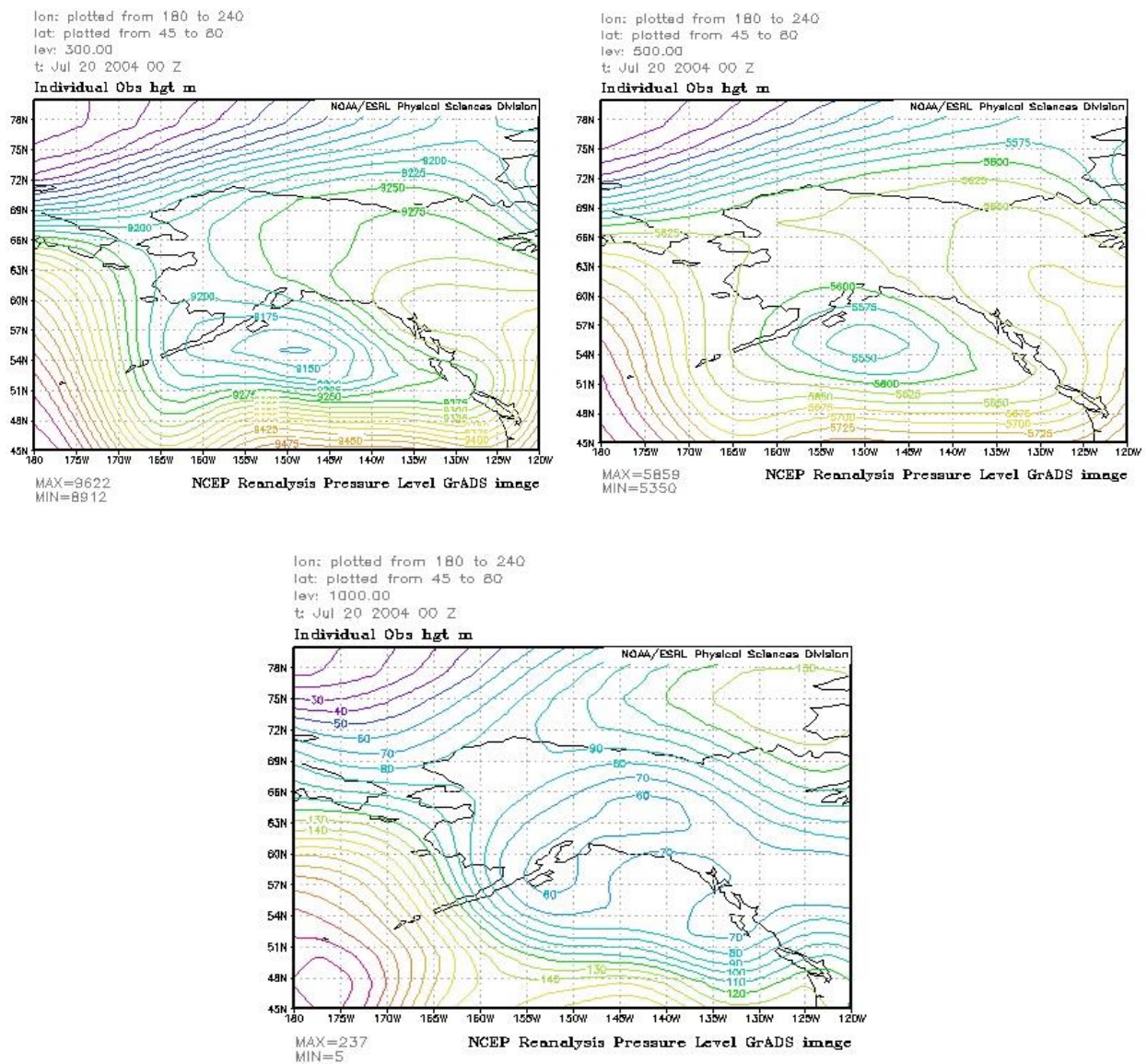
Fig. 3.13b. Geopotential heights at the 300 hPa (top left), 500 hPa (top right), and 1000 hPa (bottom) from reanalysis data on date of observed funnel cloud (July on the 20, 2004 at 00z) in GMT for the McGrath group.

Fig. 3.13c. Geopotential heights at the 300 hPa (top left), 500 hPa (top right), and 1000 hPa (bottom) from reanalysis data on date of observed funnel cloud (July on the 20, 2004 at 00z) in GMT for the McGrath group.

The surface synoptic map has two high pressure systems with McGrath located in a broad low pressure area (Fig. 3.13). The surface winds blow from the Alaska West Coast eastward through the Tanana River drainage valley, similar to the synoptic situation for the Fairbanks and Denali group (see next section for the Denali group).

At the 500 hPa pressure level, the gradient wind blows through the valley as well, but in the opposite direction. McGrath is located at the end of the Alaska Range and is in close proximity to the mountains on both sides of the valley (Figs. 1.6, 2.2). The wind blows across the mountains into the western coastal area, creating a similar downdraft along the mountain face into the valley and coastal area as for the Fairbanks group.

Investigation of the synoptic maps shows that the two observed funnel cloud events have quite similar synoptic conditions. At the 300 hPa, the polar jet is far south of Alaska over the Pacific (Fig. 3.13), while over McGrath the gradient in geopotential height is low. At the 300 hPa and 500 hPa synoptic map, both events indicate weak large scale forcing as well. Obviously, warm moist area is transported slowly over the Alaska Range where it is cooled due to the glaciers. Blue in Fig 3.14 is heavier colder air, and red is the warmer air at the same height above sea level over the valley.

In the 1000 hPa map, the synoptic forcing is weak. Under such conditions, local mesoscale features can develop (Lin 2007). The 1000 hPa map suggests that the flow is directed along the Tanana Valley. The weak synoptic forcing permits local differences in terrain and surface properties cause differential surface heating which may lead to updrafts.
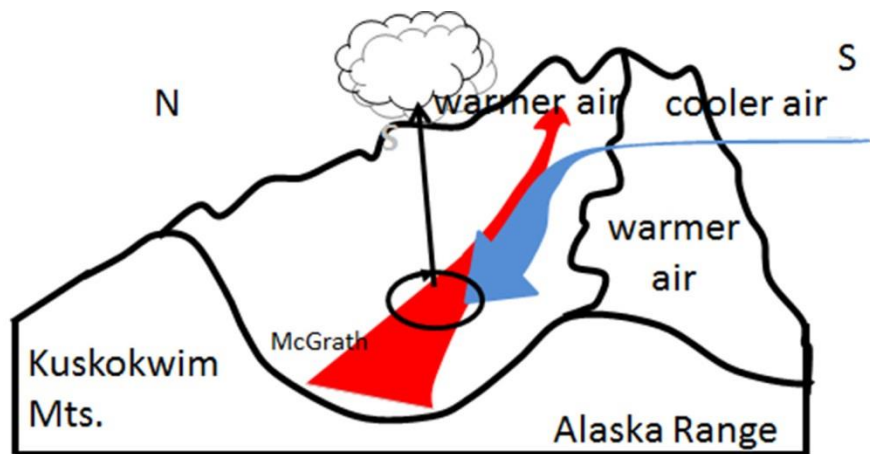
Fig. 3.14. Schematic view of the situation as obtained from interpretation of the radiosonde soundings for McGrath and the synoptic maps for the two sightings. The blue arrow represents the colder mid-tropospheric air sinking down into the valley. The red arrow stands for the warm air that moves up the valley in the ABL. The black with rotational circle arrow symbolizes the updraft of a convective cloud. Modified after a sketch from Mölders and Kramm (2014).

Together the following may occur: In the mid-troposphere, air moves over the Alaska Range and is cooled by the glaciers (Fig. 3.14). Thus, this air is relatively colder than the air at same height

over the valley and drains down of the mountains from southerly direction into the valley. In the valley in the ABL, wind blows along the valley direction. The sinking air has a southern component, i.e. the two air masses move in different directions. This feature means a wind shear, and causes vorticity. At the same time, the air of different properties mixes, which may lead to saturation as seen in the radiosonde profiles (Fig. 3.10), and clouds may form. The different directions in the lower ABL seen in the radiosonde profiles may be due to local effects associated with convection and the fact that one profile represents the condition before and the other conditions after the events.
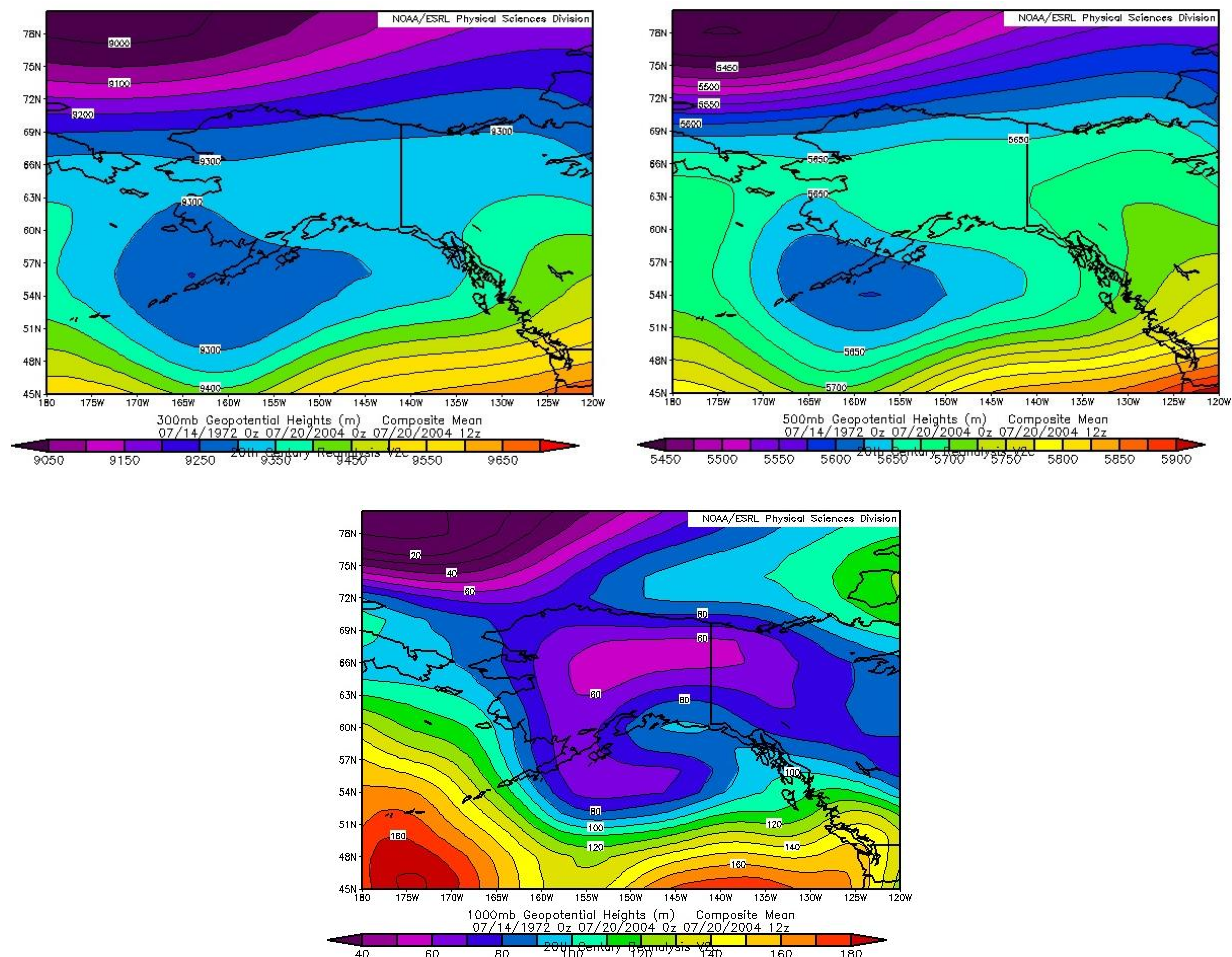
Fig. 3.15a. Composites of mean geopotential heights at the 300 hPa (top left), 500 hPa (top right), and surface map at 1000 hPa (bottom) of days with funnel cloud sightings
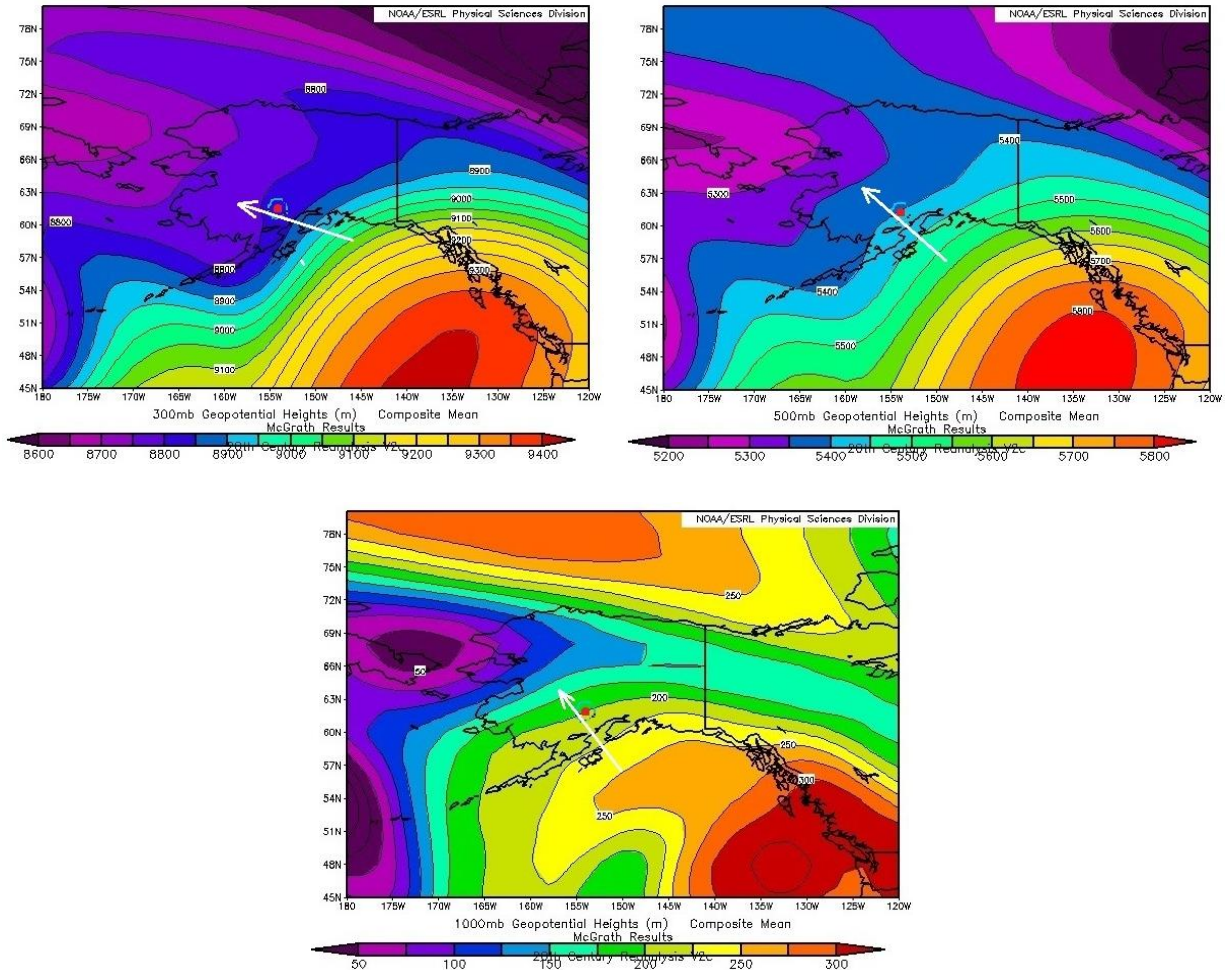
Fig. 3.15b. Composites of mean geopotential heights at the 300 hPa (top left), 500 hPa (top right), and surface map at 1000 hPa (bottom) of days with funnel cloud sightings, and days identified by the search algorithm as having similar profiles like those of funnel cloud events for the observed McGrath group.

The synoptic maps of Figure 3.15a and 3.15b are not similar. This finding suggests that the sample of observed funnel clouds may be insufficient to create a reliable algorithm for the McGrath group. However, Figures 3.15b and 3.8b are quite similar. This finding may suggest that the overall situation for funnel cloud events in the Tanana Valley is requiring weak synoptic forcing that permits the topography and land-surface cover to modify the air in the ABL by atmosphere-surface interaction.

3.4 Denali Area between Fairbanks and McGrath

As pointed out in Chapter 2, some of the sightings fell between Fairbanks and McGrath that both are located at the northern side of the same valley. Table 3.5 shows the dates of funnel cloud events that fall into the Denali group. As mentioned in Chapter 2, for the Denali group I investigated whether the funnel cloud event is better characterized by the Fairbanks or McGrath radiosonde sounding. Furthermore, the synoptic maps can provide hints.

Table 3.5. Dates and times of observed funnel clouds in the Denali area.

Year	Month	Day	Time	Radiosonde date, bfr	Radiosonde date,aft
1955	7	3		1955070312	1955070400
2000	7	11	3:43pm ADT		2000071200
2002	8	28	3pm ADT		2002082900
2002	8	28	8am AST NOAA	2002082812	
2002	8	28	3pm AST Local NOAA	2002082900	
2011	7	30		2011073012	2011073100
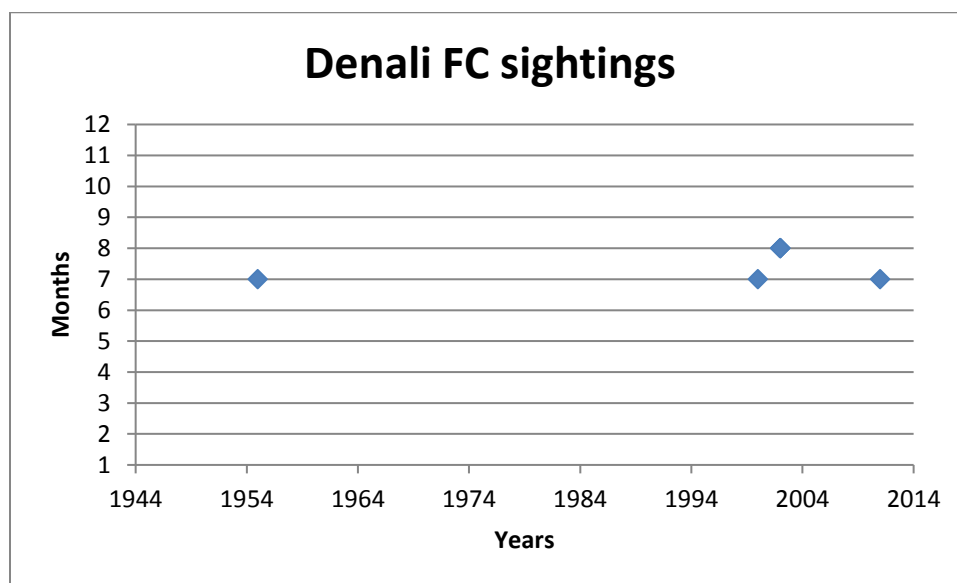
Fig. 3.16. Funnel cloud sightings by years and months for the Denali group.

The figures and tables in the following summarize results of two locations, since the Denali funnel cloud sightings occurred between the two radiosonde sites shown in Figure 2.5. Therefore, both locations must be considered for the same dates and limit ranges based on these dates.
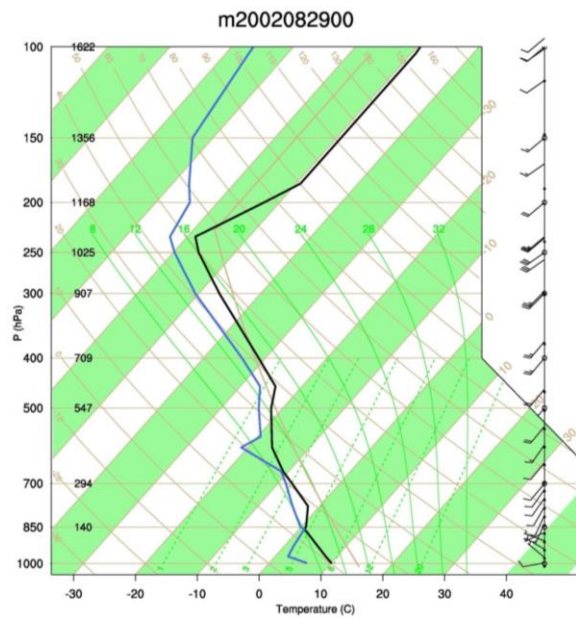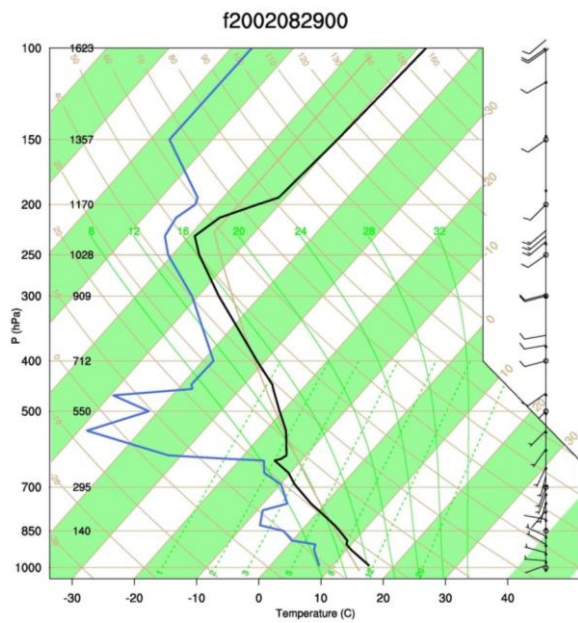
a)

b)

c)

d)

f2002082900

m2002082900

e)   f)

f2011073012

m2011073012
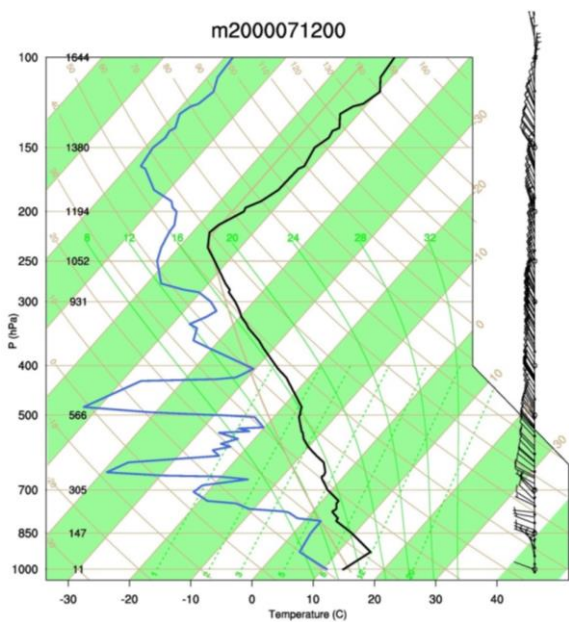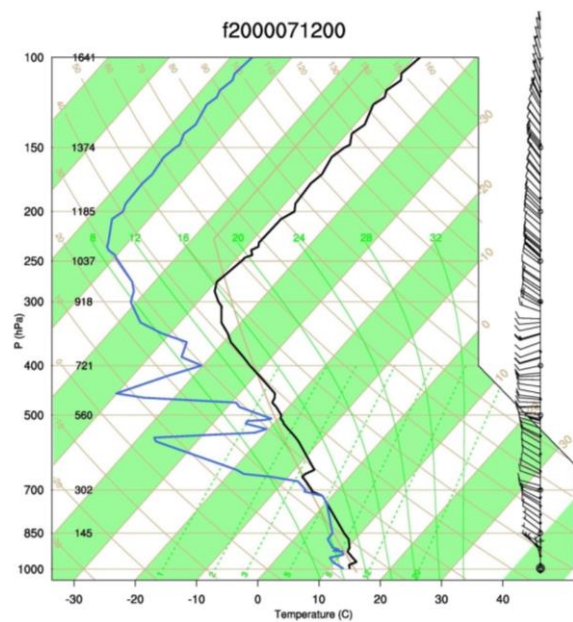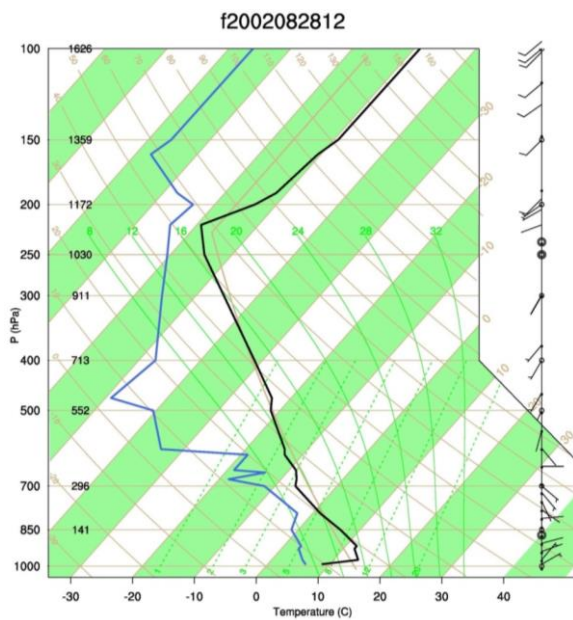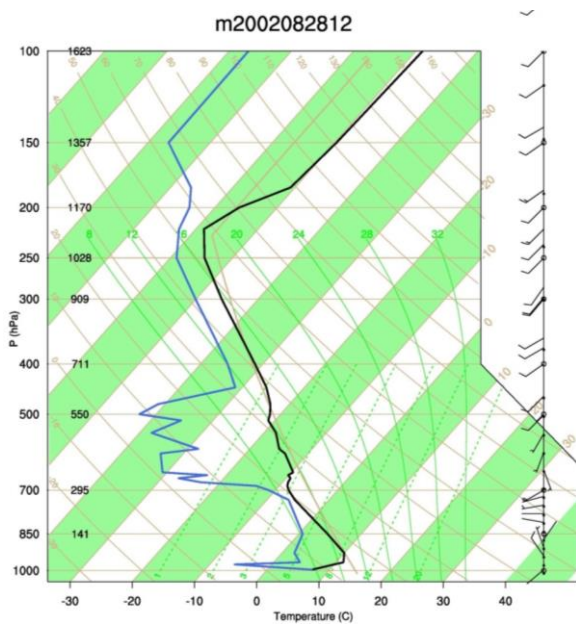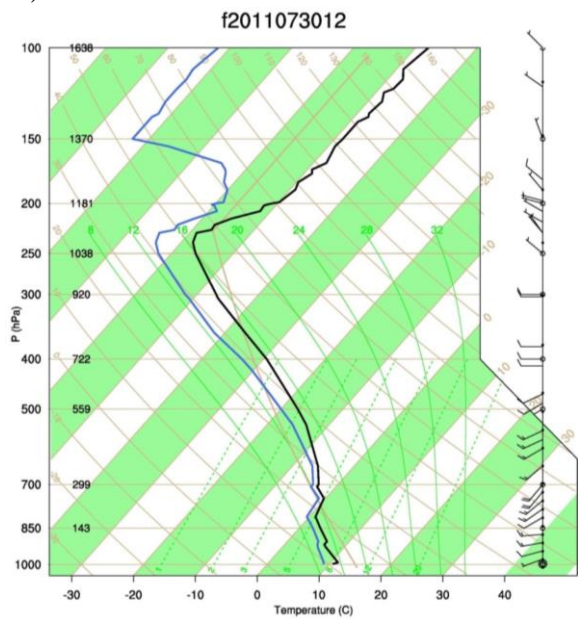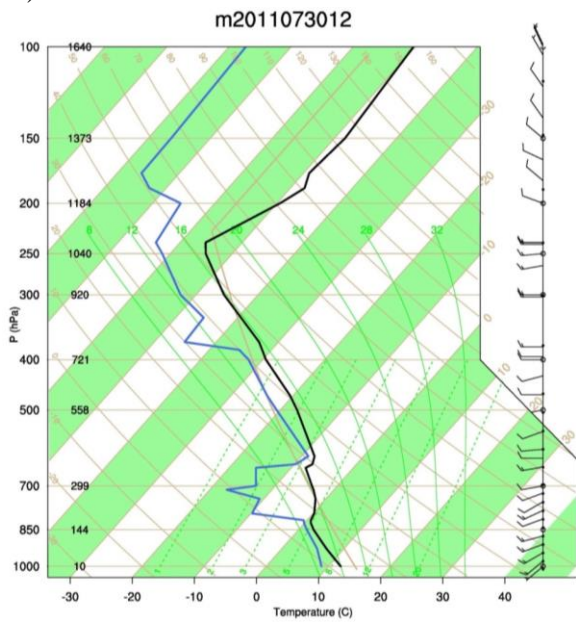
g)   h)
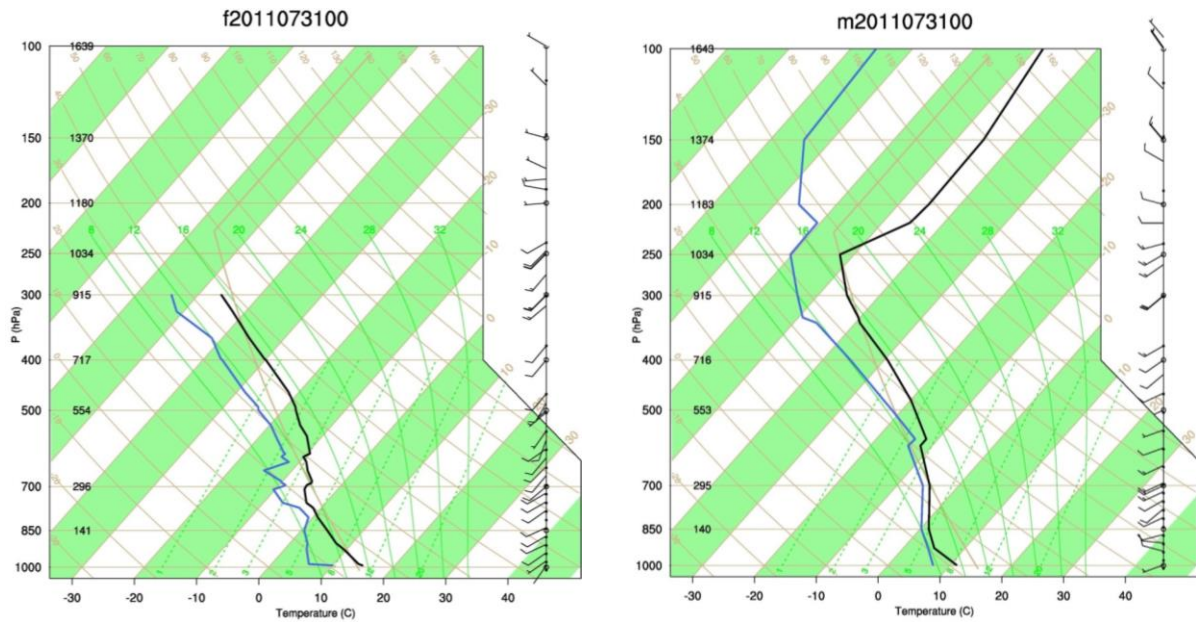
i)   j)

Fig. 3.17. Skew-T diagrams of three (a)-(j) of the reported funnel cloud events in the Denali group, two are included here since the time falls between two of the daily radiosonde launch times, but for different GMT dates with temperature (black line) and dew point temperature (blue line), wind speed and direction (barbs). The solid tan line is the US standard atmosphere. Date and time in GMT for the radiosonde profiles of Fig. 3.17: a) Fairbanks: July 12, 2000 at 00z, and b) McGrath July 12, 2000 at 00z. c) Fairbanks August 28, 2002 at 12z, and d) McGrath August 28, 2002 at 12z. e) Fairbanks August 29, 2002 at 00z, and f) McGrath August 29, 2002 at 00z. g) Fairbanks July 30, 2002 at 12z, and h) McGrath July 30, 2002 at 12z. i) Fairbanks July 31, 2002 at 00z, and j) McGrath July 31, 2002 at 00z.

Table 3.6. Ranges of air temperature (T), dew point temperature (T$_d$), and wind speed (v) as obtained for the various pressure ranges (p) for Denali based on the profiles of observed funnel clouds. See Chapter 2 for reasoning of the choice of the pressure ranges.

McGrath				
p (hPa)	Range (hPa)	T (C°)	T$_d$(C°)	v (m/s)
1000	1015-962.5	5.1 – 9.7	5.9 – 13.5	0 – 9.5
925	962.6-887.5	-.5 – 6.7	3.9 – 11.2	2 – 16.8
850	887.5-812.5	-.5 – 1.7	-.4 – 5.6	0 – 15.4
700	737.5-650	-4.4 - -7.5	-9.9 - -3.2	2.4 – 14.3
500	550-450	-47.9 - -10.3	-24.4 - -16.2	3.2 – 24.5
400	450-350	-36.6 - -31.2	-32.2 - -29.1	4.1 – 26
300	350-250	-53 - -49.1	-47 - -45.1	5.2 – 31.7
200	250-150	-66.2 - -58.6	-57.3 - -50.3	6.6 – 25.9
Fairbanks				
p (hPa)	Range (hPa)	T (C°)	T$_d$(C°)	v (m/s)
1000	1015-962.5	5.3 – 9.9	6 – 17.5	0 – 4.6
925	962.6-887.5	2 – 6.8	6 – 13.9	0 – 14.8
850	887.5-812.5	-4.6 – 3.4	2.6 – 8.3	0 – 16.3
700	737.5-650	-14.5 - -2.1	-8.9 - -2.2	0 – 21.9
500	550-450	-53.1 - -14.9	-23.2 - -16.3	1 – 15.7
400	450-350	-50.8 - -28.6	-32.3 - -29	4 – 11.4
300	350-250	-56.6 - -40	-47.6 - -45.2	0 – 13.5
200	250-150	-63.9 - -50.5	-56.7 - -51.4	1.3 – 13.5
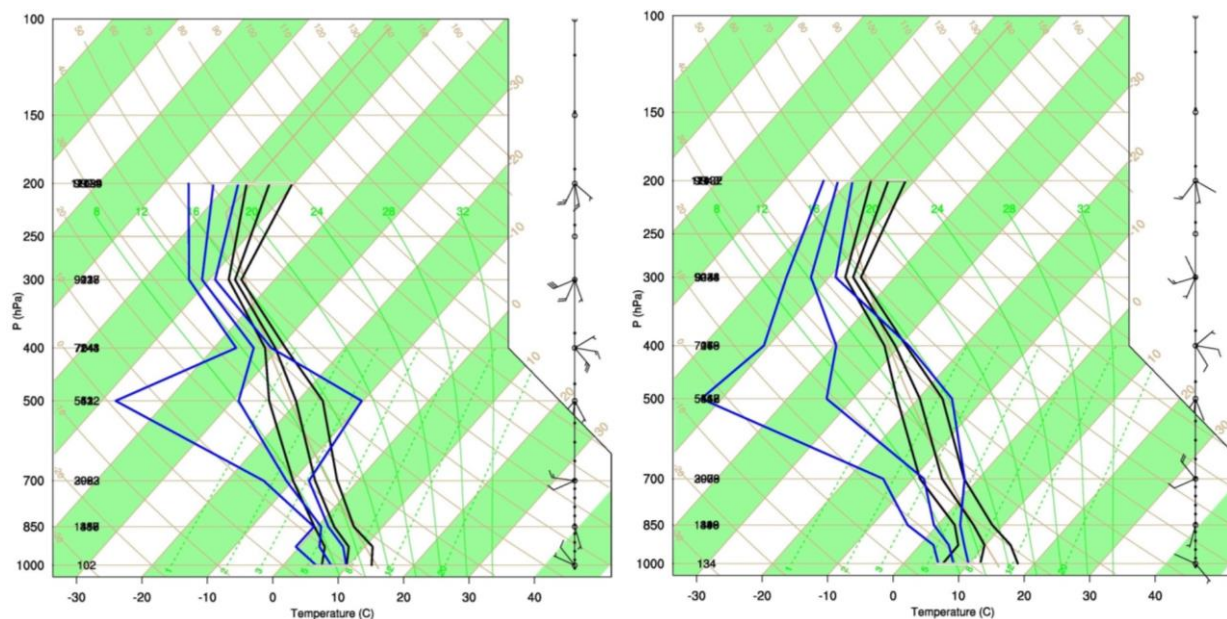
a)   b)

Fig. 3.18. Resultant ranges for potential funnel cloud profiles with CAPE greater than 500 J as obtained based on observed funnel cloud sightings for the Denali group for a) McGrath and b) Fairbanks. Note that here the Skew-T limits of minimum (left), mean (middle), and maximum (right) temperature (black lines), dew point temperature (blue lines), wind speed and wind direction (barbs). Further, minimum, mean, and maximum wind direction over the pressure ranges listed in Table 3.7 are shown.
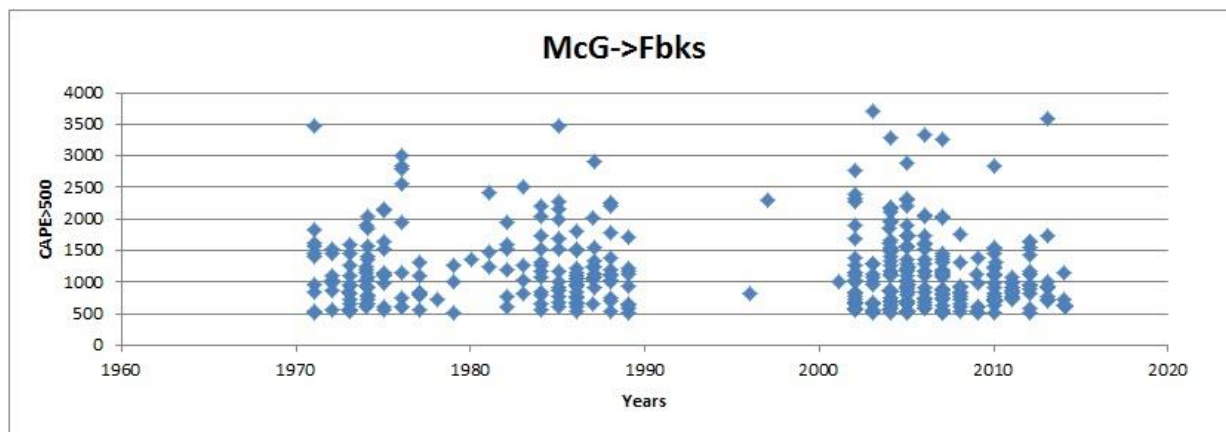
Fig. 3.19a. Frequency (number of diamonds) and CAPE (in J) of events with radiosonde profiles similar to those during the observed funnel cloud events in the Denali group as identified by the search algorithm and testing for CAPE, for a) McGrath, b) Fairbanks, and c) CAPE values from ratio between Fairbanks and McGrath. Note that between 1992 and 1994 there were problems with the dew point measurements and this data is excluded as result of the stringent 1st requirement as depicted in Figure 2.6.
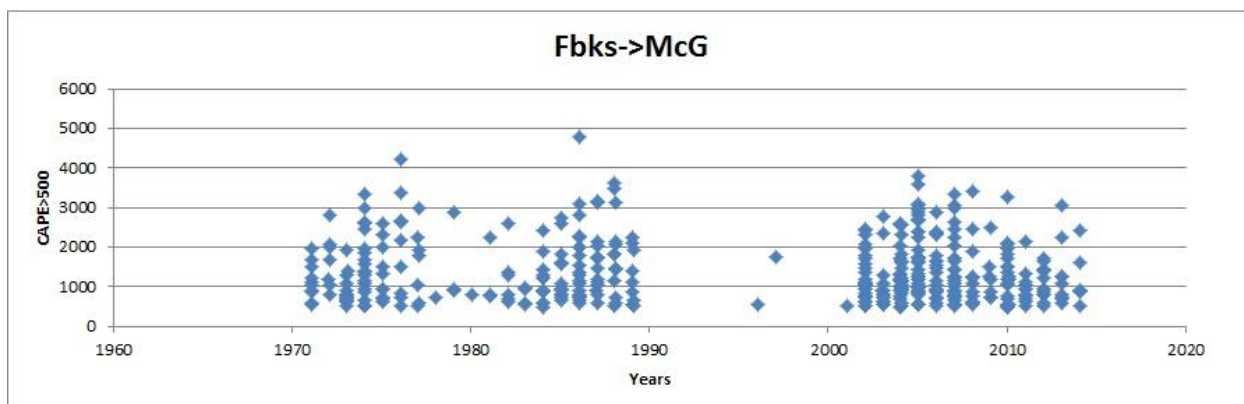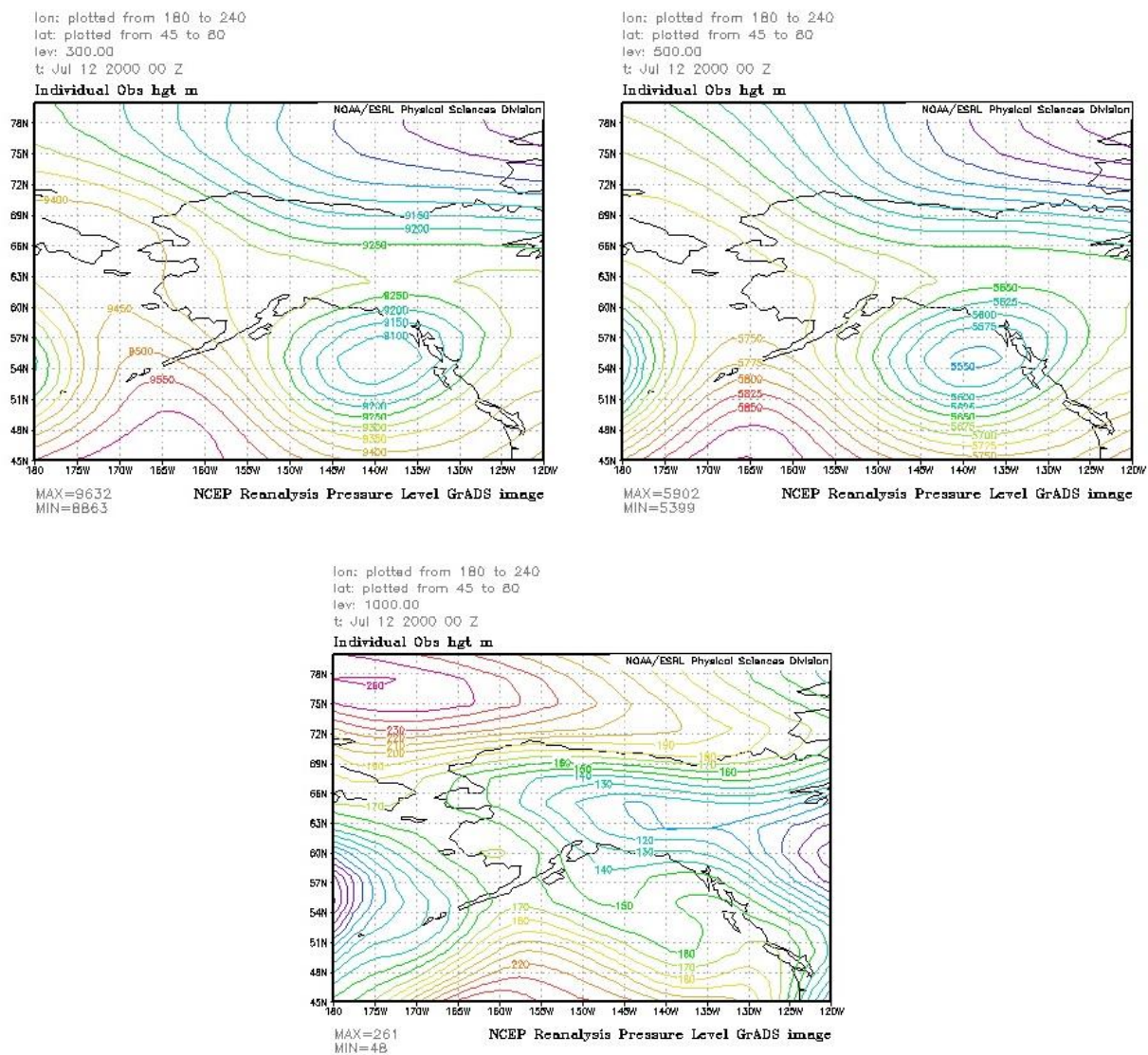

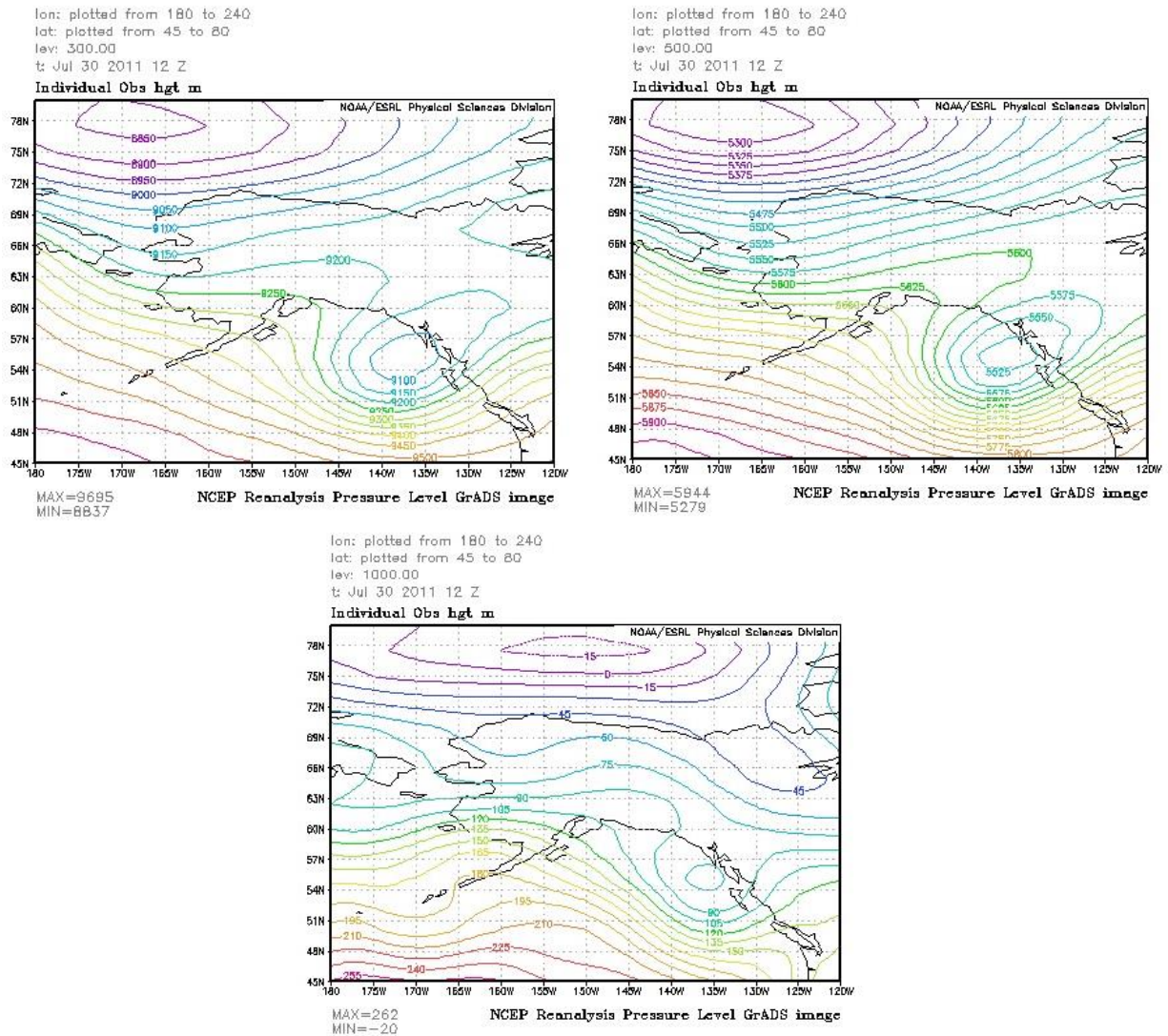Fig. 3.19b. Continue.
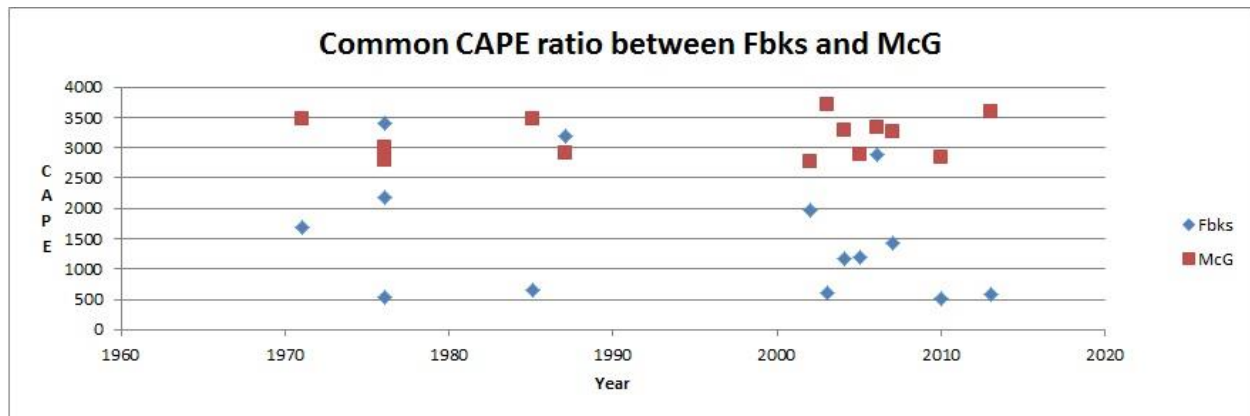
Fig. 3.19c. Continue.
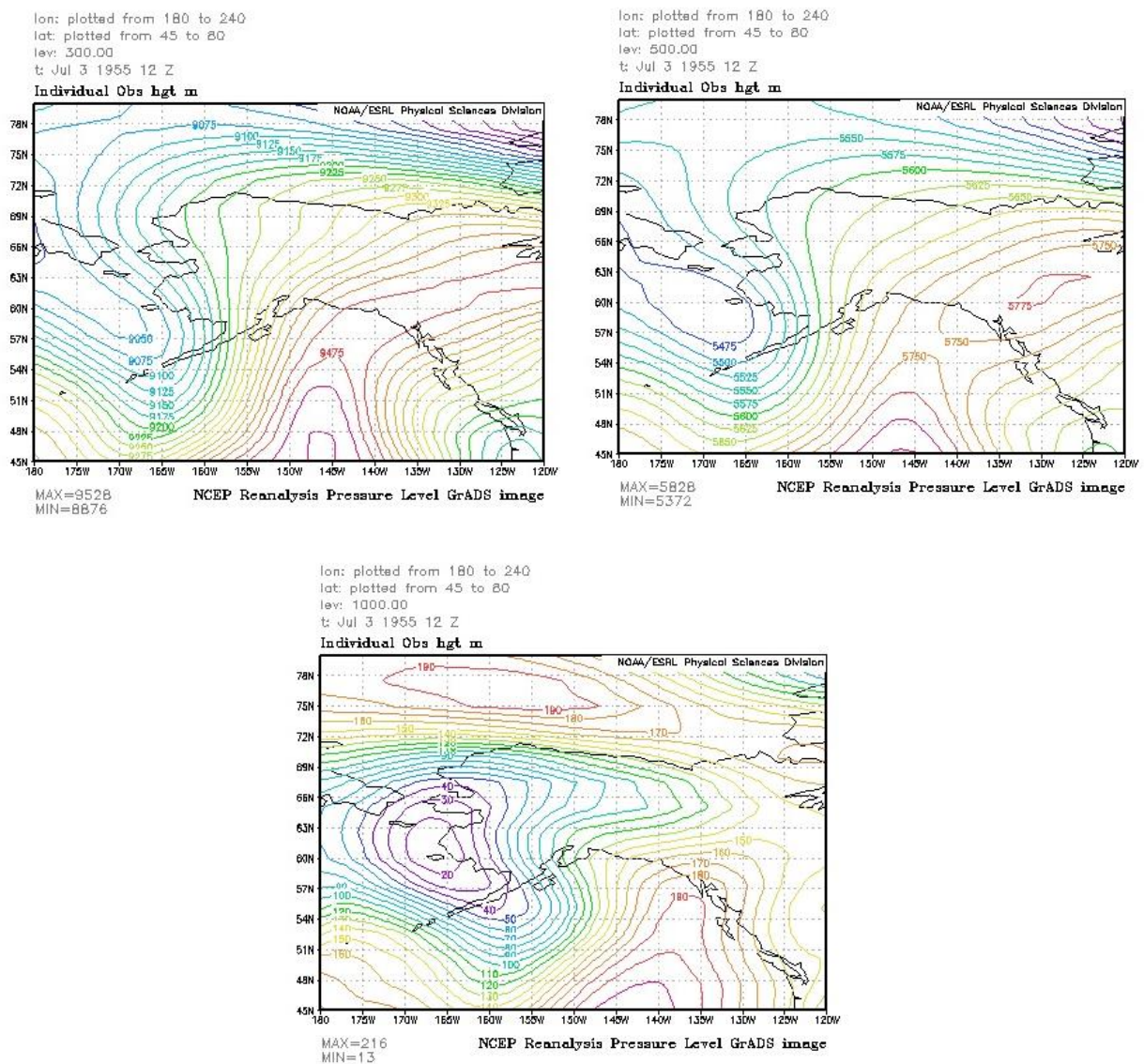
Fig. 3.20a. Geopotential heights at the 300 hPa (top right), 500 hPa (top left), and 1000 hPa (bottom) from reanalysis data on date of observed funnel cloud (July on the 3, 1955 at 12z) in GMT for the Denali group.
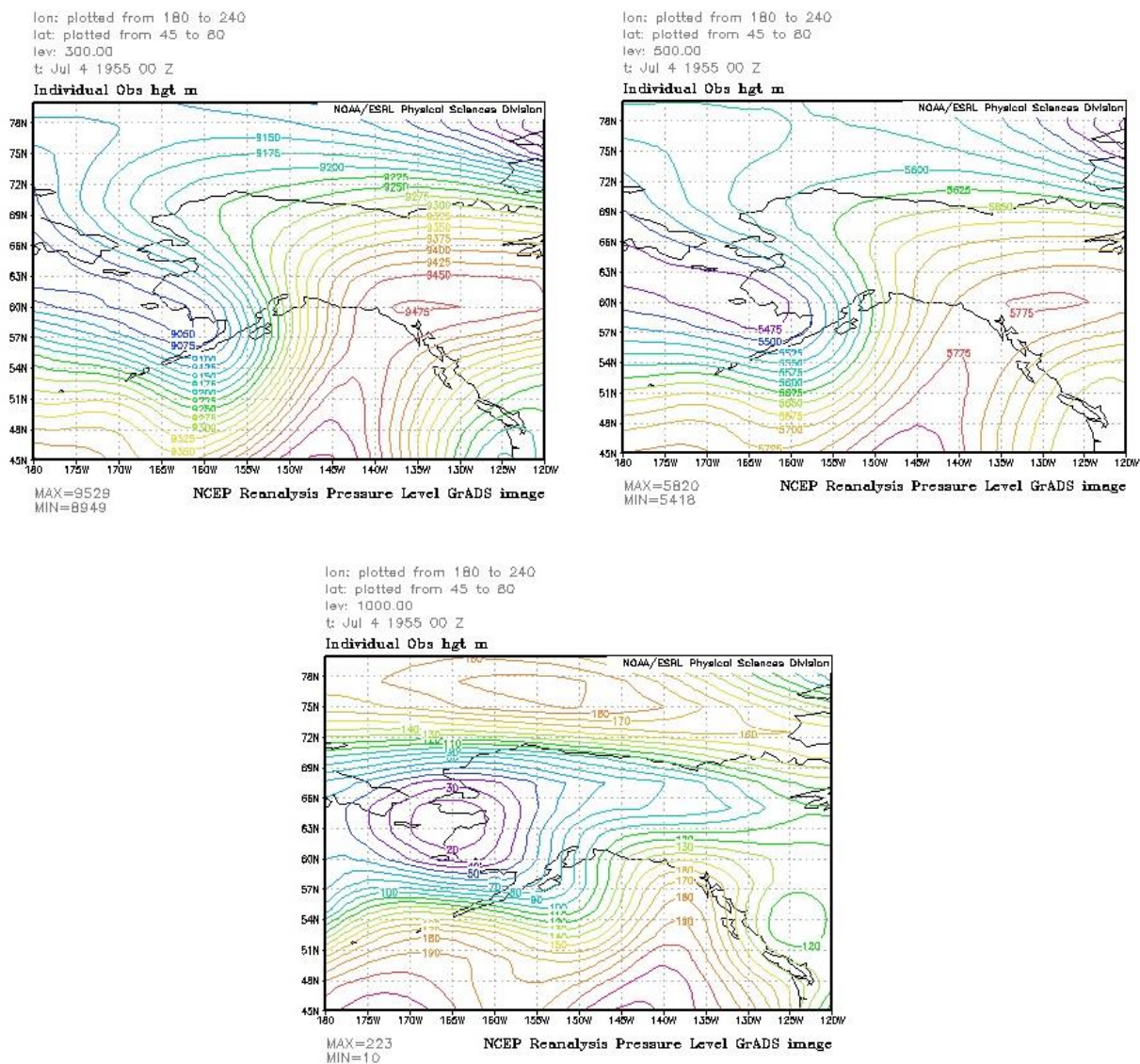
Fig. 3.20b. Geopotential heights at the 300 hPa (top right), 500 hPa (top left), and 1000 hPa (bottom) from reanalysis data on date of observed funnel cloud (July on the 4, 1955 at 00z) in GMT for the Denali group.
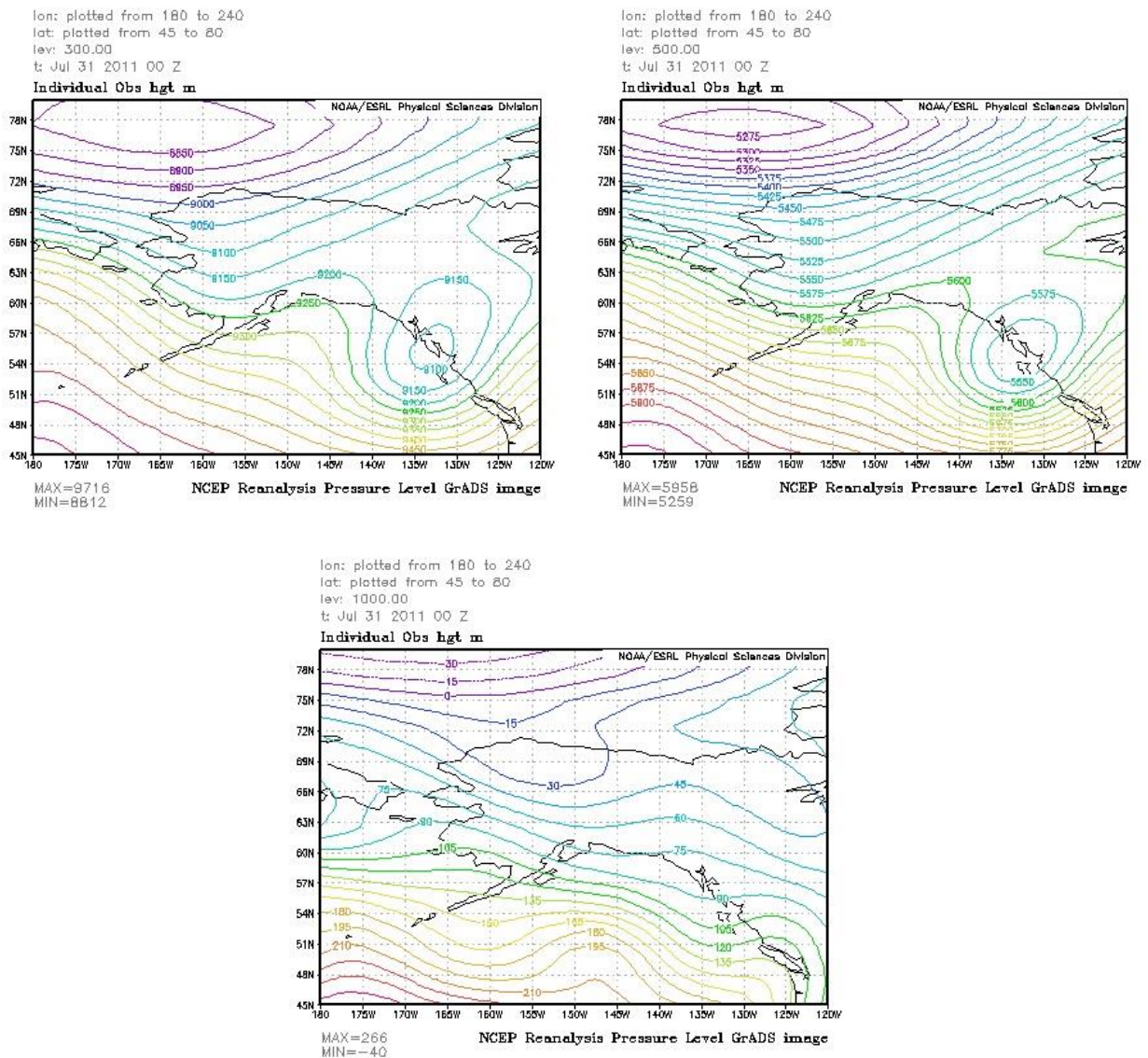
Fig. 3.20c. Geopotential heights at the 300 hPa (top right), 500 hPa (top left), and 1000 hPa (bottom) from reanalysis data on date of observed funnel cloud (July on the 12, 2000 at 00z) in GMT for the Denali group.
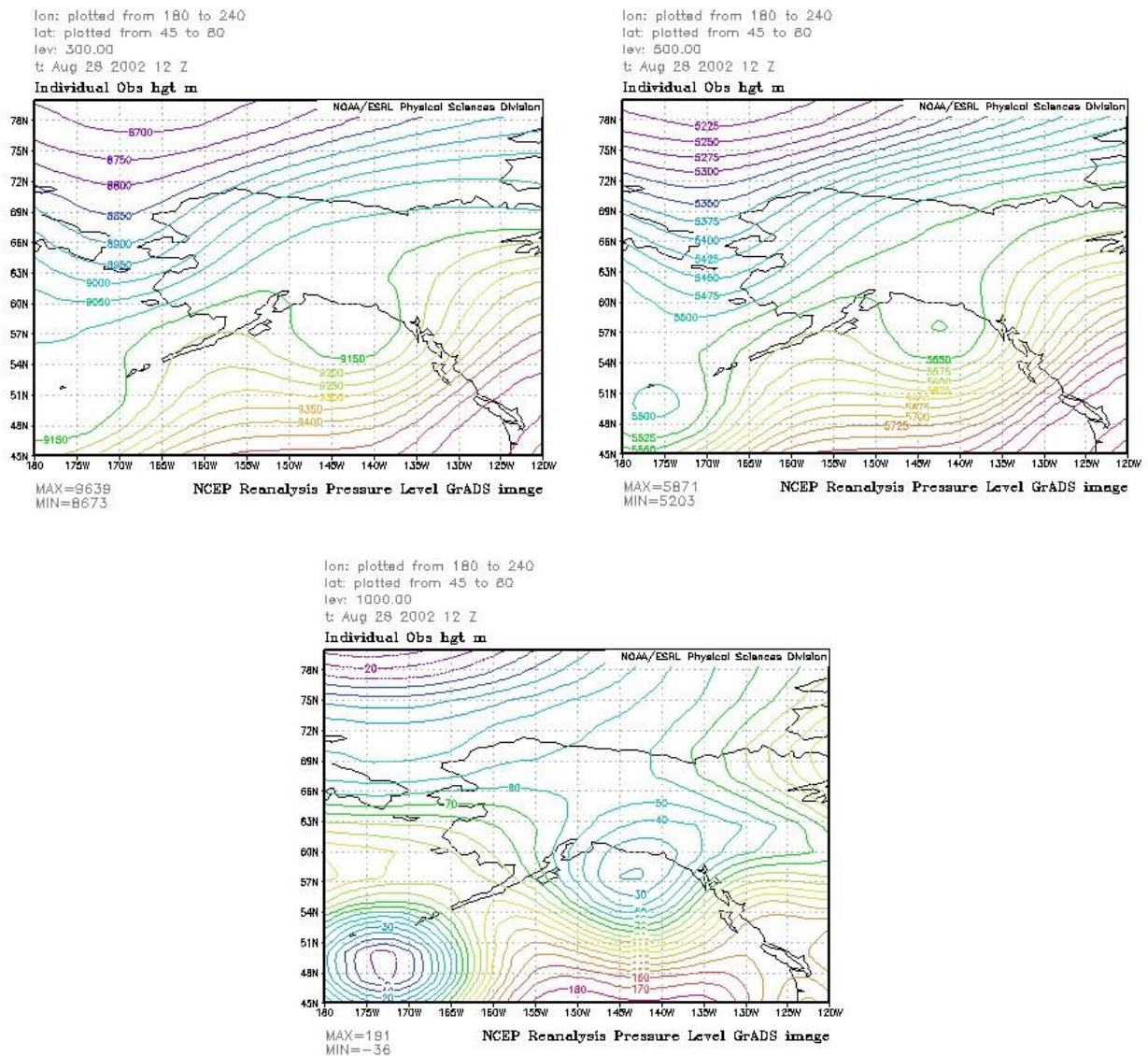
Fig. 3.20d. Geopotential heights at the 300 hPa (top right), 500 hPa (top left), and 1000 hPa (bottom) from reanalysis data on date of observed funnel cloud (July on the 30, 2011 at 12z) in GMT for the Denali group.

Fig. 3.20e. Geopotential heights at the 300 hPa (top right), 500 hPa (top left), and 1000 hPa (bottom) from reanalysis data on date of observed funnel cloud (July on the 31, 2011 at 00z) in GMT for the Denali group.

Fig. 3.20f. Geopotential heights at the 300 hPa (top right), 500 hPa (top left), and 1000 hPa (bottom) from reanalysis data on date of observed funnel cloud (August on the 28, 2002 at 12z) in GMT for the Denali group.
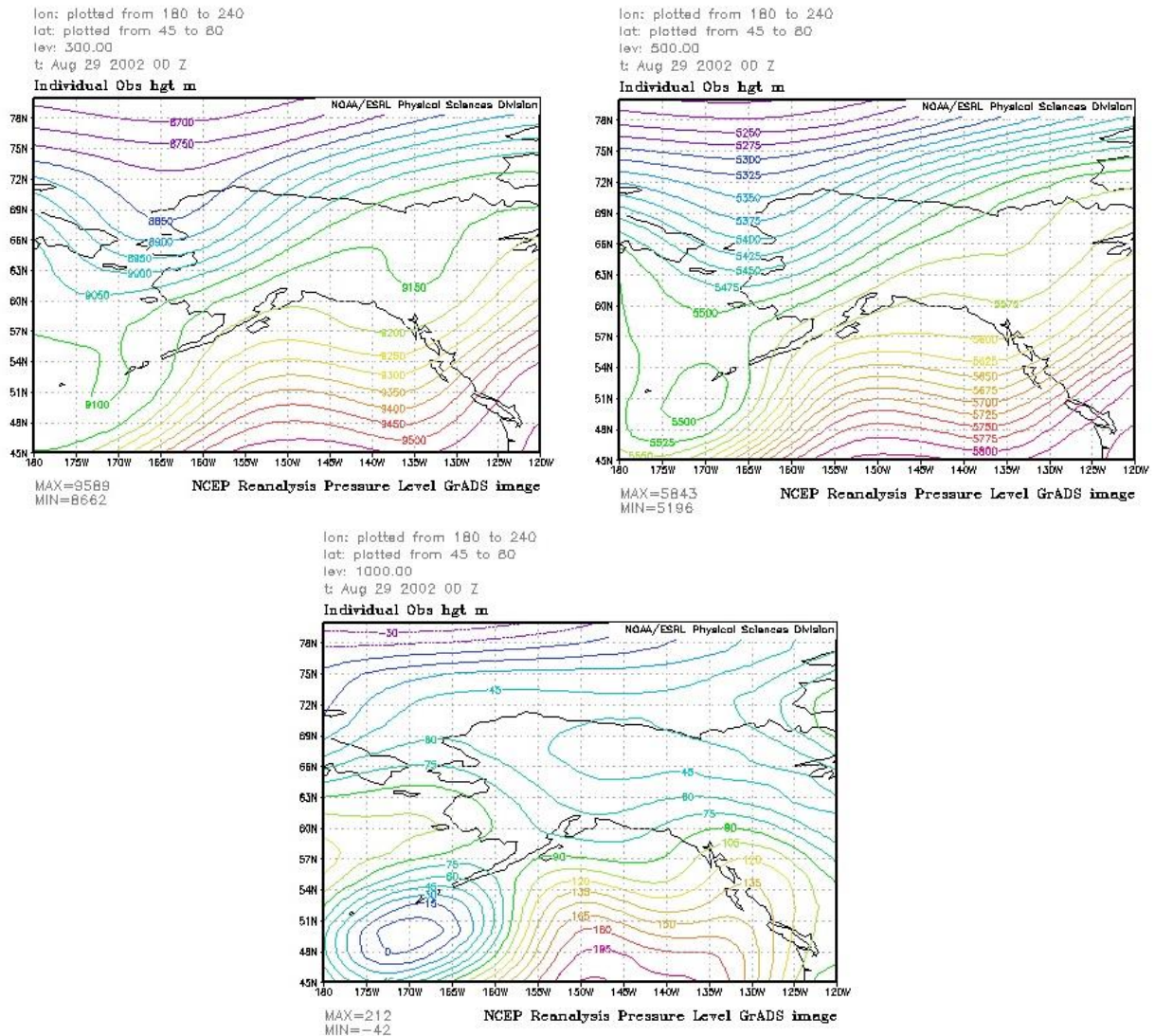
Fig. 3.20g. Geopotential heights at the 300 hPa (top right), 500 hPa (top left), and 1000 hPa (bottom) from reanalysis data on date of observed funnel cloud (August on the 29, 2002 at 00z) in GMT for the Denali group.

The synoptic surface pressure map has a high pressure to low pressure gradient across the Denali group. According to the surface synoptic reanalysis maps, winds blow west to east along the Tanana Valley. This finding is similar to the situation found for the Fairbanks group.

At the 500 hPa pressure level, the gradient winds also blow across the Alaska Range similar to the Fairbanks group with the exception that Mount Denali which is a major topographic structure.

Bieniek et al. (2012) places these locations within the same climate division. My results suggest that the dynamics and forcing for the Denali area is very similar to the one found for Fairbanks under funnel cloud conditions.
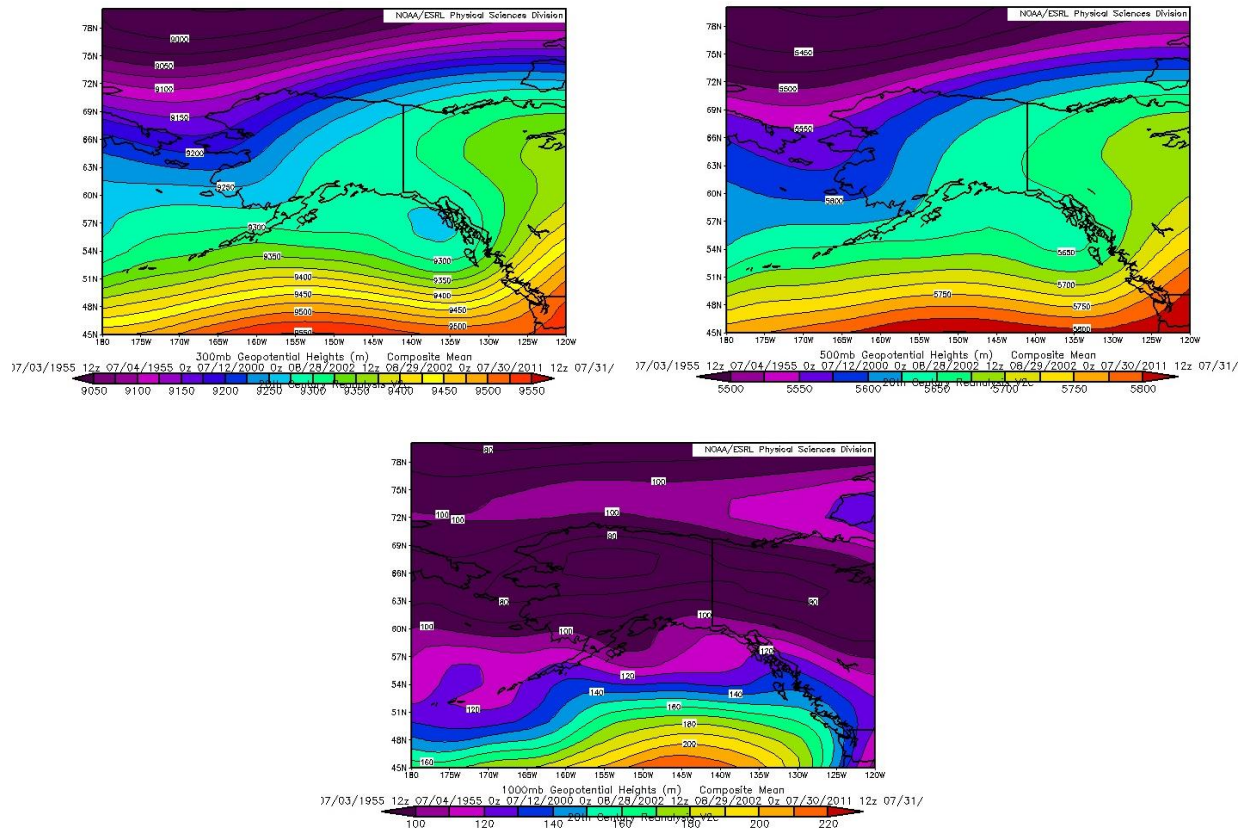

Fig. 3.21a. Composites of mean geopotential heights at the 300 hPa (top left), 500 hPa (top right), and surface map at 1000 hPa (bottom) of days with funnel cloud sightings
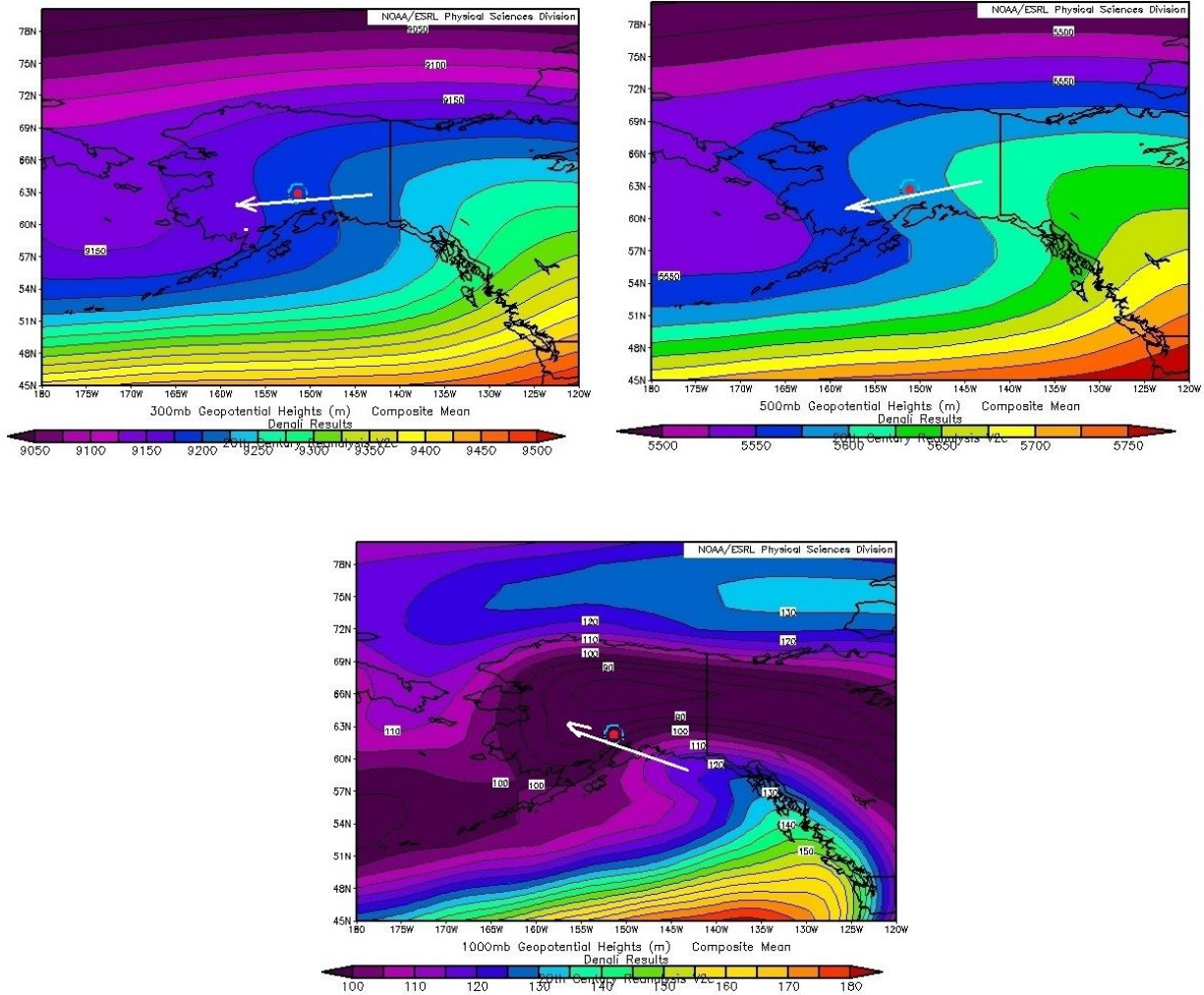
Fig. 3.21b. Composites of mean geopotential heights at the 300 hPa (top left), 500 hPa (top right), and surface map at 1000 hPa (bottom) of days with funnel cloud sightings, and days identified by the search algorithm as having similar profiles like those of funnel cloud events for the observed Denali group.

The composite surface synoptic maps are similar of the actual funnel cloud events and the days identified by the search algorithm to have similar profiles as those of funnel cloud events (Fig. 3.21a, b). The composites of means at 300 hPa and 500 hPa determined for the funnel cloud events and the similar profiles identified by the search algorithm are also similar, suggesting topography influences the Denali group.

3.5 Bethel

There were five reported funnel cloud events for the Bethel group (Table 3.7). In contrast to the groups discussed before, there is a sighting September for Bethel. All reported events occurred in the new millennium. Two times, two sightings occurred on the same day late in August. The other event occurred in late June. The fact that all events occurred later in the warm season may be a hint that the Bering Sea plays a role in funnel cloud occurrence.

Table 3.7. Dates and times of observed funnel clouds in the Bethel area.

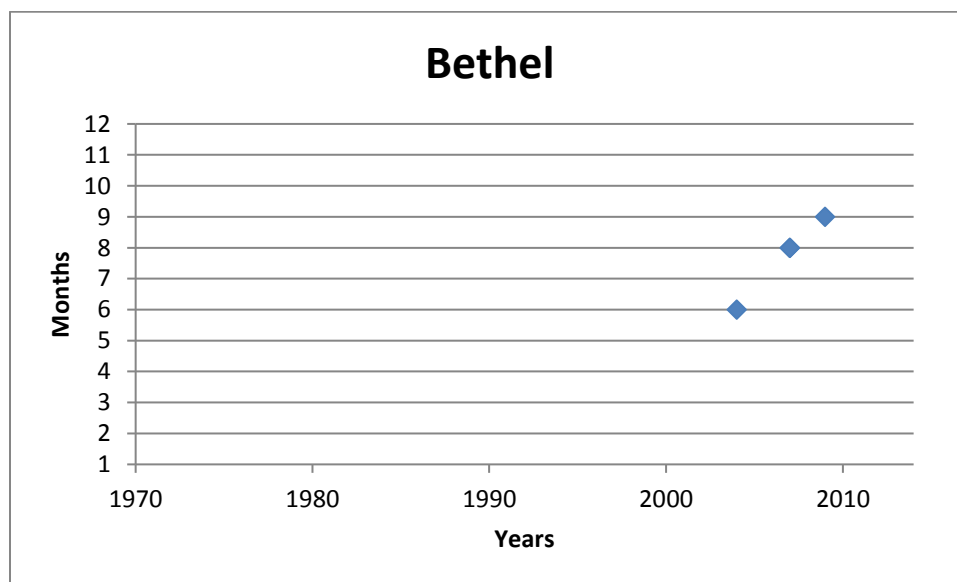| Year	Month	Day	Local Time	Radiosonde date, bfr	Radiosonde date,aft	Radiosonde Station
2004	6	21	3:55pm AST NOAA	2004072200		beth
2007	8	20		2007080712	2007080800	beth
2007	8	20	early evening,late afternoon	2007082100		beth
2009	9	7	6:45pm AST	2009090800		beth

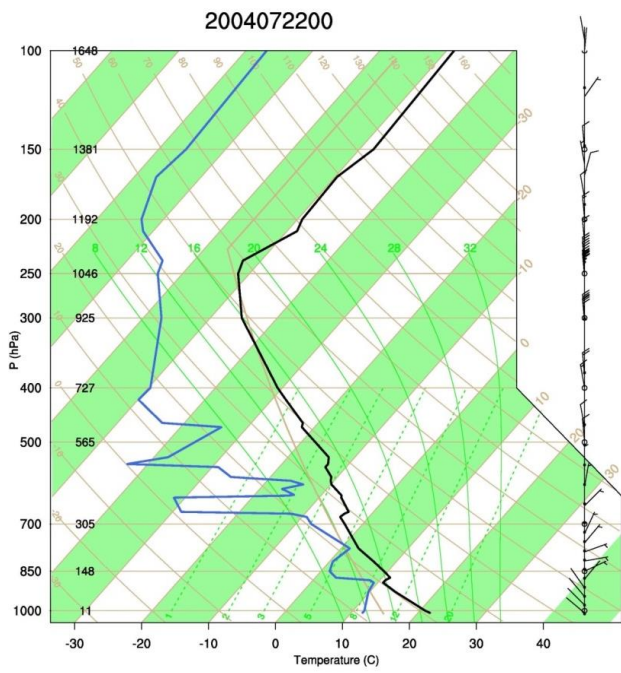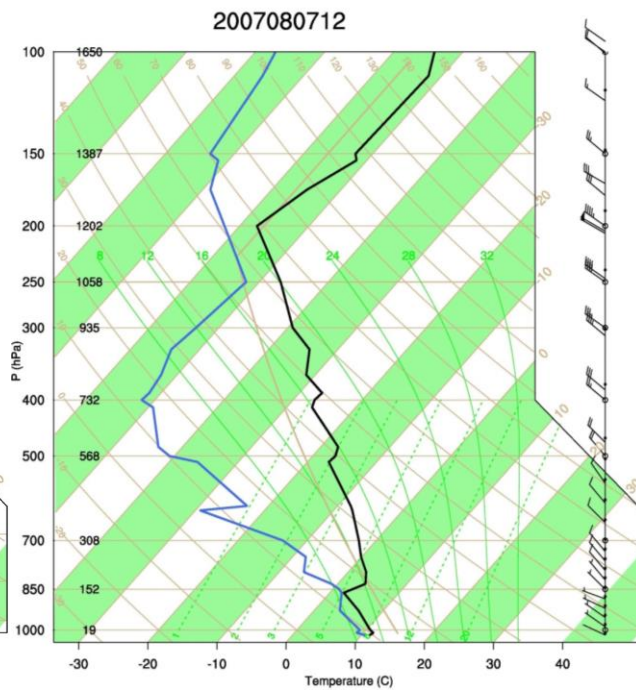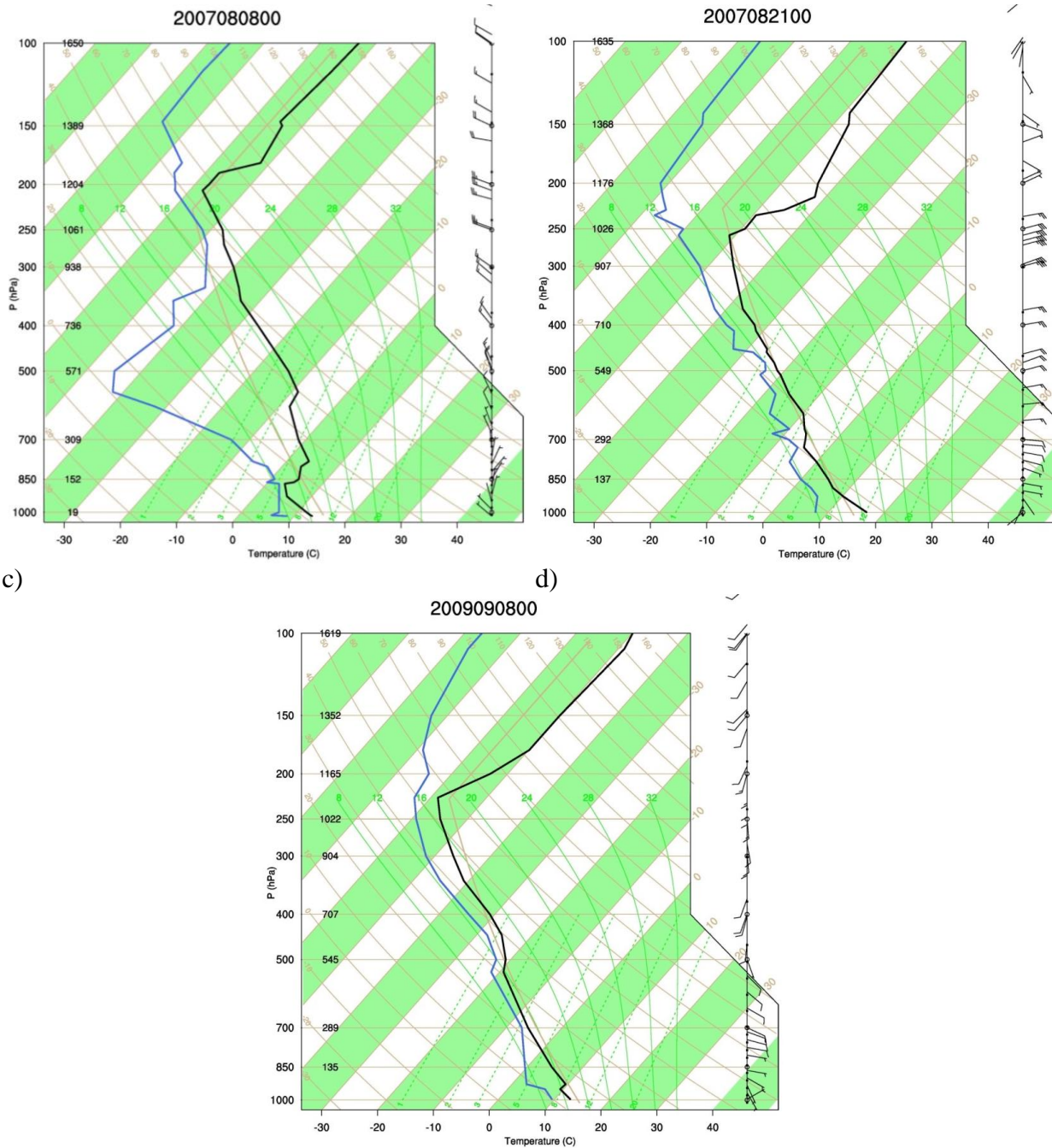Fig. 3.22. Funnel cloud sightings by years and months for the Bethel group.

a)

b)

c)   d)

e)

Fig. 3.23. Skew-T diagrams of the reported funnel cloud events in the Bethel group with temperature (black line) and dew point temperature (blue line), wind speed and direction (barbs). The solid tan line is the US standard atmosphere. List of radiosonde profiles are a) July 22, 2004 at 00z, and b) August 7, 2007 at 12z, and c) August 8, 2007 at 00z, and d) August 21, 2007 at 00z, and e) September 8, 2009 at 00z.

In Figure 3.23, the first three events, a-c, are quite similar and the last two events, d-e, are similar to each other, but different to the first three events. This feature may suggest different mechanisms. All temperature profiles except for one show an inversion in the ABL which may be a hint to a sea-breeze.

Table 3.8. Ranges of air temperature (T), dew point temperature (T_d), and wind speed (v) as obtained for the various pressure ranges (p) for Bethel based on the profiles of observed funnel clouds. See Chapter 2 for reasoning of the choice of the pressure ranges.

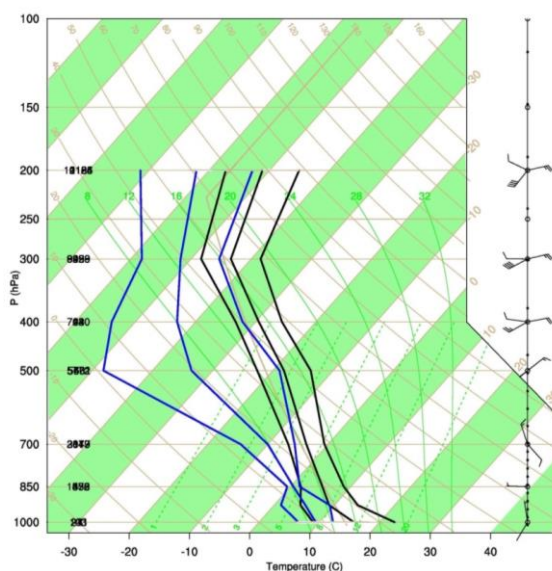| P (hPa)	Range (hPa)	T (Cº)	Td(Cº)	v (m/s)
1000	1015-962.5	6.5 – 12.3	9 – 22.5	0.7 – 3.1
925	962.6-887.5	1.1 – 9.2	4.4 – 13.9	1.1 – 3.5
850	887.5-812.5	-0.5 – 1.5	1.7 – 8.8	2.7 – 6.3
700	737.5-650	-14.5 - -5.5	-6.6 - -0.6	1.6 – 13.5
500	550-450	-48.1 - -18.9	-22.6 - -13.7	4.6 – 21.2
400	450-350	-53.9 - -32.2	-33.4 - -25.7	8.2 – 27.5
300	350-250	-58.2 - -45.3	-48.3 - -38.4	9.4 – 42.4
200	250-150	-71.4 - -52.8	-57.2 - -45.1	7.8 – 42

Fig. 3.24. Resultant ranges for potential funnel cloud profiles with CAPE greater than 500 J as obtained based on observed funnel cloud sightings for the Bethel group. Note that here the Skew-T limits of minimum (left), mean (middle), and maximum (right) temperature (black lines), dew point temperature (blue lines), wind speed and wind direction (barbs). Further, minimum, mean, and maximum wind direction over the pressure ranges listed in Table 3.8 are shown.
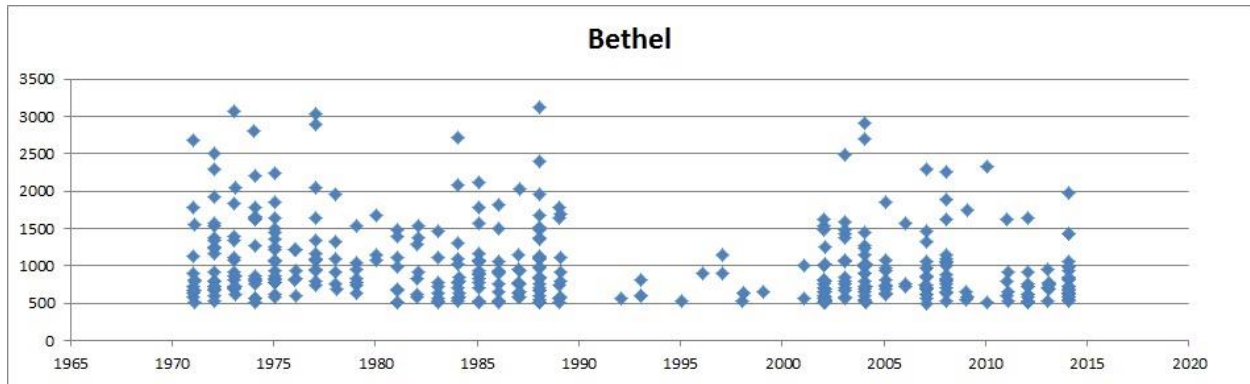
Fig. 3.25. Frequency (number of diamonds) and CAPE (in J) of events with radiosonde profiles similar to those during the observed funnel cloud events in the Bethel group as identified by the search algorithm and testing for CAPE. Note that between 1990 and 1991 there were problems with the dew point temperature measurements for which this data is excluded as result of the stringent 1st requirement as depicted in Figure 2.6.
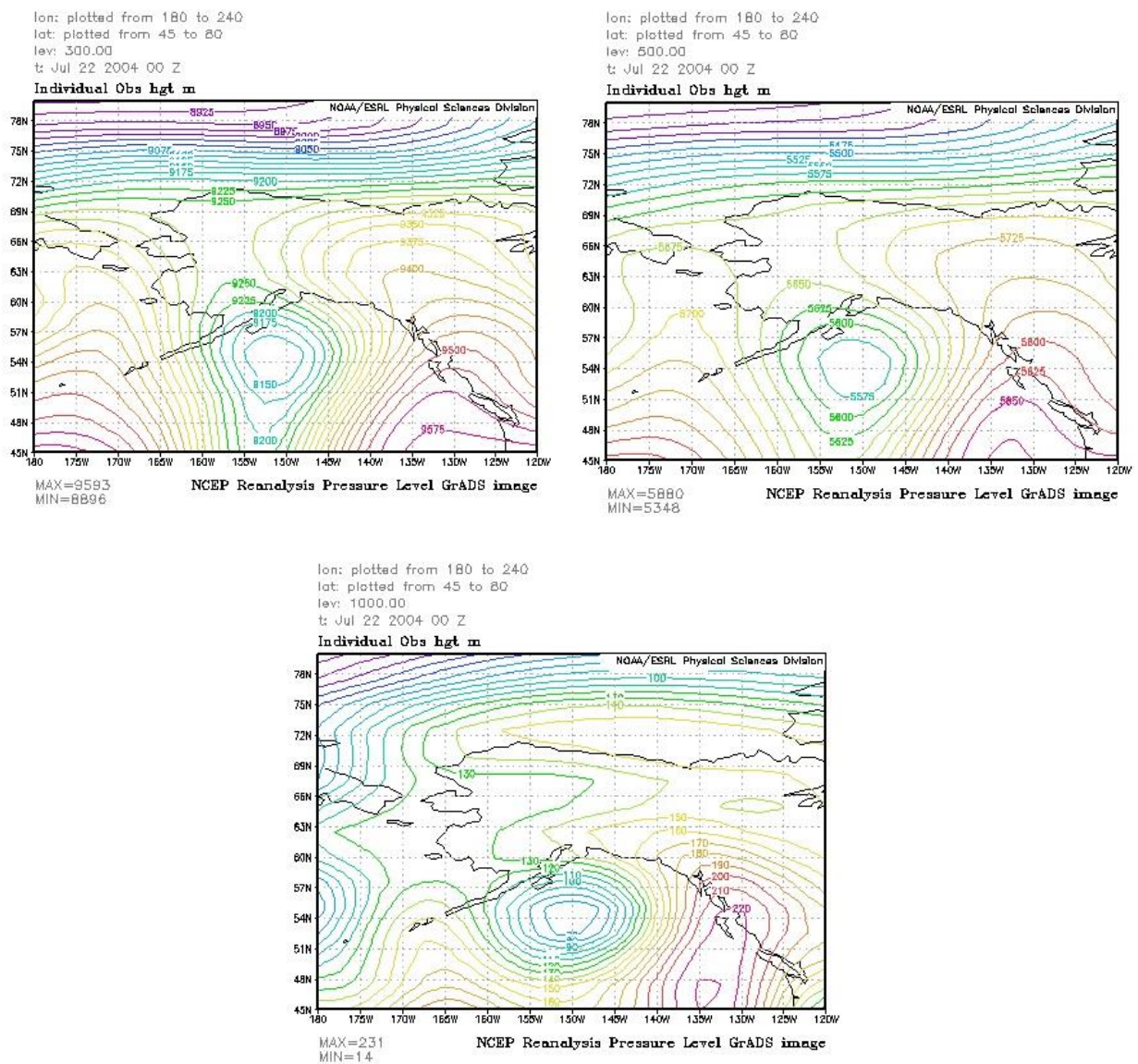
Fig. 3.26a. Geopotential heights at the 300 hPa (top right), 500 hPa (top left), and 1000 hPa (bottom) from reanalysis data on date of observed funnel cloud (July on the 22, 2004 at 00z) in GMT for the Bethel group.
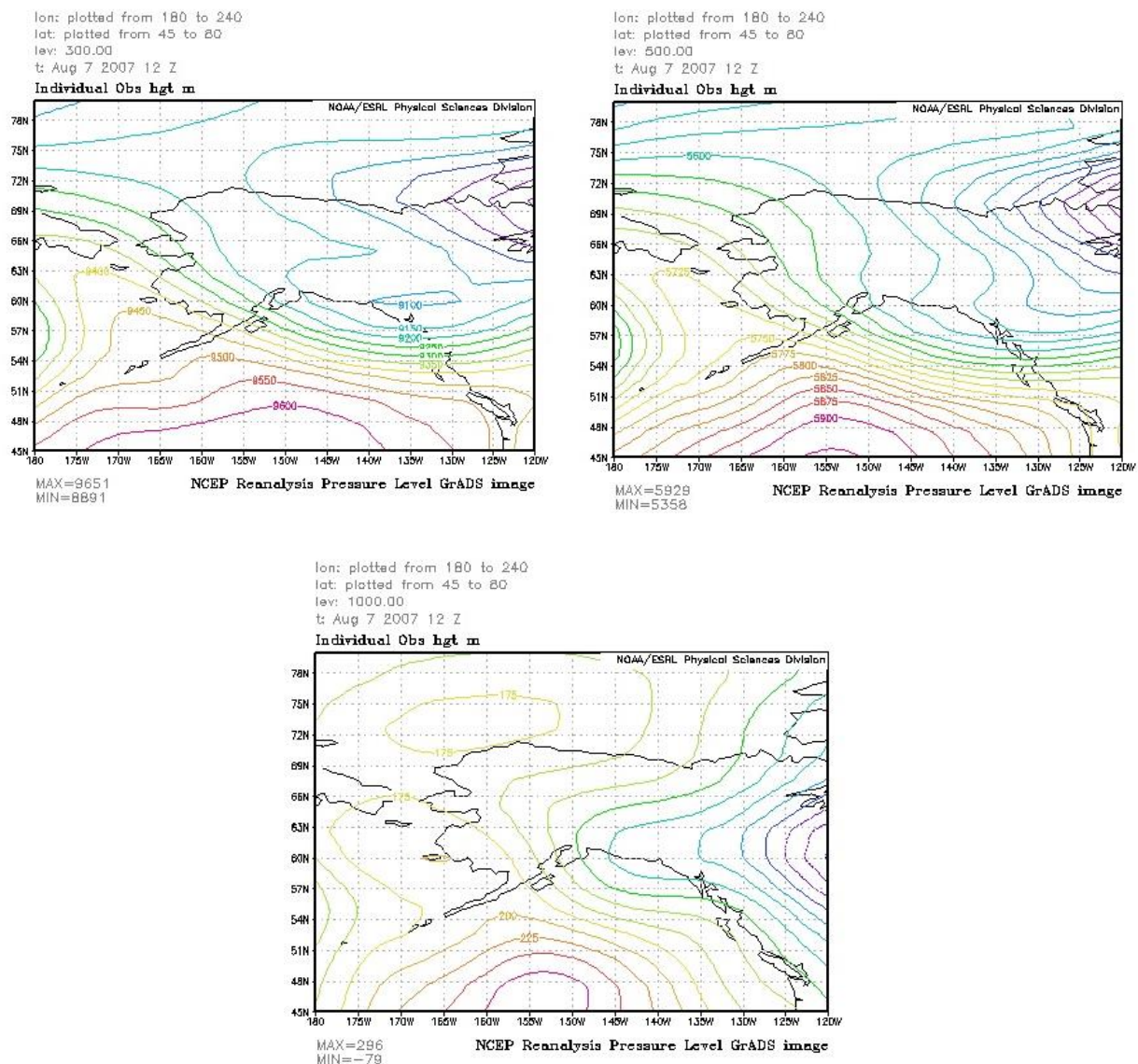
93

Fig. 3.26b. Geopotential heights at the 300 hPa (top right), 500 hPa (top left), and 1000 hPa (bottom) from reanalysis data on date of observed funnel cloud (August on the 7, 2007 at 12z) in GMT for the Bethel group.
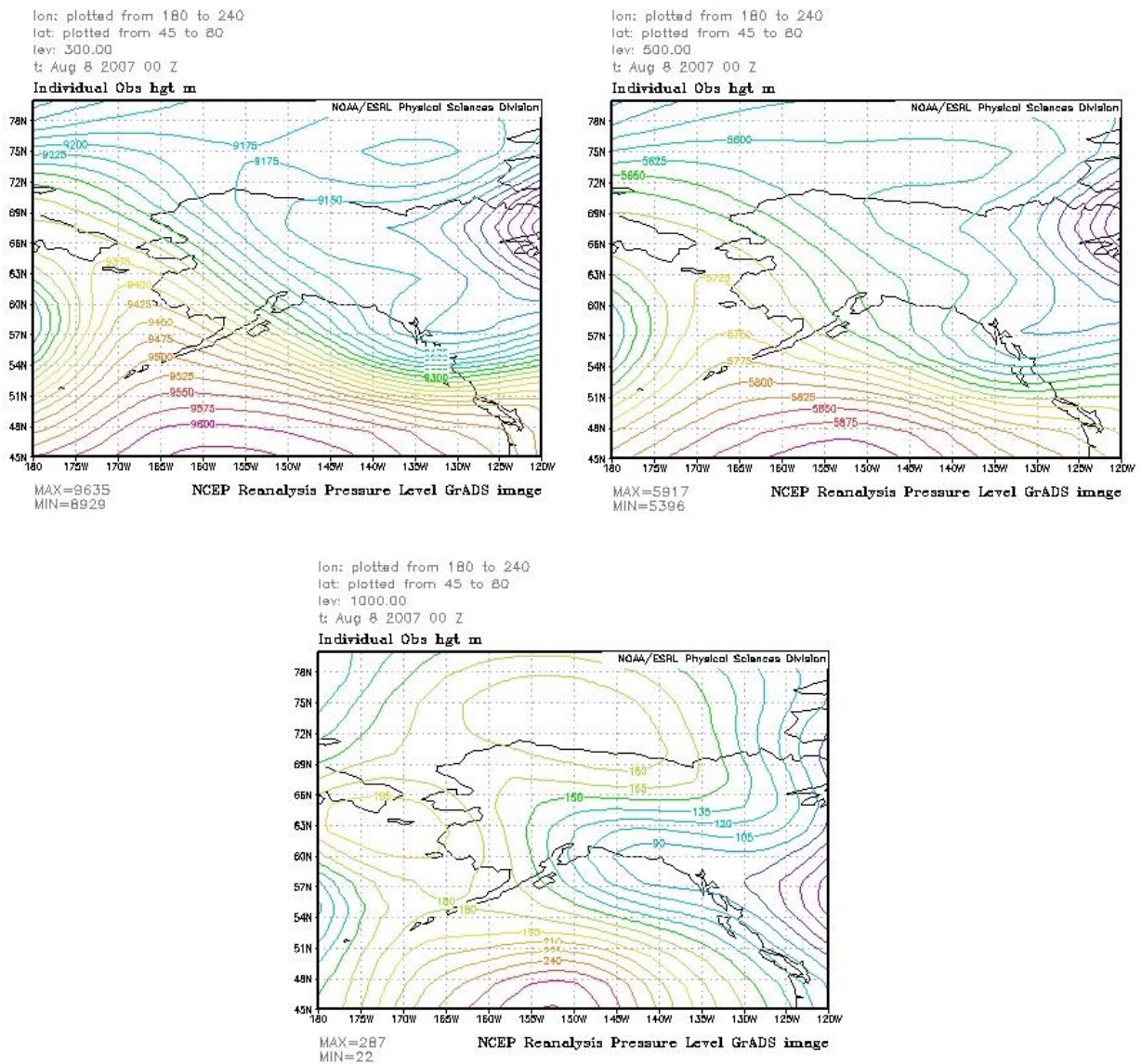
94

Fig. 3.26c. Geopotential heights at the 300 hPa (top right), 500 hPa (top left), and 1000 hPa (bottom) from reanalysis data on date of observed funnel cloud (August on the 8, 2007 at 00z) in GMT for the Bethel group.
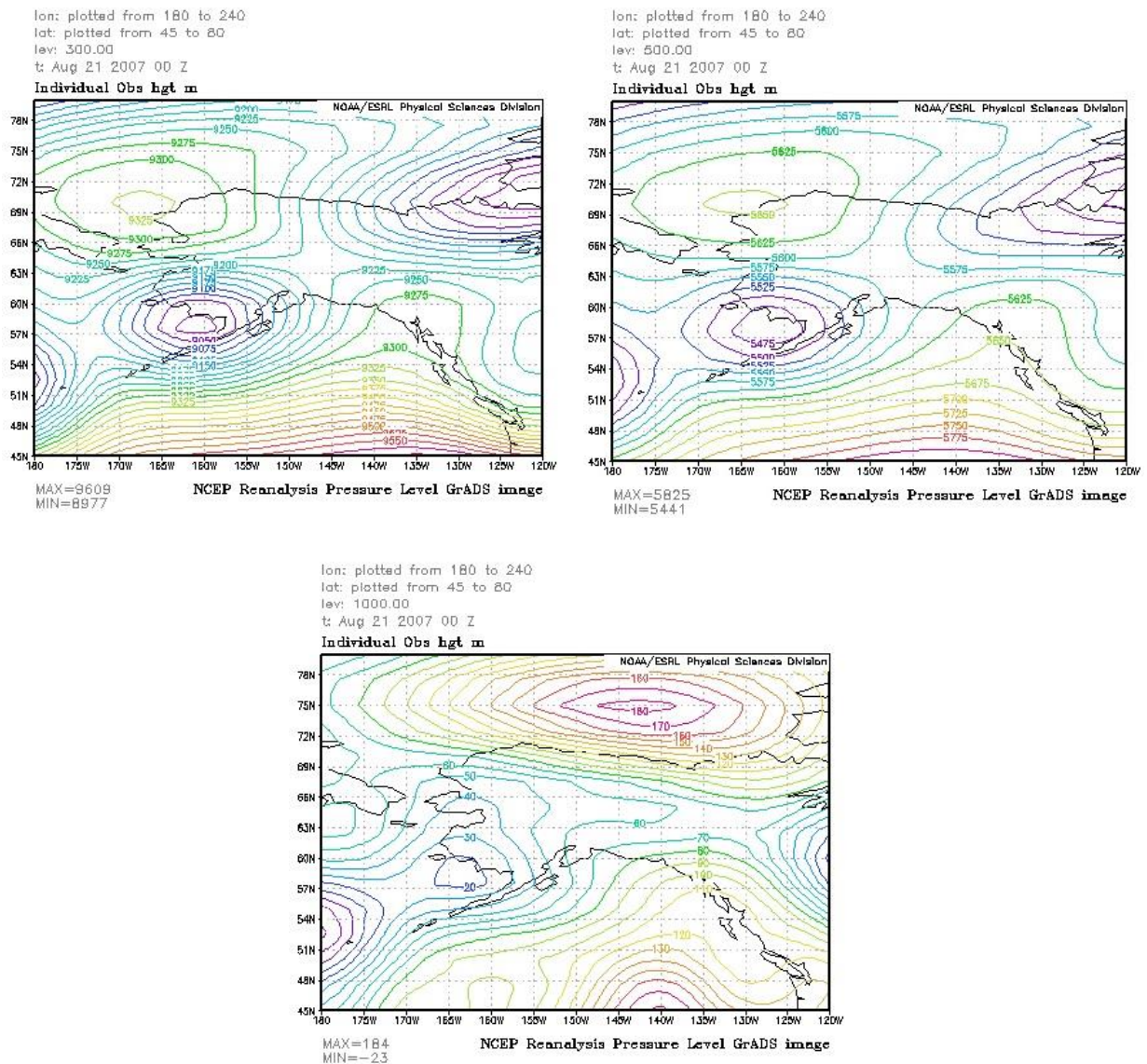
95

Fig. 3.26d. Geopotential heights at the 300 hPa (top right), 500 hPa (top left), and 1000 hPa (bottom) from reanalysis data on date of observed funnel cloud (August on the 21, 2007 at 00z) in GMT for the Bethel group.
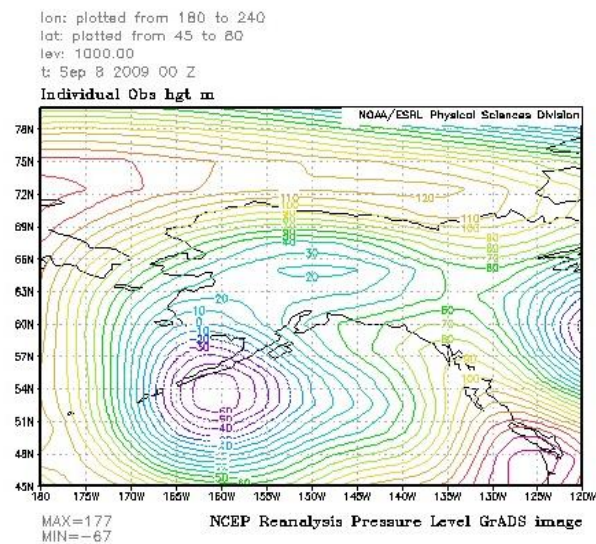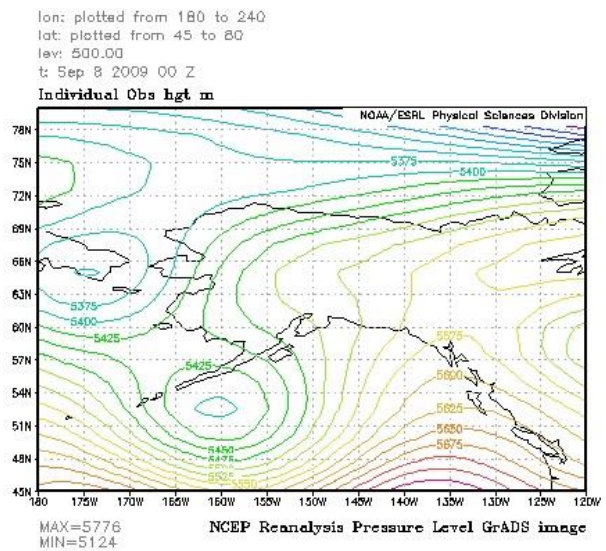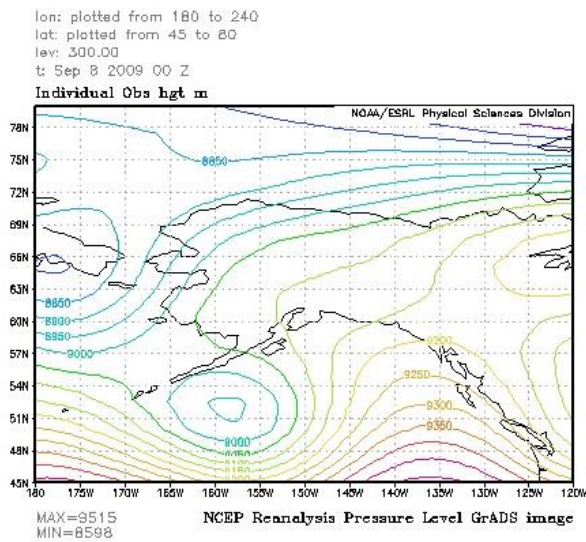
Fig. 3.26e. Geopotential heights at the 300 hPa (top right), 500 hPa (top left), and 1000 hPa (bottom) from reanalysis data on date of observed funnel cloud (September on the 8, 2009 at 00z) in GMT for the Bethel group.

The 1000 hPa pressure map has a high pressure and a low pressure in the Gulf of Alaska and the Chukchi Sea, respectively, creating a northerly or southerly surface gradient wind blowing parallel to the Alaska West Coast (Fig. 3.26).

On the 500 hPa pressure level, when the surface coastal wind blows from the land to the sea, the wind blows from the South, and when on the 500 hPa surface the gradient wind blows from North, the near-surface wind is from the sea to land (Fig. 3.27). In all cases, the large-scale forcing at the 1000 hPa and 500 hPa pressure levels is weak.
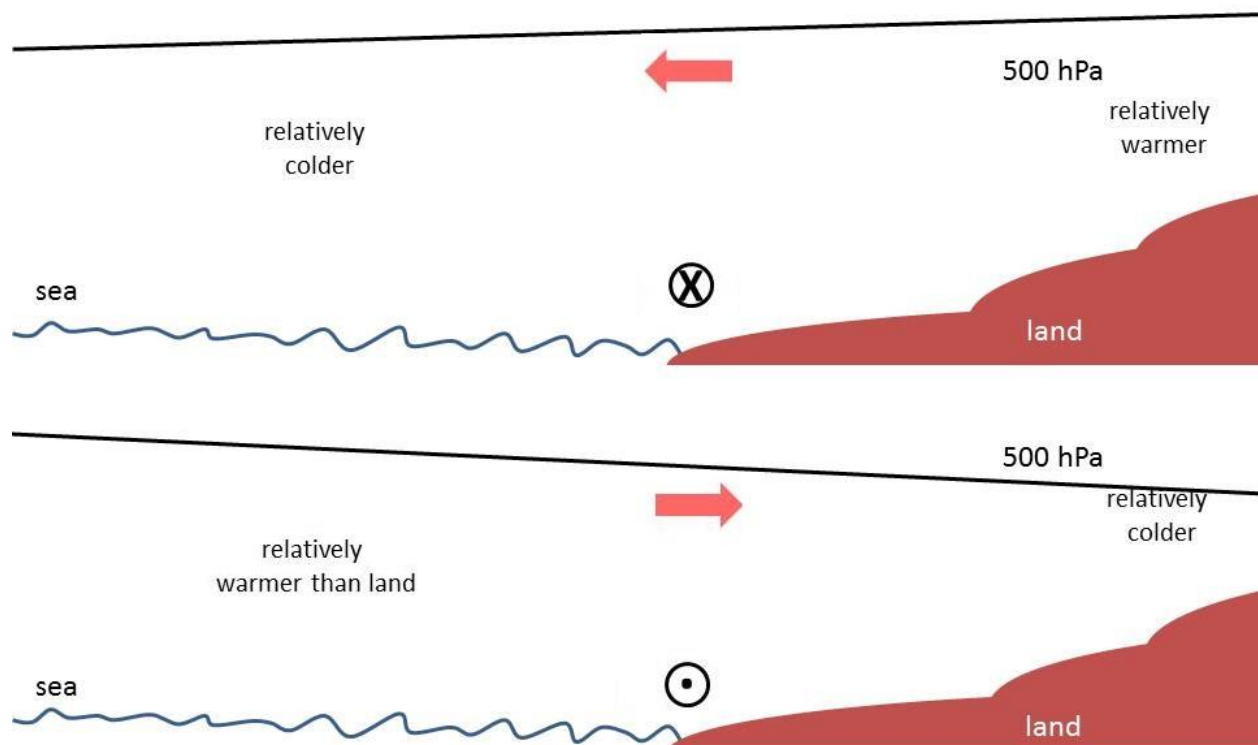

Fig. 3.27. Schematic view of the synoptic and mesoscale situation and the potential mechanism for vorticity creation.
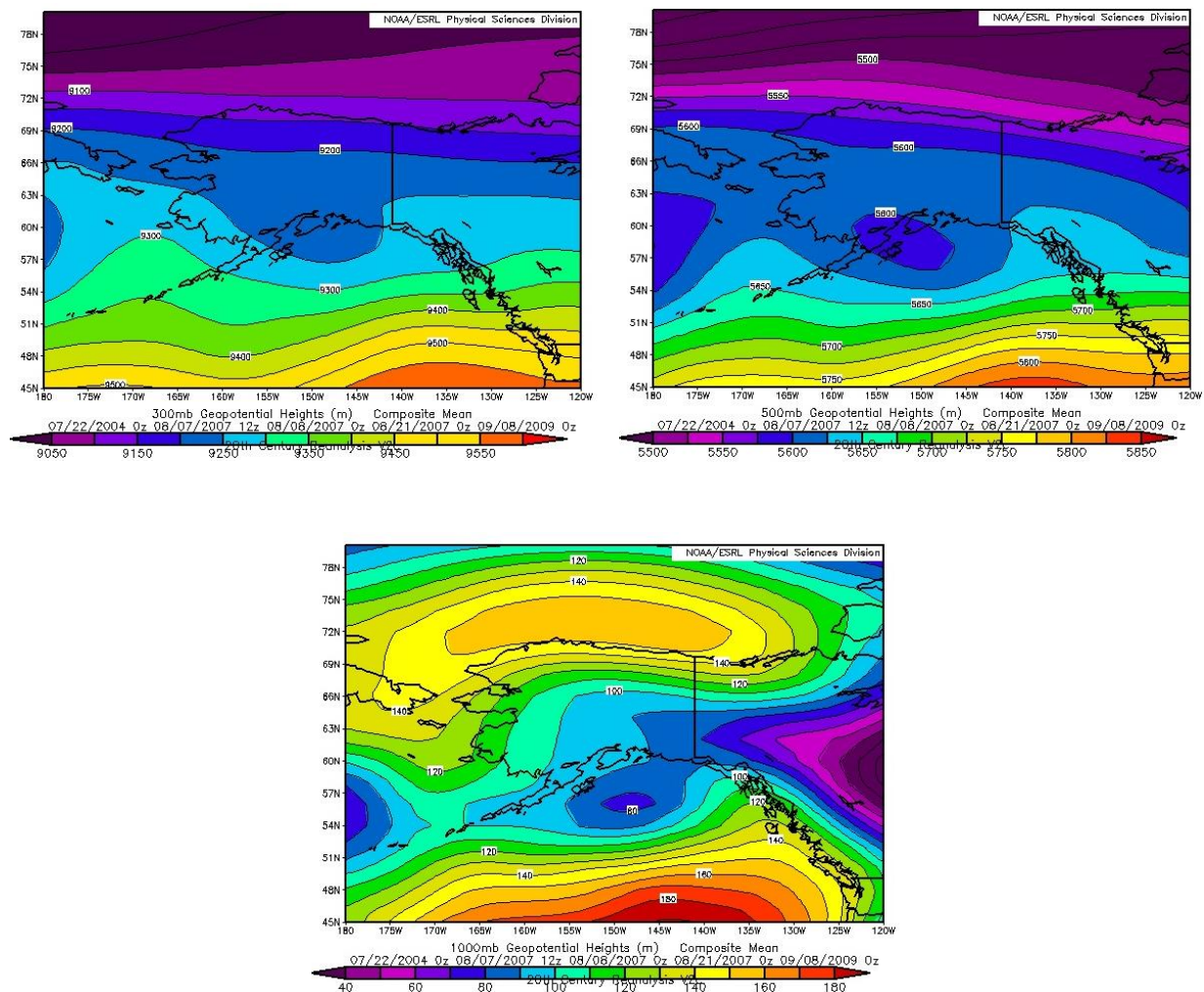
Fig. 3.28a. Composites of mean geopotential heights at the 300 hPa (top left), 500 hPa (top right), and surface map at 1000 hPa (bottom) of days with funnel cloud sightings
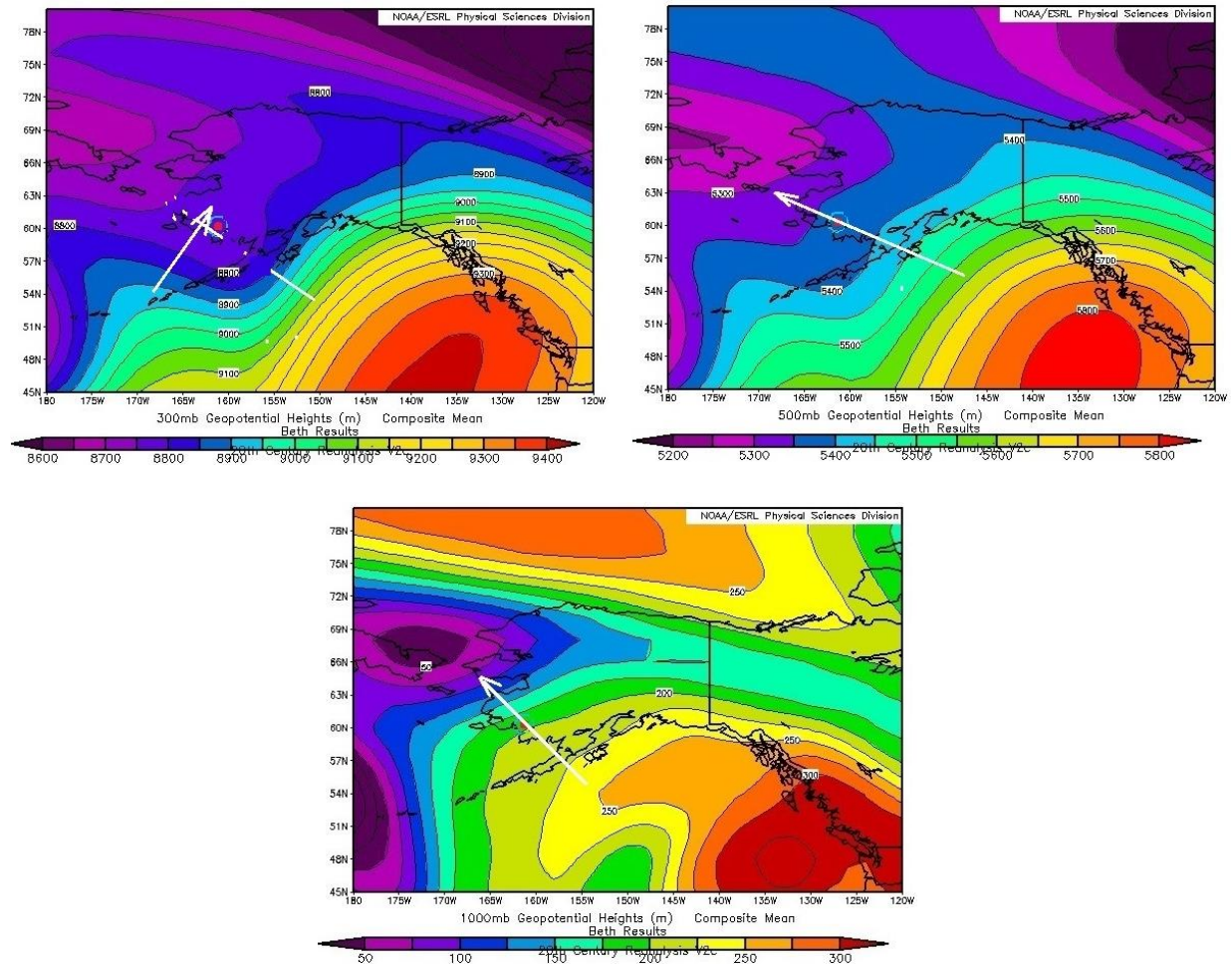
Fig. 3.28b. Composites of mean geopotential heights at the 300 hPa (top left), 500 hPa (top right), and surface map at 1000 hPa (bottom) of days with funnel cloud sightings, and days identified by the search algorithm as having similar profiles like those of funnel cloud events for the observed Bethel group.

The surface synoptic maps of both the composites for actual funnel cloud events and the composites from days identified by the search algorithm to have funnel cloud conditions are similar (Fig. 3.28a, b). The composites for real and potential funnel cloud events at 300 hPa and 500 hPa differ for the Bethel group.

3.6 Alaska West Coast Area along the Coast of Bethel.

The area encompassed by the Alaska West Coast group is depicted in Figure 2.3. The radiosonde sites are Bethel and Nome.

Table 3.9. Dates and times of observed funnel clouds in the Alaska West Coast group.

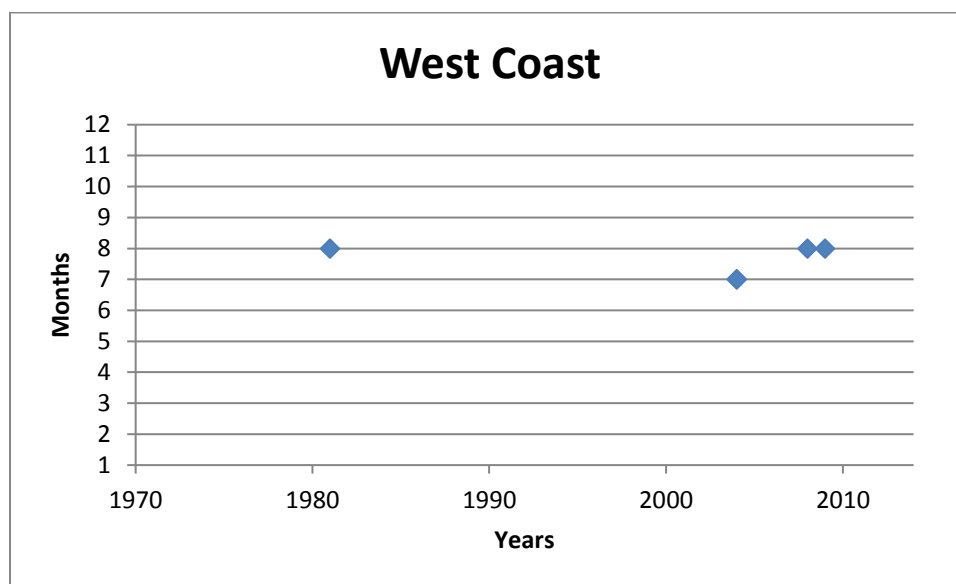| Year	Month	Day	Local Time	Radiosonde date, bfr	Radiosonde date,aft
1981	8	9	4:45pm ADT	1981080700	
2004	7	28	1:25pm AST		2004072900
2008	8	16		2008081612	2008081700
2009	8	1		2009080112	2009080200
2004	7	26	3pm AST NOAA	2004072700	

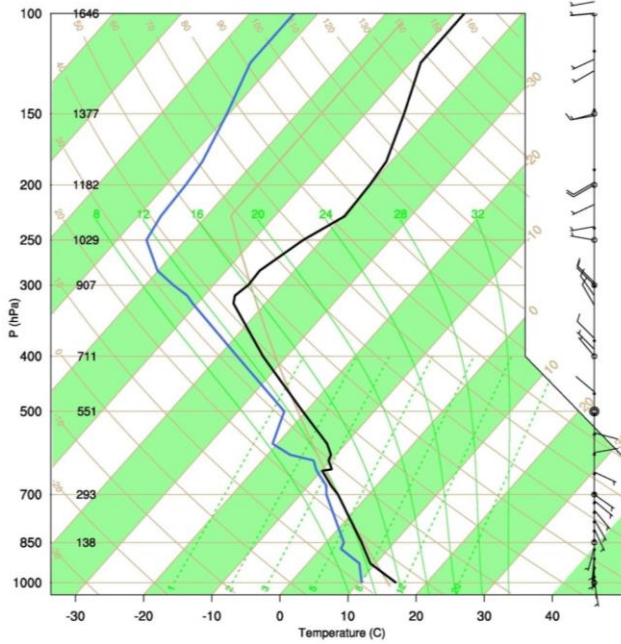Fig. 3.29. Funnel cloud sightings by years and months for the Alaska West Coast group.

a)

b)
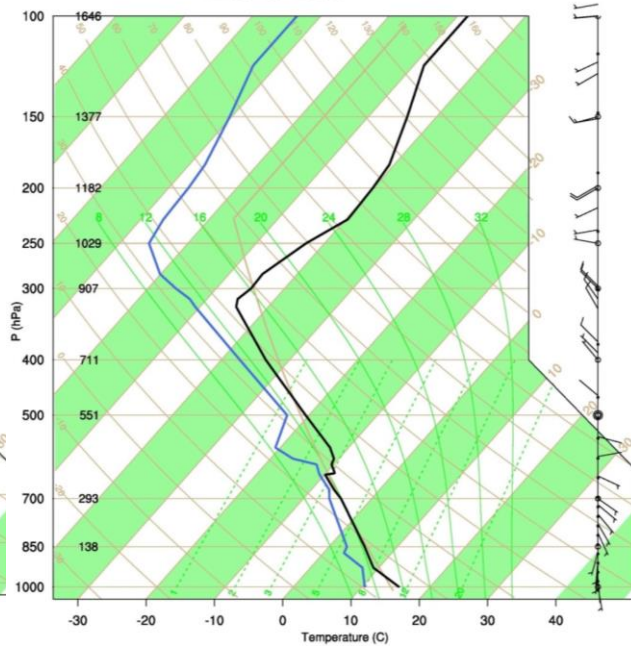
c)

d)

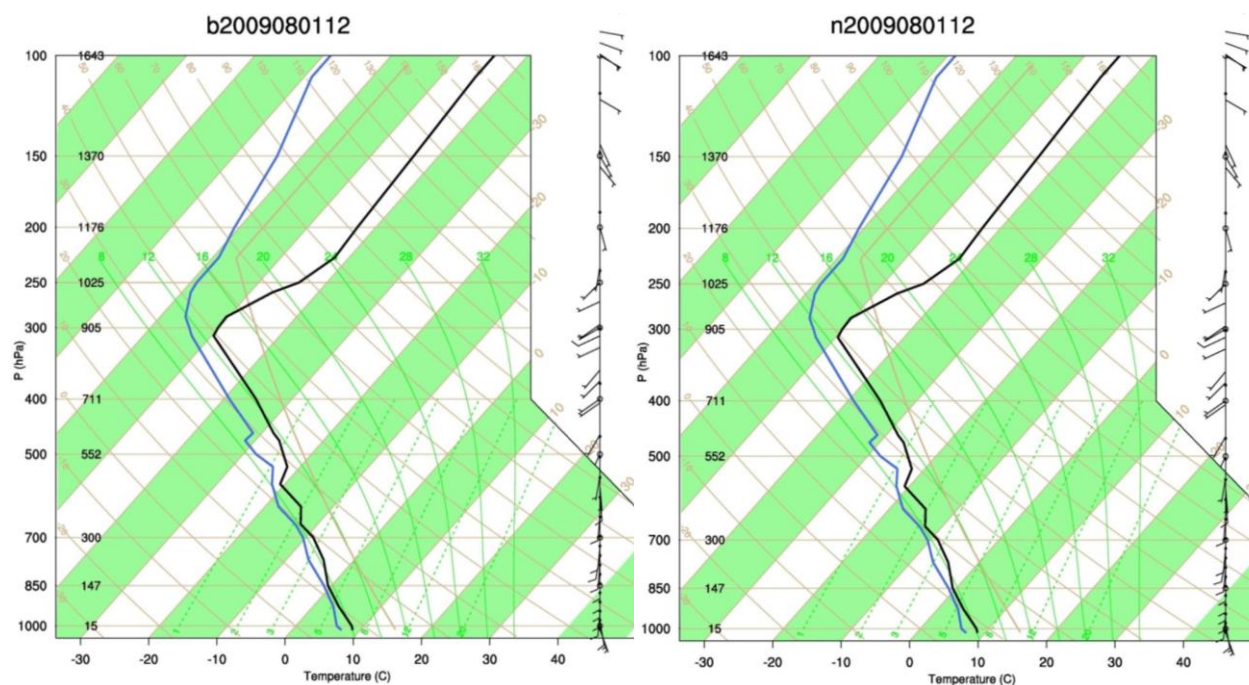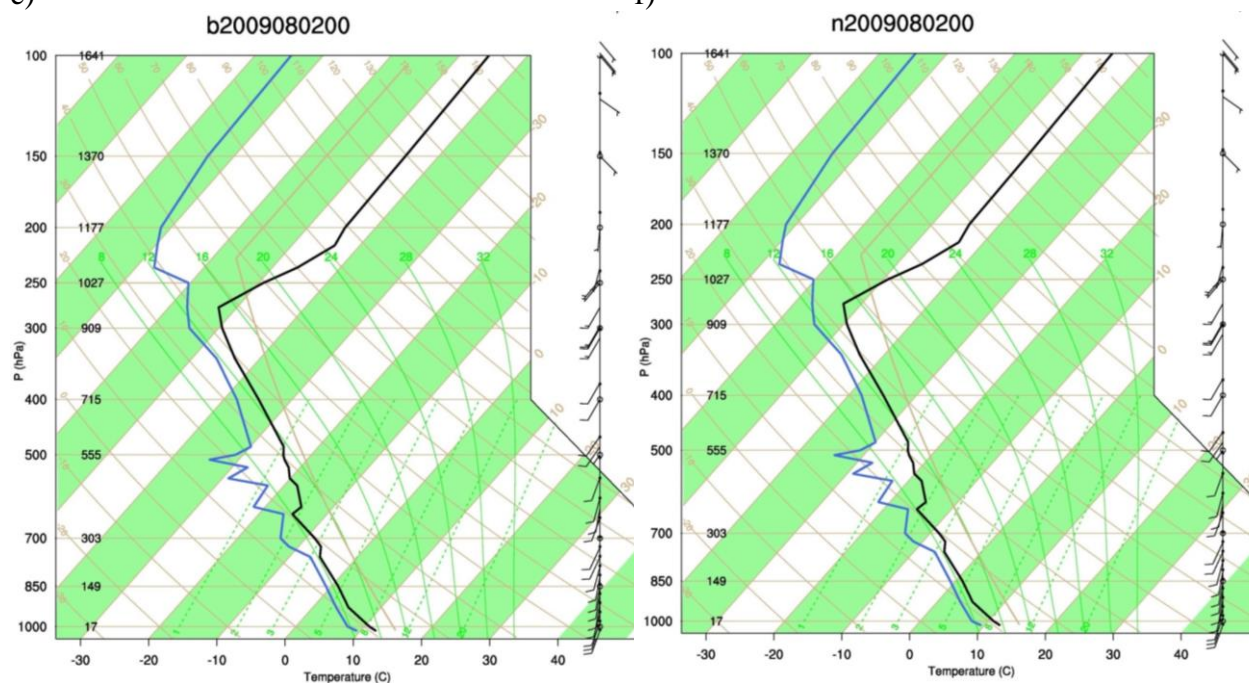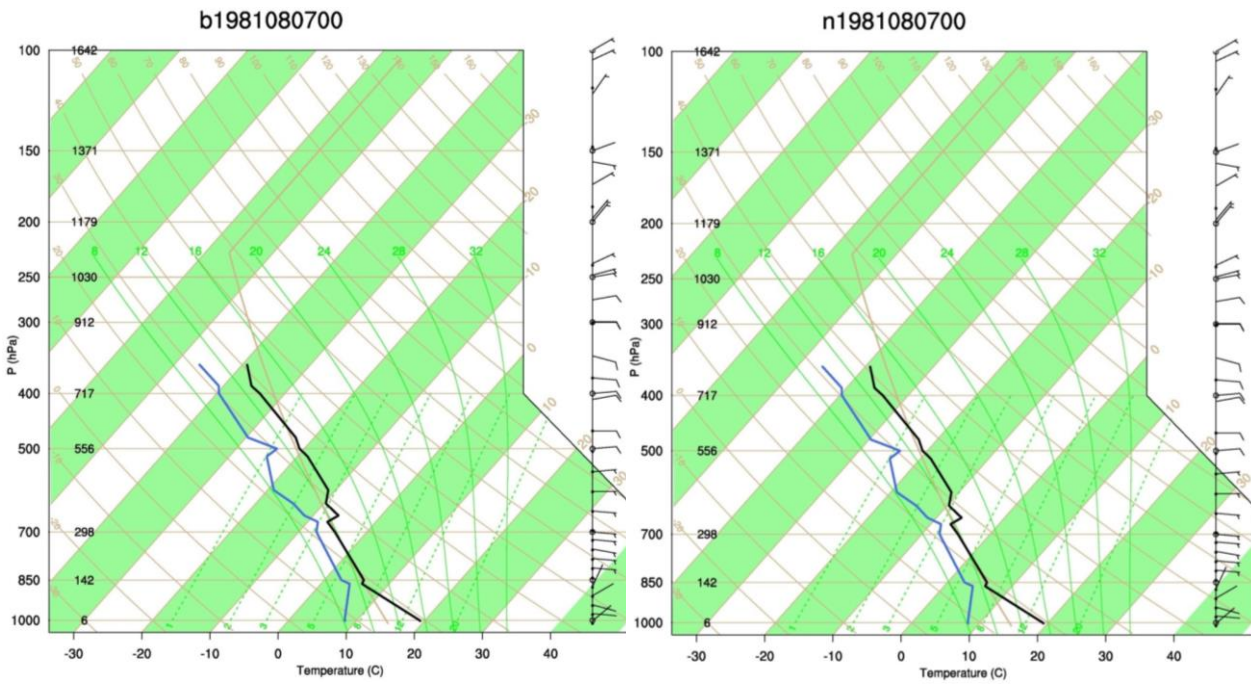e)   f)

g)   h)

b1981080700

n1981080700

i)

j)

b2008081612

n2008081612

k)

l)

m)   n)
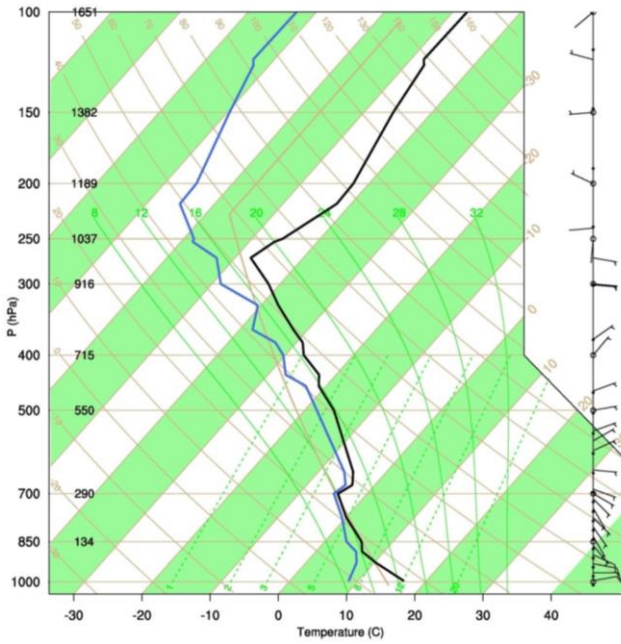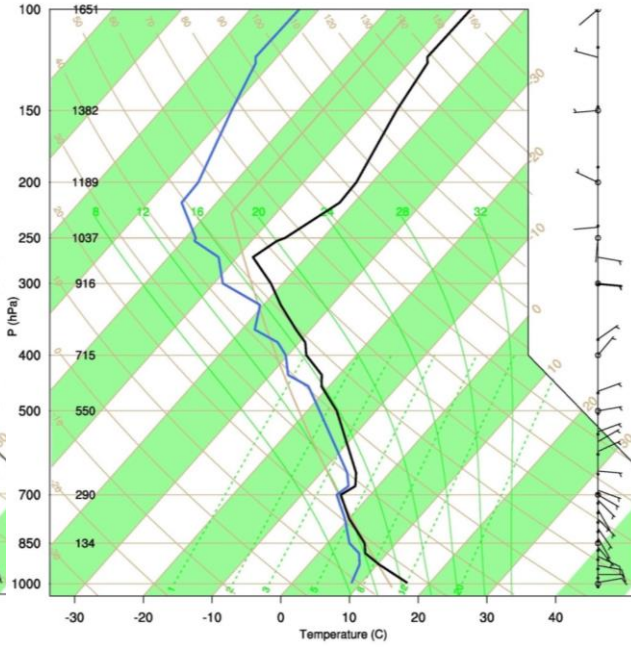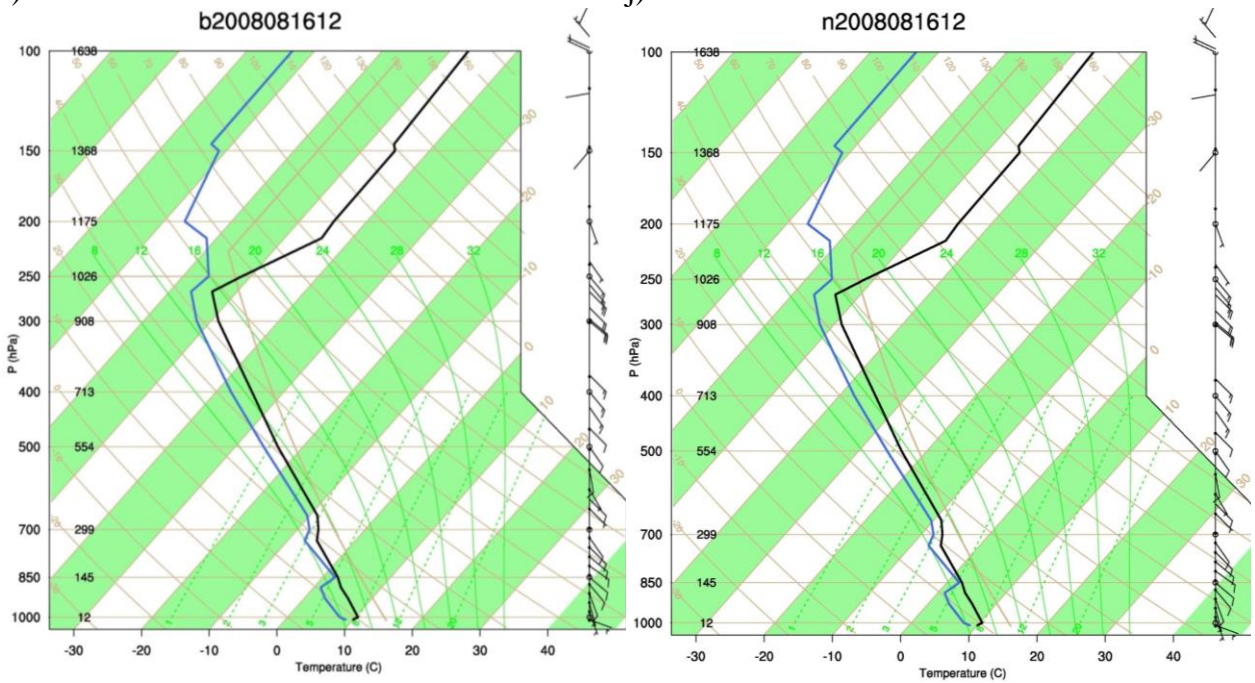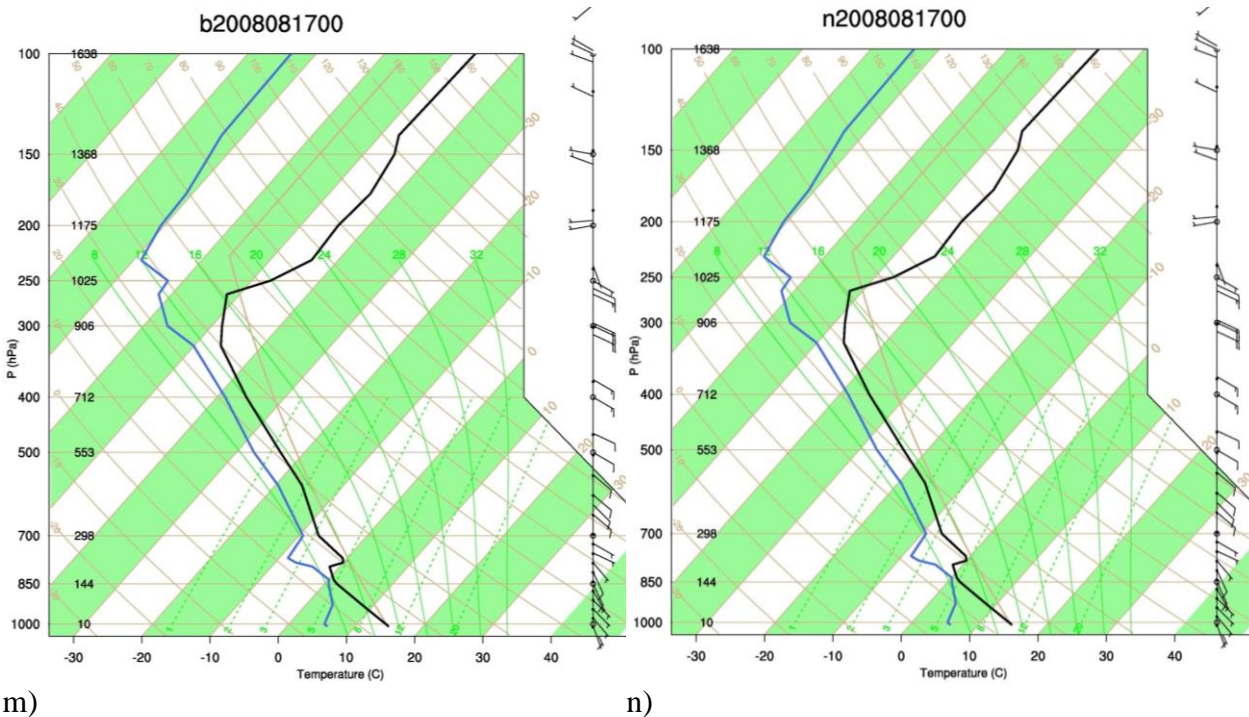
Fig. 3.30. Skew-T diagrams of the reported funnel cloud events in the West Coast group with temperature (black line) and dew point temperature (blue line), wind speed and direction (barbs). The red dashed line is the US standard atmosphere.

Table 3.10. Ranges of air temperature (T), dew point temperature (T_d), and wind speed (v) as obtained for the various pressure ranges (p) for West Coast based on the profiles of observed funnel clouds. See Chapter 2 for reasoning of the choice of the pressure ranges.

Bethel				
p (hPa)	Range (hPa)	T (C°)	T_d(C°)	v (m/s)
1000	1015-962.5	5.6 – 9.6	8.19 – 18.7	0.8 – 7.3
925	962.6-887.5	1.6 – 7.8	3.7 – 10.6	2.3 – 12.4
850	887.5-812.5	-1.1 – 3.6	-.4 – 6.4	2 – 12.2
700	737.5-650	-12.6 - -4.6	-9.2 - -3.7	3.5 – 10.4
500	550-450	-31.1 - -19.7	-26 - -17.5	2 – 12.5
400	450-350	-41.7 - -32.9	-37.6 - -29.6	3.4 – 14.5
300	350-250	-57.7 - -49.6	-51.9 - -42.6	2.6 – 20.8
200	250-150	-70 - -57.4	-49 - -45	.6 – 9

Nome				
p (hPa)	Range (hPa)	T (C°)	T_d(C°)	v (m/s)
1000	1015-962.5	2.7 – 12.9	9.7 – 20.8	2.3 – 5.5
925	962.6-887.5	2.1 – 9.8	7.2 – 12.6	0.9 – 6.6
850	887.5-812.5	-.8 – 5.7	2.18 – 7.2	2.4 – 7.1
700	737.5-650	-18.2 - .5	-7.3 - -2	1.5 – 14.6
500	550-450	-40.4 - -17.4	-23.8 - -18.4	2.4 – 14.6
400	450-350	-43 - -33.7	-34.9 - -30.7	.7 – 21
300	350-250	-58.7 - -47.3	-48.3 - -45	0 – 26
200	250-150	-71.7 - -56.4	-56.7 - -42	0 – 18.3
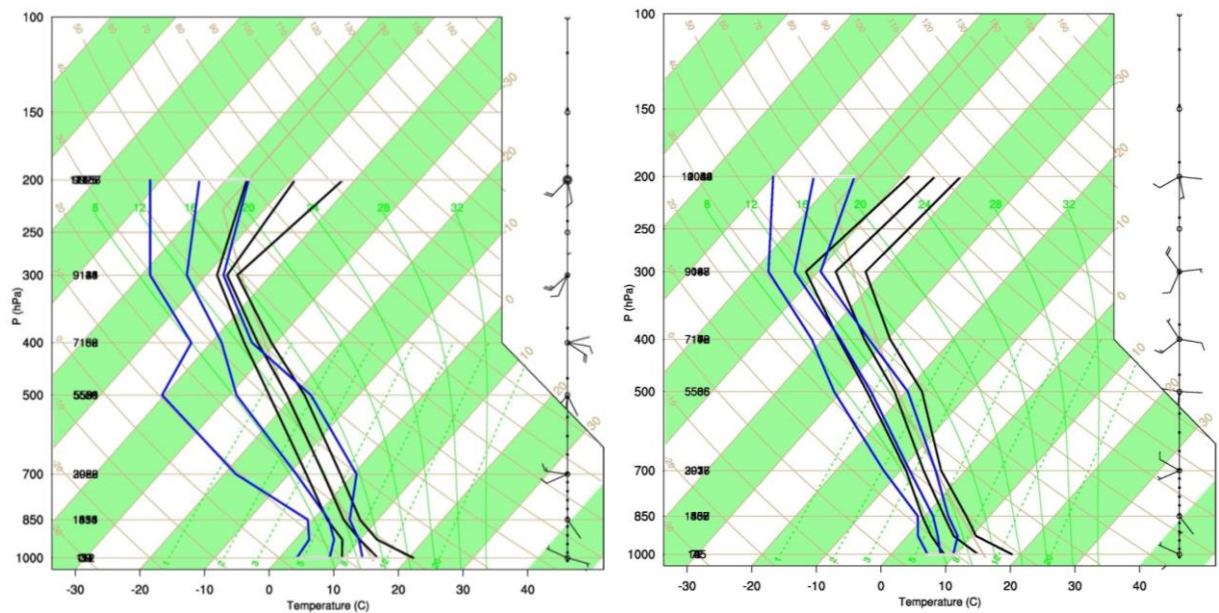
a)   b)

Fig. 3.31. Resultant ranges for potential funnel cloud profiles with CAPE greater than 500 J as obtained based on observed funnel cloud sightings for the West Coast group, a) Nome, and b) Bethel. Note that here the Skew-T limits of minimum (left), mean (middle), and maximum (right) temperature (black lines), dew point temperature (blue lines), wind speed and wind direction (barbs). Further, minimum, mean, and maximum wind direction over the pressure ranges listed in Table 3.10 are shown.
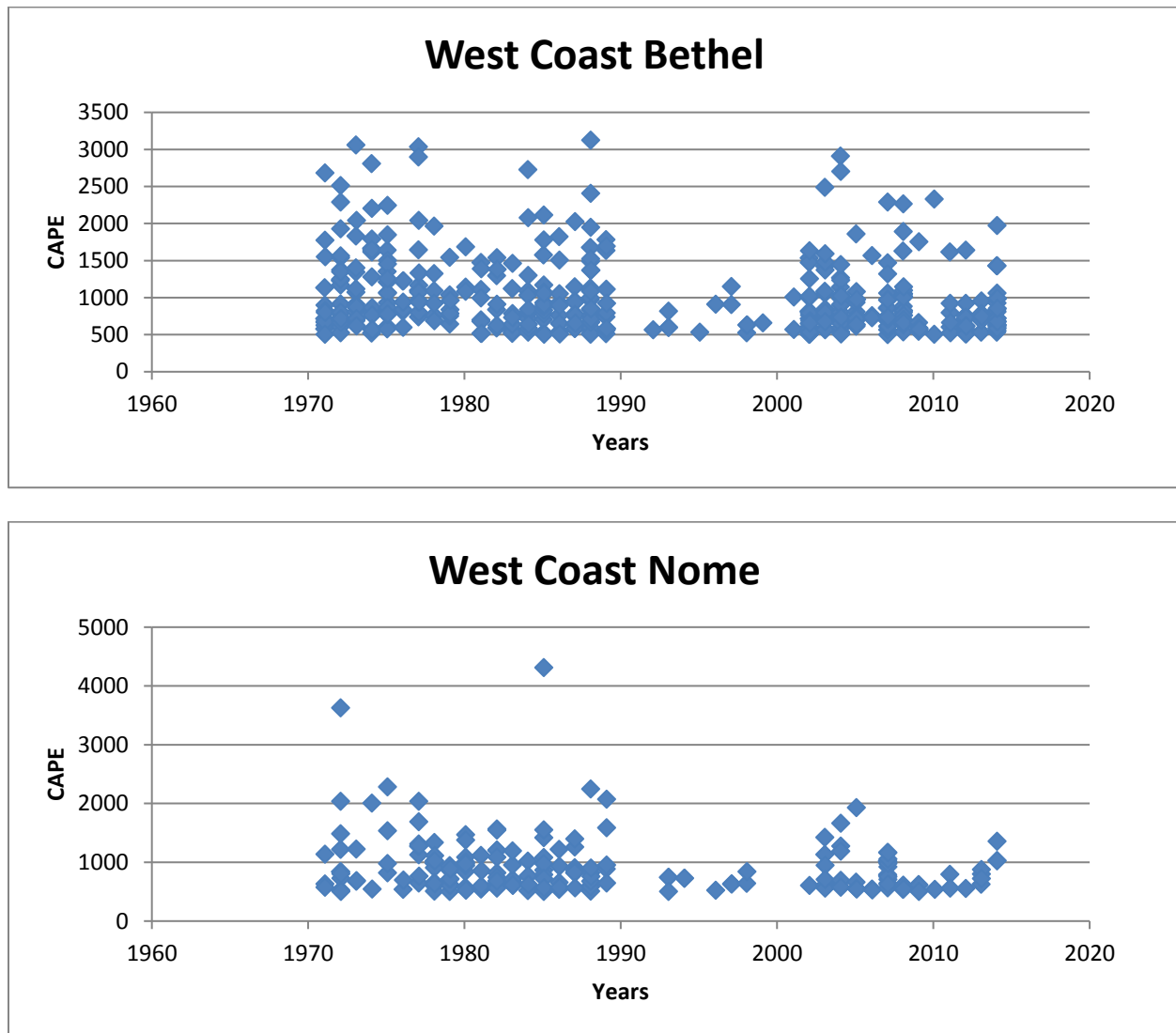
Fig. 3.32. Frequency (number of diamonds) and CAPE (in J) of events, with radiosonde profiles similar to those during the observed funnel clouds in the West Coast group, these identified by the search algorithm. Note that between 1990 and 1991 there were problems with the dew point temperature measurements for which data is excluded as result of the stringent 1st requirement as depicted in Figure 2.6.

Fig. 3.33a. Geopotential heights at the 300 hPa (top left), 500 hPa (top right), and 1000 hPa map (bottom) according to the reanalysis data of the funnel cloud events for the West Coast group.

Fig. 3.33b. Geopotential heights at the 300 hPa (top left), 500 hPa (top right), and 1000 hPa map (bottom) according to the reanalysis data of the funnel cloud events for the West Coast group.
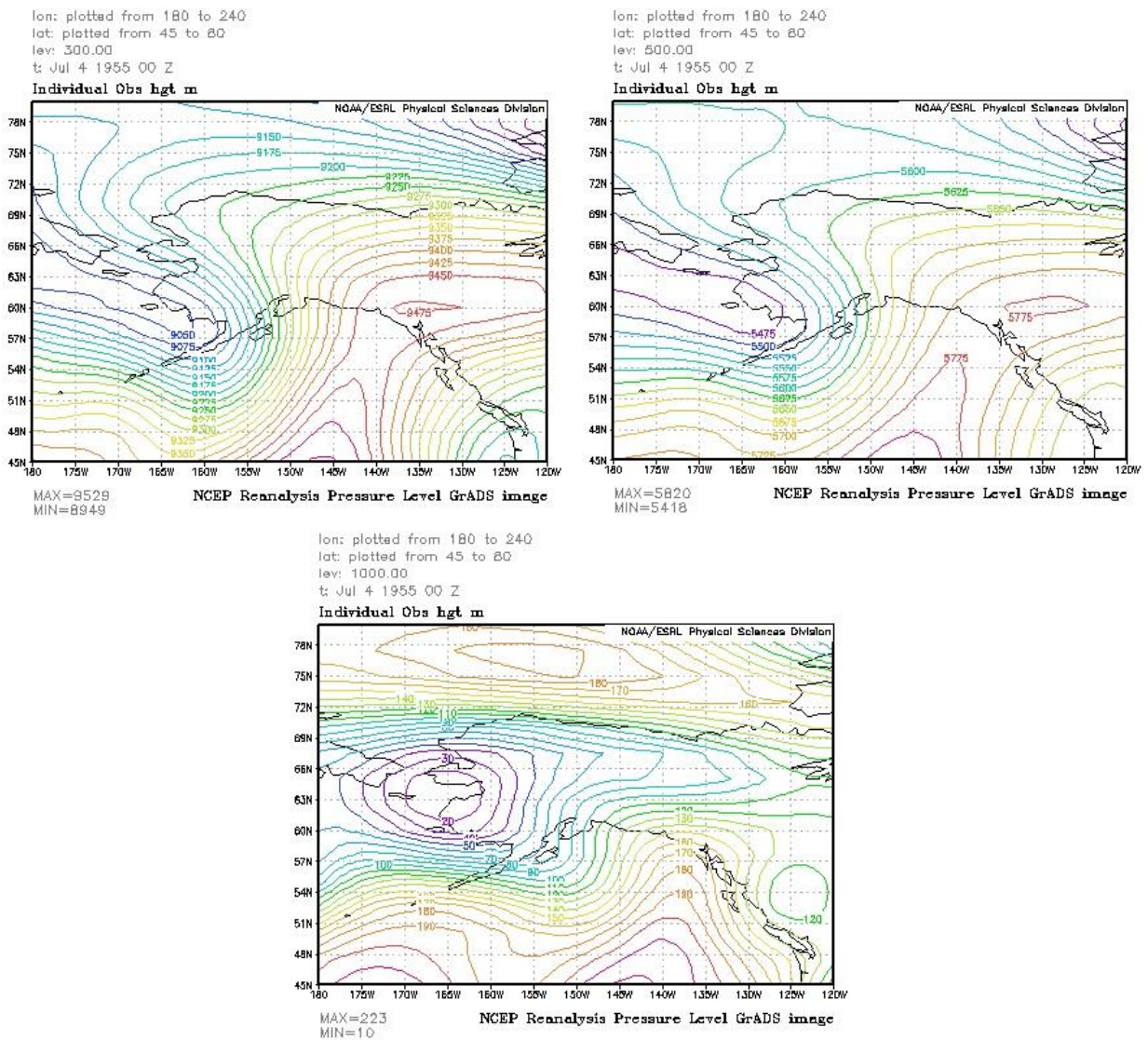
Fig. 3.33c. Geopotential heights at the 300 hPa (top left), 500 hPa (top right), and 1000 hPa map (bottom) according to the reanalysis data of the funnel cloud events for the West Coast group.
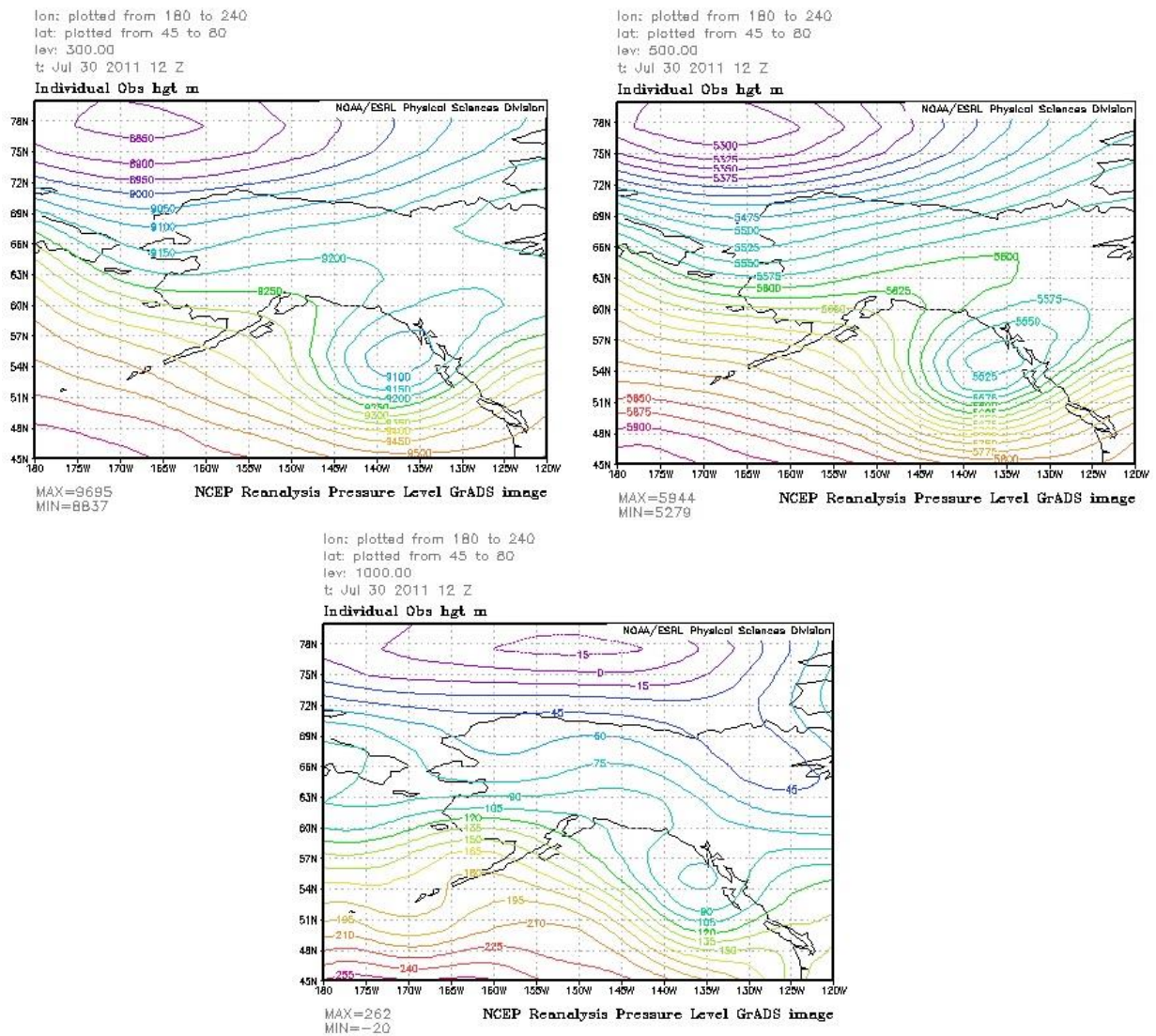
Fig. 3.33d. Geopotential heights at the 300 hPa (top left), 500 hPa (top right),), and 1000 hPa map (bottom) according to the reanalysis data of the funnel cloud events for the West Coast group.
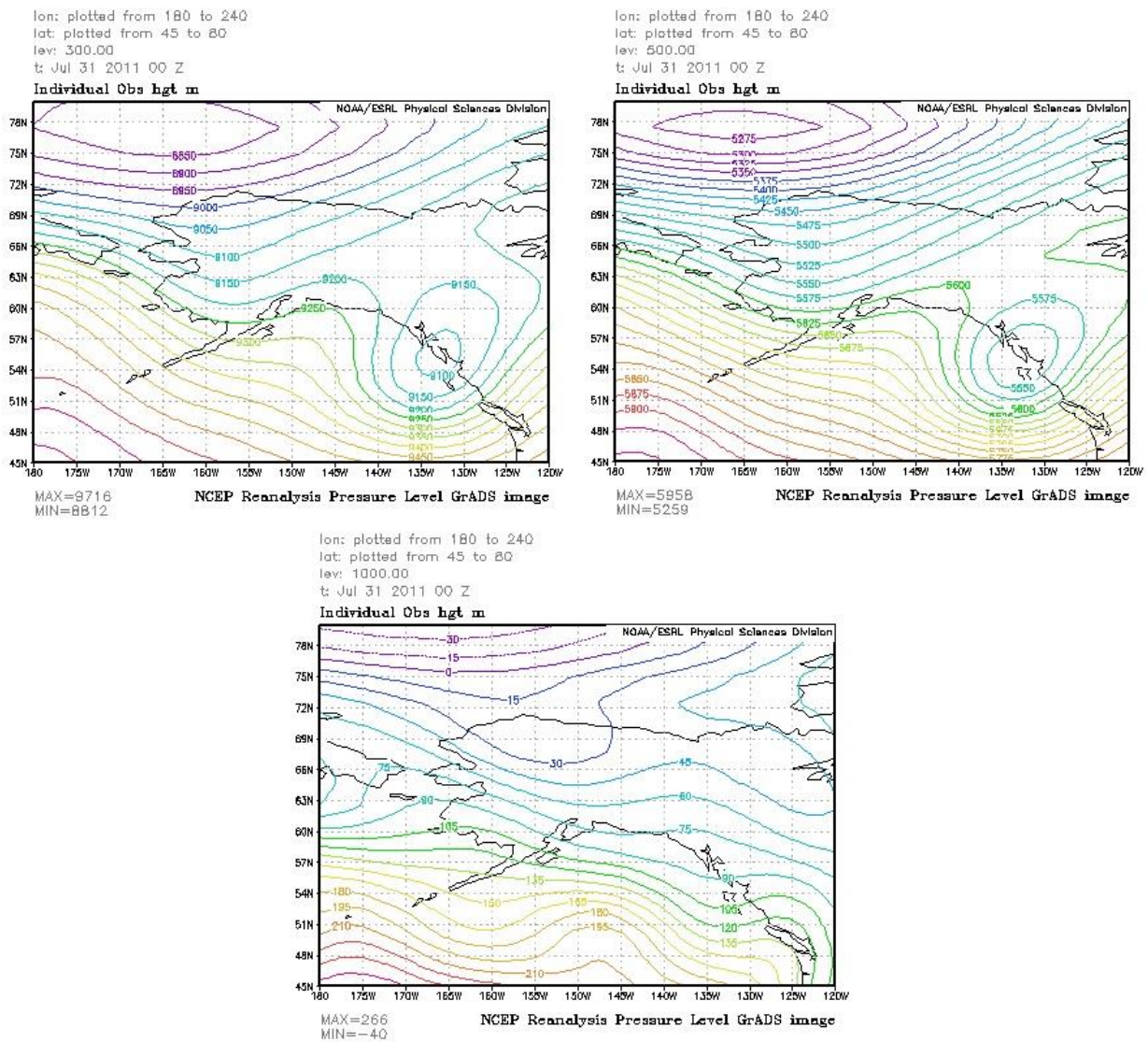
Fig. 3.33e. Geopotential heights at the 300 hPa (top left), 500 hPa (top right), and 1000 hPa map (bottom) according to the reanalysis data of the funnel cloud events for the West Coast group.
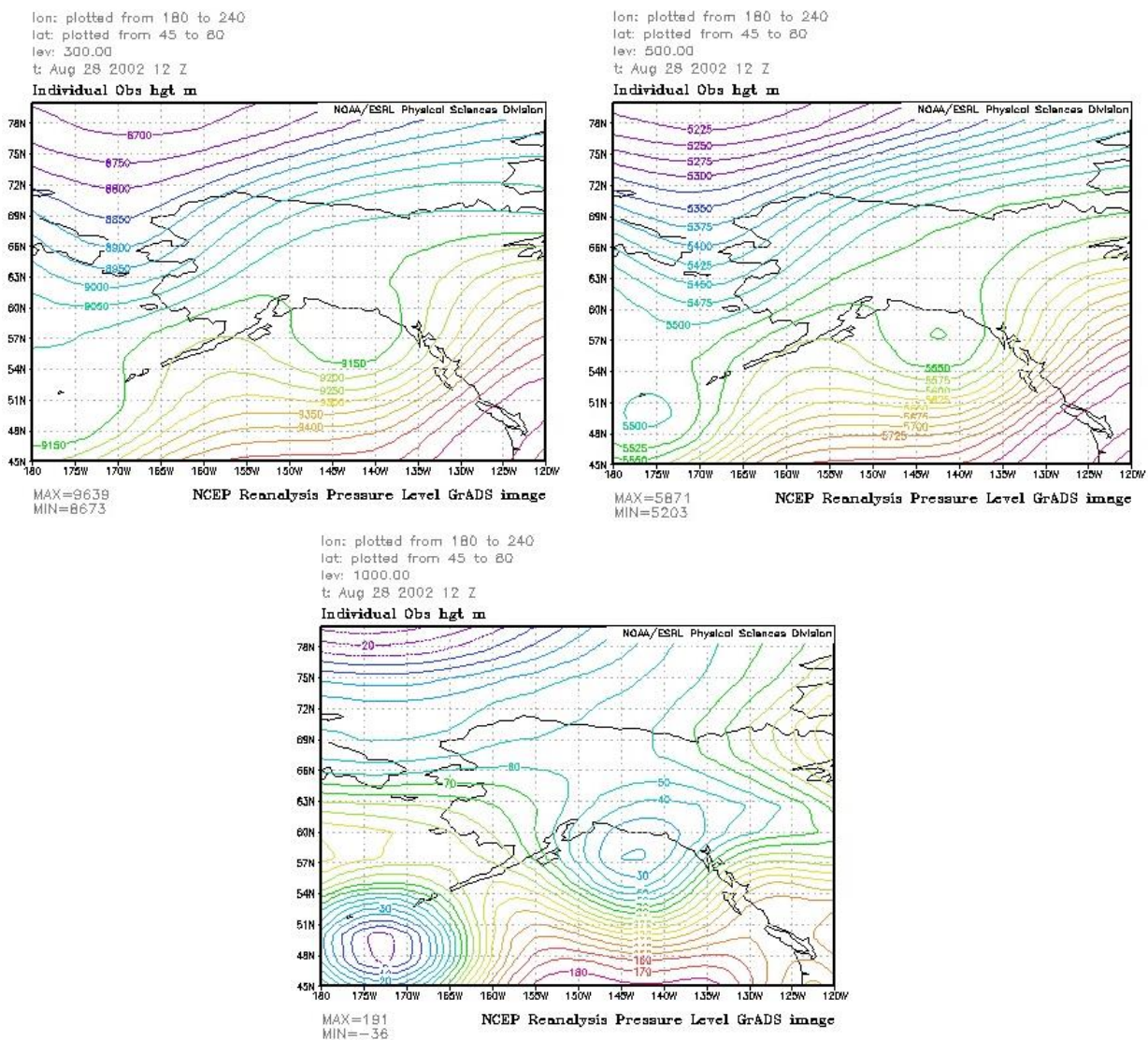
Fig. 3.33f. Geopotential heights at the 300 hPa (top left), 500 hPa (top right), and 1000 hPa map (bottom) according to the reanalysis data of the funnel cloud events for the West Coast group.
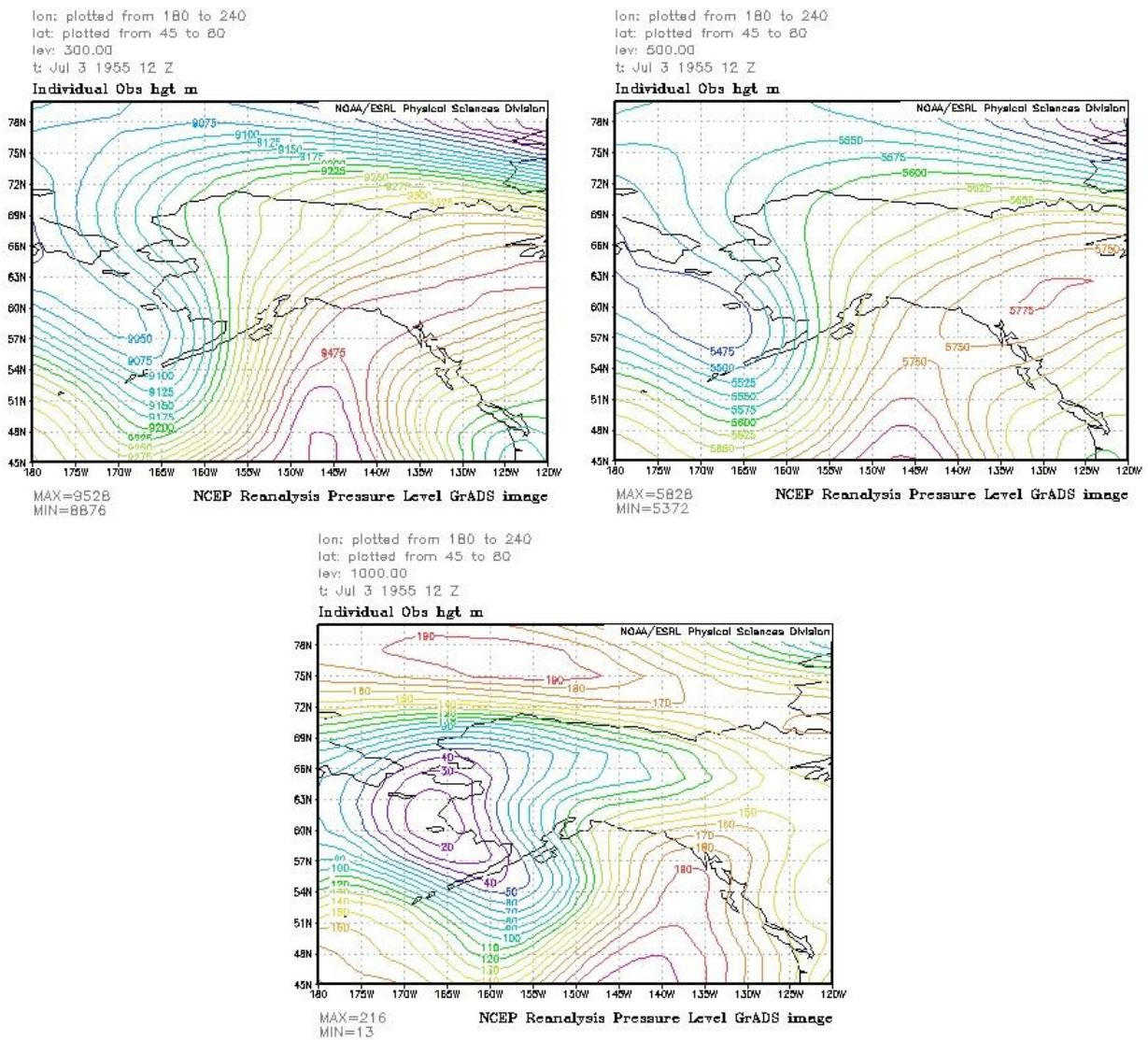
113
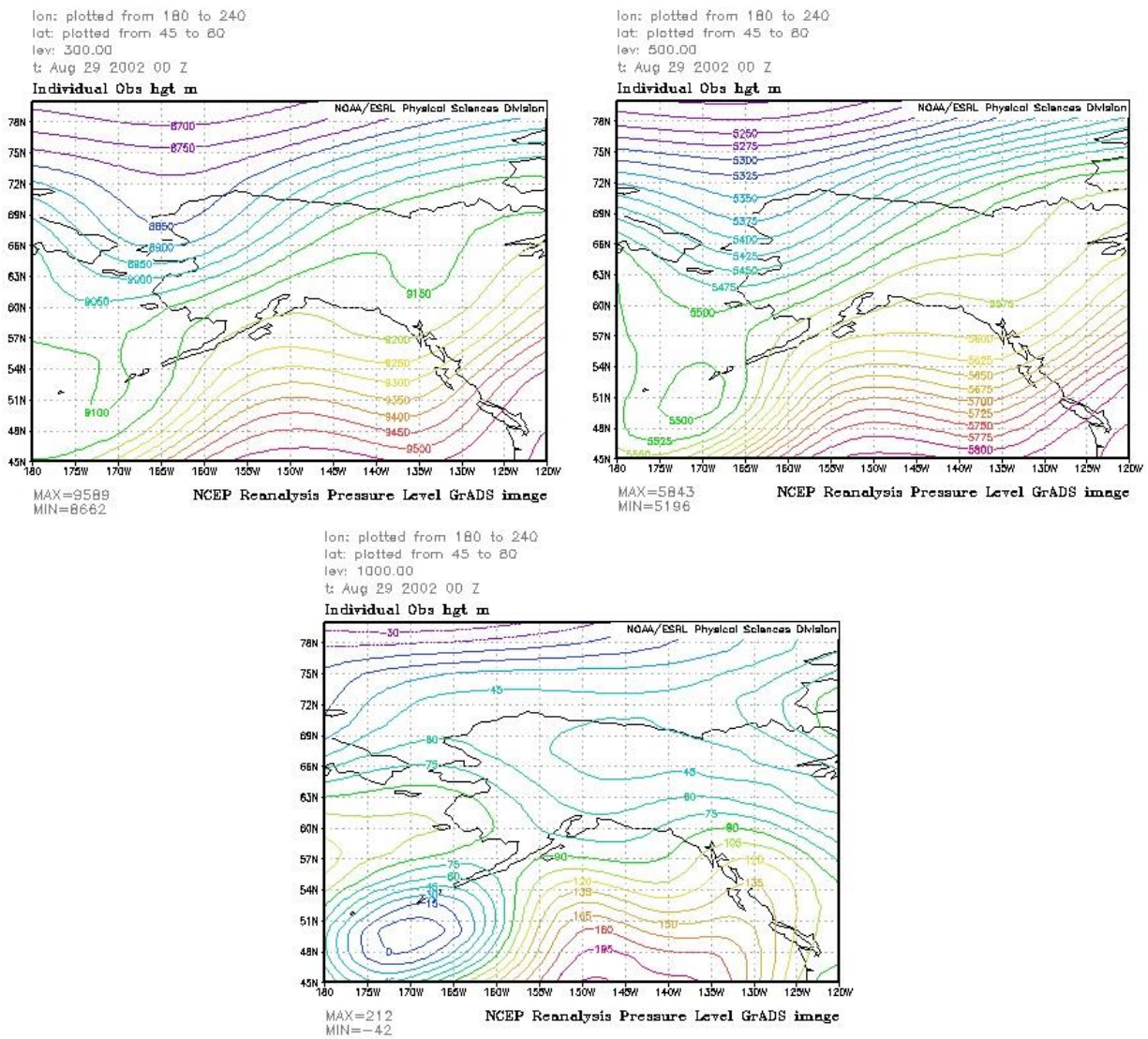
Fig. 3.33g. Geopotential heights at the 300 hPa (top left), 500 hPa (top right), and 1000 hPa map (bottom) according to the reanalysis data of the funnel cloud events for the West Coast group.

The schematic view of the potential mechanism for the Alaska West Coast is the same as for the Bethel group, which is the schematic viewed in Figure 3.27.
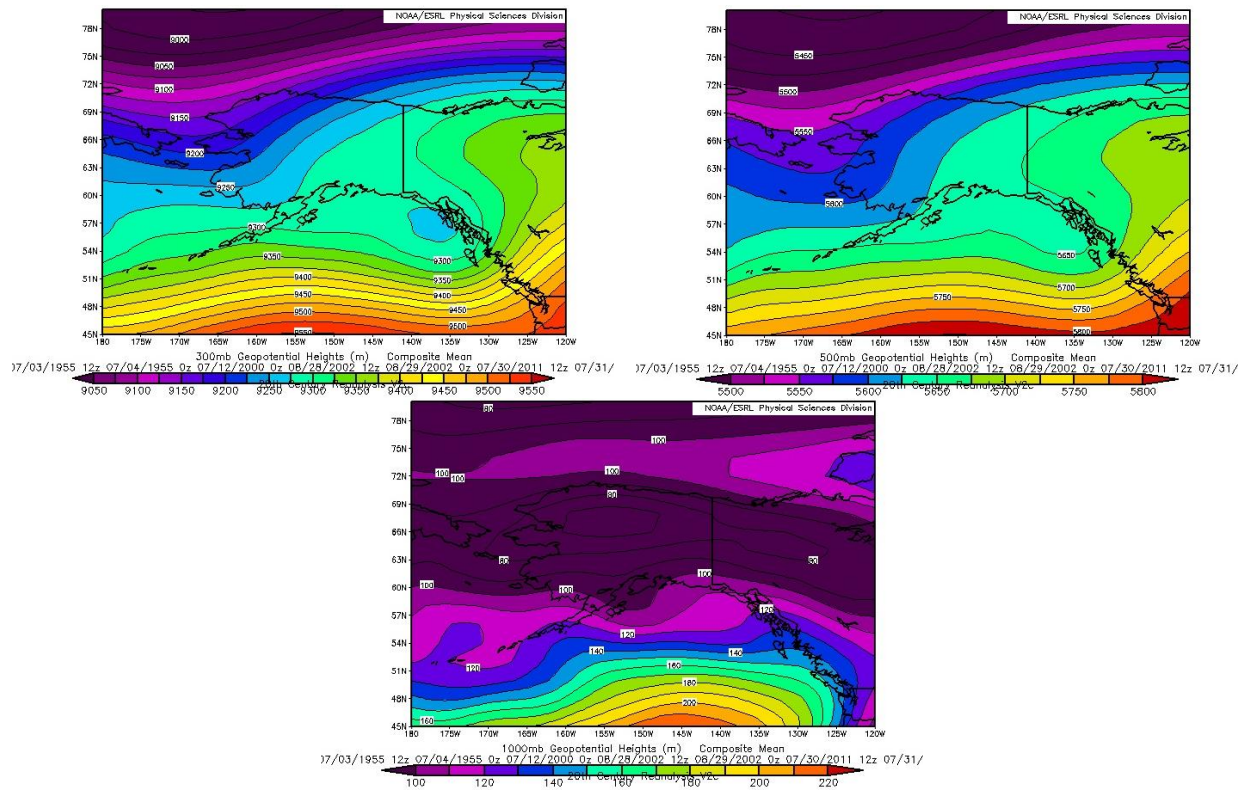
Fig. 3.34a. Composites of mean geopotential heights at the 300 hPa (top left), 500 hPa (top right), and surface map at 1000 hPa (bottom) of days with funnel cloud sightings
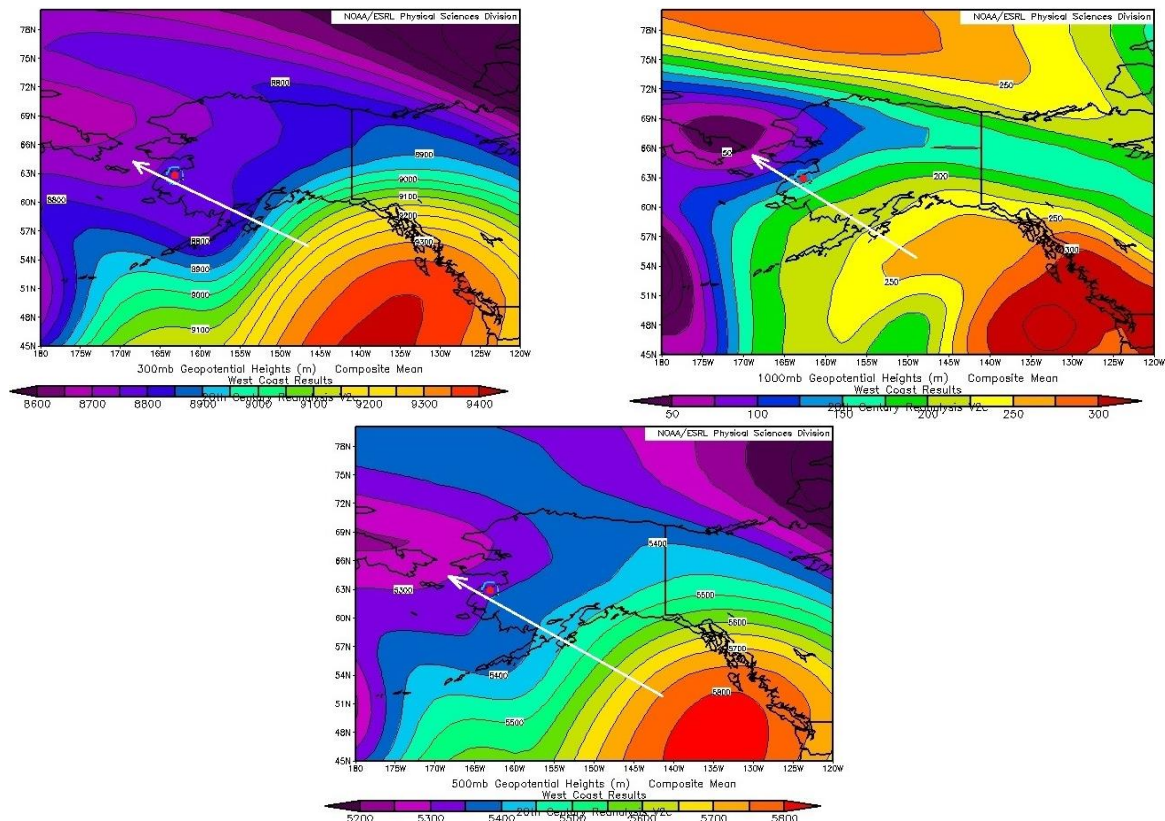
Fig. 3.34b. Composites of mean geopotential heights at the 300 hPa (top left), 500 hPa (top right), and surface map at 1000 hPa (bottom) for days identified by the search algorithm as having similar profiles to those of funnel cloud events for the observed West Coast group in Figure 3.33b.

At all levels, the composite synoptic maps of actual and potential funnel cloud events appear similar, suggesting also synoptic influence being important for funnel cloud generation.

3.7 Anchorage

There were eight reported funnel cloud events for the Anchorage group (Table 3.11). Sightings occurred between May and August. All but two of the reported events occurred in the new millennium. Two sightings occurred on the same day late in August. The other event occurred in late June. The fact that all events occurred later in the warm season may suggest that the Gulf of Alaska plays a role in funnel cloud occurrence.

Table 3.11. Dates and times of observed funnel clouds in the Anchorage area.

Year	Month	Day	Local Time	Radiosonde date, bfr	Radiosonde date,aft
1987	6	14	10:45am ADT	1987061412	1987061500
1987	8	1	9:23pm ADT	1987080200	
2002	5	12	2pm ADT		2002051300
2002	6	25	12:55pm ADT		2002062600
2002	6	25	1pm AST NOAA		2002062300
2009	5	26	6pm ADT NOAA	2009052700	
2012	7	9		2012070912	2012071000
2014	7	20	6:30am AST NOAA	2014072012	
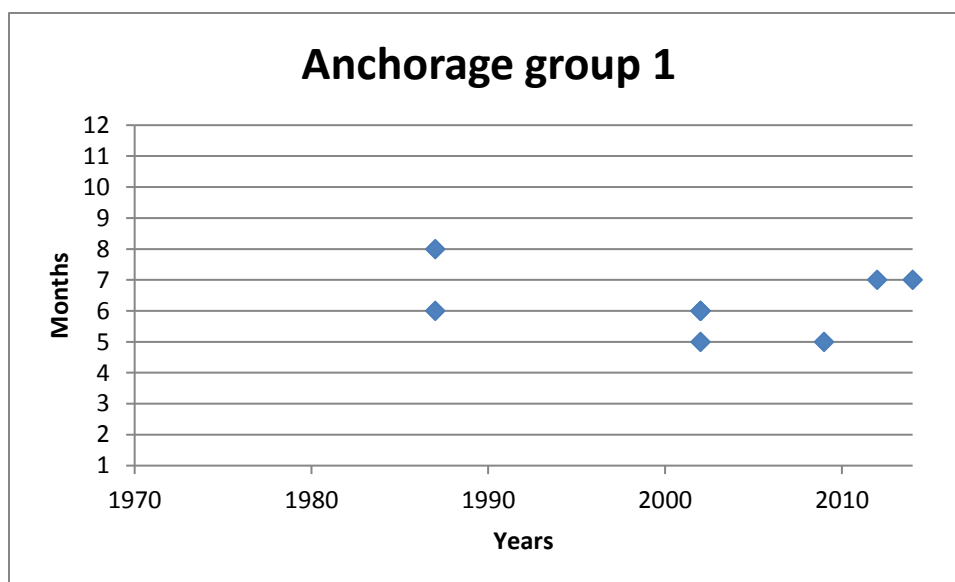
Fig. 3.35. Funnel cloud sightings by year and months for the Anchorage group.

The Skew-T diagrams for days with observed funnel cloud events suggest a layer of close to or saturated air as well as wind shear around this level in the ABL (Fig. 3.37).

a)

b)

c)

d)

e)

f)

g)

h)

119
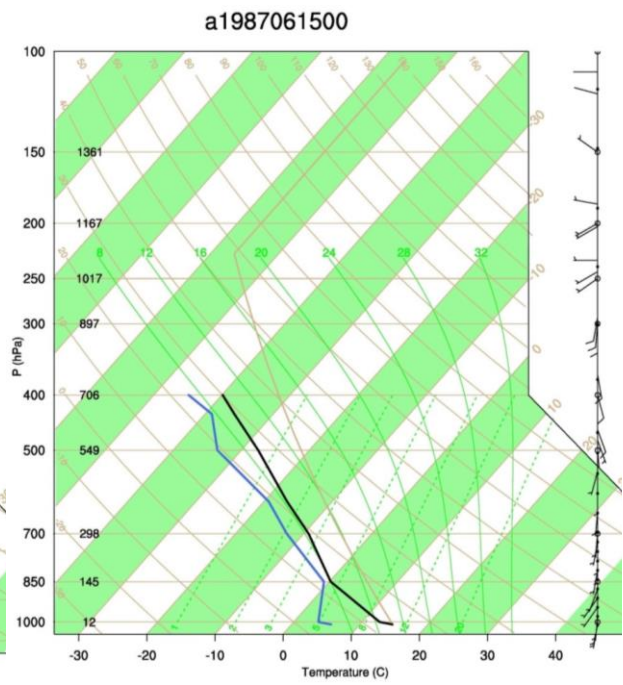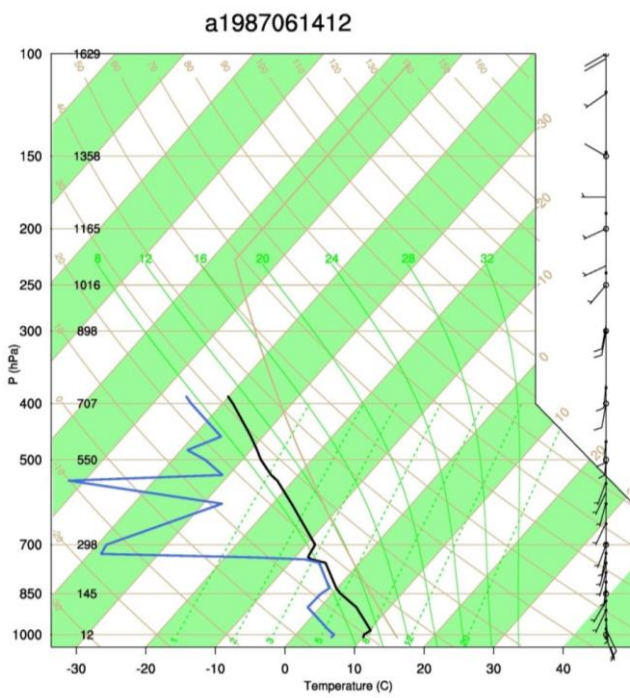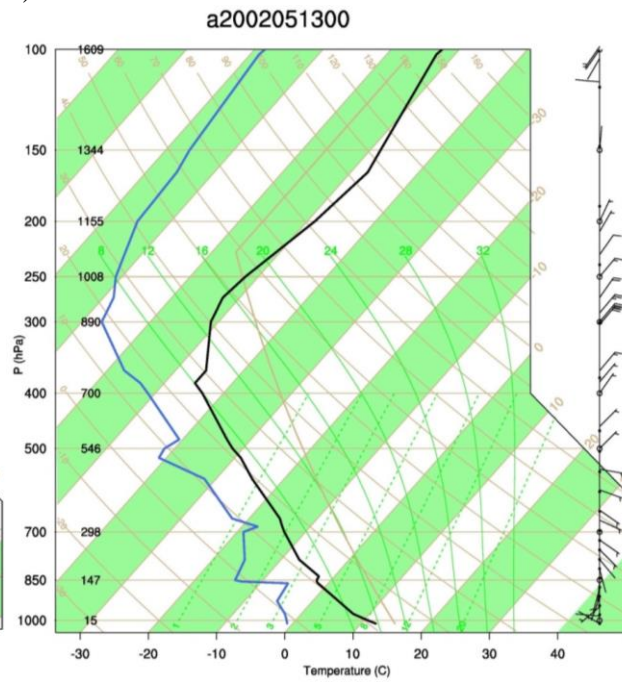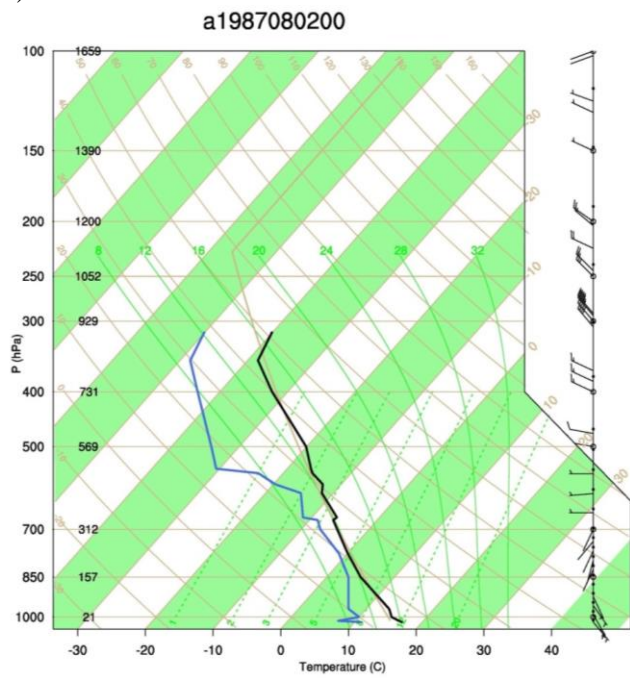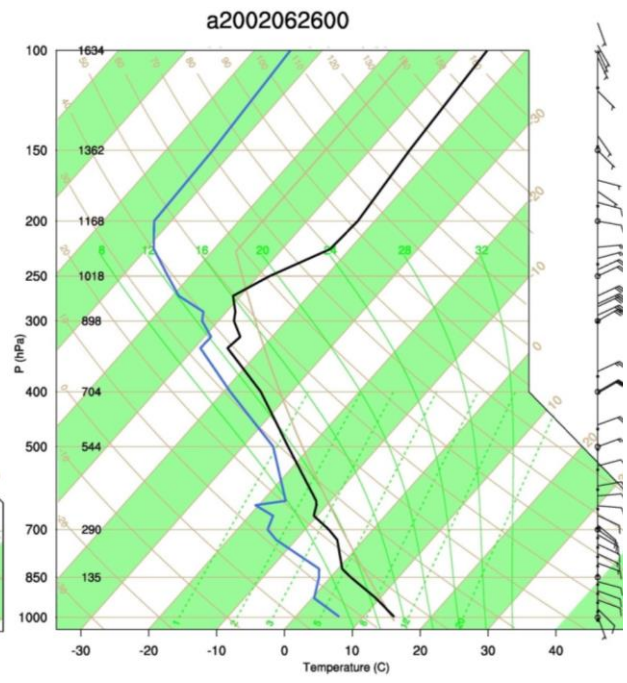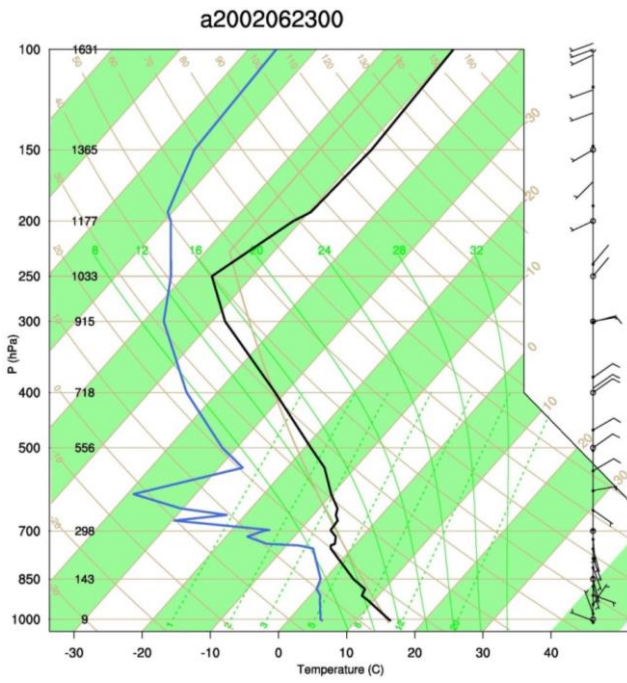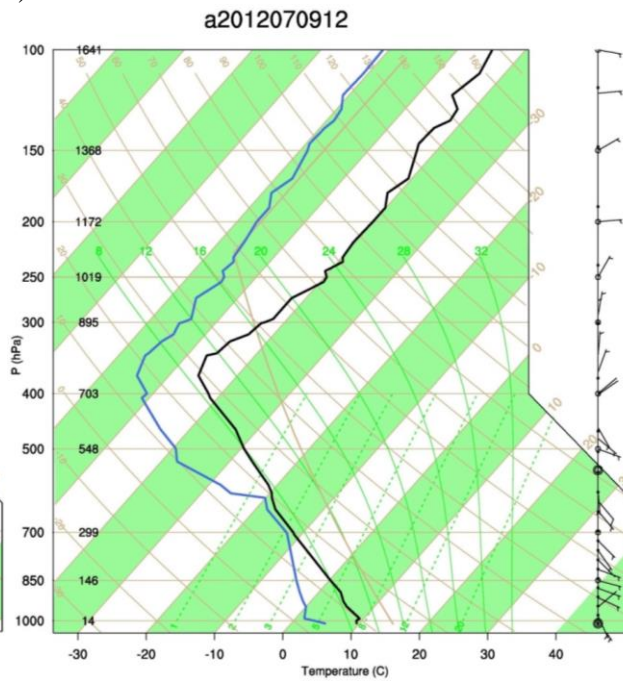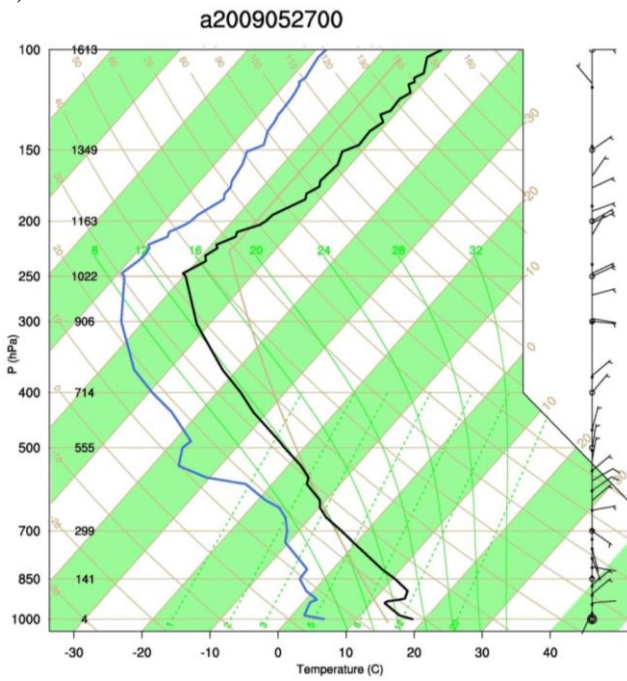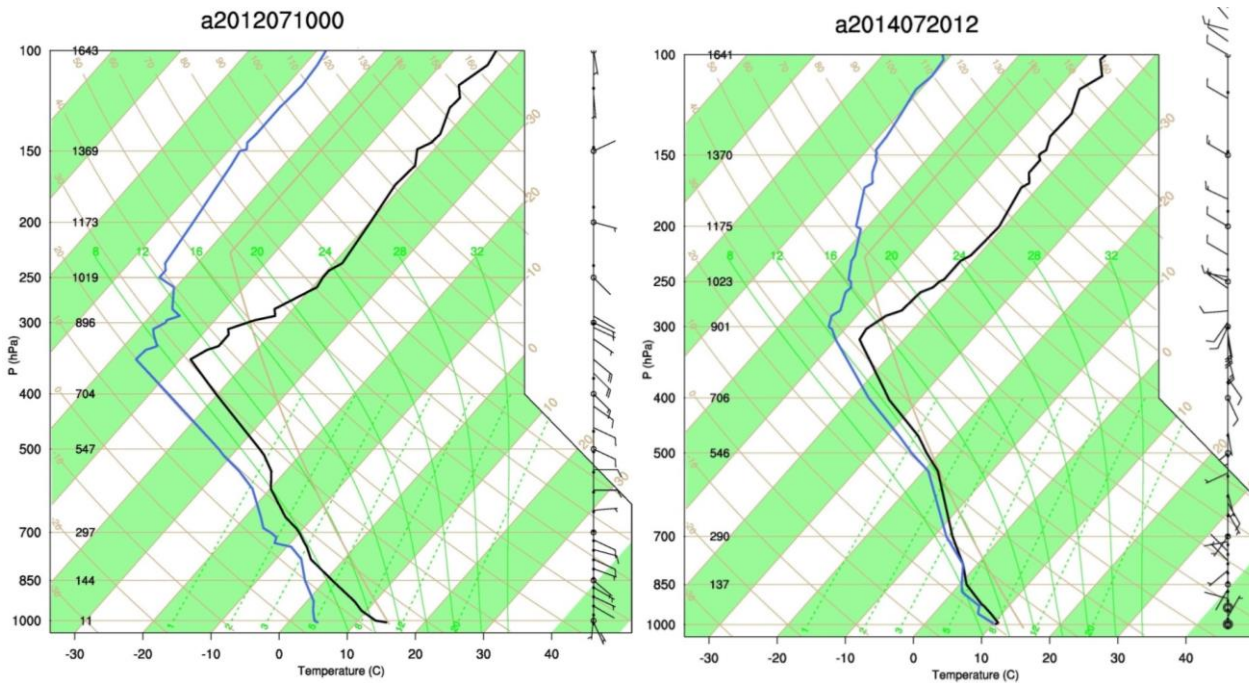
Fig. 3.36. Skew-T diagrams of the reported funnel cloud events in the Anchorage group with temperature (black line) and dew point temperature (blue line), wind speed and direction (barbs). The solid tan line is the US standard atmosphere. a) June 14, 1987 at 1200z, b) June 15, 1987 at 00z, c) June 2, 1987 at 00z, d) May 13, 2002 at 00z, e) June 23, 2002 at 00z, f) June 26, 2002 at 00z, g) May 27, 2009 at 00z, h) July 9, 2012 at 1200z, i) July 10, 2012 at 00z, and j) July 20, 2014 at 1200z.

Table 3.12. Ranges of air temperature (T), dew point temperature (T_d), and wind speed (v) as obtained for the various pressure ranges (p) for Anchorage based on the profiles of observed funnel clouds. See Chapter 2 for reasoning of the choice of the pressure ranges.

| P (hPa)	Range (hPa)	T (C°)	T_d(C°)	v (m/s)
1000	1015-962.5	-.8 – 9.4	9.5 15.3	2 – 6.4
925	962.6-887.5	-9 – 4.2	-.2 – 13.3	0 – 18.4
850	887.5-812.5	-12 – 6.4	-2.4 – 5.4	0 – 11
700	737.5-650	-36 - -1.2	-13 - -4	1.6 – 8
500	550-450	-42 – 25.7	-32 - -19.6	1.8 – 15.2
400	450-350	-50 - -38.3	-44 - -31.4	5 – 20.2
300	350-250	-77.5 - -42	-53.5 - -45.3	26.9 – 31.7
200	250-150	-78 - -63	-53.8 - -42	2.2 – 23.4
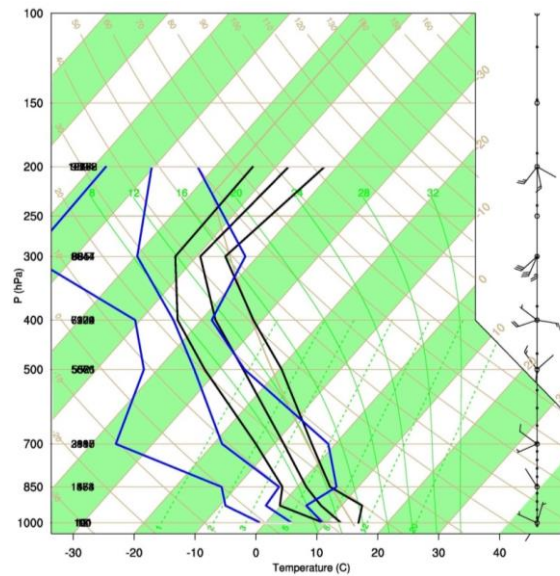
Fig. 3.37. Resultant ranges for potential funnel cloud profiles with CAPE greater than 500 J as obtained based on observed funnel cloud sightings for the Anchorage group. Note that here the Skew-T limits of minimum (left), mean (middle), and maximum (right) temperature (black lines), dew point temperature (blue lines), wind speed and wind direction (barbs). Further, minimum, mean, and maximum wind direction over the pressure ranges listed in Table 3.18 are shown.
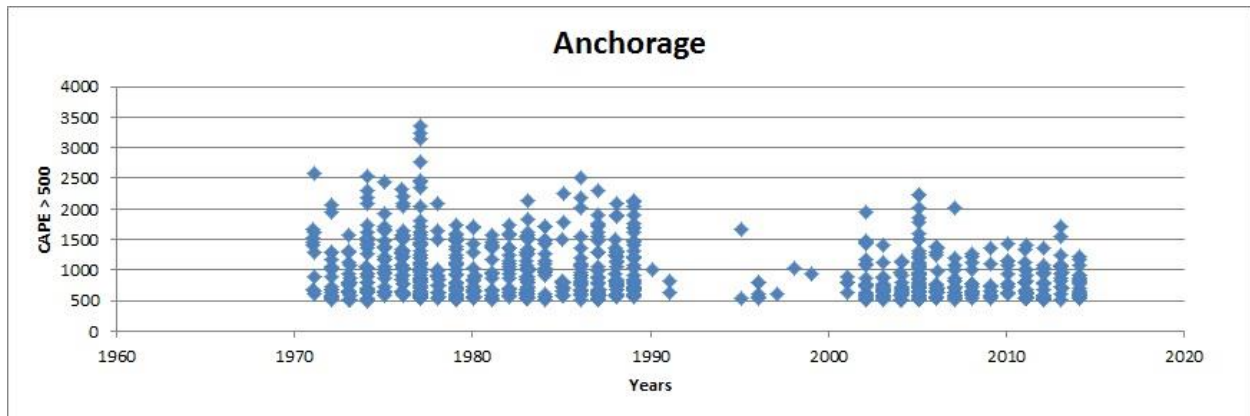
Fig. 3.38. Frequency (number of diamonds), and CAPE (in J), of events with radiosonde profiles similar to those during the observed funnel cloud events in the Anchorage group as identified by the search algorithm and testing for CAPE. Note that between 1992 and 1994 there were problems with the dew point temperature measurements and are excluded: a result of stringent 1st requirement as depicted in (Fig. 2.6).

121

3.7.1 Anchorage group 1

Fig. 3.39a. Geopotential heights at the 300 hPa (top left), 500 hPa (top right),), and 1000 hPa map (bottom) according to the reanalysis data of the funnel cloud events for the Anchorage group-1. May 13 2002 00z

Fig. 3.39b. Geopotential heights at the 300 hPa (top left), 500 hPa (top right), and 1000 hPa map (bottom) according to the reanalysis data of the funnel cloud events for the Anchorage group-1. May 27 2009 00z

Fig. 3.39c. Geopotential heights at the 300 hPa (top left), 500 hPa (top right), and 1000 hPa map (bottom) according to the reanalysis data of the funnel cloud events for the Anchorage group-1. June 14 1987 12z

Fig. 3.39d. Geopotential heights at the 300 hPa (top left), 500 hPa (top right), and 1000 hPa map (bottom) according to the reanalysis data of the funnel cloud events for the Anchorage group-1. June 15 1987 00z

Fig. 3.39e. Geopotential heights at the 300 hPa (top left), 500 hPa (top right), and 1000 hPa map (bottom) according to the reanalysis data of the funnel cloud events for the Anchorage group-1. June 23 2002 00z

Fig. 3.39f. Geopotential heights at the 300 hPa (top left), 500 hPa (top right),), and 1000 hPa map (bottom) according to the reanalysis data of the funnel cloud events for the Anchorage group-1. June 26 2002 00z

127

Fig. 3.39g. Geopotential heights at the 300 hPa (top left), 500 hPa (top right), and 1000 hPa map (bottom) according to the reanalysis data of the funnel cloud events for the Anchorage group-1. July 9 2012 12z

Fig. 3.39h. Geopotential heights at the 300 hPa (top left), 500 hPa (top right), and 1000 hPa map (bottom) according to the reanalysis data of the funnel cloud events for the Anchorage group-1. July 10 2012 12z

Fig. 3.39i. Geopotential heights at the 300 hPa (top left), 500 hPa (top right), and 1000 hPa map (bottom) according to the reanalysis data of the funnel cloud events for the Anchorage group-1. July 20 2014 12z
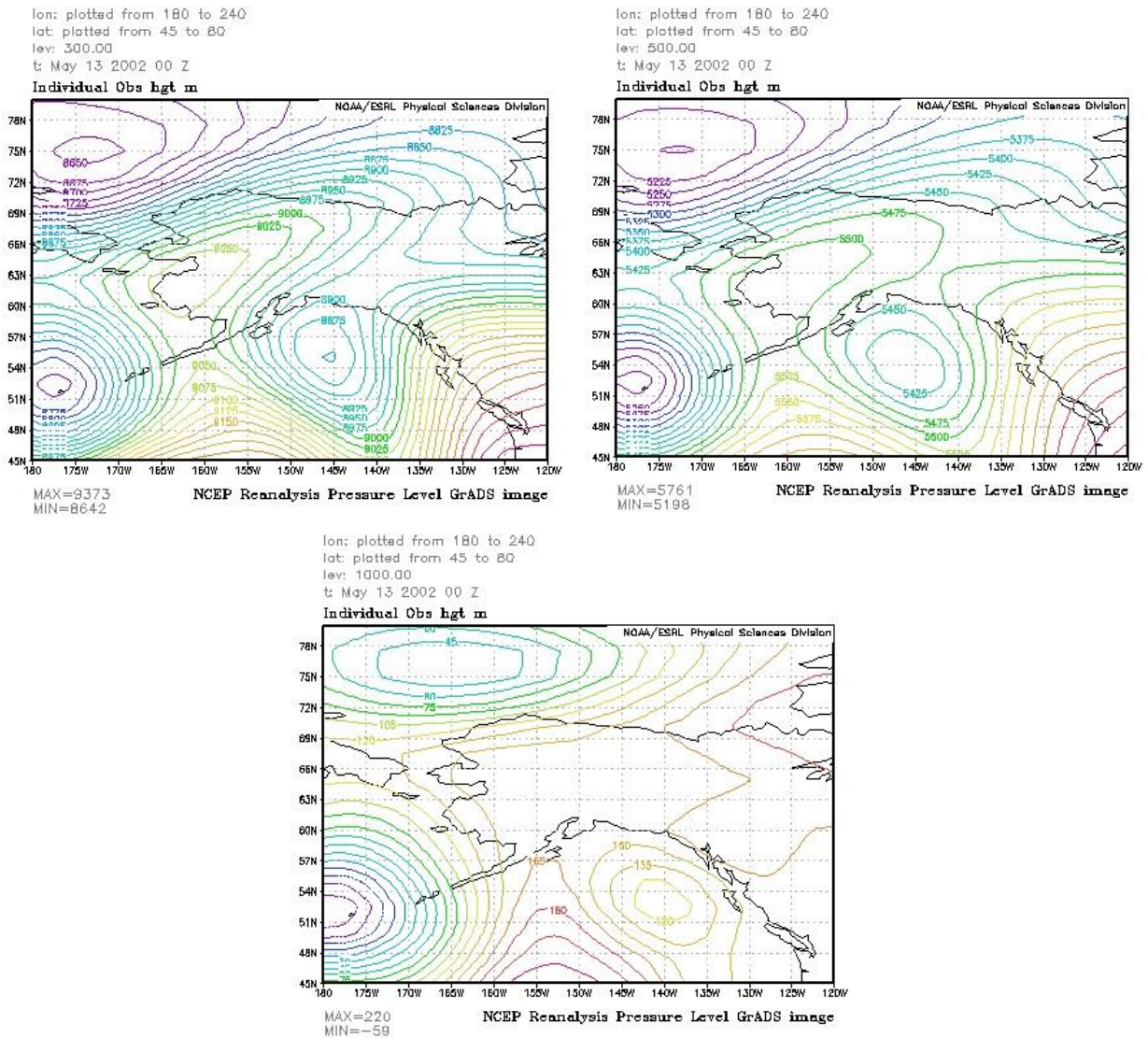
Fig. 3.39j. Geopotential heights at the 300 hPa (top left), 500 hPa (top right), and 1000 hPa map (bottom) according to the reanalysis data of the funnel cloud events for the Anchorage group-1. August 2 1987 00z

Fig. 3.40a. Composites of mean geopotential heights at the 300 hPa (top left), 500 hPa (top right), and surface map at 1000 hPa (bottom) of days with funnel cloud sightings Anchorage group-1. Anchorage group-1 represents the events in locations closest to the Cook Inlet (Fig. 2.3).

Fig. 3.40b. Composites of mean geopotential heights at the 300 hPa (top left), 500 hPa (top right), and surface map at 1000 hPa (bottom) of days identified by the search algorithm as having similar profiles like those of funnel cloud events for the observed Anchorage group-1, which represents the events in locations closest to the Cook Inlet (Fig. 2.3).

The composite surface synoptic maps of both real (Fig. 3.42a) and potential funnel cloud situations (Fig. 3.42b), both show a low in the Gulf of Alaska. The flow over the Anchorage region is common to both the real and potential situation. At the 300 hPa and 500 hPa pressure levels, the composites for real and potential events are different for Anchorage group-1. However, at these levels, the synoptic forcing is weak suggesting topographic influence.
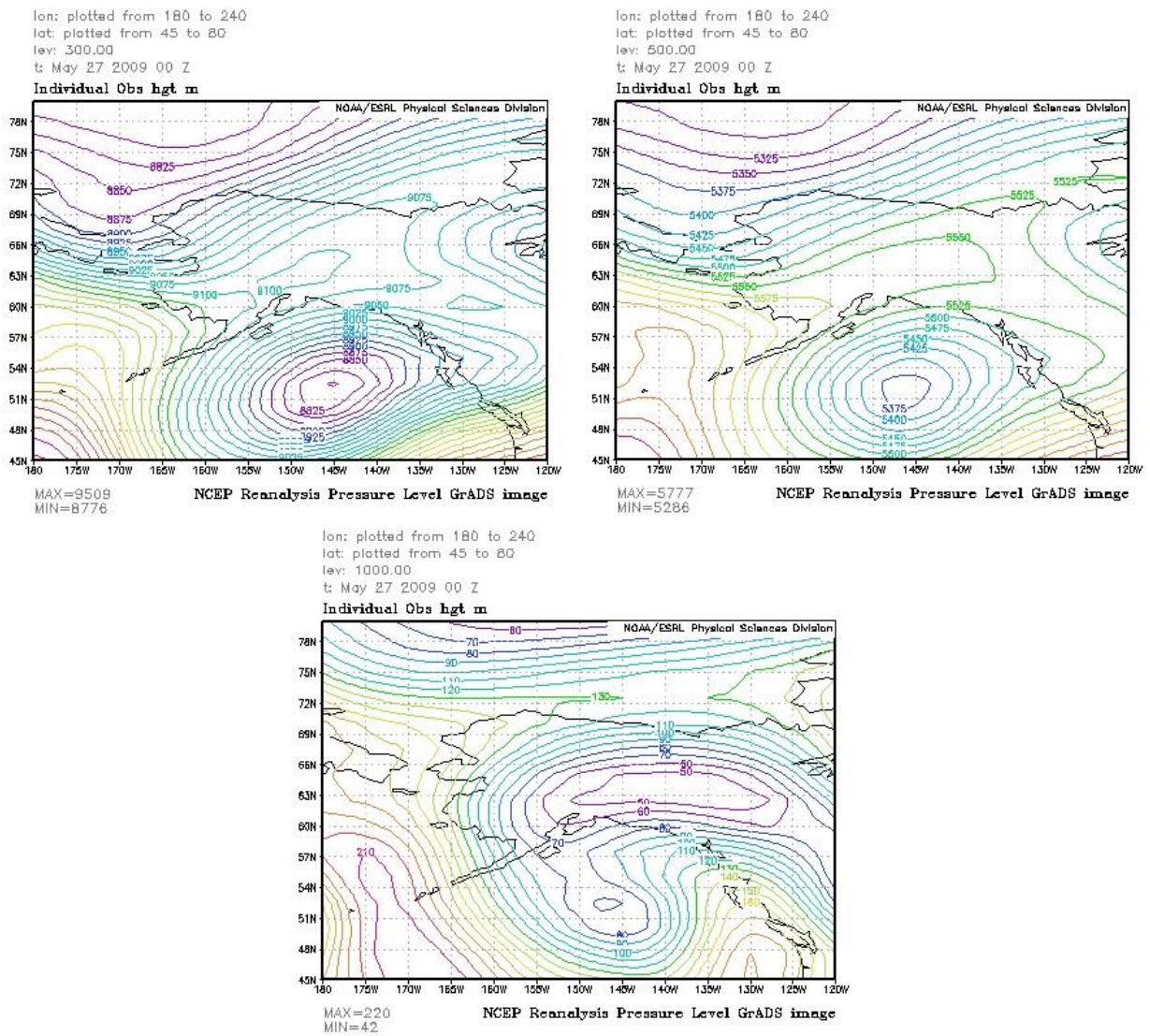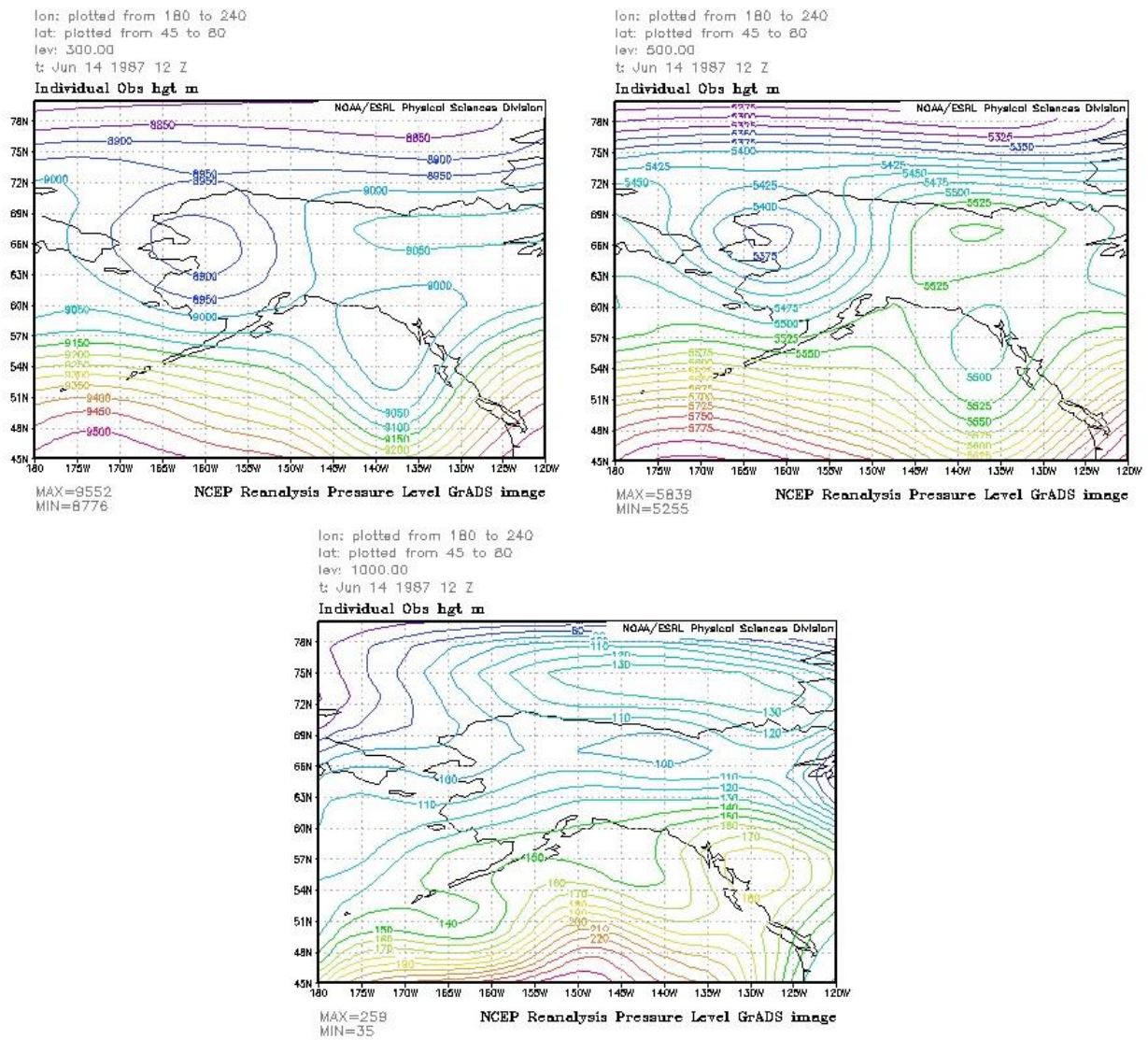
3.7.2 Anchorage group 2

Fig.3.41a. Geopotential heights at the 300 hPa (top left), 500 hPa (top right), and 1000 hPa map (bottom) according to the reanalysis data of the funnel cloud events for the Anchorage group-2. May 23 1989 00z
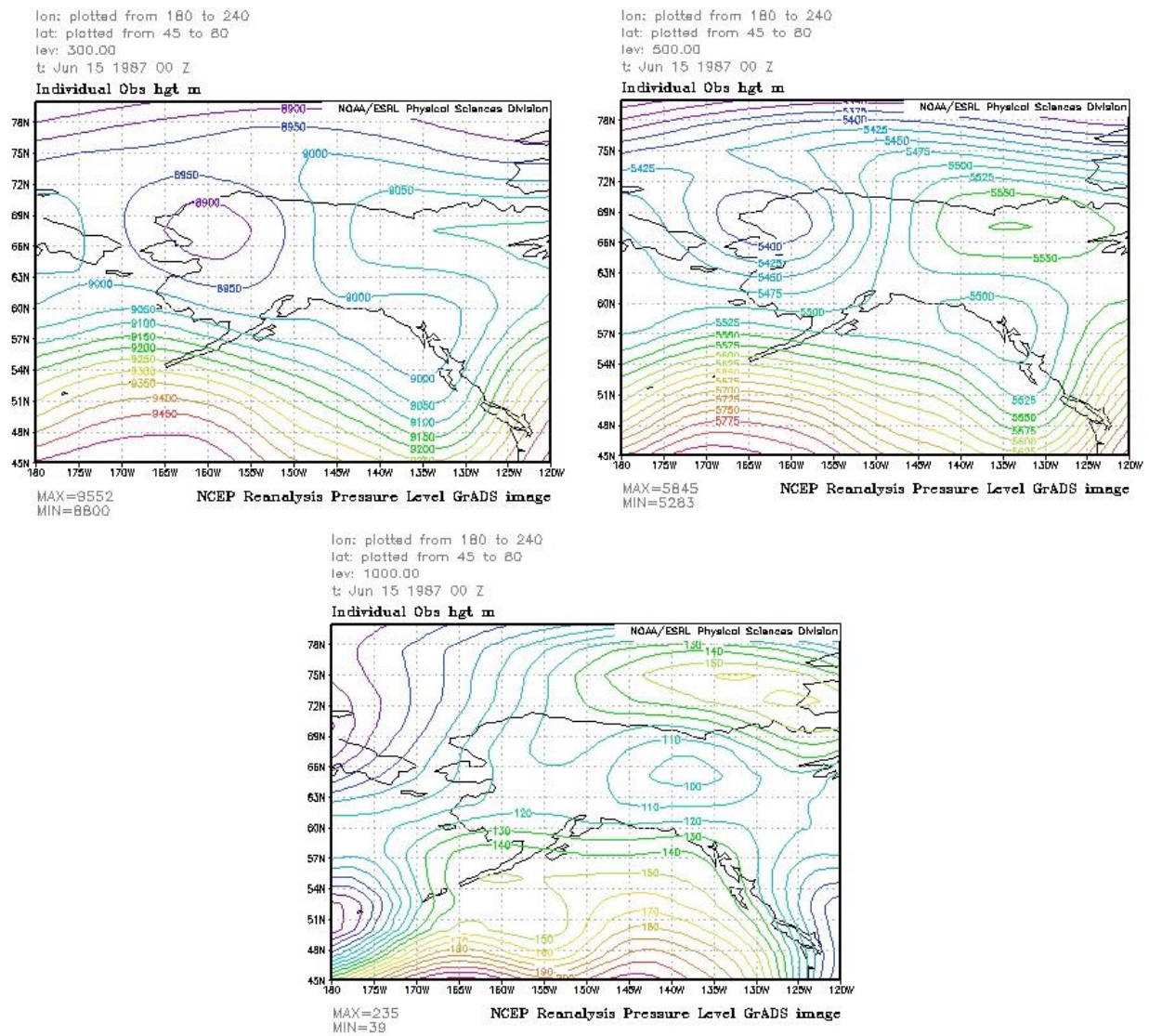
Fig.3.41b. Geopotential heights at the 300 hPa (top left), 500 hPa (top right), and 1000 hPa map (bottom) according to the reanalysis data of the funnel cloud events for the Anchorage group-2. July 4 1969 12z
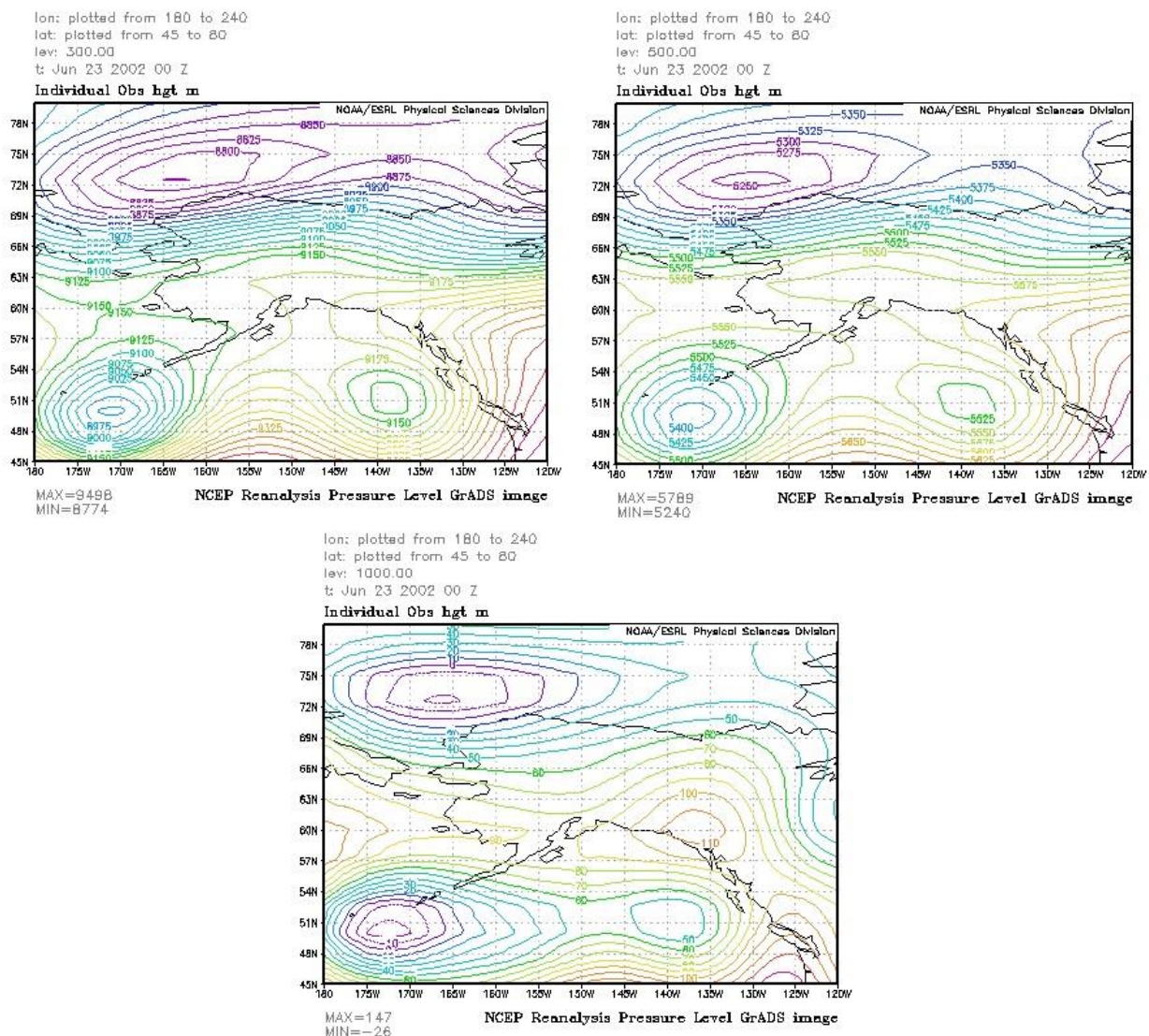
Fig.3.41c. Geopotential heights at the 300 hPa (top left), 500 hPa (top right), and 1000 hPa map (bottom) according to the reanalysis data of the funnel cloud events for the Anchorage group-2. July 5 1969 12z

Fig.3.41d. Geopotential heights at the 300 hPa (top left), 500 hPa (top right), and 1000 hPa map (bottom) according to the reanalysis data of the funnel cloud events for the Anchorage group-2. July 22 1978 12z
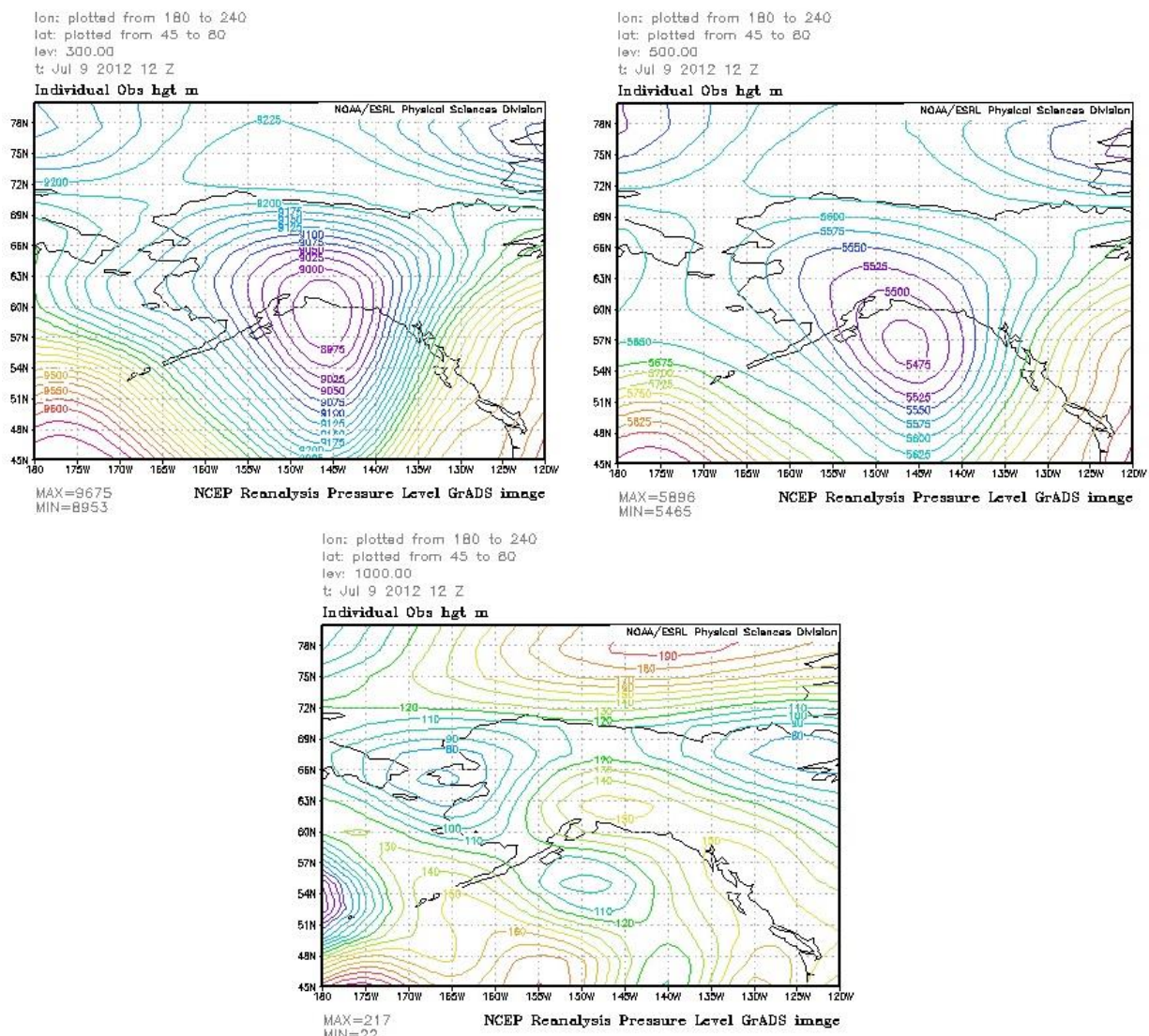
Fig.3.41e. Geopotential heights at the 300 hPa (top left), 500 hPa (top right), and 1000 hPa map (bottom) according to the reanalysis data of the funnel cloud events for the Anchorage group-2. July 23 1978 00z
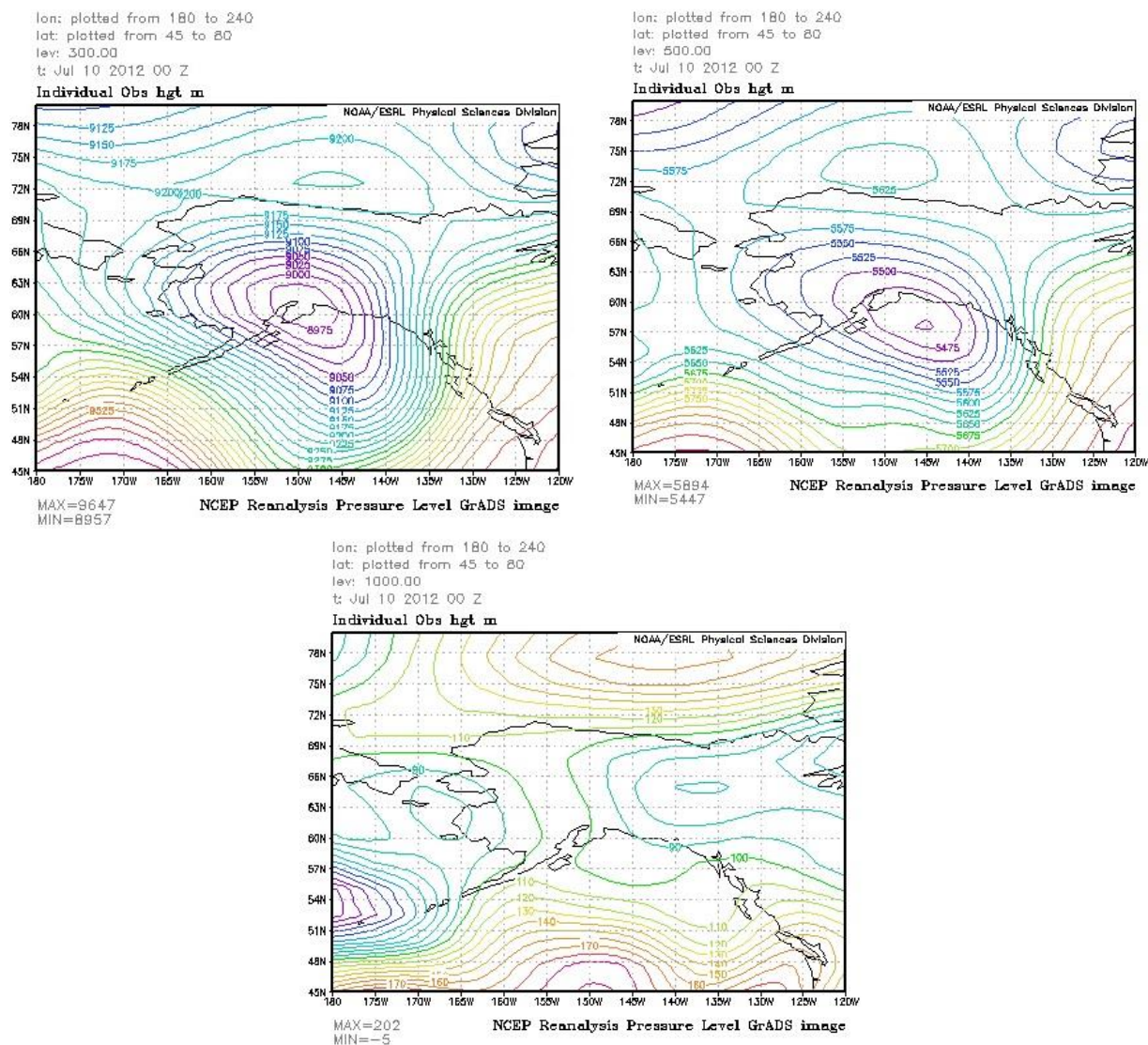
Fig.3.41f. Geopotential heights at the 300 hPa (top left), 500 hPa (top right), and 1000 hPa map (bottom) according to the reanalysis data of the funnel cloud events for the Anchorage group-2. July 28 1978 00z
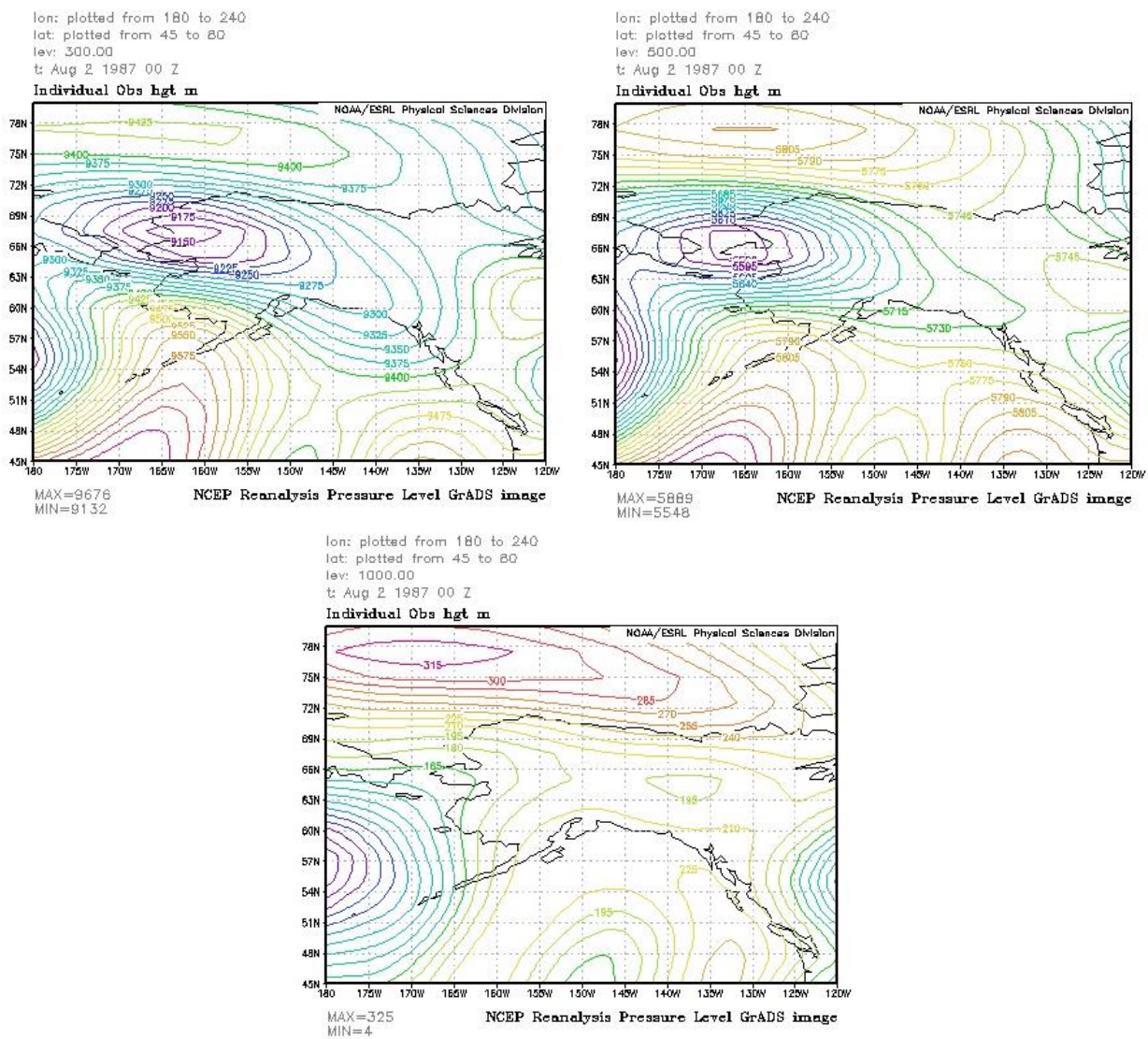
Fig.3.41g. Geopotential heights at the 300 hPa (top left), 500 hPa (top right), and 1000 hPa map (bottom) according to the reanalysis data of the funnel cloud events for the Anchorage group-2. August 5 2005 00z

Fig. 3.42a. Composites of mean geopotential heights at the 300 hPa (top left), 500 hPa (top right), and surface map at 1000 hPa (bottom) of days with funnel cloud sightings for the observed Anchorage group-2 are, which is located a little further inland than group-1 (cf. Fig. 2.3).
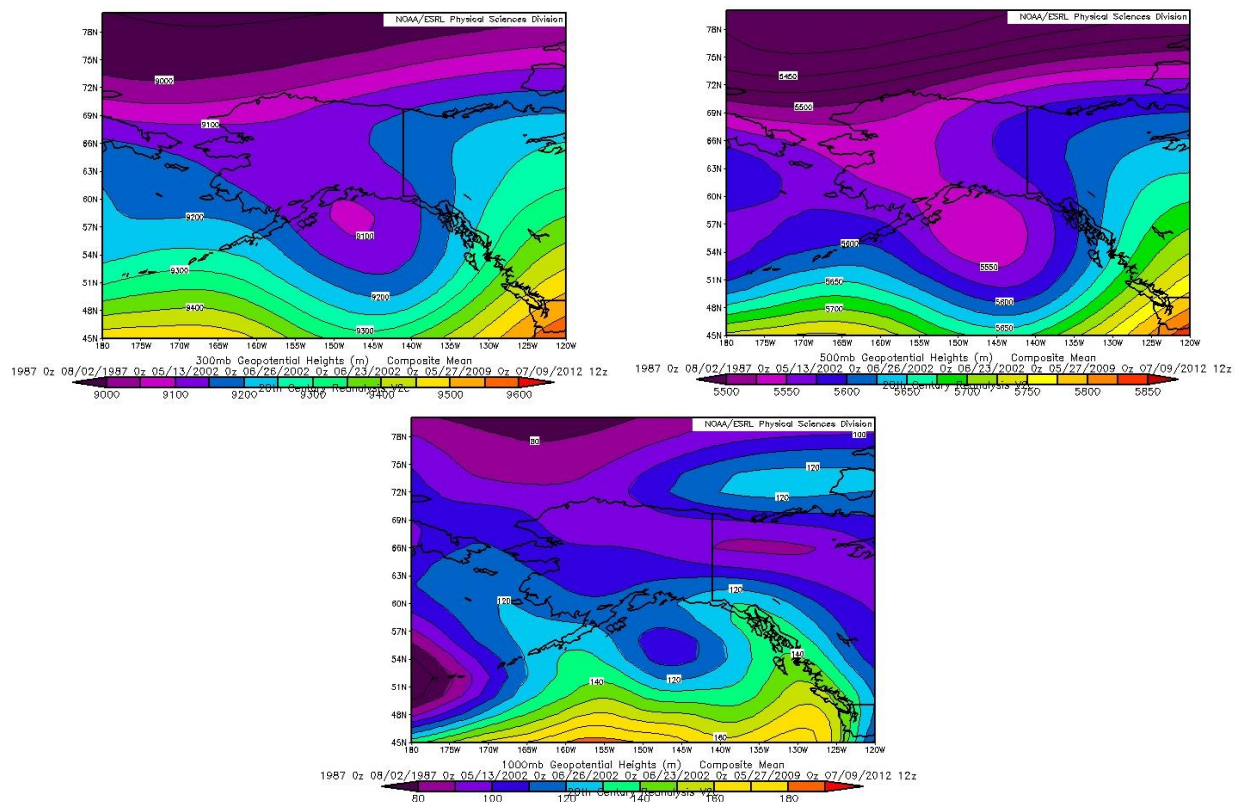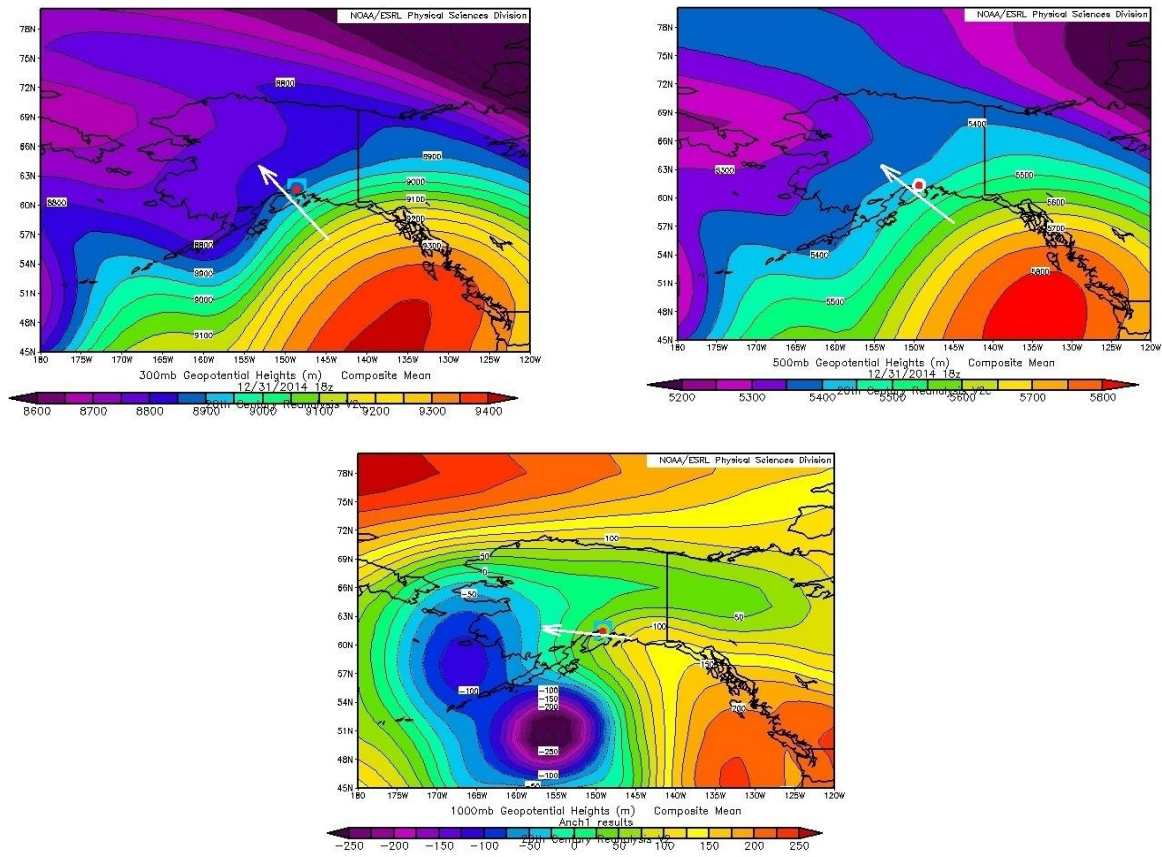
Fig. 3.42b. Composites of mean geopotential heights at the 300 hPa (top left), 500 hPa (top right), and surface map at 1000 hPa (bottom) of days identified by the search algorithm as having similar profiles like those of funnel cloud events for the observed Anchorage group-2, which is located a little further inland than group-1 (cf. Fig. 2.3)..

At all levels, the composite synoptic maps of real and potential funnel cloud situations appear similar for all of the Anchorage area suggesting that the algorithm captured situations of similar synoptic characteristics. This finding suggests that the synoptic scale forcing is an important condition for the funnel cloud formation in the Anchorage group-2.

3.7.3 Anchorage group 3
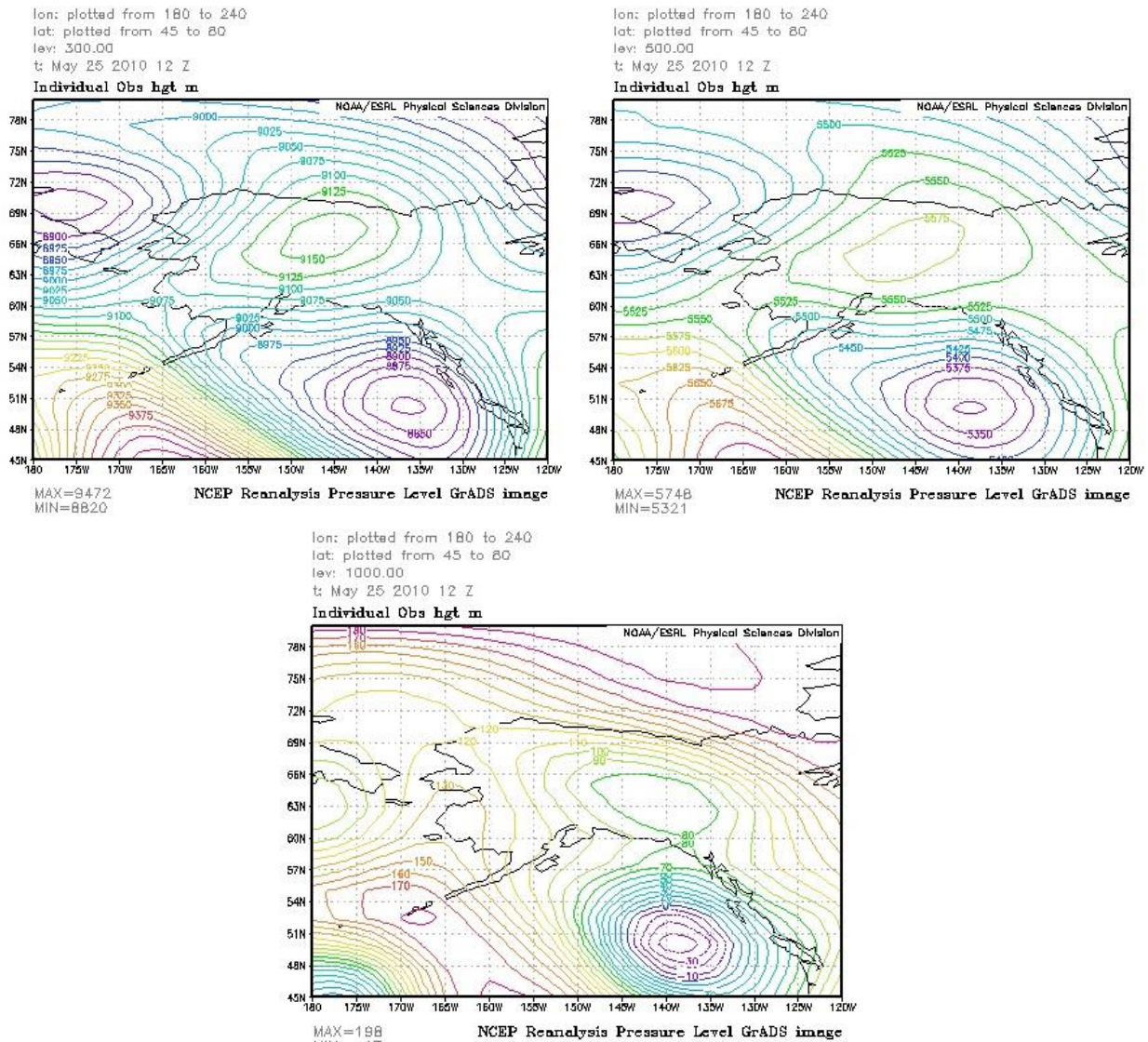
Fig. 3.43a. Geopotential heights at the 300 hPa (top left), 500 hPa (top right), and 1000 hPa map (bottom) according to the reanalysis data of the funnel cloud events for the Anchorage group-3. May 25 2010 12z.

Fig. 3.43b. Geopotential heights at the 300 hPa (top left), 500 hPa (top right), and 1000 hPa map (bottom) according to the reanalysis data of the funnel cloud events for the Anchorage group 3. May 26 2010 00z.
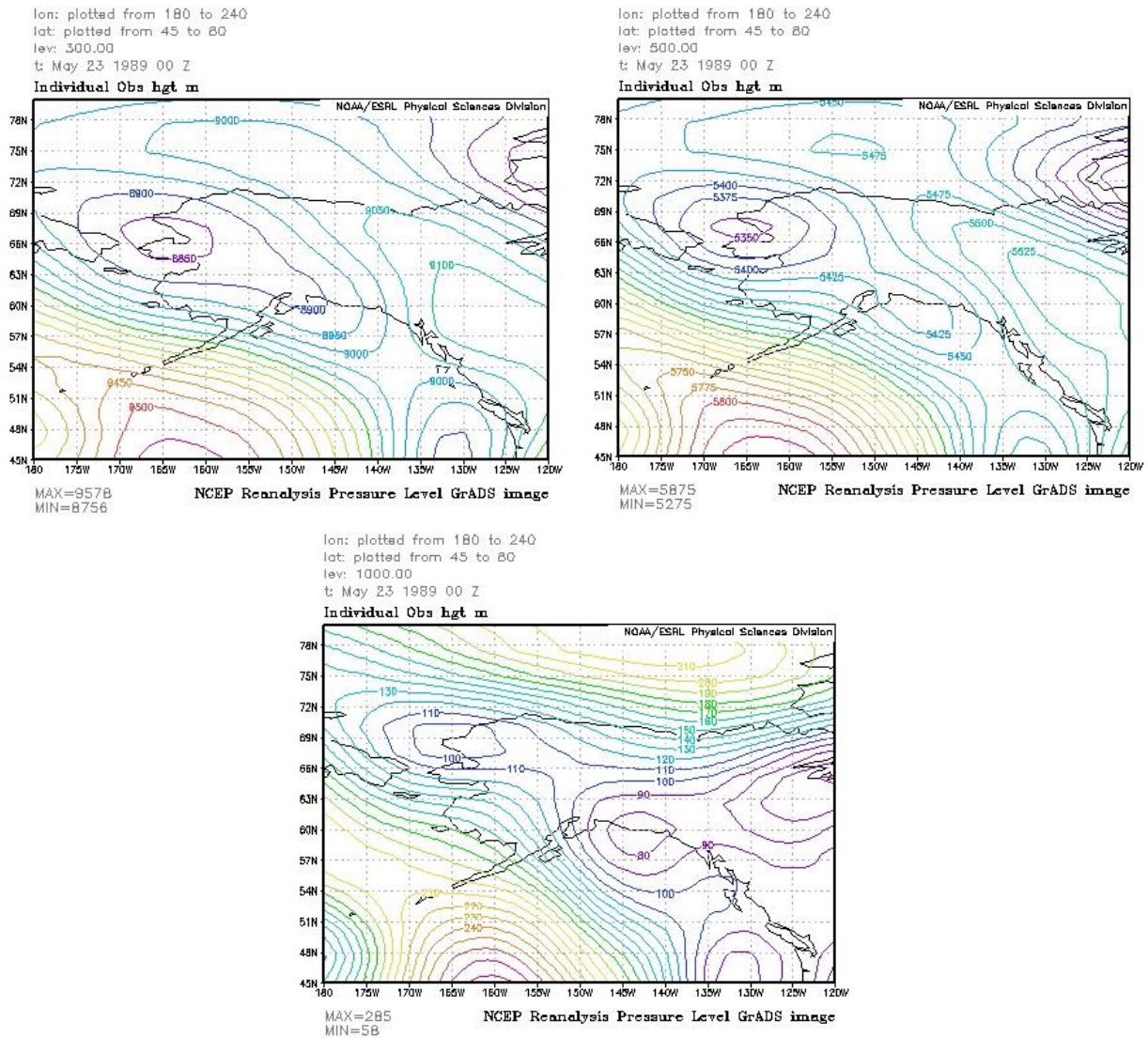
144
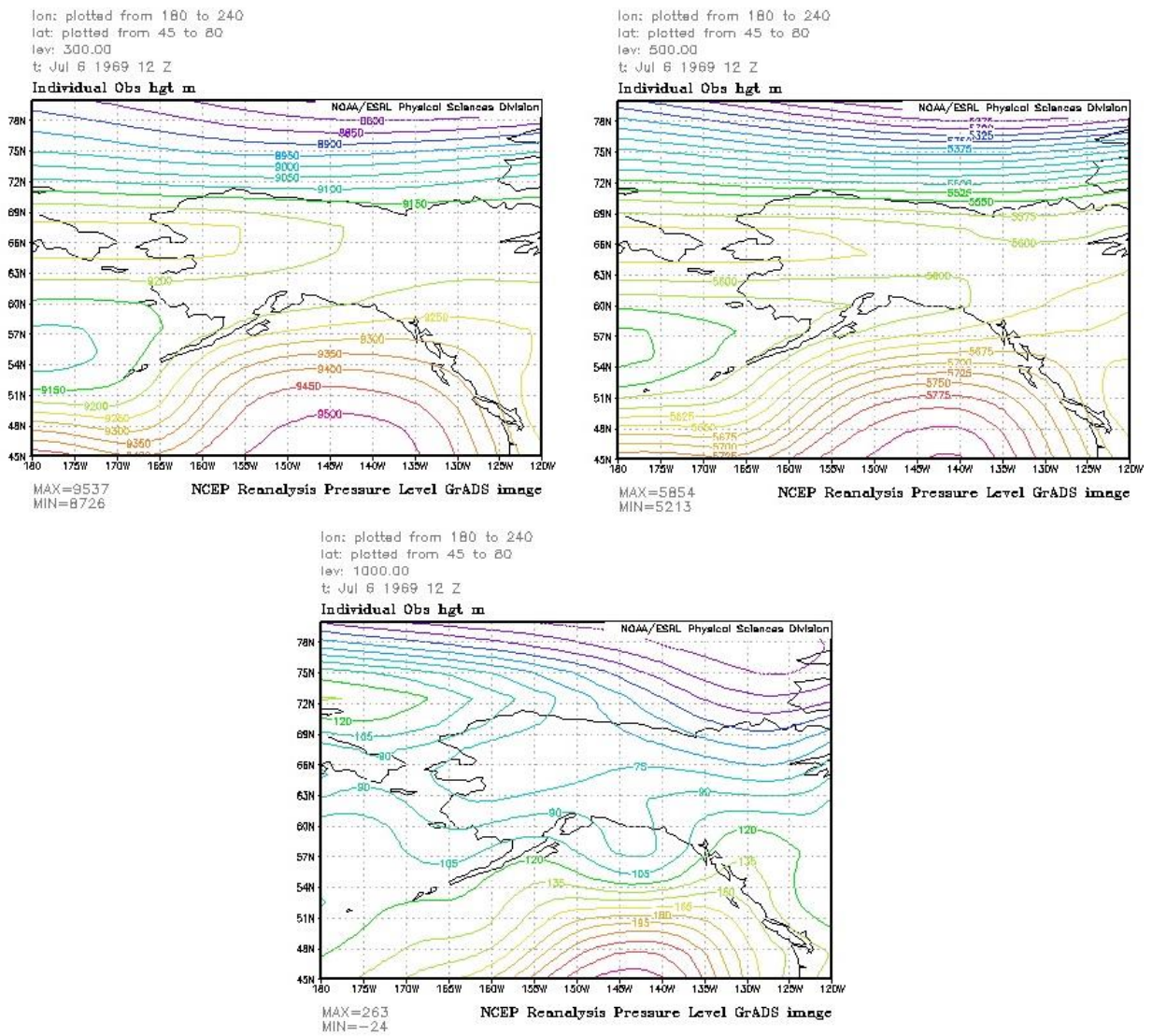
Fig. 3.43c. Geopotential heights at the 300 hPa (top left), 500 hPa (top right), and 1000 hPa map (bottom) according to the reanalysis data of the funnel cloud events for the Anchorage group 3. July 6 1969 12z.
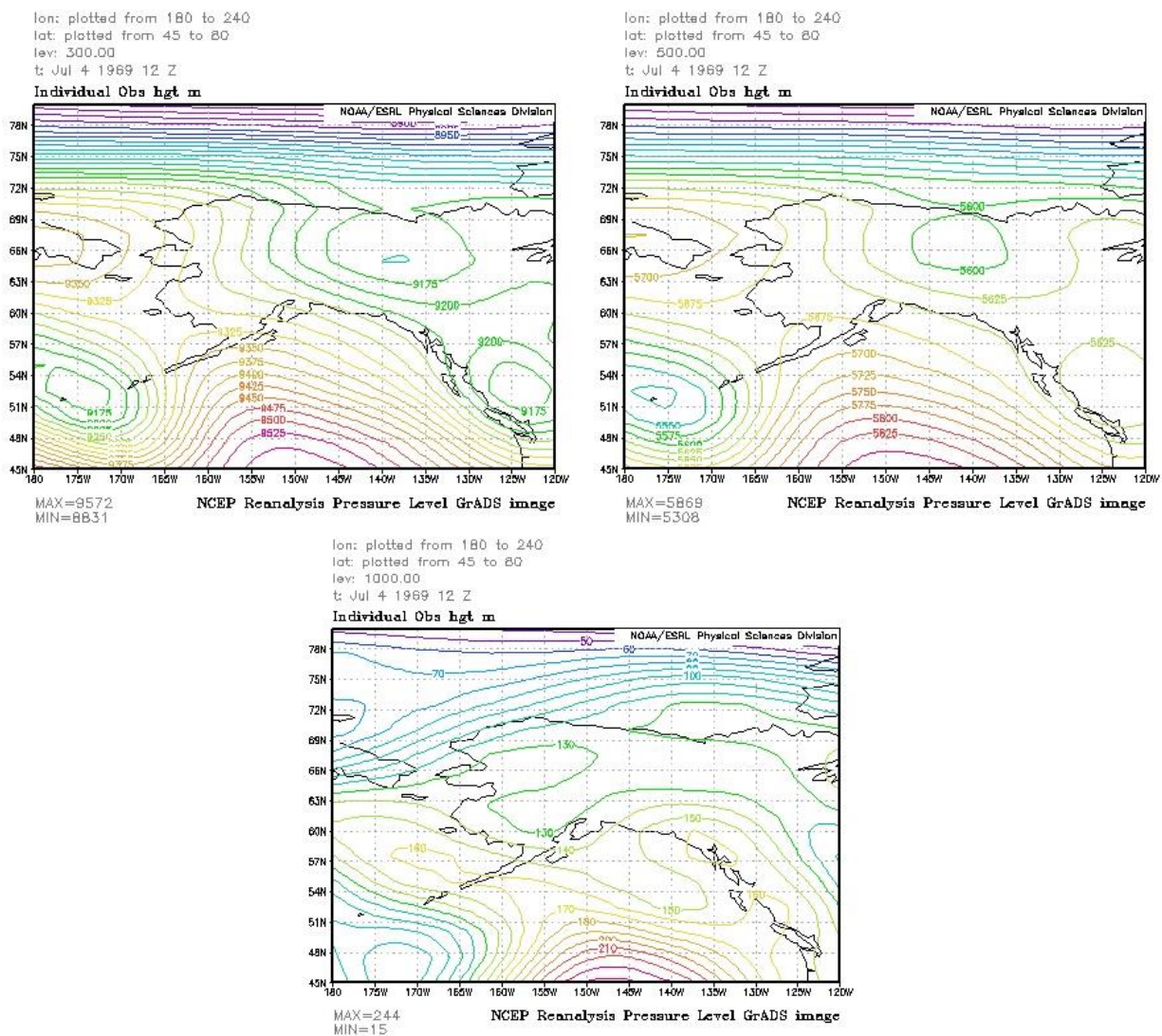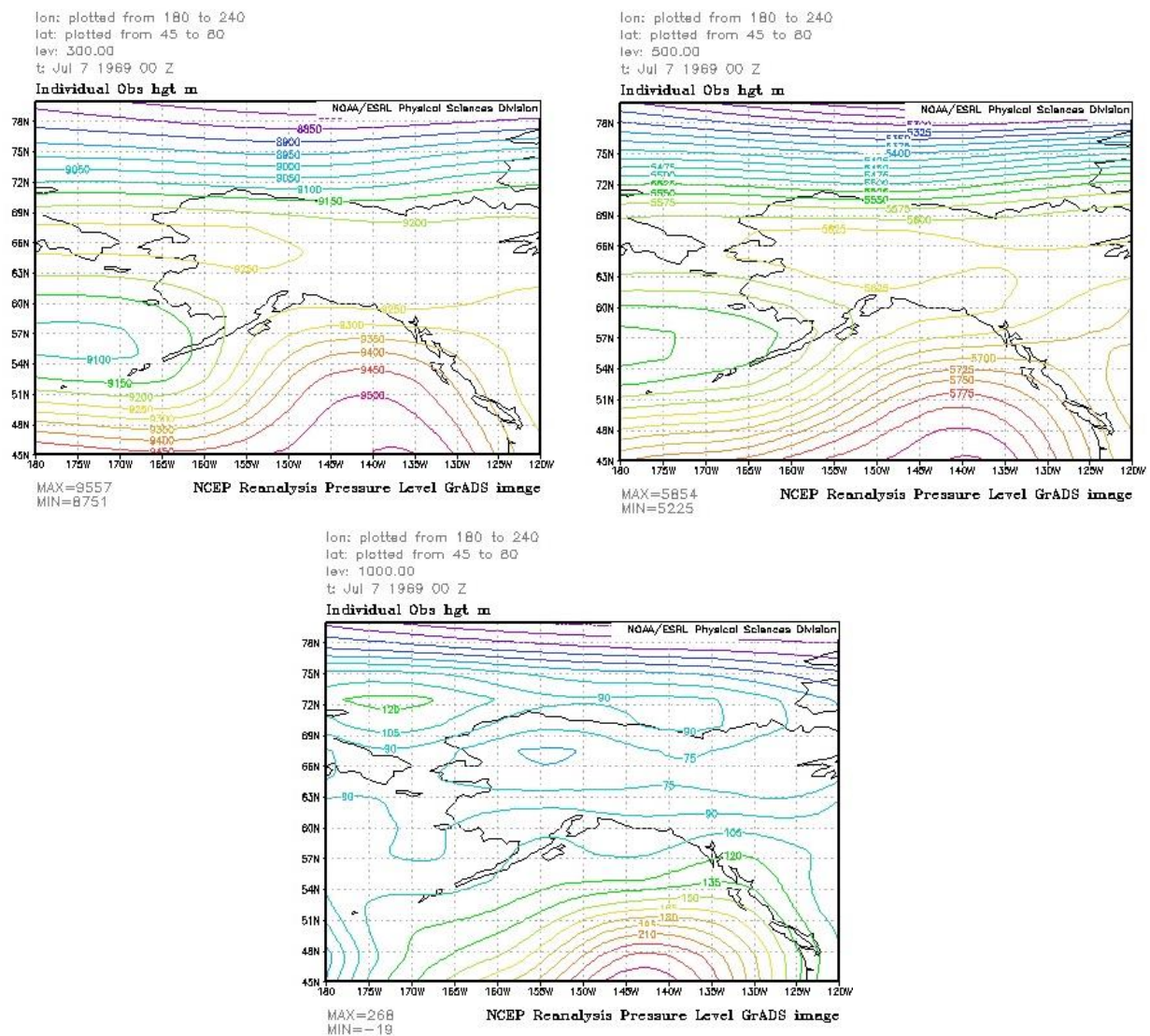
Fig. 3.43d. Geopotential heights at the 300 hPa (top left), 500 hPa (top right), and 1000 hPa map (bottom) according to the reanalysis data of the funnel cloud events for the Anchorage group 3. July 7 1969 00z.

Fig. 3.43e. Geopotential heights at the 300 hPa (top left), 500 hPa (top right), and 1000 hPa map (bottom) according to the reanalysis data of the funnel cloud events for the Anchorage group 3. July 28 1980 00z.
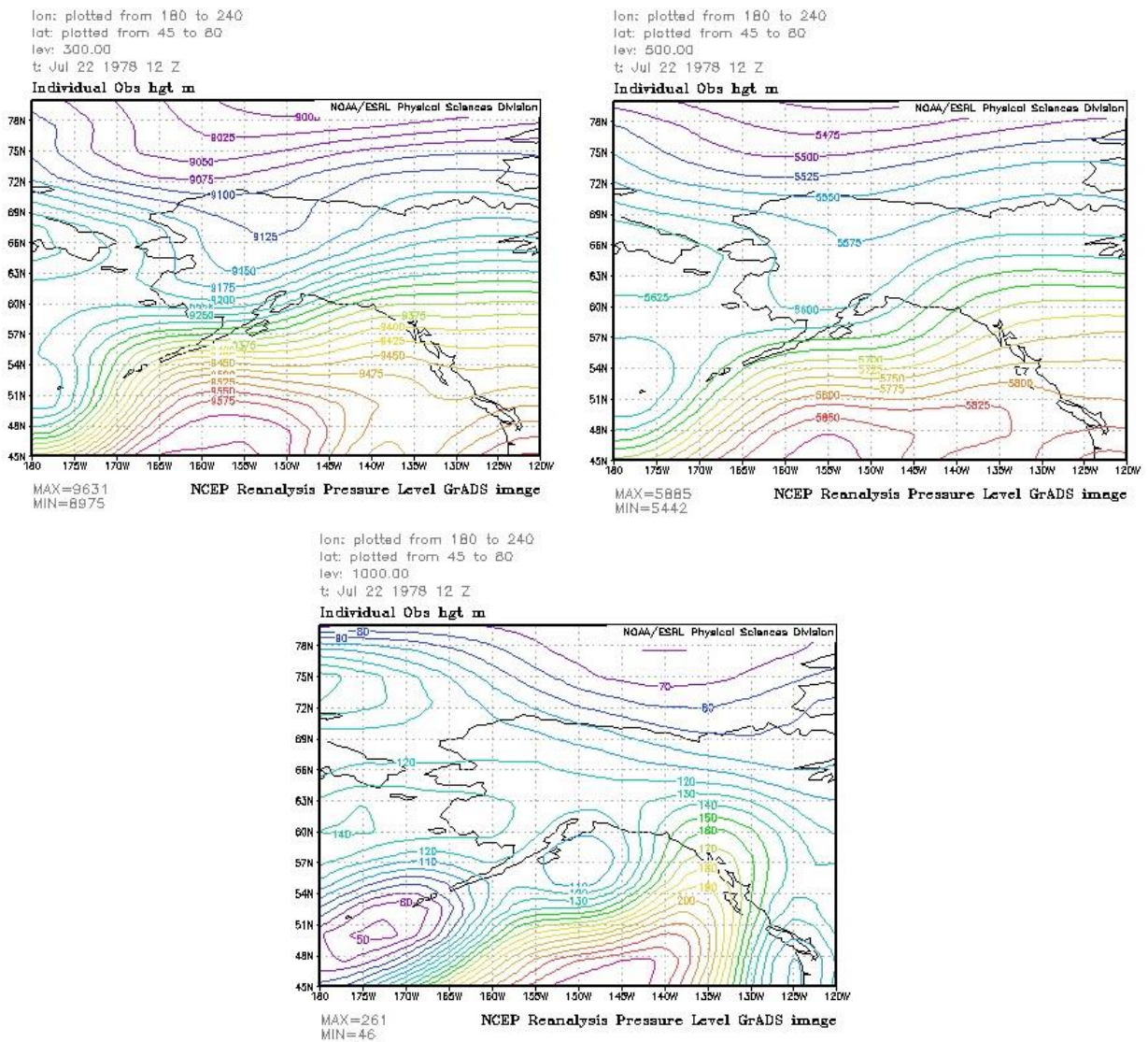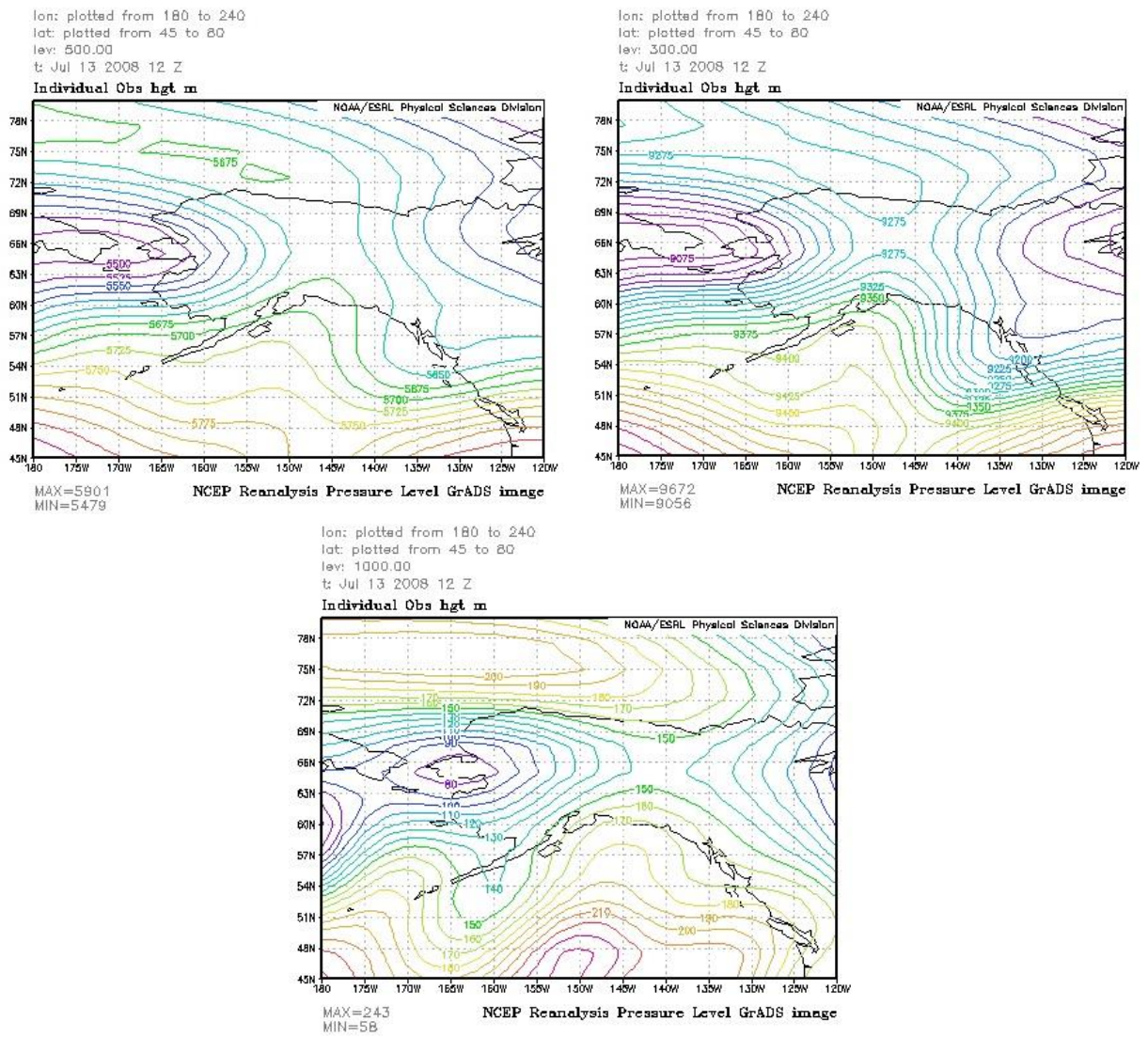
Fig. 3.43f. Geopotential heights at the 300 hPa (top left), 500 hPa (top right), and 1000 hPa map (bottom) according to the reanalysis data of the funnel cloud events for the Anchorage group 3. July 13 2008 12z.
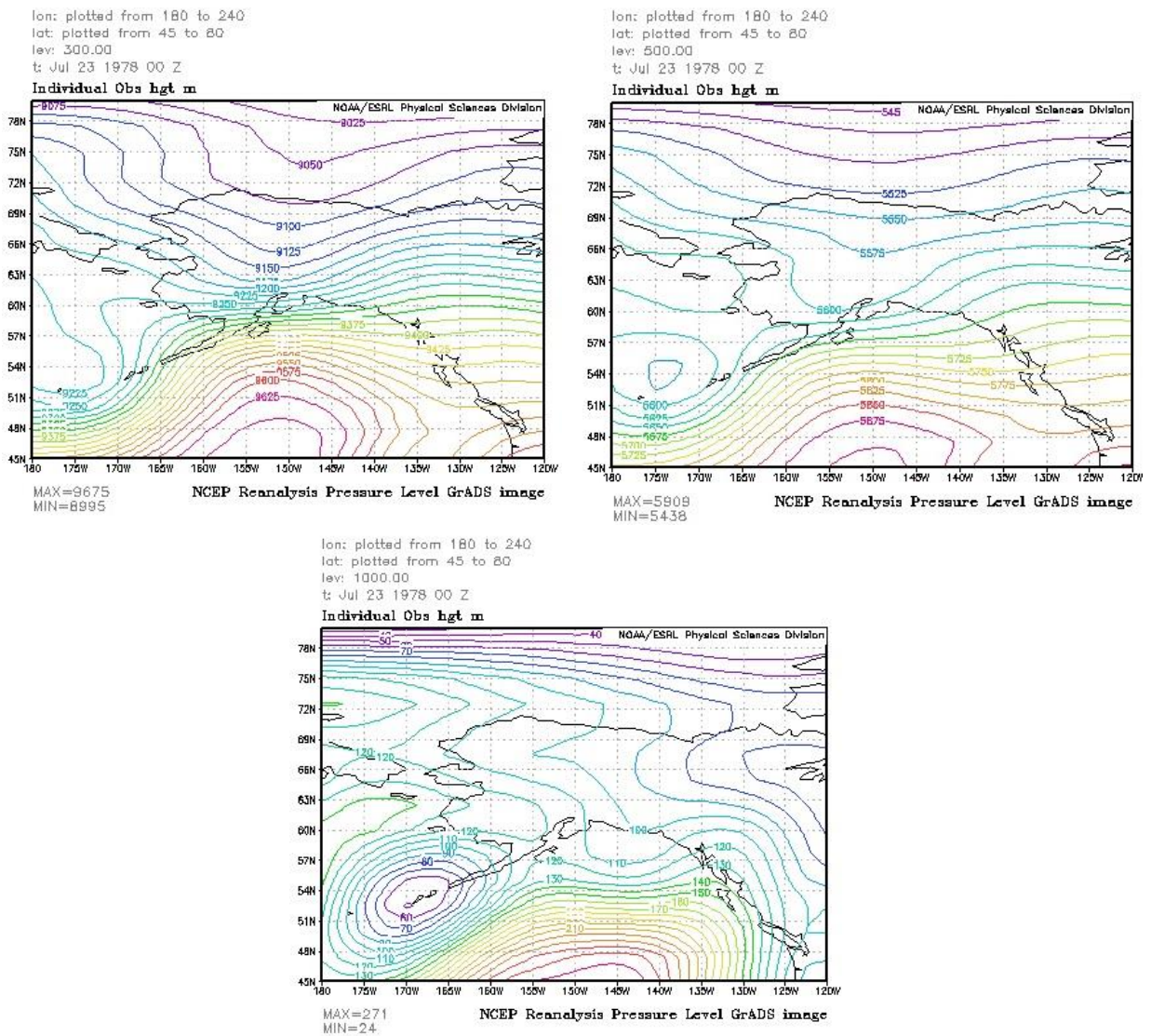
148
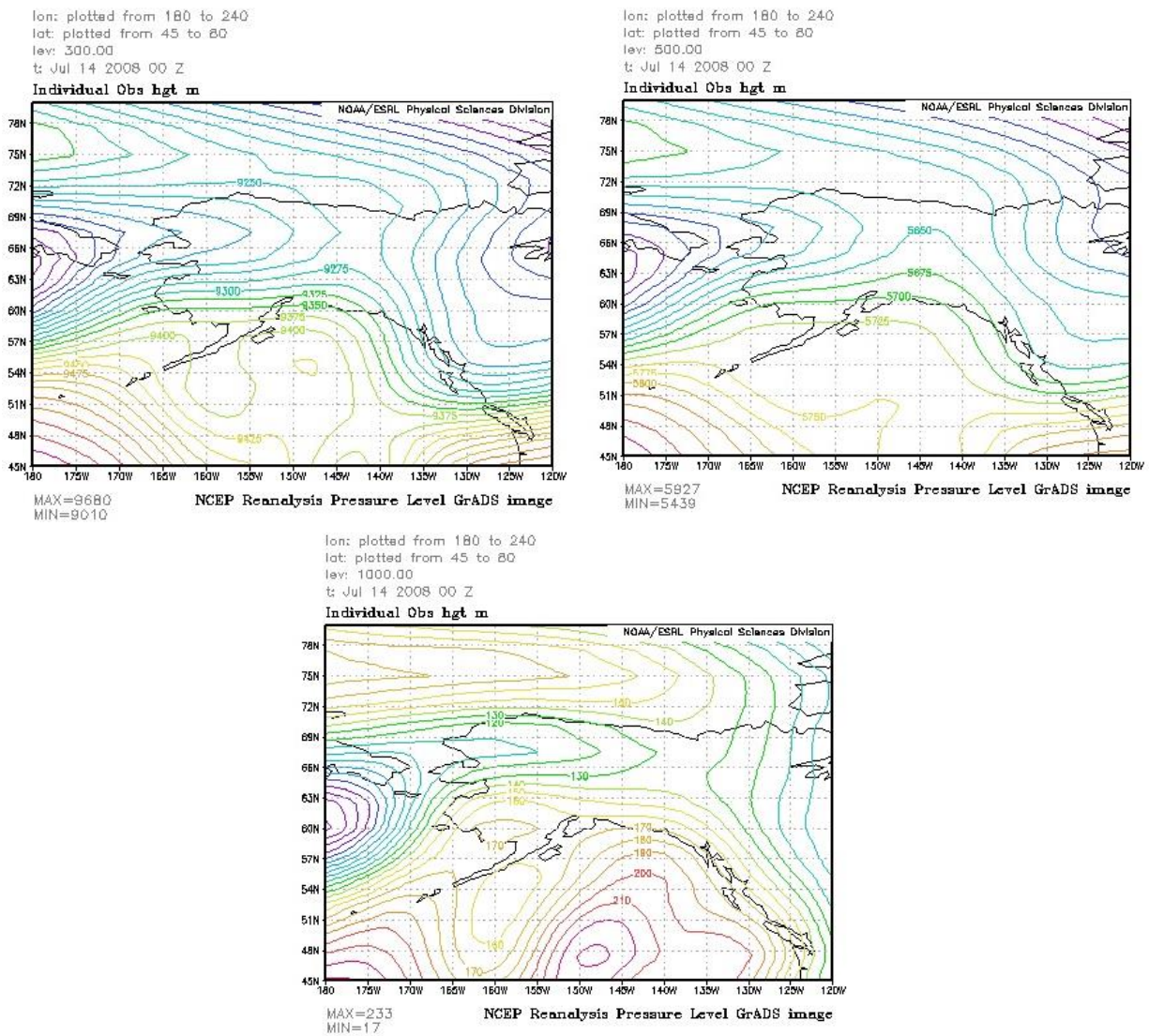
Fig. 3.43g. Geopotential heights at the 300 hPa (top left), 500 hPa (top right), and 1000 hPa map (bottom) according to the reanalysis data of the funnel cloud events for the Anchorage group 3. July 14 2008 00z.
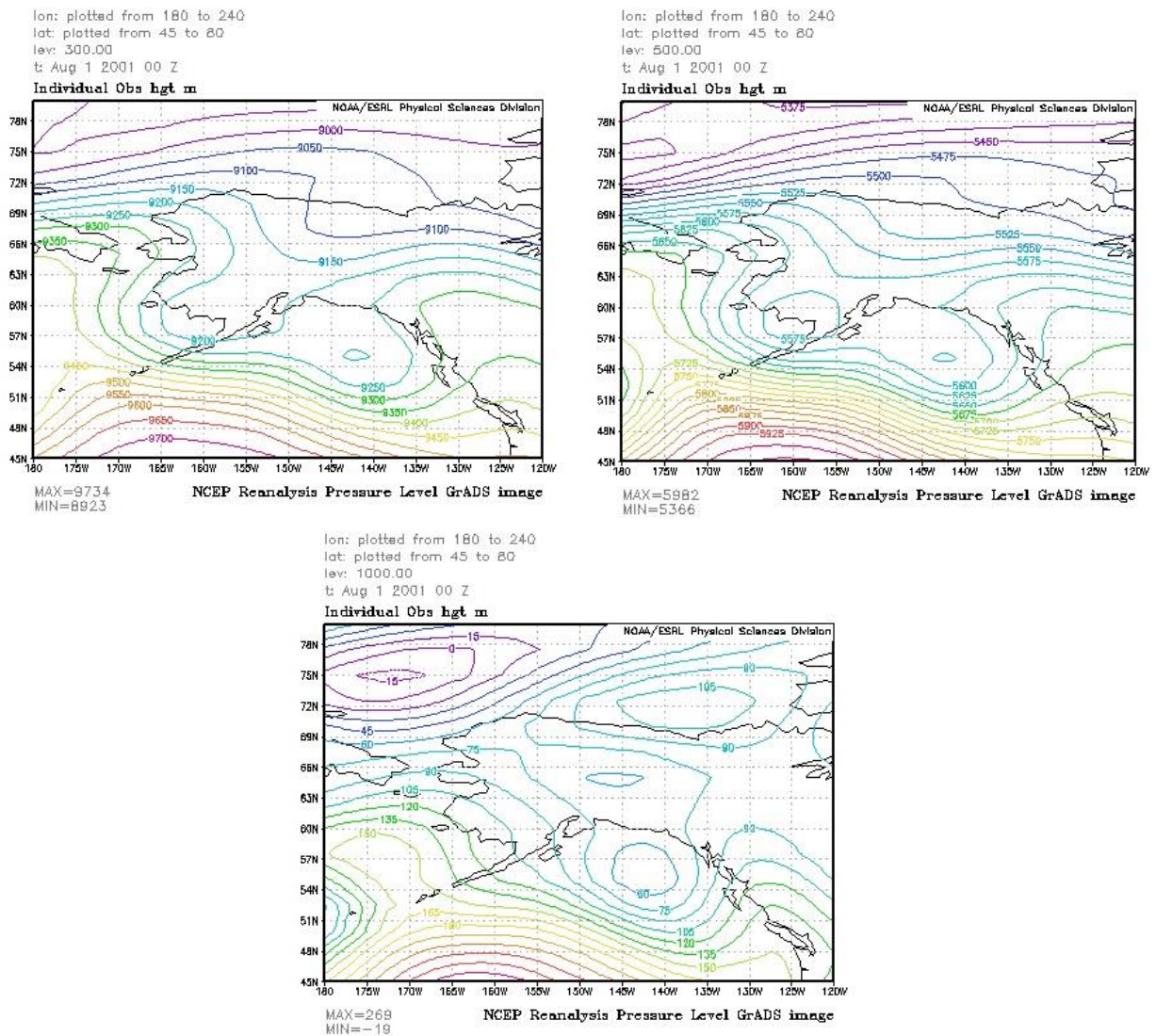
Fig. 3.43h. Geopotential heights at the 300 hPa (top left), 500 hPa (top right), and 1000 hPa map (bottom) according to the reanalysis data of the funnel cloud events for the Anchorage group 3. August 1 2001 00z.
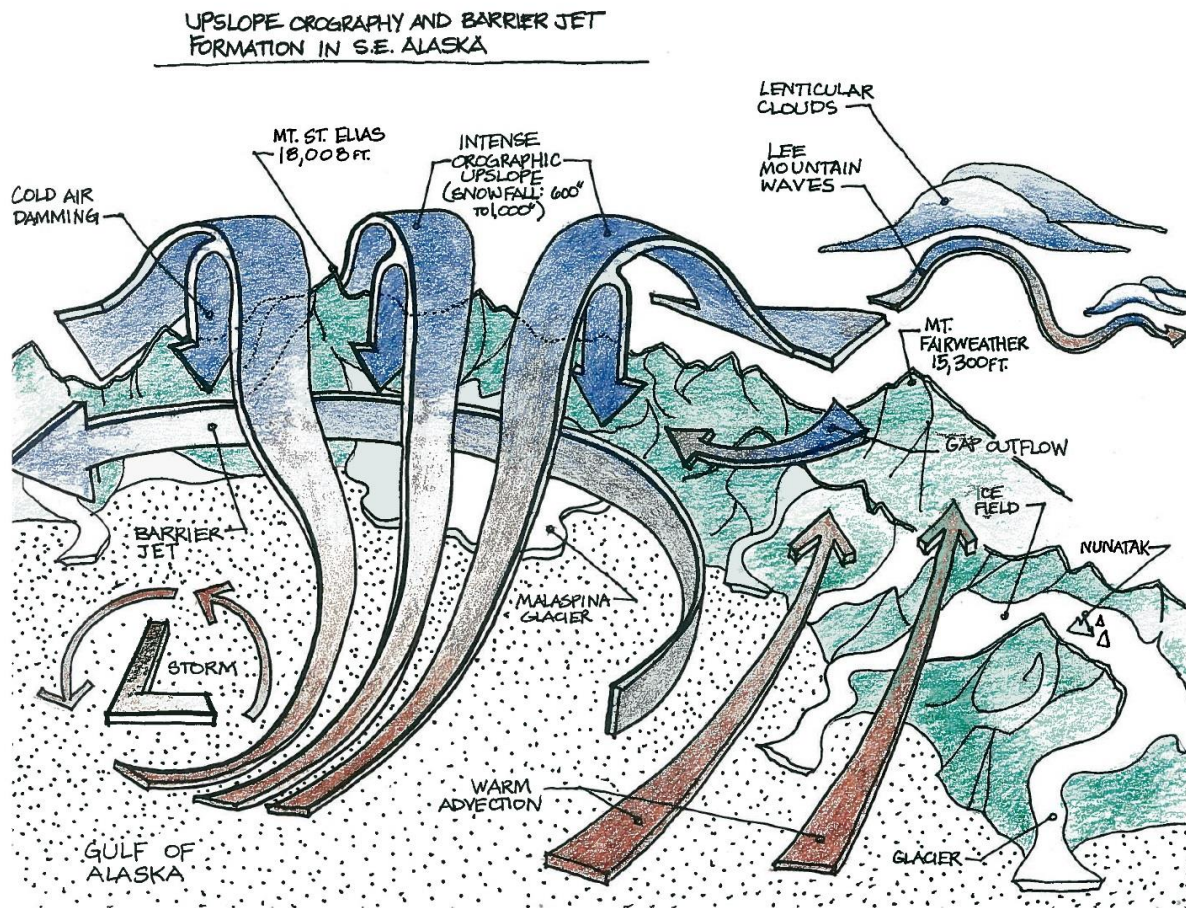
Fig. 3.44. Schematic 3D view of potential mechanism: with permission from Derek Starkenburg. Red and blue indicate warm and cold air.
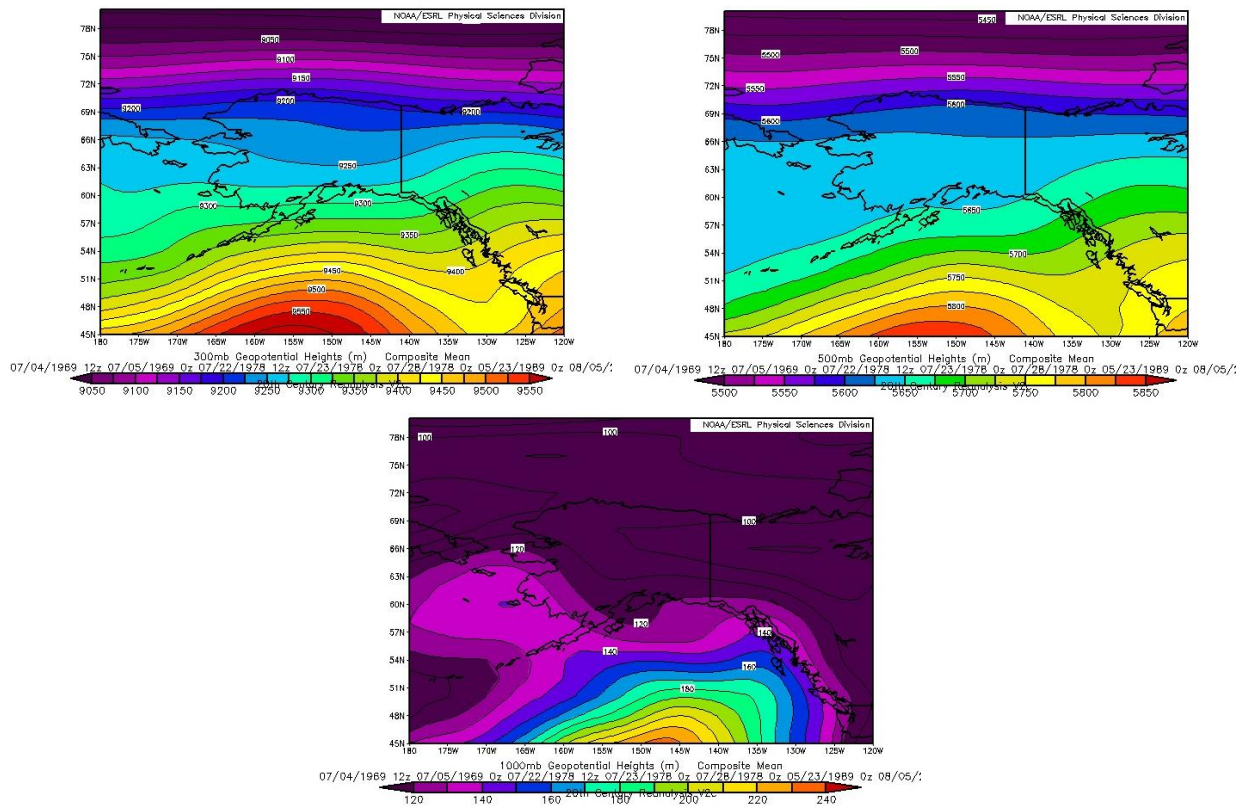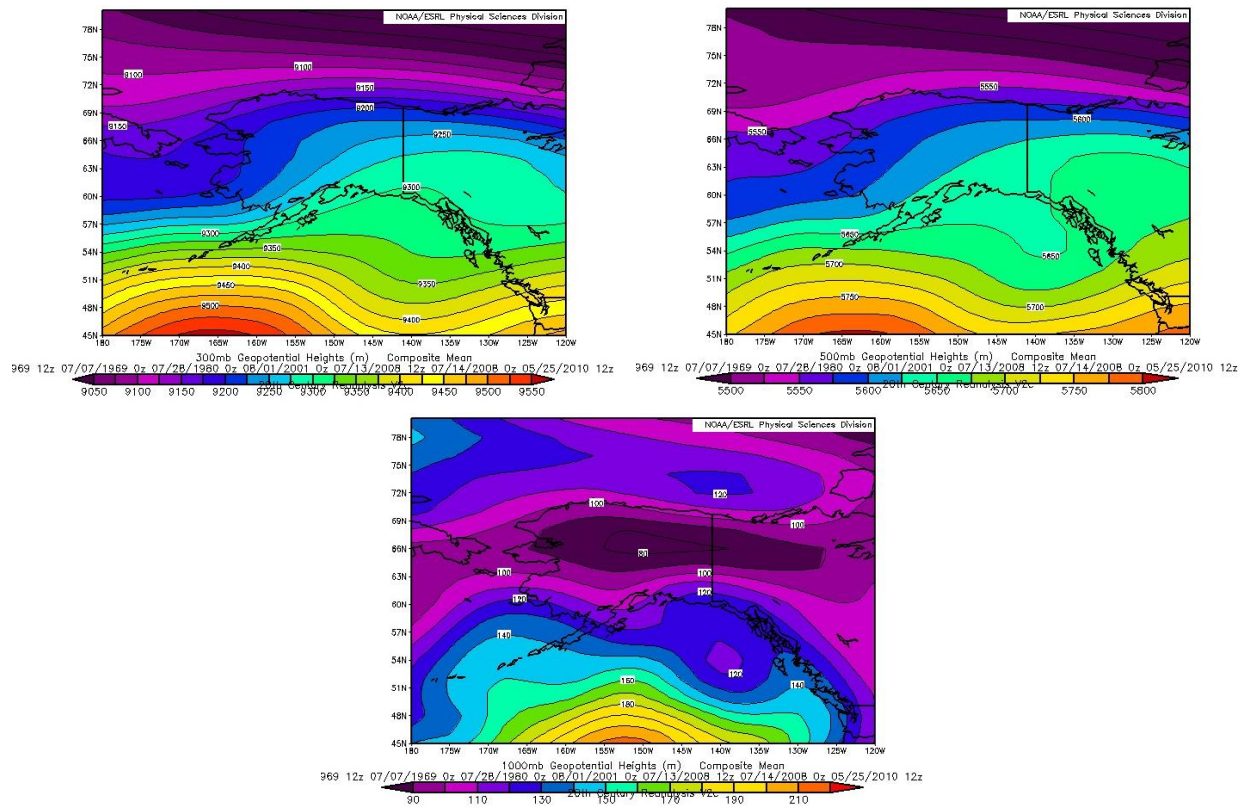
Fig. 3.45a. Composites of mean geopotential heights at the 300 hPa (top left), 500 hPa (top right), and surface map at 1000 hPa (bottom) of days with funnel cloud sightings for the observed Anchorage group-3.
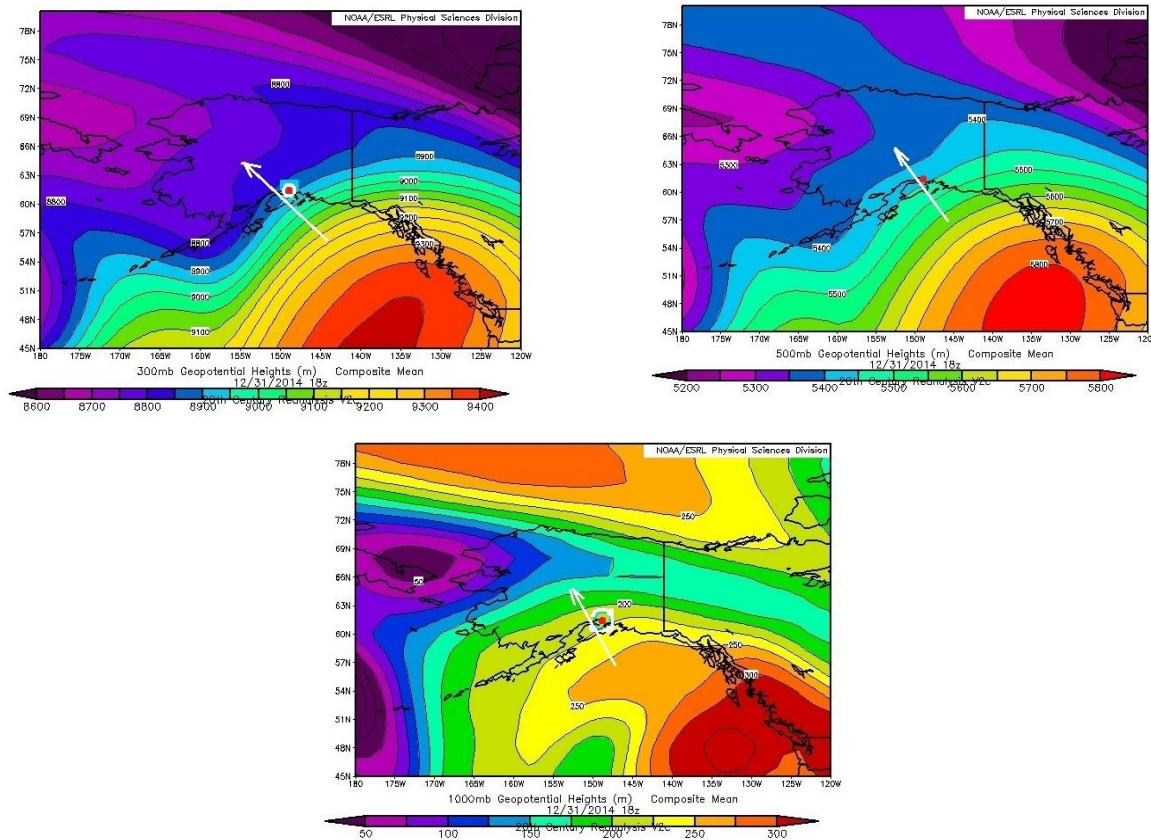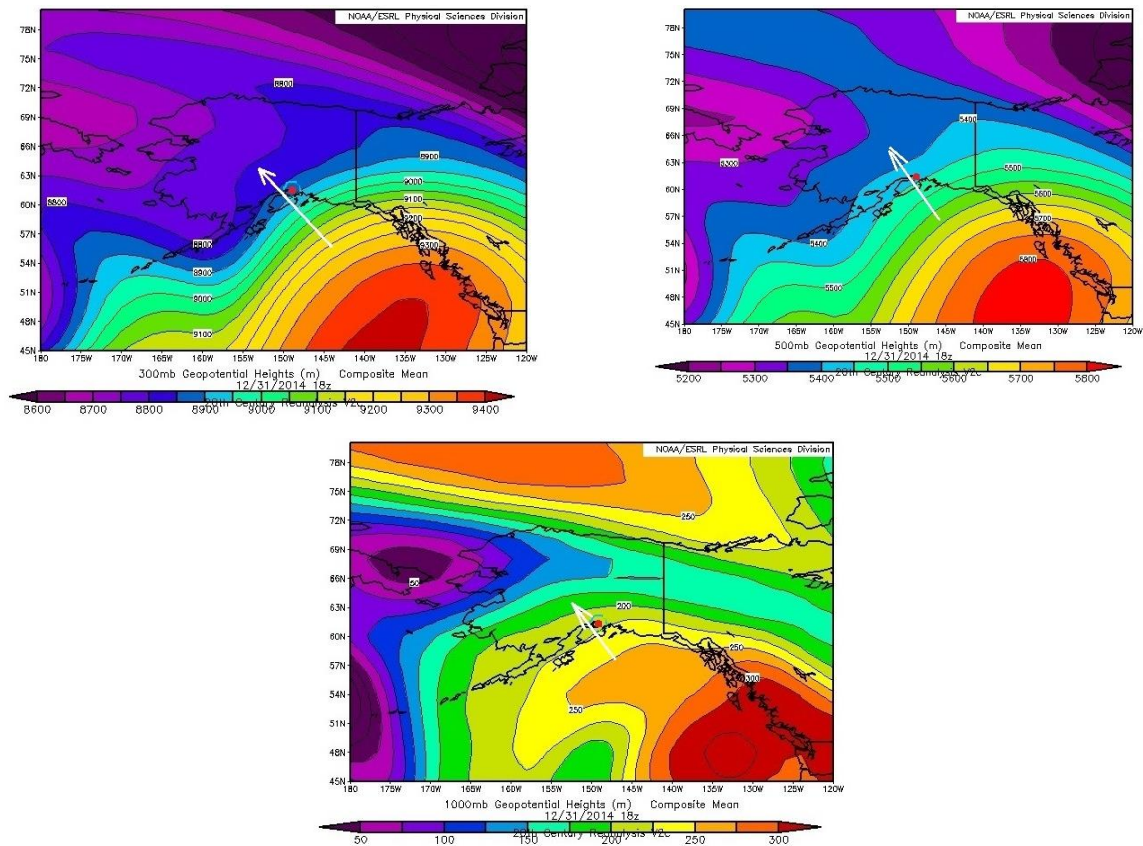
Fig. 3.45b Composites of mean geopotential heights at the 300 hPa (top left), 500 hPa (top right), and surface map at 1000 hPa (bottom) of days identified by the search algorithm as having similar profiles like those of funnel cloud events for the observed Anchorage group-3.

Like for the Anchorage group 2, the composite synoptic maps of real and potential funnel cloud situations appear similar at all pressure levels investigated for the Anchorage area, suggesting also synoptic influence.

3.8 Trend Analysis

As pointed out before, the soundings started as early as 1948. Unfortunately, the early data have no dew point temperature records. Therefore, the developed a search algorithm could not be applied for data before 1971. All 30-year climate periods that could be constructed from the available valid data would overlap. This means that I cannot assess the change in frequency in potential funnel clouds from one 30-year climate period to the next independent 30-year climate period. The same is true for the frequency of cases exceeding various CAPE threshold values. Therefore, the World Meteorological Organization definition of change from one independent 30-year climate period to the next independent 30-year climate period could not be applied to discuss changes.

In an attempt to address the question whether the increased availability of devices for documentation and increase in population may bias funnel cloud climatology, I calculated a linear trend over the timeframe of available data for all sites considered. The respective equations are displayed in Figure 3.47.

Fairbanks CAPE>500   y=-2E-06x+5869.8

McGrath CAPE>500   y=-4E-06x+9522

Bethel CAPE>500   y=-7E-06x+14472

Anchorage CAPE>500   y=-4E-06x+17217

Denali CAPE>500   y=-9E-06x+20433

155
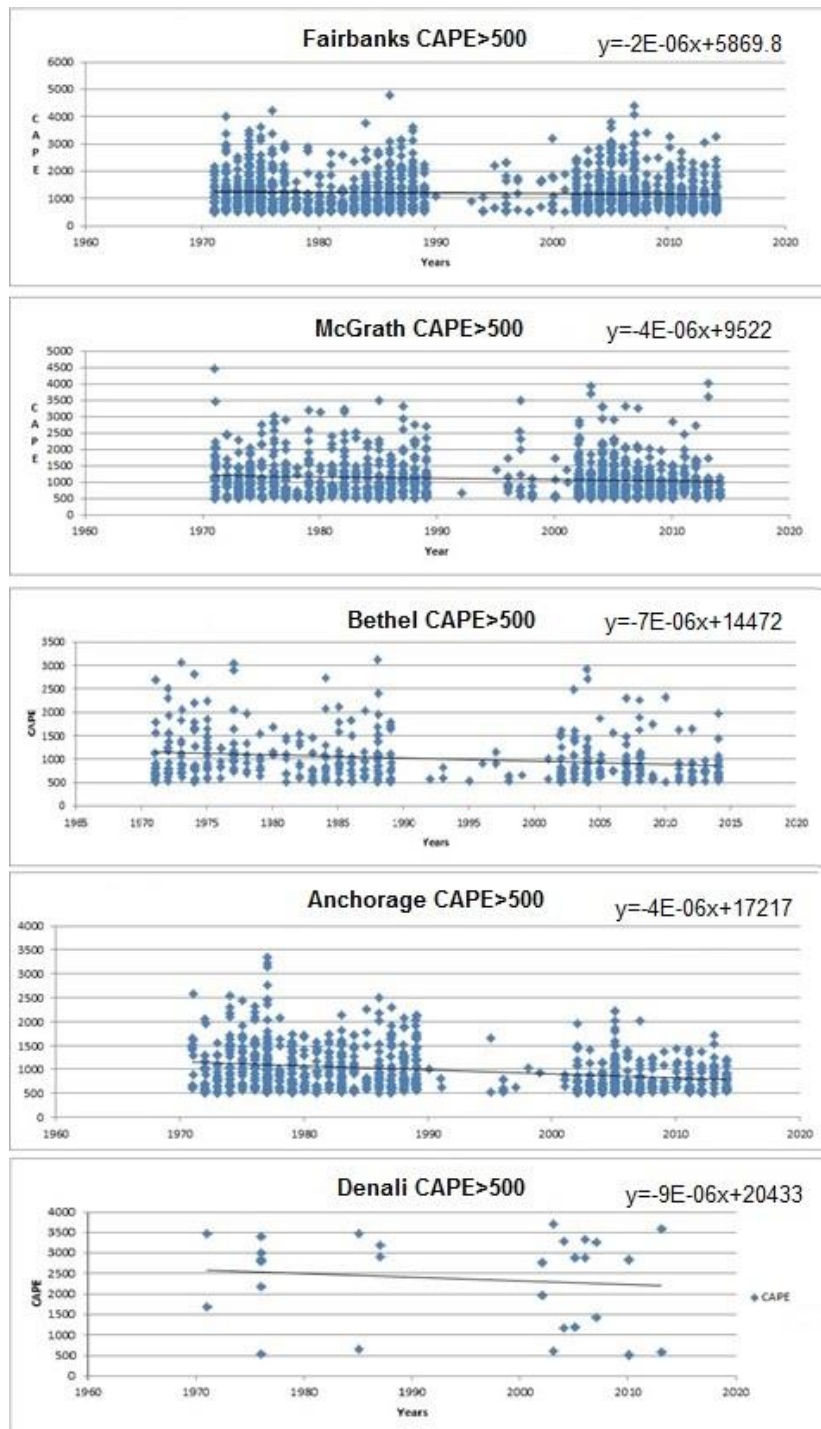
Fig. 3.46. Trend lines on CAPE and year results of all groups search algorithms results, with the exception of the Alaska West Coast that has only one result in common. In the Bethel group on the date of the 3rd July 1972 00Z UTC, Bethel's CAPE = 1563.4 J and Nome's CAPE = 3625.1 J.

Interestingly, there is barely a trend in CAPE for Fairbanks, while McGrath, Bethel, and Denali show decreasing CAPE as time progresses (Fig. 3.49). This finding confirms that in the Fairbanks area, funnel cloud formation is strongly governed by local effects. The decreasing trends for the other sites may suggest that the record of the NWS is biased by the availability of devices for documentation as the number of profiles similar to funnel cloud profiles actually decreases.

3.9 Uncertainty due to Data Resolution

As pointed out in section 2.3, I examined the loss in information caused by the need to homogenize the radiosonde data. In doing so, the search algorithm was run for the higher vertical resolution data without the limitation to pressure ranges, height, wind direction nor wind velocity. The comparative search algorithm was limited to temperature and dew point and the results were of no significant change except in where the trend line begins.
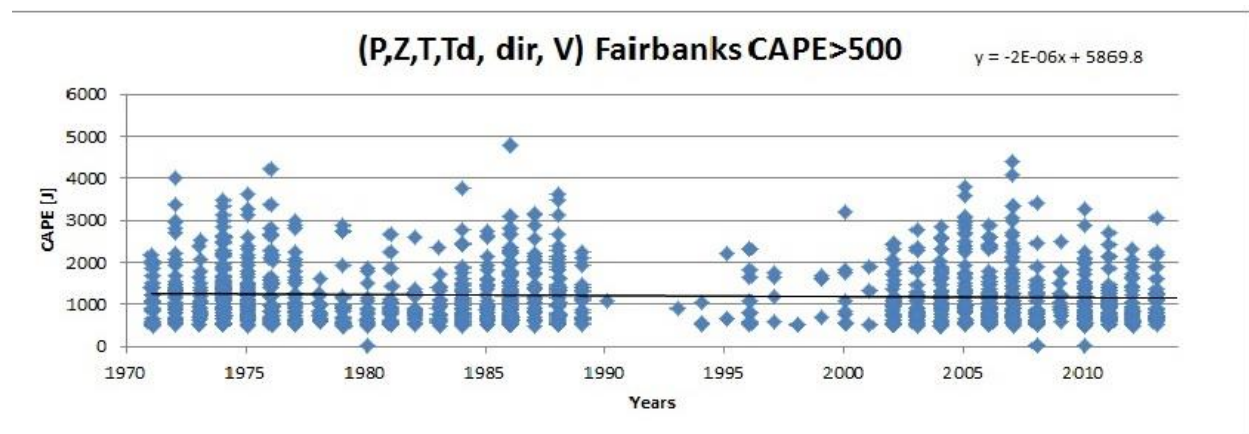
Fig. 3.47a. Two methods of variables used, a) is the stringent algorithm in which this research is based, b) is another method in which only two variables are utilized as the limit sitters.
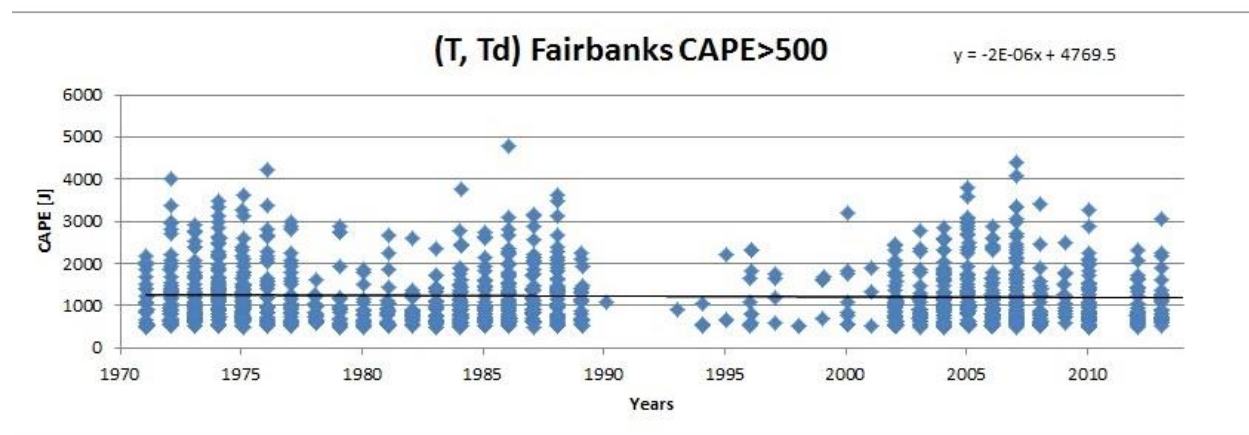
Fig. 3.47b. Continue.

In comparison of the results of the measured variables used from the radiosonde data, in figure 3.48a all the measured values had to exist and be real before being used, in the second run only the temperature and dew point was required to be real. This procedure resulted in a greater number of pressure level data being used for the less stringent requirement per radiosonde launch in comparison to the algorithm requirement of all measured variables must exist before that pressure level is used.

In comparison, whether two variables or all are used to determine what data was usable in this research, did not change the result. The reason is that temperature and dew point temperature are the main variables used.

Chapter 4 Discussion

Based on the limited observational data available and the enhancement of the data by potential funnel cloud events based on similarity testing, I have to conclude that both topography and land-sea breeze play central roles in Alaska's funnel cloud development from non-supercell storms. However, other factors influence whether and where they occur. All data suggest that the large-scale synoptic forcing at the 500 hPa and below must be weak.

Land-sea contrast leading to sea- or land breeze in conjunction with weak synoptic forcing perpendicular to the Alaska West Coast occurred during real and potential funnel cloud events for Bethel, and Nome. Topography and cold down-slope air with surface valley winds in the Interior with little to no upper synoptic forcing played a role for funnel cloud formation in the Fairbanks, Denali, and McGrath group. Both types of mesoscale forcing, land-sea contrasts and topography, played a role in Anchorage Cook Inlet valley, dependent on location over the Anchorage region. Again, the synoptic scale forcing had to be weak enough for the landscape to take control on the circulation in the ABL and hence permit funnel cloud formation.

In the Fairbanks group, all funnel cloud events occurred along the northern portion of the Tanana Valley around Fairbanks. This fact seems to be a key in the type of mechanism and dynamics at work in Fairbanks funnel cloud development. The Tanana Valley is broad at Fairbanks with many small hills out in the valley. The following hypothesis describes the dynamics at work: cold air flows down the slopes of the Alaska Range into the Tanana Valley. When encountering the comparatively warmer, humid air in the valley horizontal vorticity is created. The valley wind blows from the Southwest and stretches the horizontal vorticity northeastward into the Tanana Valley Flats. It is here where the stretched vorticity encounters the small hills, or buoyancy columns from updrafts. The hills and convection currents in the central portion of the Tanana Valley Flats force the vorticity tubes upward after overcoming the CIN. The small magnitude of surface vorticity, as found in the Skew-T diagrams, maintains the vorticity column. As clouds form, the vorticity becomes visible as funnels in these non-supercell clouds.

All the radiosonde Skew-T diagrams hint at the development of non-supercell clouds and at wind shear in the ABL, which is an integral part of the funnel clouds' dynamics. The 1000 hPa synoptic maps suggest wind's from southwest blows into the valley and forces the rotating column towards the Fairbanks and North Pole area. It is the White Mountain northern wind that limits the northward motion of the funnel cloud. This feature is unique to the funnel cloud events and potential funnel cloud events of the Fairbanks group.

The other group of funnel clouds also formed in the Tanana Valley is the Denali group. They occurred more along the southwestern part of the valley and along the Alaska Range slope. It is

this difference in location that determines the way funnel clouds are developed under little or no synoptic scale forcing. For the Denali group, funnel cloud development is similar to the one described for the Fairbanks group with the exception that the valley is not as broad as the Tanana Valley and the funnel clouds develop over the northern slope face of the Alaska Range. As the cold air of the Alaska Range drains downslope and encounters the warm, humid air in the valley, horizontal vorticity tubes develop. The heterogeneity of land-surface cover in the valley leads to differential heating and supports convection formation.

The surface valley wind stretches the horizontal vorticity of the air. When the horizontal vorticity is either affected by an Alaska Range slope wind, small ridge, or encounters a convective updraft, the former horizontal vorticity turns into a vertical vorticity column. Again, the upward motion turns the vorticity tubes upward. After overcoming the CIN, and when saturation is reached the rising air can develop into a funnel cloud along the northern slope of the Alaska Range in the southern region of the Tanana Valley floor.

The McGrath group has a different topographical setting than the Fairbanks and Denali groups, though all groups have similar atmospheric characteristics of the same region and fauna in common. The mountains on both sides of the valley are close together with McGrath being located in the northern portion of the valley. All funnel cloud sightings occurred along the southern part of the valley, i.e. over the northern slope of the Alaska Range. Due to the close proximity of the two mountain ranges at McGrath, funnel clouds develop directly from the southwest to northeasterly lower level winds in conjunction with vorticity shears in the lower ABL, when the cold downslope air from the Alaska Range encounters the warm humid air of the McGrath valley.

The funnel cloud formation of the Bethel and Alaska West Coast groups is more representative of the mechanism in the Lower 48 states with the exception that the funnel cloud development occurs in non-super cell thunderstorms. An inland (sea-breeze) and seaward (land) wind occur at the 500 hPa levels, driving the two air masses together, and the 1000 hPa, surface pressure levels has a coastal wind that flows parallel to the Alaska West Coast.

Based on the findings of this study, I conclude that funnel clouds can be forecasted, as to what extent in lead-time would require a more extensive analysis than is possible within the timeframe and scope of an MS thesis. Using synoptic map characteristics, and further studies on the forcing and wind dynamics of each location could make funnel clouds predictable in Alaska. For example: Anchorage's numerous funnel cloud sightings over the years is key. I grouped these sightings based on distance from a single radiosonde launch sight, which from a terrain and landscape perspective and potential mesoscale forcing point of view is required. Unfortunately, there is only one radiosonde site for which developing ranges for the different landscape features did not work.

While this finding at first glance suggests that the three Anchorage grouping based on radiosonde distance is a mistake, on further inspection, it documents that the Anchorage radiosonde in the lower ABL is strongly affected by local effects on days with funnel cloud sightings. This finding is confirmed when analyzing the reanalysis maps. Using the results of the synoptic analysis, the Anchorage valley can be grouped into four common groups based on location and topography.

The first group would be around the Cook Inlet including Anchorage. Here a land-sea breeze zone influenced by the mountains as well seems to create the vorticity. The second group covers the funnel cloud events along the southern slopes of the Alaska Range up to the Aleyeska Valley. For this group the topography, downslope cold air drainage (katabatic wind), and valley winds are the mesoscale forcing mechanism for vorticity creation and under saturated conditions, funnel cloud formation. The third group encompasses the funnel cloud sightings in and around Aleyeska Valley, Palmer and adjacent land surfaces. This area is also influenced by valley winds and topography initiated cold air flowing downslope (katabatic wind). The shear between these katabatic winds and the valley wind produce the vorticity that becomes visible in form of funnels when saturation is reached. The fourth and last group would be the northern slopes of Kenai Peninsula. Again, here topography and katabatic winds create the initial vorticity.

These groupings should give a better and more singular synoptic map that can be utilized as a predictor. Future field studies looking for vorticity in the ABL can ascertain the exact forcing and winds necessary for funnel cloud development. Such studies are needed for shortening the lead-time to forecast such an occurrence.

Chapter 5 Conclusion

In this thesis, I used radiosonde, radar, and reanalysis data to develop climatology of funnel clouds in Alaska, and assess changes over the time of available data as well as to propose potential mechanisms that cause funnel clouds in Alaska.

My motivation for this study was driven by the idea that the increase in sightings of tornados in the South East of Alaska and funnel clouds in the Interior could be caused by climate change. In this case, a further question would be whether further increases in climate change could mutate the funnel clouds now being recorded in the Interior into a more destructive weather phenomenon, namely tornados within the Interior of Alaska. As pointed out in the introduction, answering this question was beyond the scope of this thesis that had the goals to

- examine the climatology of funnel clouds to create a baseline to which future events and any changes can be compared to, and
- search for potential mechanisms of funnel cloud formation in Alaska.

The documentation of funnel cloud events identified 43 cases, unfortunately, in quite different areas from a climate division perspective. To enhance the database of funnel cloud events, I developed an algorithm that searched all available radiosonde data for profiles that were similar to those of reported sightings.

Since synoptic forcing associated with funnel clouds in Alaska is thought to be much weaker than in the Lower 48 states, I hypothesized that the wind shear necessary for the maintenance of severe thunderstorms does not come from a cold front, and a dryline like in the Great Plains, but from local circulations initiated from the terrain. This means that the terrain might play an important role in the formation of funnel clouds. The results showed the following: In the coastal terrain, in which the Yukon River and the Kuskoquim drain into the Bering Sea, land-sea interaction plays a role in the funnel cloud formations along the western coast of Alaska. Within the Interior, terrain plays a more prominent role most especially along the valleys between the mountain ranges and in which large drainage rivers flow. Along the southern coast, a combination of both land and sea interaction in conjunction with terrain forcing is the dominating forcing mechanism.

A fundamental step in identifying potential mechanisms for funnel cloud formation is to answer the question whether funnel cloud formation is influenced by synoptic scale forcing. The reanalysis maps of the 300 hPa, 500 hPa and 1000 hPa pressure surface on days of sightings were compared to the composite maps at these pressure level that were created by averaging the reanalysis data for days that were identified as having potential funnel cloud events. The comparison showed that all observed as well as the potential funnel cloud events shared common weak synoptic scale

forcing over the region of the radiosonde area. Thus, a major pre-requisite of my hypothesis that the topography and landscape causes funnel clouds is fulfilled.

The question whether the number of funnel cloud occurrences may be higher than reported could be answered by use of the search algorithm I developed within the framework of my thesis. The algorithm searches for similar radiosonde profiles to the profiles during funnel cloud events. Based on the results of this algorithm one has to conclude that there may here been more funnel cloud events than those being reported.

Unfortunately, the radiosonde dataset missed dew point temperature data prior to 1971 and does not start before 1948. However, the analysis of the valid data suggests that there have been funnel clouds or products of greater vigilance at least since 1971. However, no such reports occur in the reports of Elders (USA TODAY, 2005).

Based on the results of the search algorithm, the number of potential funnel cloud situations decreased for some areas. Thus, the question on whether the increase in reported funnel cloud events is due to the increase in population and devices for documentation answered with yes. This means that one has to conclude that the NWS/NOAA record has to be biased and underestimated past events.

The question whether funnel clouds are associated with thunderstorms of a given magnitude was examined by determining the CAPE. All funnel cloud events had CAPE greater than 500 J. However, according to the radiosonde data, the clouds did not reach through the entire troposphere up to the tropopause. On the contrary, the dew point temperature profiles suggest boundary layer clouds.

The question on the dynamics and thermodynamics that are forcing these funnel clouds was addressed within the framework of the analysis of the reanalysis data and radiosonde data. Creation of vorticity by mesoscale motions under weak synoptic conditions and breaking of a capping inversion as well as CAPE greater than 500 J were the thermodynamic and dynamic features. Buoyancy is created by differential heating due to the spatial patchiness of the land-cover.

The different role of importance of wind direction at pressure altitude of 500 hPa and the ABL, and CAPE, means terrain is more important; thermodynamic conditions are also more important respectively. The analysis of frequency of CAPE events showed a correlation to the NPI for Fairbanks. Based on this finding one has to conclude that in the Fairbanks area, CAPE is related to the large-scale circulation.

The question, whether funnel clouds of low magnitude velocities and/or cross-sectional area are detectable and, hence, predictable by operational observations was addressed through the analysis

of radar data. Unfortunately, their resolution is too coarse to be used unless the event occurs close enough to the radar. However, the radiosonde data in combination with synoptic maps can be used to at least identify days on which funnel clouds could form.

Alaska's funnel clouds fall under the heading of land spouts in Table 1.2, yet at the lower values of the ratings given in Table 1.2, i.e. visual appearance are mostly, from visual records, just below the cloud as the beginning of a funnel, some can be mistaken for cold down welling and rain falling from the clouds. However, there are some, mostly in the Anchorage region that do represent rope like funnels. For the F-scale F0 to F1 depending on location, the majority would be F0. For the category of location of storm in Table 1.2, the rapidly rotating updraft near convergence boundaries is more in the order of slower rotation and vorticity near a convergence boundary. Circulation depth was not determined, but I would speculate that it would be a low value. Radar detection is not possible, unless you know exactly what you're looking for and radar is ineffective at long distances. No recorded property damage has been documented as of the writing of this thesis.

References

Bieniek, P. A., U. S. Bhatt, R. L. Thoman, H. Angeloff, J. Partain, J. Papineau, F. Fritsch, E. Holloway, J. E. Walsh, C. Daly, M. Shulski, 2015; Dynamical downscaling of ERA-Interim temperature and precipitation for Alaska, Journal of Applied Meteorology and Climatology, American Meteorological Society, vol. 55, issue: 3, page: 635-654, issn: 1558-8424, 1558-8432, doi: 10.1175/JAMC-D-15-0153.1.

Bieniek, P. A., **U.S. Bhatt**, R.L. Thoman, H. Angeloff, J. Partain, J. Papineau, F. Fritsch, E. Holloway, J.E. Walsh, C. Daly, M. Shulski, G. Hufford, D.F. Hill, S. Calos, and R. Gens, 2012: *Climate divisions for Alaska based on objective methods*, J. Applied Meteorology and Climatology, **51** (7), 1276-1289

Bluestein, H. B., 1985, An observational study of a mesoscale area of convection under weak synoptic-scale forcing. Mon. Wea. Rev., 113, 520–539. doi: http://dx.doi.org/10.1175/1520-0493(1985)113<0520:AOSOAM>2.0.CO;2

Cassano, E. N., and J. J. Cassano, and M. Nolan, 2011, Synoptic weather pattern controls on temperature in Alaska, J. Geophys. Res., 116, D11108, doi:10.1029/2010JD015341.

Cooley, J.R., 1978, Cold air funnel clouds. Mon. Wea. Rev., 106, 1368-1372.

Doswell, C. A., and D. W. Burgess, 1988, On some issues of United-States tornado Climatology, Mon. Wea. Rev., 116, 495-501. Doi 10.1175/1520-0493(1988)116<0495:Osious>2.0.Co;2

Durre, Imke,. Russell S. Vose, and David B. Wuertz, 2006, Overview of the Integrated Global Radiosonde Archive, National Climatic Data Center, Asheville, North Carolina, American Meteorological Society, DOI: http://dx.doi.org/10.1175/JCLI3594.1

Fujita, T. T, and R. M. Wakimoto, 1981, Five scales of airflow associated with a series of downbursts on 16 July 1980. Mon. Wea. Rev., 109, 1438–1456. doi: http://dx.doi.org/10.1175/1520-0493(1981)109<1438:FSOAAW>2.0.CO;2

Golden, J. H., 1974, Scale-interaction implications for the waterspout life cycle. II. J. Appl. Meteor., 13, 693–709. doi: http://dx.doi.org/10.1175/1520-0450(1974)013<0693:SIIFTW>2.0.CO;2

Houze, R.L., 1993, Cloud Dynamics. Academic Press, Inc. 1250 Sixth Avenue, San Diego, California 92101-4311

Hurrell, J. and National Center for Atmospheric Research Staff (Eds). 2012: Last modified 02 Mar 2016 The Climate Data Guide: North Pacific (NP) Index by Trenberth and Hurrell; monthly and winter. Retrieved from https://climatedataguide.ucar.edu/climate-data/north-pacific-np-index-trenberth-and-hurrell-monthly-and-winter. - See more at: https://climatedataguide.ucar.edu/climate-data/north-pacific-np-index-trenberth-and-hurrell-monthly-and-winter#sthash.svKv3rTc.dpuf

Lin, Y.-L., 2007, Mesoscale dynamics, Cambridge Univ. Press, Cambridge.

Modahl, A. C., and W. M. Gray, 1971, Summary of funnel cloud occurrences and comparison with tornados. Mon. Wea. Rev., 99, 877–882. doi: http://dx.doi.org/10.1175/1520-0493(1971)099<0877:SOFCOA>2.3.CO;2

Mölders, N., 2014; personal communication.

Mölders, N., and G. Kramm, 2014, Lectures in meteorology, Springer International Publishing, Switzerland DOI: 10.1007/978-3-319-02144-7.

OFCM: Federal Meteorological Handbook, No. 3 Rawinsonde and pibal observations, FCM-H3-1997, Washington, DC, 1997. DOI: http://www.ofcm.gov/homepage/text/pubs.htm

Pielke, R. A., Jr., 2005, Are there trends in hurricane destruction? Nature, 438, E11

Smith, R., 1996, Non-Supercell tornadoes: A review for forecasters Technical Attachment. NWSFO Memphis, SR/SSD 96-8. DOI: http://www.srh.noaa.gov/topics/attach/html/ssd96-8.htm

Shulski, M., and G. Wendler, 2007, *Climate of Alaska*. University of Alaska Press, 214 pp.

Thoman, R., 2014, personal communication.

USA TODAY, posted 8/2/2005, Rare tornado touches down in Alaska. USATODAY.com

Von Storch, H., and F. W. Zwiers, 2000, Statistical analysis in climate research. Cambridge University Press, Cambridge. ISBN 0 511 01018 4 virtual (netLibrary Edition)

Wakimoto, R.M., and J.W. Wilson, 1989, Non-supercell tornados. Mon. Wea. Rev., 117, 1113-1140, DOI: 10.1175/1520-0493(1989)117%3C1113:NST%3E2.0.CO;2.

Wilczak, J. M., D. E. Wolfe, R. J. Zamora, B. Stankov, and T. W. Christian, 1992, Observations of a Colorado tornado. part i: mesoscale environment and tornadogenesis. Mon. Wea. Rev., 120, 497–521. DOI: http://dx.doi.org/10.1175/1520-0493(1992)120<0497:OOACTP>2.0.CO;2